
From Supramolecular Self-Assembly to Two-Dimensional Covalent Organic Frameworks



Dissertation
der Fakultät für Geowissenschaften
der Ludwig-Maximilians-Universität
München

Jürgen Dienstmaier

München, den 19. September 2012

Erstgutachter: PD Dr. Markus Lackinger

Zweitgutachter: Prof. Dr. Wolfgang M. Heckl

Disputation: 25. April 2013

Abstract

The two main subjects of this thesis are the realization of supramolecular self-assembled monolayers at surfaces and the formation of surface-supported two-dimensional covalent organic frameworks. Both topics, albeit different, yield long-range ordered open-pore networks with quite different stabilities, depending on the strength and type of bonds holding them together. The surface of choice is mainly graphite, which is considered an inert substrate. Graphite yields pristine clean, very large and flat surfaces when cleaved, facilitating the observation in real space of the molecular networks adsorbed on these surfaces by means of the Scanning Tunneling Microscope (STM). STM is the main experimental technique used here. It was used to image mostly at the liquid-solid interface under ambient conditions.

Using a large tricarboxylic acid adsorbate, long-range order supramolecular self-assembled monolayers were obtained. These monolayers are formed via a delicate interaction balance between adsorbates, substrate, and solvent molecules. Weak van der Waal forces mediate the adsorbate-substrate interaction; hydrogen bonds, the adsorbate-adsorbate interaction. Also, depending on the solvent used and the concentration of adsorbates dissolved in it, different polymorphs are found on the substrate. To understand the nucleation and growth mechanism that give rise to the different self-assembled monolayers, thermodynamical considerations are used. Enthalpic and entropic contributions are evaluated for several of the polymorphs found, explaining their occurrence on the basis of the Gibbs free energy per unit area. However, even if this work sheds some light on supramolecular self-assembly, adding also that much research has been done in this field, it is still very difficult to know *a priori* how adsorbates will behave on a substrate. Thus predictions of which patterns will ultimately arise are hampered.

To realize structures that are more stable than those formed via supramolecular self-assembly, several strategies have been proposed. Covalent bond formation is one of them, yielding strong and lightweight structures by using organic molecules composed primarily of light elements. The strength of covalent bonds ranges from strong to very strong, when compared to van der Waals and hydrogen bonds. This characteristic makes correction of possible structural errors difficult to almost impossible. However, when molecules with suitable functional groups are allowed to react under reversible conditions, error correction of covalent bonds becomes feasible, yielding regular structures with the energetically most favorable configurations. In this thesis, this is exemplified with the small 1,4-benzenediboronic acid molecules, yielding monolayers composed of very regular, long-range ordered covalent organic frameworks on graphite. Thermal stability is probed by exposing the structures to relatively high temperatures for prolonged times under atmospheric conditions. Further experiments with larger para-diboronic acids, under similar reversible conditions, yield the expected isotopological regular frameworks with larger unit cell parameters. This demonstrates the proof of principle for the formation of two-dimensional covalent organic frameworks.

These two main topics, supramolecular self-assembly and covalent bond formation on surfaces, constitute the basis of this thesis. It is organized as follows: A first part deals with the theoretical background of the main analytical instruments used in this work. Then, the thermodynamics of supramolecular self-assembly is presented, along with the studies of the different polymorphs found using a large tricarboxylic acid as building block. The final part deals with the formation of two-dimensional, long-range ordered covalent organic frameworks, made from organic molecules composed only of light elements. This work shows that these last mentioned networks exhibit higher thermal stabilities when compared to self-assembled monolayers held together mainly by strong hydrogen bonds. The viability of larger heteromeric isotopological networks is also explored.

Contents

| | |
|---|-----------|
| Abstract..... | 3 |
| Abbreviations | 7 |
| 1. Introduction | 8 |
| 2. Experimental Methods and Materials | 11 |
| 2.1. Experimental Methods..... | 11 |
| 2.1.1. Scanning Tunneling Microscope (STM)..... | 11 |
| 2.1.1.1. Theoretical Background | 14 |
| 2.1.1.2. Imaging with STM | 19 |
| 2.1.2. Spectroscopy | 20 |
| 2.1.2.1. Ultraviolet and Visible (UV-Vis) Absorption Spectroscopy | 20 |
| 2.1.2.2. X-Ray Photoelectron Spectroscopy | 22 |
| 2.1.2.3. Raman Spectroscopy | 23 |
| 2.1.3. Powder X-Ray Diffraction (PXRD)..... | 25 |
| 2.1.4. Thermogravimetric Analysis (TGA)..... | 26 |
| 2.2. Materials..... | 27 |
| 2.2.1. Choice of Substrate..... | 27 |
| 2.2.2. Solvents | 27 |
| 2.2.3. Molecular Building Blocks..... | 28 |
| 3. Supramolecular Self-Assembly on Surfaces | 29 |
| 3.1. Thermodynamics | 30 |
| 3.2. Parameters Affecting Supramolecular Self-Assembly on Surfaces | 33 |
| 3.2.1. Molecular Structure..... | 33 |
| 3.2.2. Intermolecular Forces..... | 34 |
| 3.2.3. Influence of the Solvent..... | 37 |
| 3.2.4. Concentration Effects | 40 |
| 3.2.5. Guest Molecules | 46 |
| 3.3. Summary | 47 |
| 4. Covalent Bond Formation on Surfaces..... | 49 |
| 4.1. Synthesis of Surface Supported 2D COFs..... | 49 |
| 4.2. Molecular Precursor | 51 |
| 4.3. Synthesis of Well-Ordered COF Monolayers from BDBA | 52 |
| 4.3.1. Synthesis through Pre-Polymerization of Precursors | 53 |
| 4.3.2. Synthesis via Direct On-Surface Polymerization | 57 |
| 4.4. Synthesis of Isoreticular 2D COFs | 57 |
| 4.5. Activation Temperature for Self-Condensation | 59 |
| 4.6. From Supramolecular Self-Assembly to 2D COF | 60 |
| 4.7. Stability of the Boroxine Ring..... | 61 |
| 4.8. Heteromeric 2D COF via Boronic Ester Formation | 62 |
| 4.9. Summary | 63 |
| 5. Conclusions | 65 |
| Appendix 1: Preparation of Ultra Flat Gold (111) Surfaces by Physical Vapor Deposition (PVD) as Substrate for Supramolecular Self-Assembly | 68 |
| Appendix 2: Stepwise Assembly Scheme and Evaluation of Formation Probabilities for Two Different Polymorphs from the Same Adsorbate | 75 |

| | |
|-------------------------------|------------|
| Publications | 80 |
| References..... | 158 |
| Acknowledgements | 171 |
| Curriculum Vitae..... | 172 |

Abbreviations

| | |
|--------|-------------------------------------|
| 2D | Two Dimensions / Two dimensional |
| COF | Covalent Organic Framework |
| DOS | Density of States |
| HOMO | Highest Occupied Molecular Orbital |
| HOPG | Highly Oriented Pyrolytic Graphite |
| IR | Infra Red |
| LDOS | Local Density of States |
| LEED | Low Energy Electron Diffraction |
| LUMO | Lowest Unoccupied Molecular Orbital |
| MM | Molecular Mechanics |
| MO | Molecular Orbital |
| PXRD | Powder X-Ray Diffraction |
| RAHB | Resonance Assisted Hydrogen Bond |
| STM | Scanning Tunneling Microscopy |
| TGA | Thermogravimetric Analysis |
| UHV | Ultra High Vacuum |
| UV | Ultra Violet |
| Vis | Visible |
| w.r.t. | with respect to |
| XPS | X-Ray Photoelectron Spectroscopy |

1

Introduction

The advent of the Scanning Tunneling Microscope (STM)¹ in 1982 gave scientists the opportunity to observe and manipulate matter at the atomic scale. Before the invention of the STM, matter could only be indirectly studied by means of other physical and chemical methods. In fact, there was no lack of these methods, for instance, spectroscopy, nuclear magnetic resonance, electron microscopy, X-ray diffraction, chromatography, electrophoresis, and mass spectrometry, to name a few. None of them permit the observation in real space of any molecule, not even to speak of single atoms. So it is understandable that in the very beginning of the STM, many scientists were skeptical about the possibilities STM opened, because it was not expected that atomic resolution could be achievable.² In fact, the STM was the first of several instruments with resolution ranging from 100 μm down to 10 pm, nowadays cooperatively known as Scanning Probe Microscopy (SPM).³ This family of instruments now permits the customary and precise observation of atoms and molecules in different environments.

Who could have predicted a scenario, where observing molecules down to almost atomic resolution was easily feasible almost at will? Futurologists of the 1960s and 70s were mostly only occupied predicting the big things to come in the XXI century; for instance, living on the moon or speaking through videophones;⁴ predictions that too many times failed to materialize. However, Richard Feynman, already in 1959, raised some issues about how it should be possible to manipulate and produce things that were many, many times smaller than the smallest miniaturization achievable at those days.⁵ Although certainly unbeknownst to him, he allegedly gave a date where it would become already possible to control matter at the atomic scale: the year 2000. He was right, beating out at least once those “think big” futurologists. There is no way he could have predicted the invention of the STM, and with it the emergence of a new field in material science: nanotechnology.

This very word, “nanotechnology”, was coined for exactly this very fine and precise manipulation of materials. Interestingly, nanotechnological implications have nowadays been felt even for non-scientists: starting with product branding, the “iPod Nano” music player by Apple and the “Nano” car by Tata derive their name from this nowadays ever-present word in common life.⁶ Although these two products not necessarily possess nanotechnology-derived parts, there are plenty of products in the market that do. These range from TiO_2 nanoparticles in sunscreen, silver nanoparticles in washing machines to particles of trace metals in food supplements.⁷

Nanotechnology is not free of risks. However so far, very few of them have been identified.^{7,8} Animal research suggests that nanoparticles may have the capability to evade the body’s natural

defense system and be able to move across cell membranes, reaching the brain and lungs, where they can accumulate.⁷ However, identifying this last mentioned facts does not necessarily mean *per se* that nanotechnology involves risks. Most probably, nanotechnology will improve our daily life instead of threatening it.

Since the STM was invented, the manipulation of molecules on surfaces has gone great lengths. It is nowadays possible to move single-molecule “cars” on a surface by means of propelling them with the STM tip, readily rolling it to its next position.^{9,10} Although these feats may call the attention even of non-scientist due to its large press coverage, nanotechnology never stops to be fascinating for scientists involved in the field of material science. For example, in the present work, the supramolecular self-assembly of molecules was studied, and the different geometrical structures found were explained by thermodynamic principles.

Supramolecular self-assembly shows promising applications in the manufacturing of electronic devices,¹¹ but these molecular aggregates lack the required stability for some applications that could be obtained with covalent bonds. Hence, this was the next step in the course of this work, the realization of regular molecular networks held together by relatively strong covalent bonds. Eventually, the formation of extended, two-dimensional (2D), surface-supported, covalent organic frameworks (COFs) has been realized here. In the future, maybe the production of 2D free-standing COFs, much resembling graphene, may also become feasible.

In the present work, the subjects covered are mainly supramolecular self-assembly of hydrogen-bonded monolayers on surfaces, and the formation of surface-supported 2D COFs. Both of these subjects were performed basically on a graphite substrate. Graphite was chosen because it is a chemically inert substrate that can be easily prepared at every new experimental run. A simple cleave with adhesive tape yields pristine clean surfaces every time, ready to use without any further treatment other than depositing the molecules of interest. The main analytical tool used was the ambient STM; however, other analytical methods were also used to confirm and explain the results found with the STM.

One of the motivations of this work was to study possible formation of ever larger regular supramolecular monolayers composed of tricarboxylic acids held together by strong hydrogen bonds. Previous studies showed that small¹² to medium-sized^{13,14} tricarboxylic acids, possessing one or several phenyl groups in its backbone, yielded porous and planar networks on a graphite substrate. The final topology of these networks could be influenced by many factors, like choice of solvent and concentration. Hence, a large tricarboxylic acid was chosen for experiments, and its several polymorphs were studied and explained using thermodynamical considerations.

Another important motivation was the formation of single-layer, extended and regular 2-dimensional covalent organic frameworks (2D COFs). The synthetic route for realizing these frameworks is already known for bulk crystals¹⁵ or even substrate-supported thin films,¹⁶ but the formation of a single, regular, defect-free layer had been elusive. Since these frameworks are held

together exclusively by relative strong covalent bonds, its physical properties are expected to be superior than those of hydrogen bonded self-assembled networks. These properties were confirmed during the course of this work. After finding a reproducible method that yielded every time 2D COFs with the small 1,4-benzenediboronic acid precursor on a graphite substrate, larger, isorecticular networks were realized using larger para-diboronic acids. By selecting the length of the molecular precursor, the size of the 2D COF cavity could be tuned. In this way, a series of several regular 2D COFs was realized.

To deal with the topics mentioned above, this work is outlined as follows: In chapter 2, a theoretical background explaining the working principles of the STM is presented. The theory behind other important analytical methods used during this work is also briefly explained. Chapter 3 deals with the supramolecular self-assembly. Using mainly a large tricarboxylic acid, different assemblies were encountered, depending on the solvent used and its concentration. Here, the thermodynamic principles governing the self-assembly of molecules on surfaces is presented and used to explain the stability of the different polymorphs encountered. Chapter 4 deals with the formation of regular and extended 2D COFs. After finding the conditions under which the molecular precursors yield the best results, isorecticular COFs with pore sizes up to 3.2 nm wide were prepared and studied. A conclusion is given in chapter 5, followed by the papers published during the course of this dissertation.

2

Experimental Methods and Materials

In this work, the most important analytical tool for examining samples was the Scanning Tunneling Microscope (STM). To independently confirm results obtained with the STM, complementary analytical methods were used. These results were also theoretically supported by models of molecular structures simulated with molecular mechanics. The molecular building blocks used were all organic molecules with certain defined structures. Depending on the function they were required to perform, they were specifically functionalized with chemical groups. The most common substrate used was graphite, which is widely available and easy to cleave. It can produce a clean surface every time with almost no effort. Graphite is also inert, thus not requiring extremely clean environments to work with. In practice, this translates as permitting work under ambient conditions.

2.1 Experimental Methods

For this work, supramolecular self-assembly and synthesis of covalent organic frameworks were carried out on planar surfaces. To probe the resulting assemblies or structures formed on these surfaces, the Scanning Tunneling Microscope (STM) was used as the main analytical instrument. The STM proved to be an invaluable tool for imaging these structures down to the molecular level, readily assessing the different molecular configurations and even offering a possibility to differentiate between self-assembly and covalent bond formation. Another analytical method of surface science employed here is X-ray Photoelectrons Spectroscopy (XPS). These two surface analysis tools were further aided by bulk analytical methods. The most relevant of them are discussed in the following.

2.1.1 Scanning Tunneling Microscope (STM)

In the year 1982, G. Binnig and H. Rohrer¹ demonstrated for the first time that an analytical instrument based on the quantum mechanical tunnel effect was feasible. This was the birth of the STM, an instrument nowadays used extensively to probe surfaces. Before the STM came into being, I. Giaever¹⁷ already proposed the possibility of gathering information about the electronic structure of surfaces by means of the quantum tunnel effect. The STM was preceded by the “topografiner”, an instrument developed in the year 1972 by R. Young.¹⁸ However, this last instrument never achieved the very high vertical and lateral resolution of the STM due to the very noisy nature of the field emission current^{18,19} and the lack of reliable feedback circuitry at those days.²⁰ Consequently, it was

never commercially produced. Unlike the topografiner, STMs do not need special electron sources; instead they rely on the bound electrons sample and tip as the only source of radiation.²¹

STM was not the first device to rely on the tunnel effect. There were already other practical uses of electron tunneling, such as the metal-insulator-metal (M-I-M) tunnel diode.²²

To operate an STM, a very sharp tip (ideally, atomically sharp) is brought very close to an electrically conducting substrate, until no more than a few atomic diameters separate both. The tip is the most critical part of the STM because it ultimately determines the image quality and resolution.²³ A small bias voltage of less than 1 V is applied between tip and surface, generating a tunneling current of electrons flowing from the tip to the substrate, or *vice versa*, depending on bias polarity. An electrically controlled piezoelectric crystal performs the lateral and vertical scanning movement of the tip. This movement creates spatial variations of the tunneling current that are used to produce contour maps or false-color images. Under normal working conditions, STMs achieve resolutions of less than 1 nm laterally and 0.1 nm vertically,²⁴ allowing the exact positioning of single atoms. Hence, imaging of organic molecules –composed of several atoms– adsorbed on conducting substrates becomes a relatively simple task. The vertical resolution is explained by the exponential variation of the tunneling current with the distance between tip and sample; the lateral resolution depends upon tip sharpness. Although good resolution sometimes may be obtained using a mechanically cut metallic wire made of Pt/Ir (90%/10%) alloy, more reproducible results are obtained with tips made by electrochemically etching tungsten (W) to a fine point. Tips made from Pt/Ir alloy have a very good resistance to atmospheric oxidation and therefore are preferred for ambient STM, whereas W tips are favored for STM uses under Ultra High Vacuum (UHV).²³ Mechanically cut tips achieve atomic resolution due to the many asperities on the surface of the tip structure. Then, if one atom of these asperities is just some atomic radii closer to the sample than any other one, atomic resolution is realized by the nature of the tunneling signal.²⁴ On the other hand, an advantage of electrochemically etching the tips is that this sharpening method can provide more reproducible tips. These tips normally lack the asperities of mechanically cut tips and therefore are better adapted for surfaces with a relative large degree of roughness.²⁴

The basic operation principles of the STM are shown in figure 2.1. The STM can be operated in two different modes, namely constant current or constant height. In the first mode, the tip scans a surface at constant tunneling current. This current is kept close to a preset value by continuously adjusting the tip height relative to the surface via a feedback loop. However, a low cut-off frequency of the feedback still allows spatial modulation of the tunneling current.²⁵ In the second mode, the tip scans the surface at nearly constant height and constant voltage. Here, the tunneling current is monitored, and its variations are plotted forming an image. For this second scanning mode, the feedback network responds rapidly enough to keep the average current constant.²⁴ Each scanning mode has its own advantages: Constant current mode can track surfaces that are not necessarily atomically flat. This mode yields more reliable information about topography height, derived from the

feedback signal. Here, the quality of the information acquired can be influenced by the sensitivity of the piezoelectric crystal driving the tip. Constant height mode allows much faster scanning of atomically flat surfaces, because the feedback and the piezoelectric crystal do not need to respond to the features being scanned by the tip.

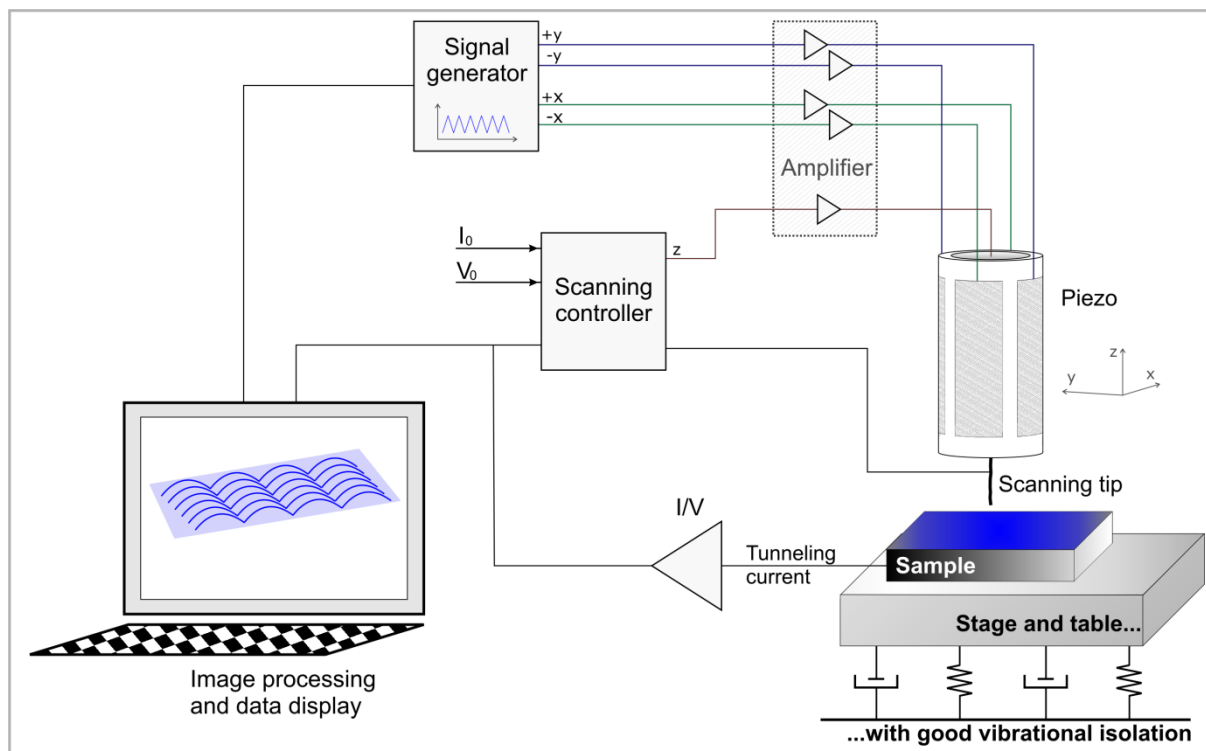


Figure 2.1: Operation principle of a STM. Schematic vibrational isolation is also shown.

The STM has proved to be a very reliable and adaptable instrument. It can work in very different environments, from Ultra High Vacuum (UHV), as initially intended,¹ to standard ambient conditions, with scanning tips immersed in non-conducting liquids, and under the appropriate insulation, even in electrolytes, as in electrochemical cells.²⁶ It can also work under very low or high temperatures.

For this thesis, two home-built ambient STM were used. They are shown in figure 2.2. Both STM heads are mounted on a vibration isolating pyramid made of differently sized copper plates, separated by rubber stands.²⁷⁻²⁹ The function of this pyramid, together with the optical table, is to damp vibrations from the floor that are more pronounced in the frequency range 0.1 to 50 Hz. The vibrations in this frequency range may impair the ability of the STM to acquire high resolution data.

The main differences between these two STMs units are: First, the manual coarse approach mechanism of the first STM shown in figure 2.2a against the automatic coarse approach for the STM shown in figure 2.2b. Second, that the scanning piezo head of the first STM is fixed on the pyramid, whereas for the second STM shown (figure 2.2b), the head is removable. This last feature of the second STM unit allows easier and faster positioning of the scanning tip on the area of interest of a sample as compared to the first fixed configuration shown.

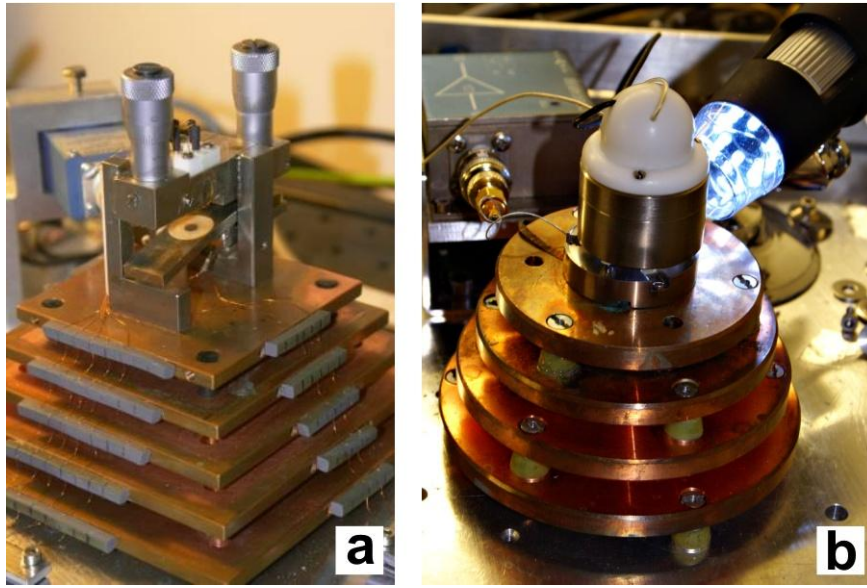


Figure 2.2: Two home-built STMs used during the course of this work. **a)** STM with a manual course approach; **b)** STM with automatic piezo-driven approach. Both are operated on an optical table to damp vibrations that may be transferred from the floor (not shown). Both STMs sit atop a pyramid made of copper plates to further minimize vibrations. The STM at **b)**, including the pyramid constructed from circular plates, was designed by Stephan Kloft.

2.1.1.1 Theoretical Background

The simplest theoretical model to explain STM operation is based on one-dimensional tunneling theory.³⁰ The tunneling effect can be understood by wavelike properties of particles, as described in quantum mechanics. If E , the kinetic energy of a particle, is lower than U , the potential energy of a barrier, there is a non-zero probability for transmission through the classically forbidden region and reappearance on the other side of the barrier. This probability P of a particle to traverse the above mentioned barrier, moving in the $+z$ direction, can be estimated by:³⁰

$$P \propto e^{-2\kappa z}, \quad (2.1)$$

where z is the thickness of the barrier and κ is a decay constant given by:

$$\kappa = \sqrt{2m(U - E)/\hbar}, \quad (2.2)$$

where m is the mass of the particle, and $\hbar = h/2\pi$. (h is Planck's constant.) In the case of STM, the thickness of the barrier is the gap separating tip and sample, known also as the tunneling junction. The particle of interest, m , is an electron of energy E ; and ψ is the wavefunction of the electron (when it is located in the sample). Thus, equations 2.1 and 2.2 can be rewritten as:

$$|\psi(z)|^2 = |\psi(0)|^2 \cdot e^{-2(\sqrt{2m(\Phi_0 - E)}/\hbar)z}, \quad (2.3)$$

where Φ_0 is the sample work function (a potential energy barrier), and $\psi(0)$ is the value of ψ at the sample surface. A graphical explanation of the tunneling effect is presented in figure 2.3.

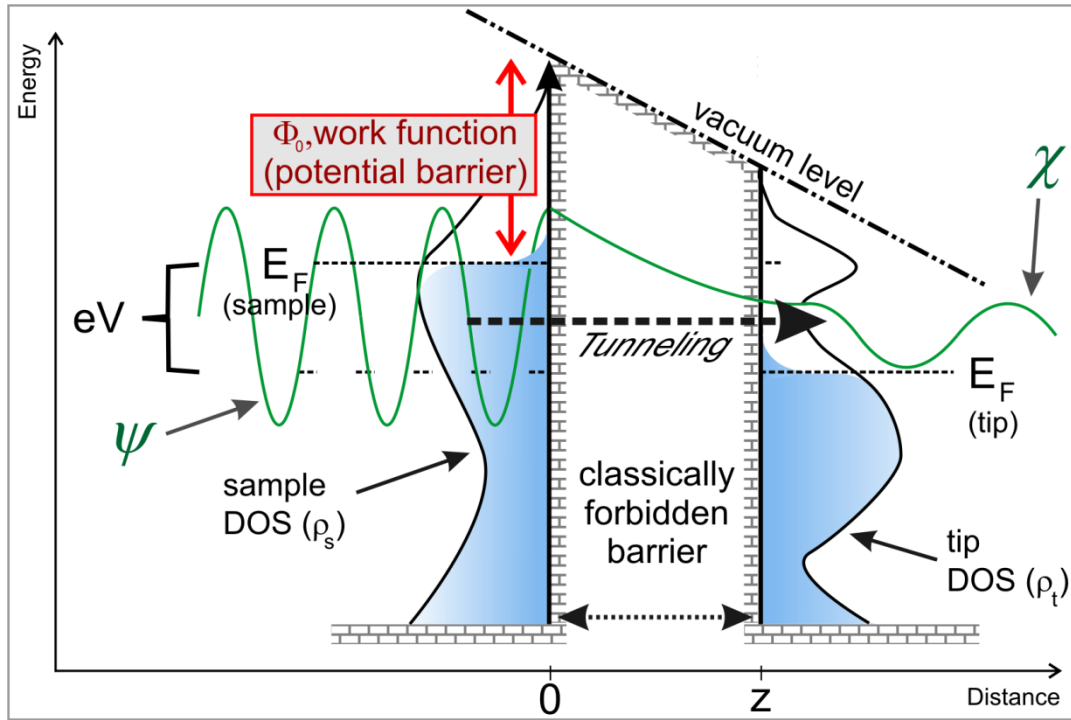


Figure 2.3: Energy diagram for the tunnel effect. The sample-tip tunneling junction is a barrier of width z . When a bias voltage is applied, electrons can tunnel from the occupied states of the sample to the unoccupied states of the tip, or *vice versa*, depending on the bias direction. Tunneling is only possible in the energy interval eV , between the sample and tip Fermi levels, E_F . ψ is the wavefunction of the electron in the sample.

This elementary model explains some basic characteristics of metal-vacuum-metal tunneling. The work function Φ_0 of a metal surface is defined as the minimum energy required to remove an electron from the bulk to the vacuum level.³¹ Φ_0 depends on the material and on its crystallographic orientation. Neglecting thermal excitation, and setting the vacuum level as the reference point of energy ($E_F = -\Phi_0$) the Fermi level becomes the upper limit of the occupied states in a metal.

For simplicity, it is assumed that tip and sample are metallic and their respective work functions are equal. Then, when the tip is brought close enough to the sample, electrons can tunnel from the tip into the sample, or *vice versa*; however, for a net tunneling current to occur, a bias voltage must be applied. Taking this into account, for small bias voltages ($eV \ll \Phi_0$), the tunneling probability of an electron of energy E located between $[E_F - eV, E_F]$ simplifies equation 2.3 to:

$$|\psi(z)|^2 = |\psi(0)|^2 \cdot e^{-2(\sqrt{2m\Phi_0}/\hbar)z} \quad (2.4)$$

Then, because the current I is proportional to the sum over all states located between $[E_F - eV, E_F]$, I can be written as:

$$I \propto \sum_{E=E_F-eV}^{E_F} |\Psi(z)|^2 . \quad (2.5)$$

In an STM experiment, the tip scans over the sample surface. To simplify the quantum mechanical treatment, the tip condition is regarded not to vary during these scans. Furthermore, electrons tunneling from the surface to the tip or *vice versa* are assumed to have constant velocity. The tunneling current is directly proportional to the number of states in the sample surface within the energy interval eV , which are available for the tunneling current. This number depends on the local density of states (LDOS) of the sample surface. The LDOS is the number of electrons per volume per unit energy at a given point in space at a given energy.³¹ For metals, it is very high, for insulators and semiconductors it is very small, and for semimetals, it lies between both.³¹ If a small bias voltage V is applied between tip and sample, the density of states (DOS) of the sample is considered to have only very small variations in the range $[E_F - eV, E_F]$. Then expression 2.5 can be written in terms of the LDOS of the sample at the Fermi level, $\rho_s(E_F)$, with the tip at a distance z from the sample, as:^{25,31}

$$\rho_s(E_F) \equiv \frac{1}{eV} \sum_{E=E_F-eV}^{E_F} |\Psi(z)|^2 . \quad (2.6)$$

Substituting 2.6 into 2.5 gives:^{25,31}

$$I \propto V \cdot \rho_s(E_F) \cdot e^{-2(\sqrt{2m\Phi_0}/\hbar)z} . \quad (2.7)$$

Proportion 2.7 indicates that a constant-current STM image is a line-contour representation of the LDOS of the sample at the Fermi energy. The typical value of the work function is $\Phi_0 \approx 5 \text{ eV}$,² giving a value of the decay constant $\kappa \approx 0.1 \text{ nm}^{-1}$.

Perturbation Theory

The large body of concepts developed studying the M-I-M tunneling junctions are fundamental for understanding the tunneling effect in STM.³¹ The most used theory for explaining the M-I-M tunneling is the time-dependant perturbation approach developed in 1960 by Bardeen.³²

For this purpose, Bardeen considered first two separate subsystems. Their electronic states are obtained by solving their stationary Schrödinger equations. The transfer rate of an electron from one electrode to the other is evaluated using time-dependant perturbation theory. In this way, Bardeen showed that the amplitude of the electron transfer, or the tunneling matrix element M , can be determined by the overlap of the surface wavefunctions of the two subsystems at a more or less arbitrary separation surface. This means that M is determined by a surface integral on a separation surface S_0 between the two electrodes as follows:³¹

$$M = \frac{\hbar}{2m} \cdot \int_{S_0} (\chi^* \nabla \psi - \psi \nabla \chi^*) dS, \quad (2.8)$$

where ψ and χ are the wavefunctions of the two electrodes. Equation 2.8 shows that M depends *exclusively* on the wavefunctions ψ and χ *in the barrier*. Applying these principles to the STM sample-tip junction, it can be conveniently considered that ψ is the wavefunction of the sample, and χ that of the tip. Then, the probability w of an electron in the sample at energy level E_ψ tunneling to a state χ of the tip of energy level E_χ is given by Fermi's golden rule:³¹

$$w = \frac{2\pi}{\hbar} |M|^2 \delta(E_\psi - E_\chi), \quad (2.9)$$

which considers only elastic tunneling, i.e. only tunneling between states of similar energy E_ψ and E_χ . When a bias voltage is applied, the tunneling current is then given by:²⁵

$$I = \frac{2\pi e}{\hbar} \int_{-\infty}^{+\infty} [f(E_F - eV) - f(E)] \rho_s(E - eV) \cdot \rho_t(E) \cdot |M|^2 dE, \quad (2.10)$$

which integrates over all possible combinations of sample and tip states. The Fermi distribution, $f(E)$, is given by:

$$f(E) = \left(e^{\left(\frac{E - E_F}{k_B \cdot T} \right)} + 1 \right)^{-1}, \quad (2.11)$$

where E is the potential energy of the electron, E_F is the Fermi level, and T is the absolute temperature. ρ_s and ρ_t are the densities of states of the sample and tip, respectively. Considering only cases with small bias voltage and at relatively low temperatures, which covers in practice the usual experimental conditions under which STM is performed, allows equation 2.10 to be simplified to the following:

$$I = \frac{2\pi e}{\hbar} \cdot \int_{E_F}^{E_F + eV} [\rho_s(E - eV) \cdot \rho_t(E) \cdot |M|^2] dE. \quad (2.12)$$

At elevated temperatures, there is a corresponding term for reverse tunneling. Equation 2.12 is valid if M is considered almost invariable in the energy interval eV . If the DOS of the tip, ρ_t , is considered constant in the energy range of interest, then the tunneling current is evaluated solely by the sample by the following equation:

$$I \propto V \cdot \rho_s(E_F - eV). \quad (2.13)$$

This last proportion states that the current is essentially determined by the LDOS of the sample at the Fermi energy.²

s-Wave Tip Model

Tersoff and Hamann^{33,34} showed for the first time that proportion 2.7 was also valid in three dimensions.² For this purpose they used a simplified model of the tip, approximating the apex to a spherical s-wave function. They also evaluated the sample LDOS at the Fermi edge $\rho_s(E_F)$ at a distance $r_0 = z + R$, where z is the distance between the apex of the tip and the sample surface; and R is the radius of curvature of the tip (see figure 2.4). In this way the solution for M , the tunneling matrix in equation 2.8, is given by:²⁵

$$M \propto \kappa \cdot R \cdot e^{\kappa R} \cdot \psi(r_0), \quad (2.14)$$

where $\psi(r_0)$ is the sample wavefunction evaluated at r_0 , and with $\kappa = \sqrt{2m\Phi_0} / \hbar$. Then, at small bias voltages, I is proportional to:²⁵

$$I \propto R^2 \kappa^{-4} e^{3\kappa R} \cdot V \cdot \rho_t(E_F) \cdot \rho_s(E_F, r_0) \cdot \psi(r_0). \quad (2.15)$$

This last equation shows that I is proportional to the sample LDOS at the Fermi level evaluated at r_0 . This model explains the high resolution on metals such as Au(110); however, does not explain large corrugation heights quantitatively.² This model also becomes less accurate for large values of R . An exact treatment of the tip would probably be far less useful since it would require more specific information about the tip wave functions, and would not reduce to an explicit equation.

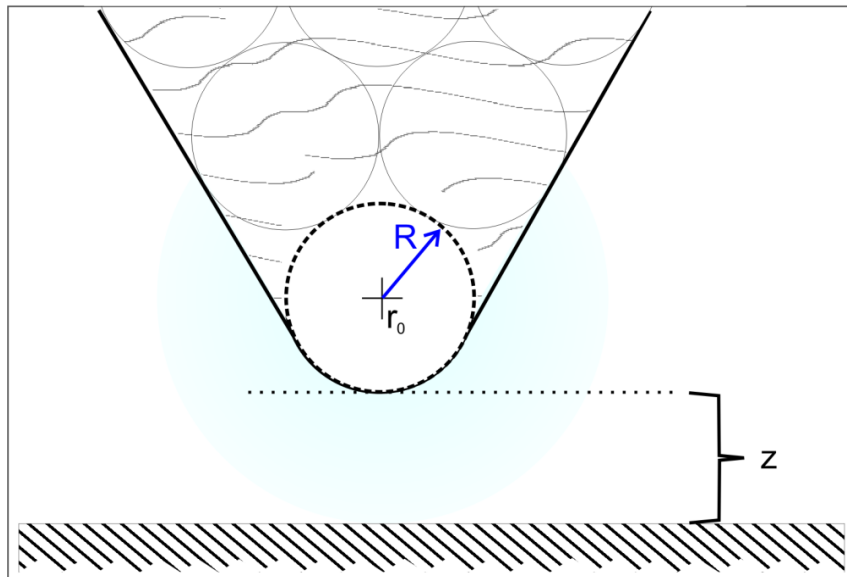


Figure 2.4: Graphical explanation of the Tersoff-Hamann tip model. The apex of the tip is modeled as an s-wave. The tunneling current is proportional to the LDOS of the sample at the Fermi level at a distance $R + z$ from the center of curvature, r_0 , of the tip.

2.1.1.2 Imaging with STM

The first STM studies were of pristine surfaces free from any adsorbed molecules. These studies facilitated the real space determination of their atomic structure. Among these surfaces were metals,³⁵ like Al(111) and Pt(100), and semiconductors,³⁶ like Si(111) and graphite.³⁷ In subsequent experiments, atoms and molecules were adsorbed on these surfaces, allowing the analysis of the interaction of adsorbates with substrates, and among adsorbates. The main processes studied with adsorbed molecules were nucleation, growth, electronic coupling to the substrate and chemical activity.³⁸

In the early days of the STM, it was assumed that most organic molecules were not visible by this technique, since they possess a large energy gap between HOMO and LUMO. Hence the first adsorbates studied with the STM were comparatively small inorganic molecules,^{39,40} like CO on Pt(100) and Pd(110), or simply atoms,^{41,42} as S on Mo(100) or O on Ni(100). Later on, the size of adsorbates was increased to include molecules of medium complexity.⁴³

When molecules adsorb on surfaces, interpretation of the resulting STM images can become intricate. The STM ability to resolve molecular adsorbates depends on the probability that the adsorbate's electronic states contribute to the tunneling current.⁴⁴ The apparent height of atoms in STM images of atomically flat surfaces is not necessarily related to their physical height over the surface.⁴¹ For example, S atoms appear mostly as protrusions above the substrate; however, O atoms commonly appear as depressions.⁴² These results were explained by Lang^{45,46} using Bardeen's approximation³² to calculate the tunneling current between two atoms on very close electronic gas surfaces (so-called "Jellium"). The electronic states of the adsorbed atoms can enhance or reduce the tunneling current through their influence on the density of states at the Fermi level.⁴¹ S increases the LDOS, while O decreases it. Using the Tersoff and Hamann theory,^{33,34} the spatial contrast can also be explained. Based on Lang's theory, Eigler showed quantitatively that a non-conducting atom, like Xe on Ni(110), can be visible with the STM.⁴⁷

Molecular Orbital (MO) Theory has been used to identify molecules by their observed STM images. Early examples include copper phtalocyanine⁴⁸ adsorbed on Cu(100) or alkyl-cyanobiphenyl on graphite.⁴⁹ These two results demonstrate that STM reveals the electronic structure of the adsorbates, rather than their real topography.⁵⁰ However, the electronic states calculated using MO for isolated molecules does not take into account the influence of the substrate. For this purpose, a modified computational methodology was proposed by Hallmark and Chian⁵⁰ in 1995 using Extended Hückel Theory to calculate extended Hückel orbitals for the combined system molecule + substrate. This then yields contour maps of occupied or unoccupied LDOS that can be compared with actual STM images. Recently, Density Functional Theory (DFT) calculations were performed to explain the electronic effects observed in alkanes adsorbed on graphite with the STM.⁵¹ Another popular method is the Electron Scattering Quantum Chemistry (ESQC) developed by Sautet and Joachim.⁵² Here the

tunneling process is treated as a scattering process, and the surface-adsorbate-tip system, as a defect in a periodic bulk.^{41,53} ESQC was successful in explaining the different contrast features obtained with benzene on Pt(111), attributing them to different adsorption sites.⁵⁴ Here, when adsorbed atoms are not well enough separated, the mechanism behind contrast formation becomes more complicated to explain.⁴¹ Also, the apparent shape of atoms recorded with the STM can be influenced by the proximity of adsorbates. This is a result of the interference between tunneling paths through neighboring adsorbates when the tip is located between the adsorbates.⁵⁵ These interferences can complicate the structure determination of adsorbates via contrast features in the resulting STM images.⁴¹

A review of various theoretical methods to simulate and explain the observed STM images of adsorbates on surfaces is given by Sautet.⁵³

2.1.2 Spectroscopy

Spectroscopy is the study of emission and/or absorption of electromagnetic radiation by matter. It is applicable throughout the entire electromagnetic spectrum and allows to gain knowledge of the elementary excitations in matter, and hence about the structure of matter. If the spectrum is recorded directly from an emission source, it is named emission spectroscopy; if recorded from an absorbing sample interposed between an emission source and a detector, it is called absorption spectroscopy. For the latter case, ultraviolet and visible (UV-Vis) spectroscopy is a typical example, and was also used in this work. When the incident radiation is reflected or scattered, it is named elastic or inelastic scattering, depending whether the incident radiation exchanges energy with the analyzed sample. Raman spectroscopy is an example of inelastic scattering. In the following, the most relevant spectroscopic analytic procedures performed during the course of this work are discussed.

2.1.2.1 Ultraviolet and Visible (UV-Vis) Absorption Spectroscopy

In the course of this thesis, UV-Vis absorption spectroscopy was used as a method to measure the concentration of molecules in solution. Typically, the solvents used were fatty acids, and the peak absorption wavelength of the solute molecules was found in the UV region. The measurements served as an independent confirmation for the very low to almost complete insolubility of some solutes in selected solvents. For instance, UV-Vis spectroscopy helped to establish with certainty why some building blocks failed to self-assemble on a substrate, when it was found that the solubility of these molecules was extremely low.

The spectrometer used had a collimated beam of light, transmitted through an optical fiber, and the detector was sensitive for wavelengths from ~180 nm through 890 nm; this range spans from middle ultraviolet up to near infrared radiation.

To measure the concentration c of solutes in solution, the following linear relationship known as the Beer-Lambert-Bouguer law is applied:

$$A = \log \frac{I_0 - I_D}{I_T - I_D} = a \cdot l \cdot c, \quad (2.16)$$

where A is the absorption or transmission, I_0 the intensity of the light transmitted by the cell containing only the solvent, I_D the background noise (dark current) measured by the detector, I_T the intensity of the light transmitted by the cell containing the sample (composed of solvent + solute), a the absorption coefficient, and l the distance the radiation travels through the solution of interest, *i.e.* the optical path length. Thus, if l and a are known, and A is measured, c can be deduced.

Under certain conditions the Beer-Lambert law fails, because a linear relationship does not hold true. This is the case for BTB (figure 3.1) dissolved in heptanoic acid above 50% saturation concentration. For TCBPB (figure 3.1) dissolved in several carboxylic acids, no deviations to this law were encountered for concentrations up to 100% saturation, because of the very low solubility of this solute in these solvents.

Figure 2.5a shows typical UV-Vis absorption spectra at different concentrations. In this example, the molecule studied is TCBPB dissolved in heptanoic acid. The chemical structure of TCBPB is shown in chapter 3 (figure 3.1). Figure 2.5b shows the regression line obtained from the absorption peak maxima, at 308.3 nm, for different concentrations. Its correlation of 99.3% proves a very good linear relationship along the measured concentrations, complying very well with Beer-Lambert's law.

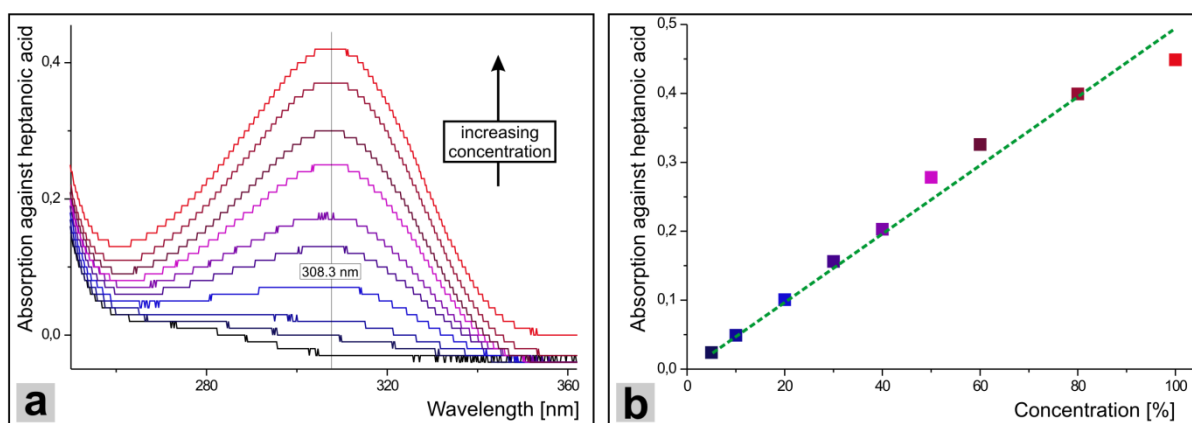


Figure 2.5: **a)** Absorption spectra of TCBPB dissolved in heptanoic acid at different concentrations for the wavelength region between 250 nm and 360 nm. The absorption peak maximum is located at 308.3 nm. The bottom (black) line presents the absorption spectrum of pure heptanoic acid, whereas the other lines present increasing concentrations from 5% to 100% saturation (100% saturation curve drawn in red). **b)** The graph shows the very good linear relationship found for concentration *versus* absorption. The absorption values are taken from the absorption maxima in a). The color code of each spectrum in a) is again represented in the color of each data point in b).

2.1.2.2 X-Ray Photoelectron Spectroscopy (XPS)

XPS can be a complementary analytical method to STM, providing additional chemical information of a sample's surface.⁵⁶ By measuring core level binding energies of the top 1 to 10 nm of a solid substrate, elemental composition can be identified.⁵⁷ XPS signals arise from a surface area that encompasses at least several molecules, hence no lateral resolved information can be obtained.⁵⁶ Assuming that the elements to be detected have a concentration greater than 0.05 atomic %, XPS can identify and quantify the elemental composition of a sample, except for H and He. It can also reveal the chemical environment of a specific element, *i.e.* to which other elements it is bound, and the type of bond, by small shifts in binding energy.

XPS is based on the photoelectric effect discovered in 1887 by Hertz⁵⁸ and explained in 1905 by Einstein⁵⁹. Briefly explained, this effect arises from the transfer of energy from impinging photons to the electrons bound to atoms on a surface, provided that the energy of the photons is greater than the binding energy of electrons. The electron's kinetic energy E_k emitted from the sample surface is given then by the following energy conservation equation:

$$E_k = h\nu - E_b - \Phi_0, \quad (2.17)$$

where $h\nu$ is the energy of the incident photon, E_b the binding energy of the electron relative to the Fermi level and Φ_0 the work function of the sample.^{56,59}

In XPS, spectra are gathered inside a UHV chamber by irradiating a sample with monochromatic X-rays of 1000 to 1500 eV emitted from Al $K\alpha$ or Mg $K\alpha$ radiation. At the same time, the amount of core-level electrons being emitted from the sample is measured, as well as their respective kinetic energy. When a substrate with adsorbed molecules is analyzed, each element, except H and He, emits a high intensity spectrum at a specific kinetic energy. The amount of detected electrons at the corresponding energy can be related to the amount of that element present in the sample. The electronic structure of the elements present on the surface is also obtained in the process. This structure gives information about the electronic states of those elements and the type of bonds formed between them. Hence, it can be deduced whether the adsorbates have formed new bonds between themselves, or between adsorbates and substrate. In the case of an organic sample, the amount of H may be estimated by the electronic state of the other elements.⁶⁰ In this work, XPS served as an independent method for confirmation of covalent bond formation between adsorbates. This was achieved by comparatively analyzing adsorbed 1,4-benzenediboronic acid on graphite, before and after a thermal treatment.

2.1.2.3 Raman Spectroscopy

Raman Spectroscopy studies the vibrational and rotational modes in molecules.⁶¹ It is based on Raman scattering, which is the inelastic scattering of monochromatic radiation. Approximately 1 in 10^7 scattered photons has a different energy than the incoming photons, meaning that the photons lose or gain energy during the scattering process. Scattering of radiation occurs because the oscillating electric field of a radiation source interacts with the electrons of the sample, thereby inducing oscillations in the molecules. This causes a change in the polarisability of the molecule. These oscillations are then re-emitted as radiation that can be read in a detector.

Elastic collisions with photons of incident energy $h\nu_i$, where h is Planck's constant and ν_i the frequency of the incident radiation, result in scattering of photons of the same energy. This is the most likely scattering process and is termed Rayleigh scattering. However, if incident photons gain or lose energy by the interaction with electrons of the sample, the scattered photons will have energies given by:

$$h\nu_f = h\nu_i \pm h\nu_0, \quad (2.18)$$

where $h\nu_0$ is the energy gained or lost by the incident photon. Assuming the energies of molecule and photon do not change during the scattering process, then:

$$E_0 + h\nu_i = h\nu_f + E_1, \quad (2.19)$$

where E_0 represents the total vibrational energy of the molecule before the collision, and E_1 after the collision. The Raman shift is then expressed as:

$$\nu_i - \nu_f = \frac{E_1 - E_0}{h}. \quad (2.20)$$

When the collision is elastic ($E_1 = E_0$) Rayleigh scattering occurs. If $\nu_i > \nu_f$ Stokes scattering takes place, if $\nu_i < \nu_f$, anti-Stokes scattering will occur (figure 2.6). In principle, the frequency of the incident radiation is not critical, since only shifts in frequency are measured.⁶²

For anti-Stokes scattering to occur, the molecule needs to be in a vibrationally excited state, whereas for Stokes scattering, the molecule can be at the ground state. Therefore Stokes lines are much more intense than anti-Stokes lines, as governed by the Boltzmann distribution of the vibrational state population.⁶²

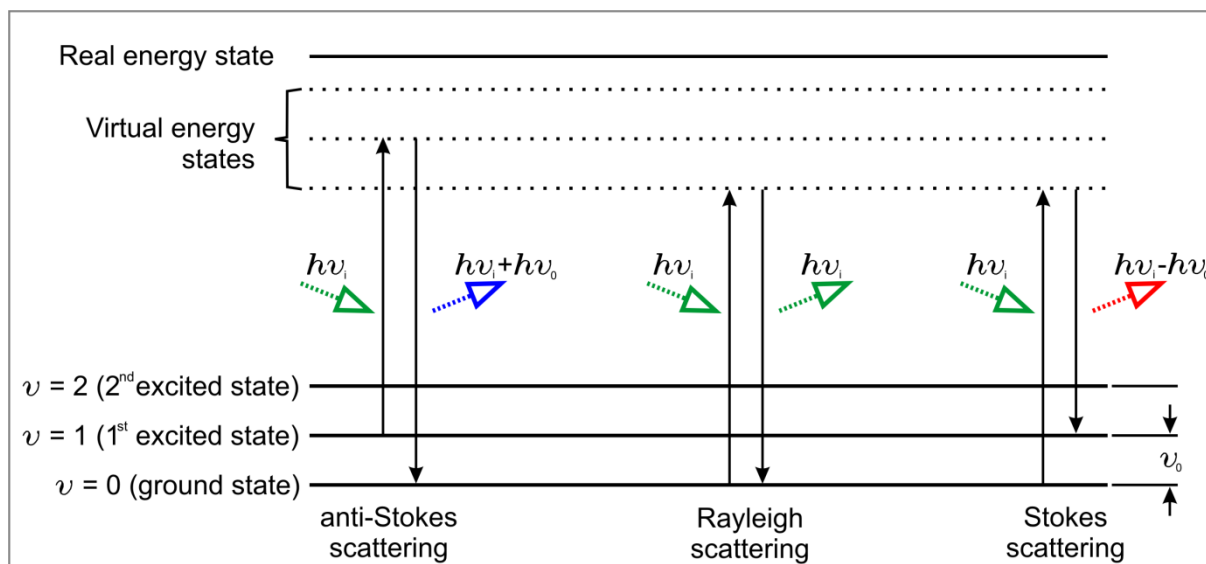


Figure 2.6: Energy transitions taking place in Raman spectroscopy. In anti-Stokes scattering the photon has gained energy from the molecule, leaving the molecule in a different vibrational state. In Rayleigh scattering the molecules is in the same state when the photon leaves. In Stokes scattering, the photon loses energy to the molecule, again changing the vibrational state of the molecule.

In practice, Raman spectroscopy uses a collimated laser beam as radiation source, because laser light is monochromatic. Lasers also permit measurements of relatively small Raman shifts, with high signal-to-noise ratios. Selection of the radiation source wavelength depends on several factors: The Raman differential scattering cross-section, the magnitude of the Raman shift in wavelength, and the potential for fluorescence.⁶³

The Raman differential scattering cross-section σ , which is the probability of an absorption process to occur, or in other words the probability of a particle-particle interaction, is given by:

$$\sigma \propto (\bar{\nu}_0 - \bar{\nu}_{vib})^4, \quad (2.21)$$

where $\bar{\nu}_0$ is the wavenumber of the incident radiation, and $\bar{\nu}_{vib}$ is the wavenumber of a vibrational mode of the molecule of interest. The consequence of equation 2.21 is that for a given vibrational mode with a specific wavenumber, a radiation source with shorter wavelength increases the Raman scattering cross-section with respect to a source of longer wavelength.

The Raman shift is constant with respect to vibrational energy, thus it is constant in wavenumber, but not in wavelength. A large Raman shift greatly facilitates the separation of Rayleigh and Raman scattered light, possibly yielding better signal-to-noise ratios with the ability to measure smaller Raman shifts.

Fluorescence can arise when the selected radiation source approaches shorter wavelengths. Fluorescence is a different inelastic scattering process which can become so pronounced that it can interfere with weak Raman signals. This problem was encountered in this work: The analysis of dehydrated samples of 1,4-benzenediboronic acid was greatly impaired by fluorescence when a Nd^{3+} green (532 nm) laser was used as radiation source. To circumvent this obstacle, a near-infrared

Nd³⁺:YAG (1064 nm) laser was used instead, which effectively doubles the radiation wavelength of the first laser source. Similar problems have also been reported in the analysis of wood constituents.⁶⁴

Raman spectroscopy is usually considered a complementary analytical method to Infrared (IR) spectroscopy, because of the existence of complementary selection rules. For a vibrational mode to be active in Raman, the polarisability of the molecule has to change during the vibration, as explained before, whereas to be IR active, the dipole moment has to change during the vibration. One example is the totally symmetric vibrations found in homonuclear diatomic molecules, which are Raman active, but IR inactive. The Raman spectral energy range spans from 200 cm⁻¹ to 4000 cm⁻¹, allowing its use for organic as well as inorganic species. Because minimal or no sample preparation is required, this analytical technique efficiently produces reliable results. Also, since the vibrational information is specific to the chemical bonds, Raman spectroscopy is often used as fingerprint technique for chemical identification of molecules.

2.1.3 Powder X-Ray Diffraction (PXRD)

Powder X-ray Diffraction is based on the interaction of X-rays with the atom's inner electron cloud. Incident X-rays interact with these electrons, re-radiating secondary, or diffracted X-rays, due to Rayleigh scattering (see figure 2.6, Rayleigh). Coherent diffraction of X-rays is related to the interplanar spacing of lattice planes in the crystalline structure, according to the following equation:

$$n\lambda = 2d \cdot \sin \theta, \quad (2.22)$$

where n is an integer, λ is the wavelength of the incident X-rays, d is the interplanar spacing in the atomic lattice, and θ is the diffraction angle between the incident beam and the scattering planes. This equation is called "Bragg's Law", and was derived in the year 1912 by W. L. Bragg and H. Bragg.

PXRD is widely applied for the characterization of crystalline materials. It provides less information than single-crystal X-ray diffraction; however, it is much simpler and faster. PXRD does not require single crystal samples; also, these crystals do not need to be large. PXRD is useful for identifying a solid material, as well as determining crystallinity and phase purity.

Ideally, the sample should be a statistically infinite amount of randomly oriented powder crystallites of less than 10 μm in size. In this way, all possible crystalline orientations are exposed to the X-ray beam. In practical terms, most instruments use a limited analytical volume to preserve good resolution, so a relatively small sample is enough to yield very good results when analyzed.⁶⁵

For PXRD, the better the monochromaticity of the X-ray radiation, the better the experimental results. The radiation emitted from an X-ray tube consists mainly of $K\alpha_1$, $K\alpha_2$ and $K\beta$. For this work, Mo- $K\alpha_1$ was the only radiation used. $K\beta$ radiation is normally removed by a filter or a monochromator. $K\alpha_2$ can also be removed by a filter, although not easily; therefore it is usually removed electronically during data processing.⁶⁵

2.1.4 Thermogravimetric Analysis (TGA)

Thermogravimetric Analysis (TGA) is a technique in which the mass (weight) of the sample is monitored as it is subjected to a controlled temperature program. This is usually performed under a controlled inert-gas atmosphere. The variations in mass are plotted as a function of temperature or time.⁶⁶ With TGA, the temperature at which reactions occur can be determined. Typical examples are dehydration reactions, polymerization, desorption, and decomposition. With the recorded variations in weight, and with some prior knowledge about the sample's chemical nature, the reactions that take place in sample can be interpreted. In this work, TGA was used to determine the onset temperature of the dehydration reaction of 1,4-benzenediboronic acid.

2.2 Materials

Both readily commercially available and specifically prepared or synthesized materials were used in the course of this work. Highly Oriented Pyrolytic Graphite (HOPG), some molecular building blocks, and all solvents used fit in the first classification; while mica-supported gold(111) and most of the molecules studied belong to the second classification. Due to the small scale at which experiments were performed, only small amounts of material were necessary, almost resembling microscale chemistry.

2.2.1 Choice of Substrate

Suitable supporting substrates for STM analysis of deposited molecules should be ultra flat, *i.e.* they should possess large, very flat regions spanning an area of many thousands of square nanometers, preferably at least $50 \times 50 \text{ nm}^2$. Some natural minerals meet this requirement when cleaved, for example, naturally occurring graphite, molybdenite (MoS_2) and mica. However, these materials must also be electrically conductive, which expels mica out of this group. Usually, substrates used for STM analyses are prepared by other methods, like finely polishing a single crystal, as in the case of metals, by synthetic production, as with HOPG, or by Physical Vapor Deposition (PVD) on a very flat surface. This last approach is usually the preferred method to prepare Au(111) surfaces for STM analyses due to the small amount of expensive materials necessary. These surfaces are usually supported by a clean glass substrate or by natural mica mineral. More information about this procedure can be found in appendix 1.

In this work, the most used supporting substrate for studying molecules was graphite. It was freshly prepared by cleaving a HOPG crystal with adhesive tape. In the early days of STM, graphite was regarded an inappropriate substrate for molecular deposition due to multiple observed artifacts mimicking adsorbed organic molecules.^{67,68} However, after substantial experimentation, most of these artifacts have been hitherto recognized as inherent features of graphite and successfully explained.⁶⁹⁻⁷² Consequently, graphite has become very popular as a supporting substrate for liquid-solid STM experiments.

2.2.2 Solvents

In order to image molecules on substrates under the STM, it is first needed to deposit these molecules. Langmuir-Blodgett film deposition was among the first techniques used.⁶⁸ However, this method has come into disuse, being superseded by molecular vapor deposition in UHV or by dissolving the molecule of interest in a solvent and then applying the solution onto a substrate. In this

last case, the solute molecules eventually adsorb on the substrate, rendering them observable with the ambient STM at the liquid-solid interface.

The solvents used in this work are almost non-volatile and have virtually zero electric conductivity. The first characteristic assures, in practical terms, a stable concentration during the time laps of the STM analysis. The second characteristic produces an insulating environment for the scanning tip, avoiding problems with leakage currents. Hence, the tunneling electrons flow only between tip and sample, exclusively imaging the surface or the molecules adsorbed on it. It also renders any insulation of the scanning tip unnecessary,⁷³ further simplifying the experimental procedure.

The old rule in chemistry, “like dissolves like”,⁷⁴ aids in selecting the solvents that dissolve the molecules used in this work. The organic molecules used (see section 2.5.3) dissolve best in organic solvents that possess similar functional groups. Therefore for tricarboxylic and diboronic acids solutes, fatty acids or alkanolic alcohols solvents readily dissolved these molecules. As a counterexample, dodecane, an alkane, did not dissolve TCBPB, a large tricarboxylic acid.

2.2.3 Molecular Building Blocks

In this work, the molecules studied were all organic. They are composed mainly by one or several phenyl rings, σ -bonded or fused. The molecules are functionalized by carboxylic acids, boronic acids or alcohols. Carboxylic acids were used to study supramolecular self-assembly, while boronic acids were mainly required to react and form new, larger compounds and networks interconnected by covalent bonds. Alcohols were used either for self-assembly or for bond formation with boronic acids. Relevant details of each molecule used, and the reactions and processes they undergo, are presented in the following chapters.

Molecular precursors were obtained from several sources. Some are commercially available, like 1,4-benzenediboronic acid; others were synthesized by collaborating research groups. One of these groups is headed by Prof. Michael Schmittel, located at the University of Siegen. This group synthesized the large tricarboxylic acids. The other group is headed by Prof. Thomas Bein, in collaboration with Prof. Paul Knochel, at the Chemistry Department of the LMU in Großhadern. This last group supplied the para-diboronic acids, except for 1,4-benzenediboronic acid.

3

Supramolecular Self-Assembly on Surfaces

In self-assembly, disorganized objects autonomously and spontaneously form specific organized structures. These objects can mostly interact only with their closest neighbors. The process may use an extremely large number of individual components, building networks that can span lengths that are thousand times the size of any individual component. The structures are in dynamic equilibrium with additional building blocks in the surroundings. This implies that self-assembly is a completely reversible process. It allows the individual constituents to move and reach the energetically most stable configuration, and has the potential for self-repair or self-heal. Self-assembly has been widely studied in non-living systems and was proposed to play an important role even in living organisms.⁷⁵ Self-assembly has been observed in 3-dimensional systems, for instance, in crystallization or in atmospheric weather systems;⁷⁵ in 2-dimensional ones, like the formation of surface-supported self-assembled monolayers; down to 1-dimension, for example, building nanowires.⁷⁶ Lessons learnt from natural self-assembled systems have been applied to artificial systems. For instance, mathematical algorithms were used to control the physical interactions between modules in robots.^{77,78}

The field of surface-supported self-assembly began in 1946 when Zisman *et al.* demonstrated the adsorption of a monolayer of surfactant molecules onto a metal surface.⁷⁹ It received greater attention when Nuzzo and Allara showed in 1983 the solution-based self-assembly of thiols on a gold surface, via disulfide adsorption of di-n-alkyl.⁸⁰ Since then, further research has yielded self-assemblies that consist of a variety of organic^{12,81,82} and inorganic building blocks,⁸³ on many different substrates from metallic,⁸⁴⁻⁸⁷ to chalcogenides,⁸¹ to graphite⁸⁸⁻⁹² (non-metallic). For the direct in-situ observation of these assemblies down to the molecular level, the Scanning Tunneling Microscope (STM) has proved to be an utmost important tool.

Potential applications of molecular self-assembly have already been identified and some practical uses are emerging. A promising example is the removal of oil droplets on water by coating a cylindrical gold rod with a hydrophobic self-assembled monolayer that consists of long alkanethiol chains.⁹³

In the following, the molecules directly involved in the self-assembly process, *i.e.* the molecular building blocks, are denoted “adsorbates” or “solutes”. Both terms refer to the same building blocks, but distinguish whether they are still dissolved in solution or bound to a surface.

3.1 Thermodynamics

Like any other spontaneous process in nature, the formation of a self-assembled monolayer can only occur if the associated change in the Gibbs free energy ΔG is *negative* at constant temperature and pressure. ΔG is expressed by equation 3.1 as follows:

$$\Delta G = \Delta H - T\Delta S . \quad (3.1)$$

Here, ΔH is the change in enthalpy, ΔS the change in entropy, and T the temperature of the system.

Self-assemblies usually emerge from an initially disorganized state and converge towards a more ordered state, yielding a *negative* net change in the entropy of the system. Although this may seem counterintuitive for a spontaneous process, it is explained by the overall change in entropy of the universe ΔS_{univ} , given by:

$$\Delta S_{univ} = -\Delta G / T . \quad (3.2)$$

ΔS_{univ} is positive for *all* spontaneous processes and ultimately drives all reactions. Hence, self-assembly can only take place if the associated negative value of the change in enthalpy (ΔH) in equation 3.1 is smaller than the positive term $-T\Delta S$.

Nucleation, diffusion, adsorption, desorption, and ripening processes control the growth of surface-supported self-assemblies. As the assemblies increase in size, the Gibbs free energy of the system progressively decreases. This continues until a dynamic equilibrium is reached, reflected in a minimum of the Gibbs free energy. Thus, the assemblies become thermodynamically stable.

Under ideal circumstances, self-assemblies achieve their final configuration by arranging and rearranging the building blocks relative to each other, in order to find patterns with the lowest possible Gibbs free energy under the given conditions. These conditions are imposed by external and internal factors, like temperature, choice of solvent, solute concentration, and choice of substrate.⁹⁴ If the system is at room temperature, the participating forces should be in the range of $k_B T$, where k_B is the Boltzmann constant. Weak intermolecular interactions fulfill this energy requirement. Those include, for example, hydrogen bonds, van der Waals, π - π interactions, weak polar forces, etc.^{94,95} The interactions most relevant for this thesis will be discussed in section 3.2.2. Because these interactions are reversible in nature, and the equilibrium achieved is dynamic, the system has the ability to correct structural errors; that is, to self-heal. Thus, regular and extended, almost error-free, supramolecular networks, can be realized.

If perturbations to the ideal conditions occur during self-assembly, the resulting final state can be different to those attained under ideal conditions. Upon removal of these perturbations, the system may be in a meta-stable state of equilibrium. Transformations to the most stable states can take place slow enough to allow for their experimental observation. Factors altering ideal conditions need only be mild, for example, small local changes in temperature, presence of step edges on the substrate, solvent evaporation in the time lapse of the experiment, and hence increase in the concentration (in liquid-

solid self-assembly). Observation of the existence of different assemblies and structures under similar experimental conditions is a proof of the co-existence of structures with very similar ΔG .

To assess the thermodynamic contributions that play a role in self-assembly as given in equation 3.1, namely the change in enthalpy (ΔH) and the change in entropy (ΔS), a separate analysis of both contributing factors is presented in the following.

The enthalpy change due to self-assembly, ΔH , comprises mainly the adsorbate-substrate and adsorbate-adsorbate interaction energies. These are the most important interactions when the process takes place in vacuum. This picture becomes more complicated when self-assembly takes place at the solid-liquid interface. Here, other contributions to ΔH have to be taken into account, like solvation enthalpy and co-adsorption of solvent molecules on the substrate. The first two interactions, adsorbate-adsorbate and adsorbate-substrate, can be estimated via quantum chemical calculations or Molecular Mechanics (MM). Solvation enthalpies can be experimentally measured in a calorimeter. However, due to the sparing solubilities of the solutes in the organic solvents used,^{12,96,97} the very small enthalpy changes (in the order of ~ 3 kJ/mol)⁹⁸⁻¹⁰⁰ are of minor importance when compared to adsorbate-substrate and adsorbate-adsorbate interactions (see table 3.1). Hence, this issue will not be addressed further. Co-adsorption of solvent molecules is difficult to quantify, and therefore its total influence is complicated to calculate. However, its estimated contribution has to be included in the entropy and enthalpy evaluations.

In order to estimate the total entropy change, ΔS_{total} , a model proposed by Whitesides¹⁰¹ and co-workers is applied. This model was developed to explain entropic changes occurring in the self-assembly of particles in solution. Here, the model is applied to 2-dimensional substrate-based solution self-assembly, on the basis that the proposed relations are applicable for both cases. The total entropy change can be partitioned as follows:

$$\Delta S_{total} = \Delta S_{conf} + \Delta S_{trans} + \Delta S_{rot} + \Delta S_{vib}, \quad (3.3)$$

where the terms on the right hand side of equation 3.3 are: conformational, translational, rotational, and vibrational entropy, respectively.

Conformational entropy, ΔS_{conf} , is of great importance in systems where their individual components can experience large changes in their conformation, as is the case when polymers and proteins fold. When small and relatively rigid molecules self-assemble, as those used here, conformational changes upon assembling are minimal. Thus, ΔS_{conf} is considered to be almost zero for all practical purposes, and can therefore be safely neglected.

Translational entropy, ΔS_{trans} , can be calculated by the following equation:

$$\Delta S_{trans} = R \cdot \ln \left[\frac{1}{c} \left(\frac{2\pi \cdot m \cdot k_B T \cdot e^{\frac{5}{3}}}{h^2} \right)^{\frac{3}{2}} \right], \quad (3.4)$$

where R is the gas constant, m the mass of the solute, k_B Boltzmann's constant, T the absolute temperature, e Euler's number, h Plank's constant, and c the solute concentration. Equation 3.4 is a form of the Sackur-Tetrode equation. It was first deduced by means of statistical mechanics to estimate the absolute entropy of an ideal single-atomic gas, which only consists of translational entropy. However, when applied to molecules in solution, equation 3.4 significantly overestimates the translational entropy. In order to avoid this overestimation, the concentration c can be referred to the free volume of the solvent as obtained by the hard cube approximation.¹⁰¹

The rigid body rotational entropy, ΔS_{rot} , can also be estimated from statistical mechanics by the equation:

$$\Delta S_{rot} = R \cdot \ln \left[\frac{\sqrt{\pi}}{\gamma} \left(\frac{8\pi^2 \cdot k_B T \cdot e}{h^2} \right)^{\frac{3}{2}} \sqrt{(I_1 \cdot I_2 \cdot I_3)} \right], \quad (3.5)$$

where γ is related to the symmetry of the solute molecule, and I_1 , I_2 , and I_3 are its principal moments of inertia. Equation 3.5 gives the rotational entropy of a molecule in the gas phase,^{101,102} and can be directly used to calculate the rotational entropy of molecules in solution with ~2% uncertainty.¹⁰¹

Vibrational entropy can be estimated using the following equations that are also derived from statistical mechanics:^{103,104}

$$\Delta S_{vib} = k_B \cdot \sum_{i=1}^n \left[\frac{\varepsilon_i / T}{e^{\varepsilon_i / T} - 1} - \ln(1 - e^{-\varepsilon_i / T}) \right], \quad (3.6)$$

and

$$\varepsilon_i = h \cdot \nu_i / k_B. \quad (3.7)$$

Here ε_i is the vibrational energy, n is the index of all normal modes, and ν_i is the vibrational frequency of the i^{th} normal mode. The total vibrational entropy is the sum over all vibrational modes. For almost all vibrational modes at 25°C, $T\Delta S_{vib}$ values are very small, especially in relation to typical values of ΔS_{trans} and ΔS_{rot} . Hence it is assumed that ΔS_{vib} is negligible and can be discarded in the calculation of the total entropy change.

Taking all of the considerations above into account, the total entropy change can be greatly simplified when the two main contributors are the only ones considered, as expressed in equation 3.8:

$$\Delta S_{total} \approx \Delta S_{trans} + \Delta S_{rot}. \quad (3.8)$$

Using equation 3.8, the total entropy loss when molecules form surface-supported self-assembled monolayers from solution can be calculated easily.

3.2 Parameters Affecting Supramolecular Self-Assembly on Surfaces

The final self-assembled structures obtained with the molecular building blocks are directed by many factors. The most important ones will be analyzed and discussed here.

3.2.1 Molecular Structure

Normally, the molecules (adsorbates) that build the self-assemblies possess purposely designed geometries, functional groups, and positioning of these groups relative to one another. Thus, the building blocks encipher basic information about the final self-assembly structure. In this thesis, the aim is to synthesize regular and extended open-pore networks. To this end, three-fold symmetric molecules, possessing a carboxylic acid functional group at each lobe, were used.^{12-14,97,105} Figure 3.1 shows some of these molecules, along with their isotopological smaller variant, trimesic acid (TMA). All these molecules are equipped with a rigid backbone comprised of one or several phenyl rings. These rings promote the planar adsorption of the molecules on graphite, allowing the formation of hydrogen bonds between them via their carboxylic acid groups.

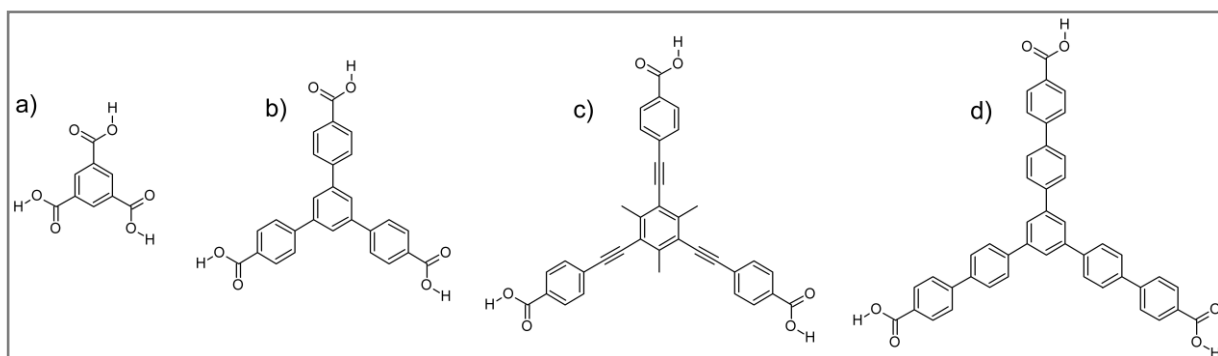


Figure 3.1: Isotopological tricarboxylic molecules that possess three carboxylic acid groups oriented at 120° with respect to each other. **a)** Trimesic acid, TMA (benzene-1,3,5-tricarboxylic acid); **b)** BTB (1,3,5-benzenetribenzoic acid); **c)** MeCEPBA (4-{2-[3,5-bis[2-(4-carboxyphenyl)-1-ethynyl]-2,4,6-trimethyl-phenyl]-1-ethynyl}); **d)** TCBPB (1,3,5-tris[4'-carboxy(1,1'-biphenyl-4-yl)]benzene). Image adapted from reference 96.

Although the desired self-assembly structure, a regular open-pore network of hexagonal cavities is encoded in each molecule's design, self-assembly of other polymorphs cannot be excluded. This is because other competing interactions can dominate the self-assembly process. These can arise between adsorbates or between adsorbate and solvent molecules. This issue will be addressed in more detail in the next sections.

3.2.2 Intermolecular Forces

Because self-assembly is a process where additional building blocks are in dynamic equilibrium with the final structures, the interactions holding them together need to be reversible. This discards the formation of irreversible bonds, like covalent or ionic, and favors utilization of comparatively weak bonds, as explained in the following.

Adsorbates arriving at a surface interact with it via chemisorption or physisorption, thereby lowering the free energy of the system. For chemisorption, strong interactions between adsorbate and substrate are mediated through charge transfer or charge sharing. Typical examples thereof are thiols on gold substrates. For physisorption, interaction energies are smaller than for chemisorption, leaving the electronic structure of the molecules and substrate involved unperturbed. Weak van der Waals forces are typical interactions that mediate physisorption and are always present between interacting molecules.^{97,106} The lack of possible stronger interactions between the adsorbates used here and graphite substrate, *i.e.* covalent or electrostatic bonds, leave van der Waals forces as the dominating adsorbate-substrate interactions. Although these interactions amount to less than 5 kJ/mol,¹⁰⁶ taken collectively they become a very strong force for the stabilization of physisorbed assemblies.

π - π interactions can arise among aromatic molecules¹⁴ or between adsorbates and a substrate. Although this type of interaction may be neglected in molecules of less than 10 carbon atoms, it becomes important as the adsorbates increase in size.¹⁰⁷ Overall, π - π interactions can be regarded as a weak force and are already taken into account within the aforementioned van der Waals interactions. However, in particular cases, this specific type of interaction has been suggested to favor the formation of self-assemblies where π - π stacked molecules adsorb upright on graphite, instead of yielding the expected network of flat-laying adsorbates.¹⁴

The adsorbates presented in figure 3.1 are built from phenyl rings and therefore intended to self-assemble flat on a substrate. When the substrate is graphite, the interaction of flat-laying benzene with this substrate becomes additionally promoted when benzene is substituted with carboxylic acid (COOH) groups. This is explained by the presence of the carbonyl group (C=O), which possess electron-withdrawing properties, and hence decreases the π -electron density of benzene. Thus diminishing the π - π repulsion that arises between the delocalized π -electrons of benzene and graphite.¹⁰⁸ This fact may also be applied to molecules composed of several σ -bonded benzene rings, as are the adsorbates used here.

The larger the molecular surface exposed towards an adsorbing substrate, the greater the magnitude of the adsorbate-substrate interaction. Hence, the more restricted the lateral mobility of individual adsorbates along the surface (2D diffusion) upon adsorption. To quantify these interactions on a graphite substrate, Molecular Mechanics (MM) simulations, based on the Dreiding force field, were used. The results for the tricarboxylic acids shown in figure 3.1 are presented in the following table.

Table 3.1: Adsorbate-graphite interaction energies for flat-laying molecules calculated using MM, based on the Dreiding force field. The larger the molecular surface towards the substrate, the greater the interaction energy.

| Adsorbant | Projected van der Waals surface area (planar to the substrate) [nm ²] | Adsorbate-substrate (graphite) interaction energy [kJ/mol] |
|-----------|---|--|
| TMA | 0.65 | 115.6 |
| BTB | 1.22 | 256.6 |
| MeCPEBA | 1.86 | 354.1 |
| TCBPB | 2.09 | 392.3 |

While the interactions presented above mainly mediate the adsorption of molecules on a substrate, hydrogen bonds (H-bonds), on the other hand, account mainly for intermolecular interactions among accordingly functionalized adsorbates. H-bonds are considered strong intermolecular interactions that play a very important role in designing and directing the assembly's final structure. A main reason for this can be found in the inherent directionality of hydrogen bonds, where linear geometries that follow the free electron lone pair direction are favored over bent geometries.¹⁰⁹ However, this directionality is considered soft, and significant deviations from linearity are tolerated.^{109,110}

Hydrogen bonds can be classified, in decreasing energetic order, as strong (F–H···F < O–H···O < N–H···O < N–H···N) and weak (C–H···O < C–H···N < O–H··· π < N–H··· π < C–H··· π).¹¹⁰ Although the strong H-bonds are expected to direct crystallizations patterns in bulk structures, weak C–H···O bonds are also known to play an important role, mainly when carbonyl groups are present as hydrogen bond acceptors.¹¹⁰ In 2D self-assemblies, one of the preferred functional groups used is the carboxylic acid group, which is expected to yield a strong (60 kJ/mol),¹¹¹⁻¹¹³ cyclic two-fold H-bond as detailed in figure 3.2. In this arrangement, two carboxylic groups interact “head-to-head” forming a stable dimer.

The motif depicted in figure 3.2 was observed in the self assembly of small molecules as TMA^{12,82} and medium-sized BTB¹³, and others carboxylic acids.^{106,114} Deviations from the cyclic dimer were observed in the TMA flower^{12,82} and super flower structure¹¹⁵, however interestingly, strong O–H···O hydrogen bonds were still formed. The geometrical design of large molecules as MeCPEBA and TCBPB, retaining the same three-fold symmetry and positioning of the carboxylic acid functional groups at 120° relative to each other as TMA and BTB, was expected to likewise lead to self-assemblies via the exclusive formation of strong O–H···O H-bonds. Although O–H···O H-bonds were indeed observed, the single (4–8 kJ/mol)^{116,117} and two-fold weak C–H···O H-bonds were quite commonly encountered in the self-assemblies of these large adsorbates.^{96,118} The two-fold “displaced” C–H···O H-bond motif is depicted in figure 3.3.

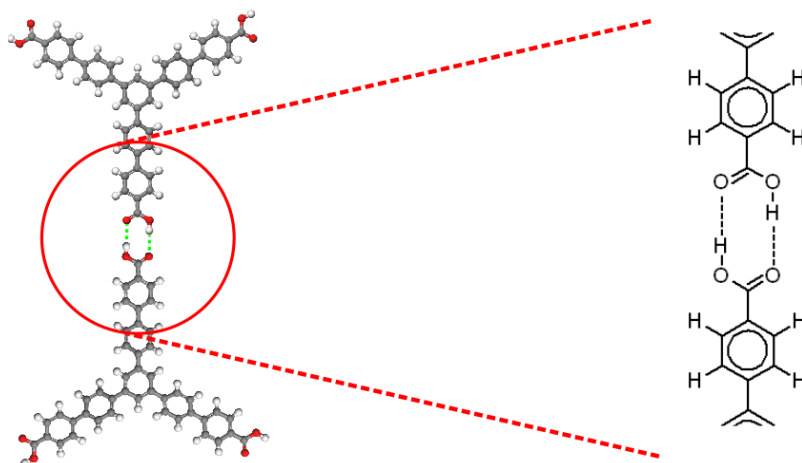


Figure 3.2: The red circle highlights the “head-to-head” cyclic interaction motif of a strong two-fold O–H···O H-bond between two carboxylic acid groups of TCBPB.

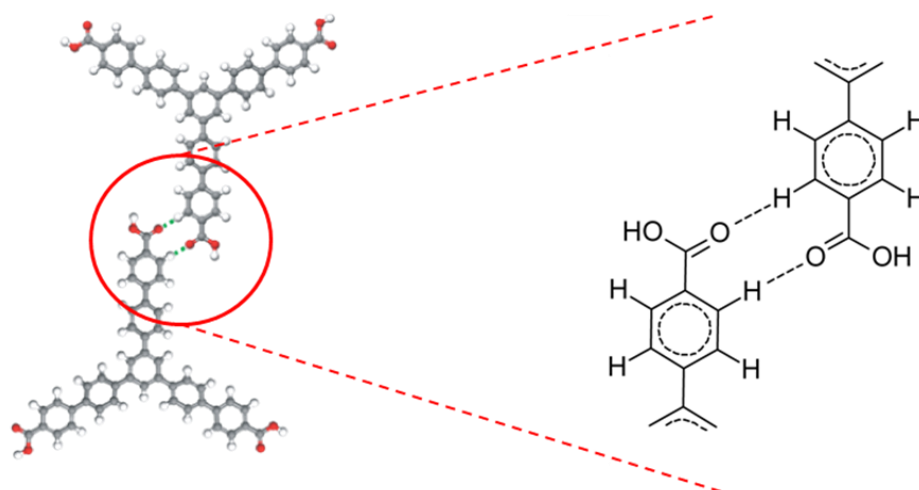


Figure 3.3: “Displaced” H-bond motif of a weak two-fold C–H···O H-bond observed in the self-assembly of large tricarboxylic acid molecules of MeCPEBA and TCBPB.

Cyclic H-bonds, as those depicted in figures 3.2 and 3.3, increase their bonding strength by the so-called Resonance Assisted Hydrogen Bond (RAHB).¹¹⁰ Here, the hydrogen bond donor and acceptor atoms are connected via π -conjugated double bonds. This implies the presence of a covalent character in the hydrogen bond, which is consistent with its known bond directionality.¹¹⁹ This principle can be applied to intra- and intermolecular hydrogen bonds, and is also conceivable for a cyclic two-fold C–H···O H-bond,^{120,121} hinting towards a cooperative enhancement also for this type of H-bonds.

The formation of the “displaced” dimer motif shown in figure 3.3 has three direct consequences:

- Functionalization of the cavities formed in an open-pore self-assembly,
- formation of chiral assemblies, and
- formation of self-assemblies with higher packing densities

In the first case, the functionalization arises via the possible formation of strong O–H···O hydrogen bonds with the adsorbate's carboxylic acid groups that point into the pores. In the second case, the displaced motif possess an inherent chiral structure that will form organizational chiral assemblies.¹²² Steric constraints or intermolecular directional forces are responsible for the formation of displaced dimers.¹²² However, it must not be overseen that the adsorbates giving rise to these chiral dimers are intrinsically achiral. Since energetically equivalent enantiomers are always formed in equal proportions, the global chiral symmetry of the self-assembly is maintained.¹²² The third case is explained by the closer proximity of the building blocks, as compared to polymorphs composed by the head-to-head dimer motif.

The synthesis of self-assemblies may be complemented with other reversible, weak bonds known from other systems: Among these are the halogen-halogen interactions,^{123,124} and directional interactions formed by halogens and O or N atoms induced by polarization. An example of the latter case is the iodo···nitro synthon (-I + -NO₂).¹²⁵

3.2.3 Influence of the Solvent

In liquid-solid self-assembly, the solvent plays an important role as the adsorbate's transport medium to the substrate via diffusion.¹²⁶ Another, hitherto not fully understood factor, is its role in determining the final self-assembly structure.¹²⁷ Some explanations for the solvent influence have been proposed: The dielectric constant of the solvents can affect the stability of H-bond motifs,^{13,128} or if co-adsorption of fatty acid solvent molecules occurs, depends on the relative H-bond densities of the self-assemblies.¹²⁹

As mentioned in section 3.2.1, in liquid-solid self-assembly, TMA¹² and BTB¹³ almost always formed structures by means of a cyclic two-fold O–H···O hydrogen bonded dimer motif as their basic H-bond moiety (figure 3.2). Exceptions are the flower, superflower and other minor structures found for TMA.^{12,115} However, these structure were still held together by strong O–H···O H-bonds, although some of them totally or partially in different hydrogen bonding schemes as that shown in figure 3.2.¹² Larger molecules, like MeCPEBA^{14,118} and TCBPB,⁹⁶ showed both the possibility to assemble via the two-fold O–H···O hydrogen bonded dimer motif or via the displaced two-fold C–H···O H-bonded dimer motif (figure 3.3). For these two large molecules, the final structure was experimentally found to depend on the solvent. A possible explanation will be proposed in the following.

Carboxylic acids have the capability to form strong two-folded intermolecular H-bonds, as explained before. TCBPB and the other solutes mentioned possess three carboxylic acid groups each.

When dissolved in fatty acids, each one of these carboxylic acid groups of TCBPB can form a two-fold $\text{O-H}\cdots\text{O}$ H-bond with one solvent molecule. This bond is reinforced by RAHB. In principle, it is also possible to have solute-solute $\text{O-H}\cdots\text{O}$ hydrogen bonds, but given their sparing solubilities in the fatty acids (49.3 μM of TCBPB in heptanoic acid), the ratio of solvent to solute molecules is very high (saturated TCBPB in heptanoic acid: $\sim 143000:1$) rendering solute-solute interaction very improbable.

When a drop of this solution is applied onto a graphite substrate, TCBPB molecules reach the substrate still solvated, *i.e.* H-bonded to three solvent (fatty acid) molecules. Due to the large adsorbate-substrate interaction (see table 3.1), TCBPB molecules have a long enough interaction time on the surface that allows them to eventually diffuse laterally and approach each other. When the TCBPB adsorbates approach each other, the fatty acid molecules that are still attached to the carboxylic acid groups of TCBPB can hamper the formation of cyclic and strong two-fold $\text{O-H}\cdots\text{O}$ hydrogen bonds between adsorbates. Instead, $\text{C-H}\cdots\text{O}$ H-bonds form between adsorbates, because the sites available to form them are not obstructed. If in this situation more TCBPB molecules assemble to this first two molecules in the same way, a nucleus is created, and the characteristics of a displaced motif is replicated as the self-assembly grows larger.

It was observed experimentally that TCBPB dissolved in heptanoic acid forms self-assemblies built almost exclusively from displaced dimers, whereas if dissolved in octanoic or nonanoic acid, the proportion of $\text{O-H}\cdots\text{O}$ H-bonds between TCBPB increases, accompanied by a decrease in displaced dimer formation. Figure 3.4 illustrates this behavior, which appears to be independent of concentration.

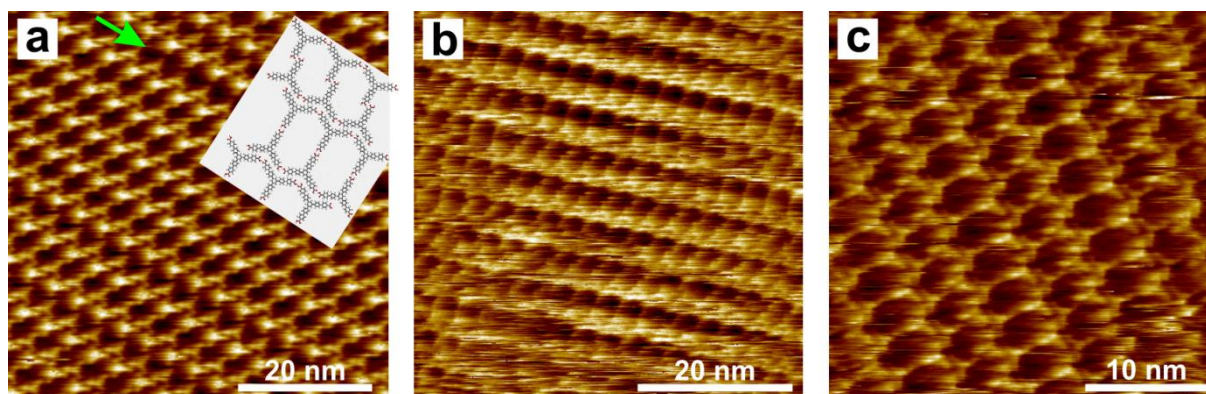


Figure 3.4: STM images at the solid-liquid interface of TCBPB dissolved in different fatty acids at ambient conditions. **a)** Solvent: heptanoic acid. The displaced dimer motif is almost always present in detriment of the head-to-head one. An exception is marked by the arrow. The inset highlights the two different dimer motifs (not to the same scale as the image). **b)** Solvent: octanoic acid. The presence of the head-to-head dimer becomes more prominent. **c)** Solvent: nonanoic acid. The head-to-head dimer motif is more or less represented in equal amounts as the displaced one.

The solvent dependency that yields “displaced” or “head-to-head” cyclic H-bond motifs with TCBPB has similarly been observed with MeCPEBA dissolved in fatty acids: In octanoic acid, only the displaced motif was found, whereas in nonanoic acid, both motifs were observed.¹¹⁸

On the other hand, BTB, a smaller tricarboxylic acid with the same three-fold geometry, yielded only the “head-to-head” O–H···O motif in comparable self-assembly studies.^{13,97} This can be rationalized by its higher solubilities than TCBPB in the same fatty acid solvents. In these solvents, the possibility BTB has to form O–H···O H-bonded cyclic dimers made via its carboxylic acid groups with other BTB molecules while still in solution is higher due to these higher solubilities. For instance, BTB in heptanoic acid at saturation concentration is 770 μM ,⁹⁷ whereas TCBPB at saturation concentration in the same fatty acid, 49.3 μM :⁹⁶ a $\sim 15\times$ factor difference. Hence, it could be possible that two-fold O–H···O H-bonded cyclic BTB dimers adsorb directly from solution onto the substrate. If more BTB dimers assemble to this arrangement, a nucleus forms.¹³

Coming back to the case of TCBPB, when an alcohol is used as solvent, the displaced dimer motif has *never* been observed, but only the head-to-head, as depicted in figure 3.5. Again, it can be rationalized by the ability of the solvent to form O–H···O H-bonds with the adsorbate. Whereas it was explained that fatty acids can form strong two-fold O–H···O H-bonds with the solute, alcohols, on the other hand, can only form one O–H···O H-bond per molecule with the adsorbate. They are less strong than those formed between fatty acids and TCBPB, and are also not reinforced by RAHB. So when adsorbates reach the substrate, they are much less restricted to form two-fold O–H···O H-bonds between them. STM images of the corresponding structures are shown in figure 3.5 for 1-nonanol and 1-undecanol. This behavior was found to be independent of concentration.

Overall, this attempt to explain the formation of either displaced or head-to-head dimers does not clarify completely the emergence of different polymorphs encountered here. The concentration is also an important factor that can also define the most stable assembly. The next section deals with this issue.

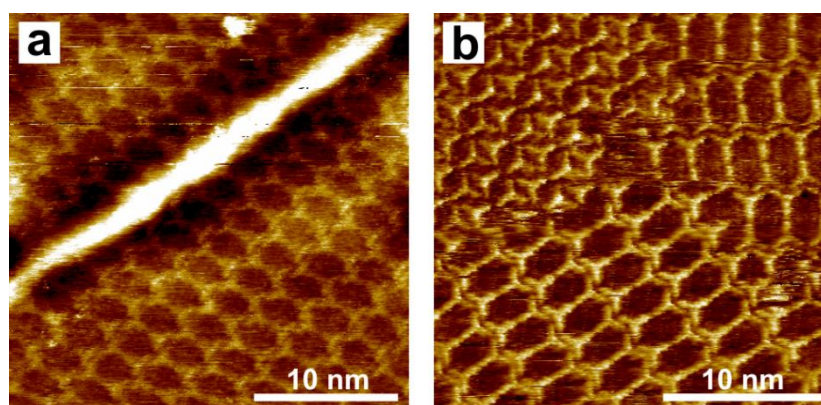


Figure 3.5. STM images of self-assembled TCBPB monolayers obtained at the solid-liquid interface with different alcohols as solvents. **a)** In 1-nonanol at 50% saturation concentration and **b)** in 1-undecanol at 100% saturation concentration. In both cases the head-to-head dimer motif is present, but not the displaced dimer. The top left part in **b)** shows a structure with higher packing density that does not possess any of the two H-bonded dimers described in figure 3.2 and 3.3.

3.2.4 Concentration Effects

In the previous section it has been shown that the solvent has a direct influence on the self-assembly. To complete the picture, the concentration of the solutes in solution has also been studied in detail. The concentration has a pronounced effect on the 2D self-assembly.^{96,97,130}

In several different systems it has been observed that at the higher the concentration, the more densely packed the self-assembled monolayer.^{130,131} Self-assemblies of BTB⁹⁷ and TCBPB⁹⁶ in heptanoic acid are along the lines of these observations. BTB exclusively assembles in the densely packed row structure from a solution at 100% saturation concentration down to some point above 50% saturation concentration. At 50% saturation, domains of this structure co-exist with domains of the less dense chickenwire structure. The latter becomes the dominant structure when the solution becomes more diluted. A similar behavior is observed with TCBPB in heptanoic acid. The concentration dependence is summarized in figure 3.6 for the three polymorphs found. The corresponding STM images are shown in figure 3.7. Models for each structure are given in figure 3.8.

Motivated by the two most common polymorphs found for the system TCBPB dissolved in heptanoic acid, namely oblique-I and displaced chickenwire, a step-by-step growth model of ensembles that lead to the formation of either of both self-assembled monolayers is presented in appendix 2. An ensemble is defined here as an aggregation of molecules with specific positioning relative to each other, stabilized via the displaced H-bond motif (figure 3.3). An ensemble may grow towards the formation of a stable nucleus. However, it is not yet defined as a stable nucleus.

This growth model allows a probabilistic interpretation at any formation step, of the relative chances that any of the two polymorphs have to eventually yield a stable self-assembled monolayer. The probabilistic relationships for ensembles made up of two up to five molecules (self-assembly formation steps 1st to 4th), are shown in table 3.2. In the first formation step (1 TCBPB + 1 TCBPB → 1 displaced dimer), the displaced dimer may be a starting point for any of the two polymorphs with a 1:1 chance (that is, with the same probability). This is because the displaced dimer is a common motif of both polymorphs. The second formation step adds one TCBPB molecule to the dimer formed in the first step. Taking this second step as a new starting point, the formation probabilities of both polymorphs with respect to the previous step change. This idea can be extended by adding more TCBPB molecules to the previous step, and evaluating the respective new formation probabilities. It must be noted that this is a very simplistic interpretation of the events that lead to the formation of the self-assemblies; however, it allows to pinpoint that, as more molecules attach to an existing ensemble, oblique-I becomes the most probable polymorph to eventually self-assemble.

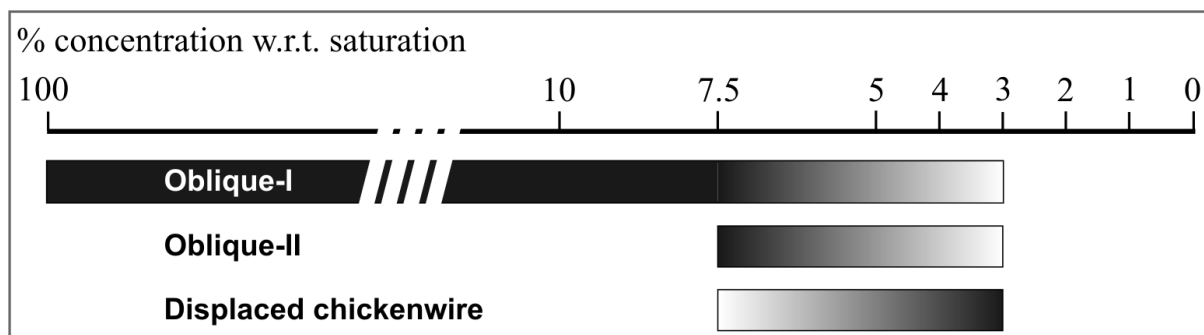


Figure 3.6: Occurance of the various self-assembled monolayer phases of TCBPB in heptanoic acid with respect to the saturation concentration. The darker the color, the larger the surface portion covered by the respective phase. Image adapted from reference 96.

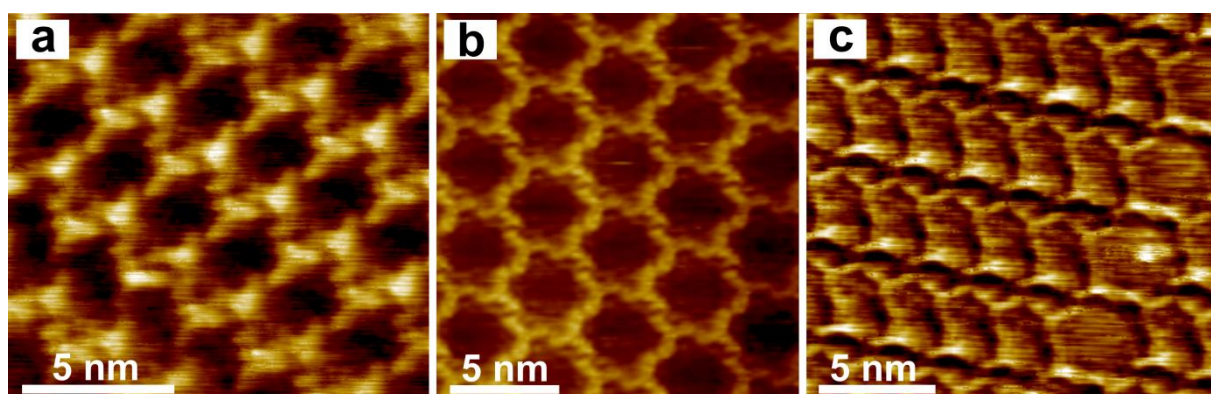


Figure 3.7: STM images at the solid-liquid interface of all three TCBPB monolayer polymorphs found in heptanoic acid: **a)** oblique-I, **b)** displaced chickenwire (drift corrected), and **c)** oblique-II intergrown with a single row of displaced chickenwire. Images taken from reference 96.

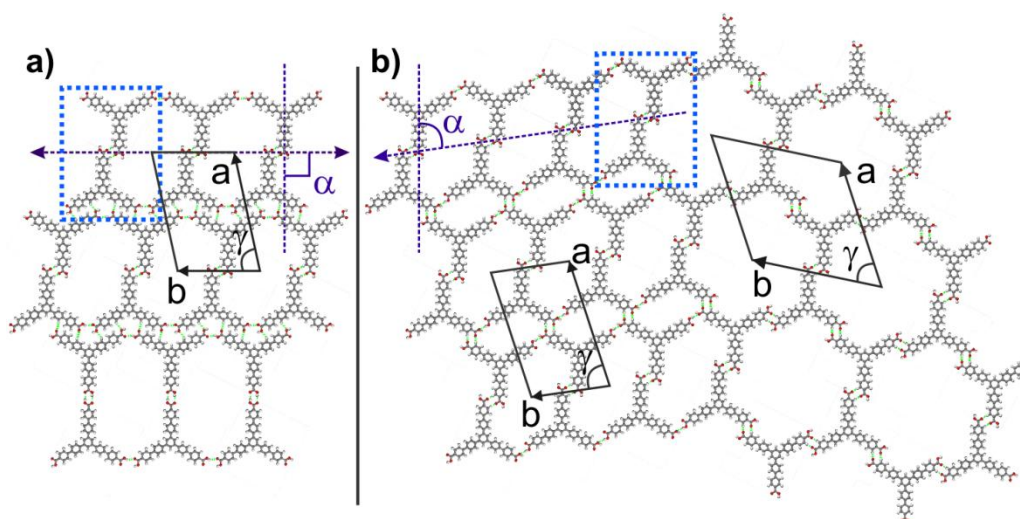


Figure 3.8: Proposed models of the three polymorphs with unit cells indicated. The dotted rectangle highlights the displaced TCBPB dimer motif. Dashed purple lines with arrows indicate the row direction and the definition of the dimer axis, respectively. **a)** Top two rows: Oblique-I ($\alpha \approx 90^\circ$); lower row: Oblique structure formed by two TCBPB molecules “head-to-head” O–H \cdots O H-bonded, as shown in figures 3.4 and 3.5. **b)** Oblique-II (left hand side, $\alpha \approx 81^\circ$), and displaced chickenwire (right hand side). Figure adapted from reference 96.

Table 3.2: Relationships found among TCBPB ensembles at the 1st, 2nd, 3rd, and 4th step of their formation. Only ensembles leading to the formation of oblique-I, displaced chickenwire, or none of both were considered. See appendix 2.

| Ensemble formation step | Number of molecules involved | Probabilistic relationships | | |
|-------------------------|------------------------------|--------------------------------|--|--|
| | | Ensembles leading to oblique-I | Ensembles leading to displaced chickenwire | Ensembles <i>unable</i> to lead to any of both |
| 1 st | 2 | 1 | 1 | 0 |
| 2 nd | 3 | 2 | 1 | 0 |
| 3 rd | 4 | 3 | 1 | 0.4 |
| 4 th | 5 | 4 | 1 | 2.3 |

By inspecting the ratio

$$\frac{\text{ensembles leading to oblique}}{\text{ensembles leading to displaced chickenwire}}$$

from table 3.2 at every formation step, it is observed that for n molecules self-assembling in a stepwise fashion (*i.e.* one-by-one) this ratio can be expressed by the following rule:

$$(n-1)^{\text{th}} \text{ ensemble formation step} = \frac{\text{ensembles leading to oblique}}{\text{ensemble leading to disp. chickenwire}} = (n-1):1. \quad (3.8)$$

It is valid for $n > 1$, and confirmed for integer values up to $n = 5$ (4th formation step). This confirmation does not imply that this rule ceases to successfully predict the relationship at steps higher or lower than those shown.

The preeminence observed in the growth model for ensembles leading to oblique-I at every successive formation step can be interpreted at the molecular level. This dominance of oblique-I can be understood by the flexibility of the configurations of its ensembles. These configurations can be compressed, achieving more densely packed structures, as compared to displaced chickenwire. They will be eventually stabilized by a higher number of H-bonds with higher energy than those in displaced chickenwire. By the same thinking, if ensembles leading to oblique-I cannot be compressed and stabilized, only the remaining ensembles, those leading to the less dense displaced chickenwire, are able to eventually nucleate.

The probabilistic interpretation above would indicate that oblique-I would be the overall dominant structure. In fact, it is the structure assembling in the widest concentration ranges in heptanoic acid, from 100% saturation concentration down to even 3% saturation (figure 3.6). However, when thermodynamics is taken into account, it is possible to explain why not only oblique-I, but other structures can emerge.

*

The experimental evidence shows the predominance of self-assembly phases with higher packing densities at higher solute concentrations. This can be explained by thermodynamics, which suggests that the free energy difference between self-assembled structures determines the prevalence of any one polymorph at a given concentration.^{118,130} However, a kinetic process may be in control of the self-assembly. A model for a possible kinetic influence on structure selection will be explained in the following.

When a solution is applied on a substrate, a flux F of adsorbates impinges on the surface. This flux is controlled by the gradient of the concentration perpendicular to the substrate. It is directly proportional to the concentration gradient $\partial c/\partial z$ of the adsorbates in the solution,⁹⁷ as shown in equation 3.8:

$$F = -d \frac{\partial c}{\partial z}, \quad (3.9)$$

where c is the concentration of adsorbate molecules in solution, d is the bulk diffusivity in solution and z the spatial coordinate perpendicular to the substrate. $\partial c/\partial z$ becomes zero when the thermodynamical equilibrium is reached, *i.e.* when the monolayer growth is completed. Not all molecules colliding with the substrate readily adsorb on it, and those who readily adsorb *increase* the concentration of adsorbates on the substrate. Hence, the flux F must be proportionally scaled down by a numerical factor $K < 1$ to obtain the actual adsorption rate. This rate, again, builds up the concentration θ of adsorbates *on the substrate*. θ can be calculated at any given moment by the following equation:

$$\theta = K \cdot d \cdot \frac{\partial c}{\partial z}. \quad (3.10)$$

The value of θ increases over time as more molecules from solution adsorb on the substrate building the self-assembled monolayer. Thus θ is a function dependent on time t . An average value of θ can be calculated for the time interval of the self-assembly formation. The following equation gives this average value, $\bar{\theta}(t)$:

$$\bar{\theta}(t) = \left(\frac{1}{t_f - t_o} \right) \cdot \int_{t_o}^{t_f} \theta(t) dt, \quad (3.11)$$

where t_o can be defined as the time when adsorbates start to impinge at the surface, t_f may be taken as the time when the self-assembly formation ends, *i.e.* when a stable monolayer has been formed ($t_f > t_o$). In this way, an average value of the concentration of the adsorbates on the substrate during the time span of monolayer self-assembly can be calculated. $\bar{\theta}(t)$ can be evaluated for different values

of c ; however, for different systems, physical comparable results can be obtained provided the considered t_o and t_f are the same.

$\bar{\theta}(t)$ is a helpful value to calculate the *mean distance* that an adsorbate can travel *on the substrate*, until a stable structure is formed. To this end, the mean free path formula for molecules in an ideal gas is adapted for this 2D situation as follows:

$$\bar{\ell}(t) = \frac{1}{4 \cdot r \cdot \bar{\theta}(t)} \quad , \quad (3.12)$$

where $\bar{\ell}(t)$ can be defined as the 2D mean free path on a substrate. As it can be observed, the concentration $\bar{\theta}(t)$ has an inverse proportional effect on $\bar{\ell}(t)$. Hence, lower initial concentrations in solution facilitate longer 2D mean free paths for the adsorbates on the substrate than at higher concentrations.

Two extreme cases can be analyzed: At high initial c (short $\bar{\ell}(t)$), the initial arrangements of adsorbates will promptly be stabilized due to fast adsorption and consequent reduction of the available space. These arrangements will likely tend to pack even tighter, forming a nucleus that will favor the growth of thermodynamically metastable polymorphs with higher packing densities. On the other hand, at low initial c (long $\bar{\ell}(t)$), the arrangements of adsorbates that first form have enough time and space to rearrange and explore other possible and more stable molecular configurations before a nucleus is created. This will promote the growth of polymorphs with lower packing densities and possibly higher stabilities. Thus, the higher the solution concentration, the higher the chances that a structure with high packing density forms, and *vice versa*.

The importance of the available free space for the adsorbates to arrange, rearrange and nucleate, is well represented in the value of $\bar{\ell}(t)$, the 2D mean free path on a substrate. However, not only kinetics, but thermodynamics play a role in determining which polymorph will self-assemble on a substrate. Ultimately, no self-assembled polymorph can form if it is not thermodynamically stable under the respective conditions.

*

For the case of TCBPB self-assembling on HOPG, a structure with a low packing density is enthalpically favored over an assembly with a high packing density from the point of view of a single molecule.¹³⁰ ΔH values for four different conceivable assemblies of TCBPB were calculated by taking into account the adsorbate-substrate and the adsorbate-adsorbate interactions of single TCBPB. These values are listed in table 3.3. Details of these calculations can be found in reference 96. It can be seen that ideal chickenwire possess the most favorable ΔH . However, taking into account the unit cell area ($\Delta h = \Delta H / (\text{unit area})$), oblique-I becomes the most favored assembly. In the same way, the

entropic contributions at different concentrations have been evaluated using equation 3.8 for each polymorph and normalized by their respective unit area ($\Delta s = \Delta S/(\text{unit area})$). When these values are multiplied by the actual temperature (300 K), the $-T\Delta s$ value for each polymorph gives a very good idea of the entropic penalty that each structure has to overcome to self-assemble from solution. It is high at higher concentrations, and *vice versa*; hence it is the highest for oblique-I, and the lowest for ideal chickenwire, from the point of view of the packing densities. Δh and Δs add up to give the total Gibbs free energy gain per unit area. These values show that an assembly with a high packing density is favored over one with low packing density. This is presented again in table 3.3 for two different concentrations.

The co-existence of more than one polymorph indicates that the Gibbs free energies of those structures are of comparable magnitude. The coexistence of two polymorphs is observed in the system TCBPB in heptanoic acid at concentrations below 7.5% saturation (figure 3.6), and at 100% saturation when TCBPB is dissolved in 1-undecanol (figure 3.5b). The values presented in table 3.3 for Δg at 4% saturation for the four polymorphs show a relatively small difference between displaced chickenwire and oblique-I, thereby justifying this statement.

Table 3.3: Comparison of several calculated values of the three experimentally observed polymorphs of TCBPB in heptanoic acid and of one hypothetical polymorph at two different concentrations. **Bold** numbers highlight the energetically most favorable values; *italics*, the least favorable ones. $\Delta h = \Delta H/(\text{unit area})$; $\Delta s = \Delta S/(\text{unit area})$; $\Delta g = \Delta h - T\Delta s$.

| | Structure | | | |
|--|---------------|------------|-----------------------|-------------------|
| | Oblique-I | Oblique-II | Displaced chickenwire | Ideal chickenwire |
| Total ΔH per molecule [kJ mol^{-1}] | -418.4 | -415 | <i>-410</i> | -482 |
| Packing density [10^{14} cm^{-2}] | 0.22 | 0.22 | 0.15 | 0.10 |
| Δh [$\mu\text{J cm}^{-2}$] | -15.28 | -15.16 | -10.21 | <i>-8.00</i> |
| $-T\Delta s$ [$\mu\text{J cm}^{-2}$], saturated | +4.22 | +4.22 | +2.88 | +1.92 |
| $-T\Delta s$ [$\mu\text{J cm}^{-2}$], @4% saturation | +4.52 | +4.52 | +3.08 | +2.05 |
| Δg [$\mu\text{J cm}^{-2}$], saturated | -11.06 | -10.94 | <i>-7.33</i> | <i>-6.08</i> |
| Δg [$\mu\text{J cm}^{-2}$], @4% saturation | -10.77 | -10.64 | -7.13 | -5.95 |

Experimentally, oblique-II is found only in conjunction with the displaced chickenwire assembly, hinting towards a complete dependence of the former on the *previous* formation of the latter. This means that displaced chickenwire serves as a nucleating agent for oblique-II. This could be explained in the following way: Once displaced chickenwire has nucleated, the higher Δg of oblique-II, as compared to that of displaced chickenwire (see table 3.3) dominates and hence this polymorph is formed, thereby hampering the formation of more displaced chickenwire. This suggests oblique-II is

meta-stable at concentrations higher than 7.5% saturation. The experimental evidence also reveals the growth direction of oblique-II, which is almost perpendicular ($\alpha = 81^\circ$) to a straight row of displaced chickenwire. This is highlighted by the arrow in figure 3.8b. No parallel row of oblique-II was ever observed without the presence of displaced chickenwire at one of its ends. So oblique-II relies on displaced chickenwire for both nucleation and as growth template.

*

The displaced chickenwire assembly is exclusively found with TCBPB dissolved in heptanoic acid at concentrations of 7.5% saturation or below, and has never been found in octanoic or nonanoic acid, or in alcohols like 1-nonanol and 1-undecanol. Further conclusions based on this result imply that upon dilution, a different structure is not necessarily formed. For instance, TCBPB dissolved in nonanoic acid always yields the same mixture of rows that consist of head-to-head or displaced H-bonded dimers regardless of the concentration, down to 10% saturation; below this concentration no stable monolayer could be found anymore. The same is true in 1-undecanol, where three different polymorphs were observed: a disordered one,⁹⁶ and the two structures shown in figure 3.5b. In this case, no clear concentration dependency down to 35% saturation was found. Below this threshold concentration, again, no stable monolayer could be found anymore on the substrate.

These experimental findings demonstrate the solvents' ability to stabilize different self-assembly phases. It also asserts the fact that the parameters affecting supramolecular self-assembly cannot be regarded as working independently. Only heptanoic acid can yield the two less dense assemblies (oblique-II and displaced chickenwire) at low concentrations, whereas only 1-undecanol can form the densest assembly found so far for TCBPB (figure 3.5b). These findings, or in this case, lack thereof, confirm again the dependency of oblique-II on the previous nucleation of displaced chickenwire.

3.2.5 Guest Molecules

2D open-pore networks are excellently suited to host guest molecules in their pores.^{82,132} However, if an adsorbate does not yield a porous, but a densely packed network, the presence of potential would-be guests can induce structural changes in the self-assembly. Thereby, pores can be created, acting as suitable hosts where the guests are then allocated.^{133,134}

For instance, a transformation of a self-assembled monolayer from a densely packed (figure 3.9a) into a porous, occupied network has been observed (figure 3.9b), when a drop of coronene dissolved in heptanoic acid was added to a structure previously self-assembled from saturated BTB solution in heptanoic acid. The concentration of the solution containing coronene can range from 100% saturation down to 10% saturation. The densely packed row structure found before the coronene

guests were added is transformed into an open-pore chickenwire assembly, where the pores are filled by the guests. The exact number of coronene molecules inside the pores cannot be deduced from the STM images. Geometrically, it is possible to accommodate up to four planarly adsorbed coronene molecules per pore, as shown in figure 3.9c. Later molecular dynamics studies showed the ejection of one of these four BTB molecules from the pore. This result was then rationalized with thermodynamics. Having three coronene molecules per pore increases the adsorbate-substrate interaction per coronene molecule, as compared to having four molecules per pore. Entropically, three coronene molecules inside a pore increase the degrees of freedom of each one, as compared with four.¹³⁵

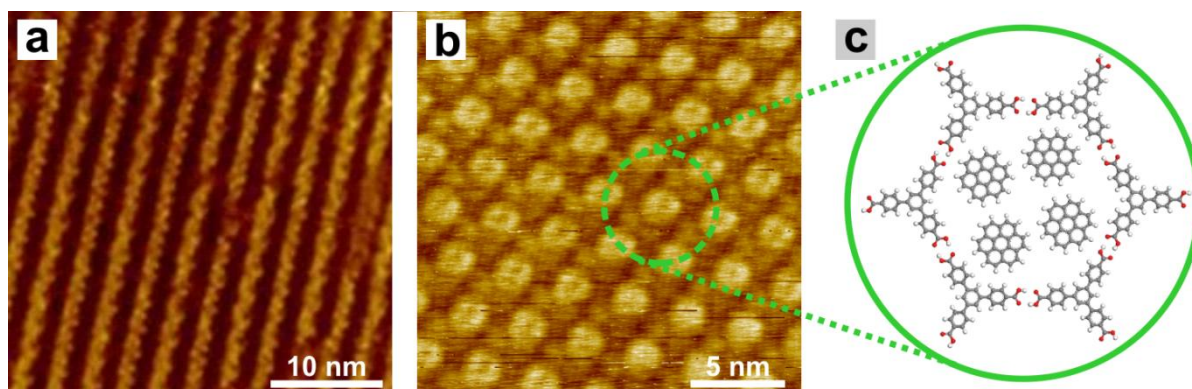


Figure 3.9: STM images of BTB dissolved in heptanoic acid obtained at the solid-liquid interface at ambient conditions. **a)** At 100% saturation concentration; **b)** after adding a drop of a solution of coronene in heptanoic acid at 100% saturation concentration. A transformation of the densely packed polymorph is observed, yielding an open-pore network, whose pores can be occupied by up to 4 coronene molecules, as schematized in **c)**.

3.3 Summary

Liquid-solid supramolecular self-assembly is a process in which the adsorbates are in dynamic equilibrium with the molecules in the supernatant solution. This equilibrium is facilitated by reversible intermolecular bonds, like hydrogen bonds, permitting structural error correction. The ability to heal structural errors readily yields assemblies that are almost defect-free. In this way, surface patterning and functionalization can be easily achieved. However, these same bonds that hold these networks of adsorbates together are not strong enough for some applications. Hence, such networks cannot resist harsh environments, for instance, long thermal exposures. This problem, namely the formation of regular networks interconnected with strong bonds, will be tackled in the next chapter.

Judicious knowledge of the factors that control and influence self-assembly makes it possible to steer the process of polymorph selection. Internal factors, like molecular geometry and functional groups already encode some information regarding the possible self-assembly final structures. Although important, those aforementioned factors can be influenced externally by the type of solvent used to dissolve the molecules and their concentrations in these solvents, which were the main topics

discussed during this chapter. There are other factors as well, like temperature⁹⁷ and type of substrate that also compete and drive the molecular building blocks to self-assemble into a given final polymorph.

The main goal of the above mentioned factors is the understanding and realization of supramolecular self-assembled monolayers with final structures designed in advance, without the need of extensive experimentation, or even without any experimental procedure at all. In particular, this knowledge will facilitate the formation of long-range ordered open-pore networks. These could be used as hosts for guest molecules,^{132,136} as chemical nanoflasks for chemical reactions,¹¹ or for organic electronics. Along these lines, TCBPB is a molecule with a suitable geometry to assemble into open-pore polymorphs, as are the structurally similar tricarboxylic acids, MeCPEBA, BTB and TMA, that were designed to form chickenwire networks with tunable pore size.

4

Covalent Bond Formation on Surfaces

Covalent Organic Frameworks (COF) are a class of crystalline materials built from light elements (H, B, C, N, O), and interlinked by strong intermolecular bonds. These materials possess long-range order, as well as a strong and rigid structure. For their synthesis, a balance of kinetic and thermodynamic factors is needed, promoting reversible bond formation.¹³⁷

Bulk COFs were synthesized for the first time by Yaghi and co-workers¹⁵ in the year 2005. In a one-step reaction, layered crystals composed of planar and porous covalent sheets were produced (graphite-like structure). Covalent bonds within the sheets strongly interconnect individual atoms, while long-range order is maintained; however, only weak forces, like van der Waals interactions, hold the sheets together. Some years later, again Yaghi and co-workers succeeded in producing a crystal composed entirely of covalent bonds.¹³⁸

The layered morphology of the first COFs, along with its regular arrangement of cavities, inspired a research interest to synthesize single 2D layers comprised only of covalently linked atoms. These monolayers are in a sense similar to porous self-assemblies (chapter 3), while the covalent interlinks add interesting properties like high temperature resistance and rigidity. The first surface-supported systems resulted in short-range order monolayers or small domains.^{139,140} Later, these systems were successfully extended to almost completely cover their supporting substrate;¹⁴¹ and recently, they were grown as thin films of several monolayers height.¹⁶

4.1 Synthesis of Surface-Supported 2D COFs

Reticular chemistry, the strategy used to purposely form 3D COFs, can also successfully be applied to the synthesis of surface-supported 2D COFs. Extended and regular networks can be formed with starting materials that are rigid, thus maintaining their structural integrity throughout the reaction process. These starting materials are functionalized with specifically selected chemical groups, which can form extended structures held together by strong covalent bonds.¹⁴² Long-range ordered structures can be achieved if the bond formation is reversible in nature, maintaining desired attributes of self-assembly, like the ability to dynamically self-repair. For this purpose, the reaction conditions are controlled to promote the formation of reversible bonds. In this way, the formation of thermodynamically favored arrangements is promoted.¹⁴³

The synthesis of surface-supported 2D COFs can be classified as a polymerization process. The monomers, or in this case “adsorbates”, react to form one-dimensional chains or two-dimensional networks. If the chains or networks contain more than 1000 monomers, they can be designated as

“polymers”. Typically, the 2D polymerization is initiated by heat, UV radiation, starter molecules or an electric pulse. The reaction terminates when no free monomers exist anymore.

Among the principles described before, the first method that yielded covalently interlinked surface-supported structures was the application of electric pulses on a STM tip, promoting the local polymerization of previously self-assembled monolayers.¹⁴⁴⁻¹⁴⁷ Although very regular domains were formed by this method, it is not suitable for large-scale applications. Other methods applied heat to the self-assembled structure or irradiated it with UV light, readily yielding covalent interlinked building blocks. The main limitations of these last two methods were the degradation of the adsorbates, the difficulty in limiting defect formation caused by very fast radical reactions, and last but not least, the irreversibility of some processes imposed by Ultra High Vacuum (UHV) conditions, due to complete desorption of molecules from the substrate.^{141,148} Here, only relatively small, and sometimes isolated, domains of no more than a few nanometers length of the desired polymers were synthesized.^{139,140,149,150}

These limitations can be overcome by selecting molecules with functional groups that show the required attributes, and by inducing their reaction under reversible conditions, as stated before. Boronic acid and diols are prototypical functional groups that possess the aforementioned attributes. When three boronic acid molecules react with themselves, they yield a *planar* boroxine ring, releasing water in the process. When one diboronic acid reacts with a diol, it forms a *planar* boronate ester linkage, with water as a by-product. To illustrate these reactions, the self-condensation of 1,4-benzenediboronic acid (BDBA), and the formation of the ester bond with 2, 3, 6, 7, 10, 11-hexahydroxytriphenylene (HHTP), are shown in figure 4.1. The geometrical representations of the reaction products in figure 4.1 show the thermodynamically most favorable configuration.^{141,143} Because no steric hindrance arises between the boroxine ring or the ester linkage and the molecular backbones, the resulting condensed and larger molecule are essentially *planar*. Supplying di- or multitopic molecules, possessing two or more of the previously mentioned functional groups in adequate arrangements, will enable the reaction to continue practically indefinitely, thereby forming chains and eventually *planar* sheets, as illustrated in figure 4.2 for BDBA.

“Condensation polymerization” is the term that best describes the above mentioned reactions. In this type of polymerization, a condensation product is released, typically a small molecule as water, as is the case here. This model is also valid for other molecules that are functionalized with the aforementioned functional groups, and specifically, for the work carried out in this thesis.

Other functional groups yielding reversible bonds that could be employed successfully to synthesize COFs in reversible reactions are aldehyde ($-CHO$) and amine ($-NH_2$). Molecules that incorporate these groups could eventually condense to form an imine bond ($-CH=N-$), whereby one water molecule is released.¹⁵¹

BDBA and HHTP were the first monomers ever used to produce bulk COFs.^{15,152} However, the catalog of COFs has been steadily expanded by altering the topology and backbones of the

monomers. In this way, many different layered bulk COFs were synthesized, mainly using boronic acid functional groups,¹⁵³⁻¹⁵⁷ and seldomly using others, like nitrile¹⁵⁸ or terephthalohydrazide + triformyl monomers.¹⁵⁹ Because the chemical reactions detailed in figure 4.1 can only yield 2D planar sheets, as represented in figure 4.2 for BDBA, realization of single surface-supported monolayers must be thermodynamically feasible. Therefore, these same functional groups and monomers are used here to achieve this goal.

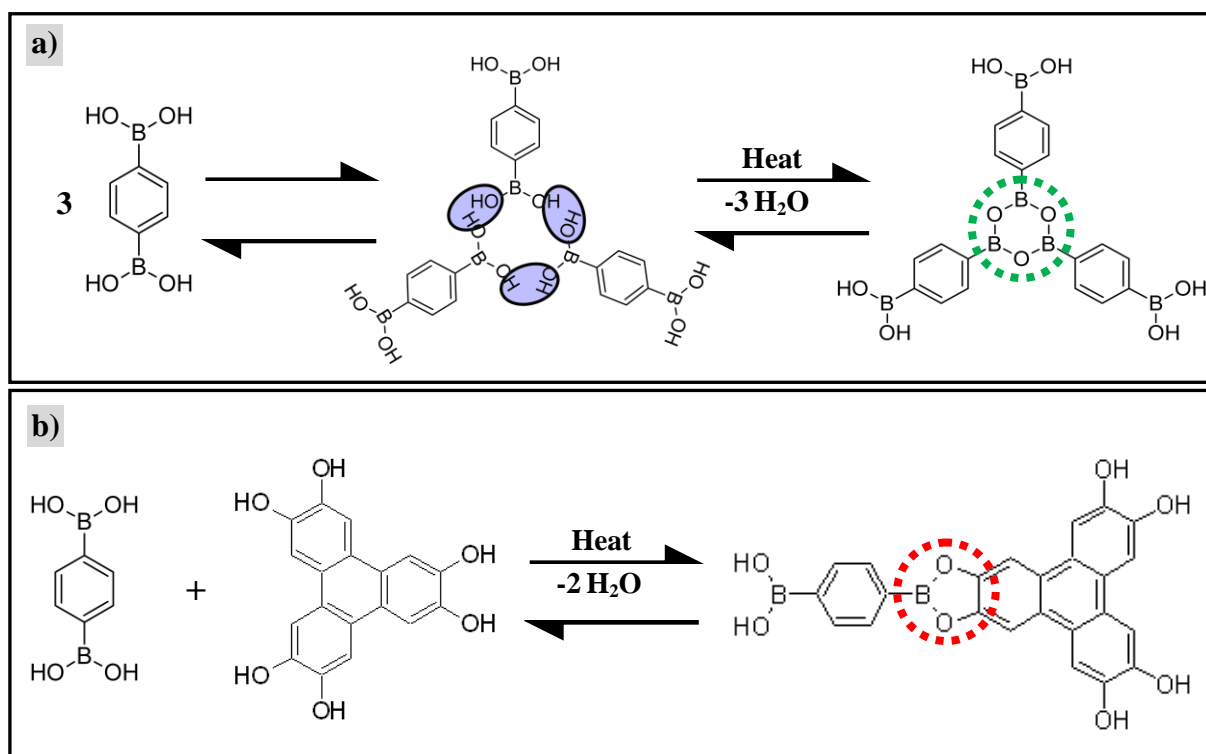


Figure 4.1: Condensation reaction schemes. **a)** Formation of a boroxine ring (highlighted in green), starting with three BDBA. In the process three water molecules are released, highlighted in light-blue. **b)** Formation of a boronate ester (highlighted in red) between one BDBA and one diol (HHTP), releasing two water molecules. Under reversible conditions, the geometric configurations adopted are the energetically preferred. They are shown here for both final products.

4.2 Molecular Precursors

Linear ditopic diboronic acid precursors with D_{2h} symmetry and one three-fold symmetric diol, as depicted in figure 4.3, were used for the synthesis of fully reticulated surface-supported 2D COFs. All precursors possess a rigid and stable aromatic backbone, preventing the degradation of the molecules under the reaction conditions. A prototypical rigid and very stable molecule is benzene.¹⁶⁰ Hence, structural backbones are preferably made of one or more phenyl rings, σ -bonded or fused. All linear diboronic acids were polymerized by self-condensation, while HHTP (**VI**) was reacted only with BDBA (**I**). The cavity sizes of the 2D COFs depended directly on the molecular precursors used.

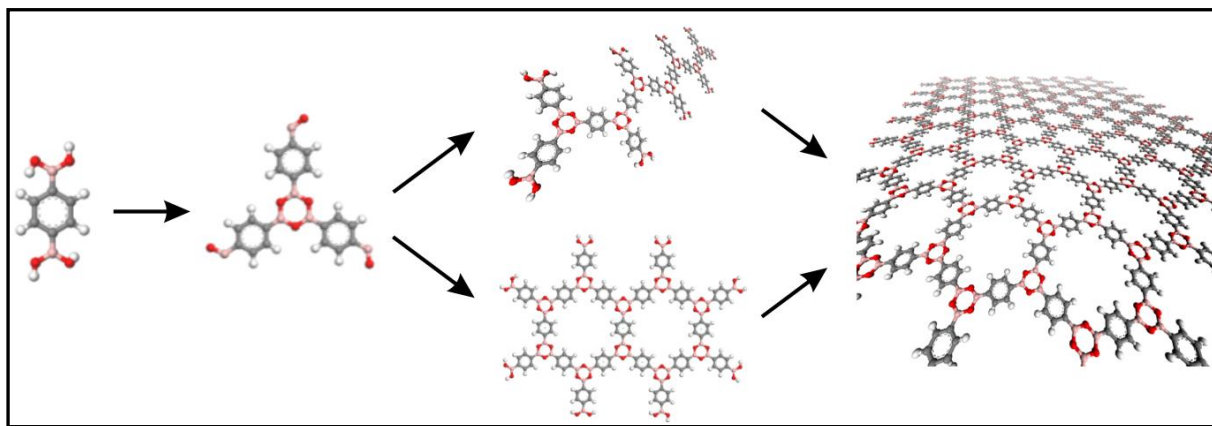


Figure 4.2: Stepwise reactions of BDBA to grow extended planar COF sheets. Reaction intermediates consist of linear chains or small domains. However, those eventually condense and yield planar layers. These reaction steps are also valid for other molecules functionalized with boronic acid and alcohol groups, as long as the reaction proceeds under reversible conditions. Color code: C = grey; H = white; O = red, B = pink.

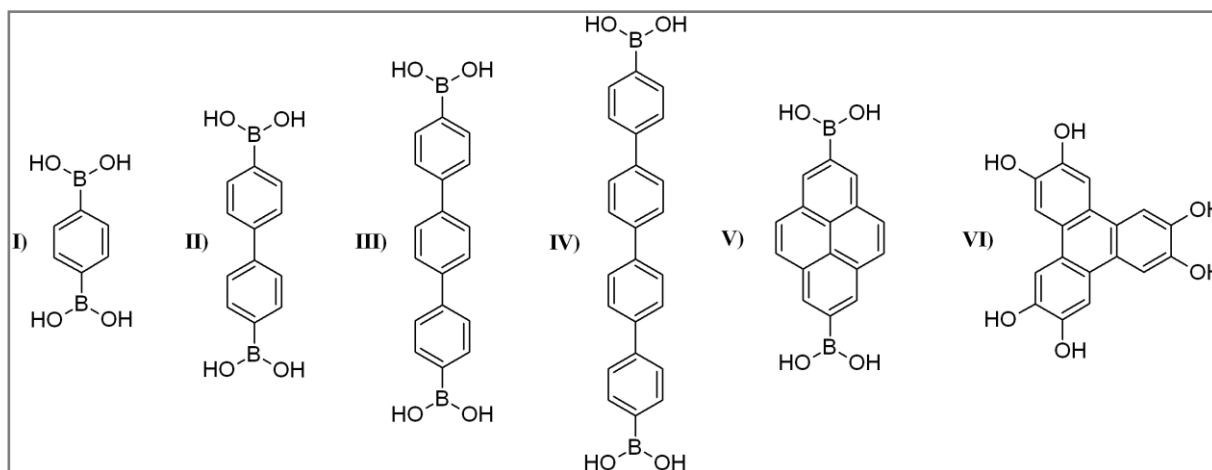


Figure 4.3: Molecular building blocks used to synthesize 2D COFs. **I)** 1,4- benzenediboronic acid (BDBA); **II)** biphenyldiboronic acid; **III)** terphenyldiboronic acid; **IV)** quaterphenyldiboronic acid; **V)** 2,7- pyrenediboronic acid; **VI)** 2, 3, 6, 7, 10, 11-hexahydroxytriphenylene (HHTP).

4.3 Synthesis of Well-Ordered COF Monolayers from BDBA

To synthesize 2D COF monolayers from BDBA (**I**) monomers, two different approaches were followed: In the first one, COF precursors were prepolymerized into bulk nanocrystals, which were then post-processed on a HOPG surface. In the second approach, on-surface polymerization of BDBA on HOPG was directly achieved, resulting in a straightforward method for routine 2D COF preparation. Both methods are briefly explained in the following. More detailed information can be found in reference 161.

4.3.1 Synthesis Through Pre-Polymerization of Precursors

The synthesis of crystalline precursors, or “precursor-COFs”, enables the in-depth understanding of the polymerization process. For this aim, pre-polymerization of BDBA was achieved in an oven at 250°C for 2 h under the presence of water to assure reversible conditions. This treatment readily yields nanocrystalline precursors-COFs.¹⁶¹ The precipitate was dispersed in fatty acids and deposited via drop-casting onto HOPG, readily adsorbing on the substrate. Stabilization on the substrate of the precursor-COFs was enhanced by their increased surface areas, as compared to single BDBA molecules. The ambient STM shows small domains of ~10 nm in length adsorbed on the HOPG substrate, as depicted in figure 4.4. The 2D FFT shown in the inset in figure 4.4b demonstrates the hexagonal symmetry of the nanocrystals, proving the formation of small single sheets of COF-1. Lattice parameters are given in table 4.1.

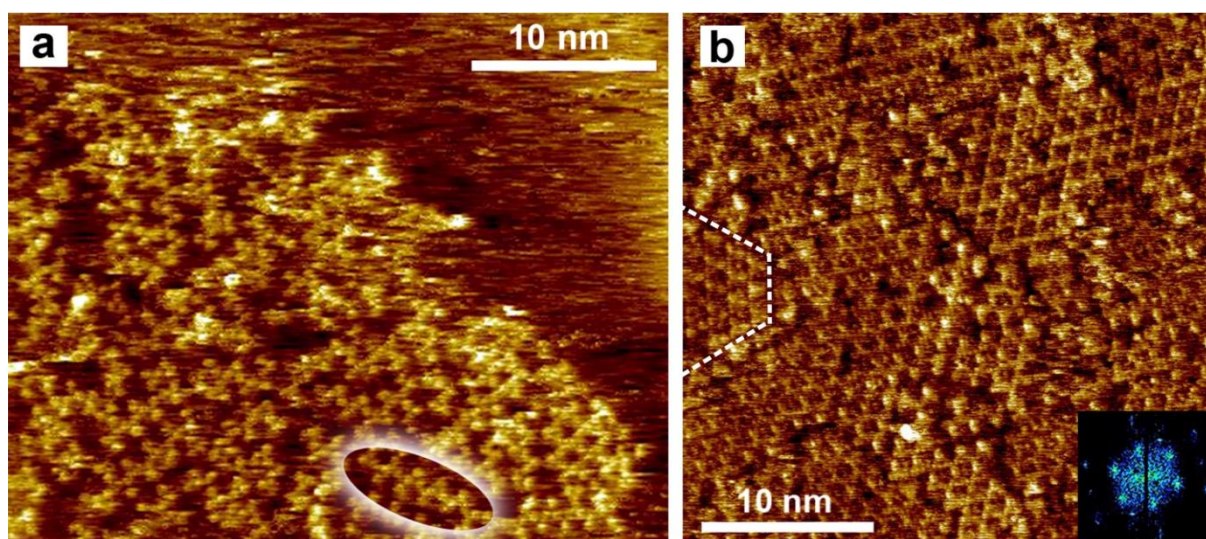


Figure 4.4: STM images of precursor-COFs on HOPG prepared by drop-casting. **a)** Chains that represent fragments of the COF-1 in-plane structure (a representative example is highlighted by the ellipse), as proposed in figure 4.2. **b)** 2D domains, with lateral extensions of typically < 10 nm and internal hexagonal structure. The inset depicts the 2D FFT of the STM image. Both samples were prepared using heptanoic acid. The STM images were acquired at the liquid-solid interface with the tip immersed into the liquid. Most domains have similar azimuthal orientations, an example for an occasionally observed exception is marked by dashed lines. Images taken from reference 161.

Further proof of the formation of precursors-COF nanocrystals is independently provided by powder X-ray diffraction (PXRD), and infra red (IR) and Raman spectroscopy.

The PXRD diffractogram (Mo-K α_1) gives broad peaks that originate from the finite precursor-COF nanocrystal sizes. $I \neq 0$ reflections indicate stacking in the [001] direction, with a layer separation of 0.335 nm. Using the Rietveld refinement via the line-broadening model based on the Scherrer equation, the average crystal size was estimated to amount to ~8 nm in lateral direction, and 1.0 nm along the [001] axis (~3 layers' thickness).¹⁶¹ The lateral direction estimated with the Rietveld

refinement is in good agreement with the lateral extension of the 2D COF domains imaged with the ambient STM using precursor-COFs dispersed in fatty acids.

IR and Raman also proved the expected reversibility of the boroxine ring formation reaction by comparing the spectra of the precursor-COFs, unreacted BDBA molecules, and precursor-COFs slowly rehydrated in water, respectively. Only the spectra of precursor-COFs show the characteristic signature of boroxine rings, accompanied by the almost complete vanishing of the characteristic peaks belonging to boronic acid. This last described situation was effectively reversed when the precursor-COFs were rehydrated, reproducing again the spectra of unreacted BDBA.¹⁶¹

The powder X-ray diffractogram can be found in figure 4.5, and the IR and Raman spectra, in figure 4.6.

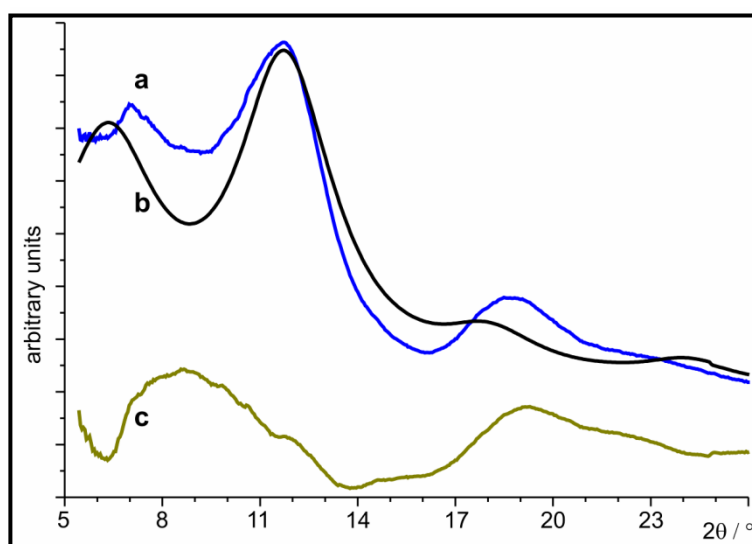


Figure 4.5: a) Powder X-ray diffractogram (Mo-K α_1) of thermally treated BDBA, *i.e.* pre-polymerization into precursor-COFs (blue curve) b) Simulated curve of a) based on the previously published COF-1 crystal structure (black curve)¹⁵. The Rietveld refinement allows to estimate a precursor-COF crystal size of 7.8 nm in lateral direction and 1.0 nm along the [001] axis ($\chi^2 = 3.145$).^{162,163} c) Difference curve between measured and simulated curve, *i.e.* (a) – (b). Image taken from reference 161.

The drop-cast precursor-COFs on HOPG were post-processed to induce ripening and increase the domain size. First, precursor-COFs were drop-cast using polar (heptanoic acid, nonanoic acid and 1-undecanol) and non-polar (dodecane) solvents. Then, the crystals were positioned inside a partially open reactor containing 50 to 100 μL of water. It was then put inside a pre-heated oven at 120°C for 1 hour. The reactor valves were left deliberately slightly open to allow water vapor to leave, ensuring an almost constant atmospheric pressure during the process. After this procedure, the reactor was allowed to cool down for 30 minutes, and the solvent-free HOPG substrates were imaged again with the ambient STM. The images shown in figure 4.7 confirm the ripening of precursor-COFs into larger 2D COF domains. Although the images presented were obtained using nonanoic acid as a solvent (or

dispersion agent), similar data was obtained alternatively using the aforementioned solvents. The line profile in Figures 4.7 proves the formation of one single monolayer of COF-1.

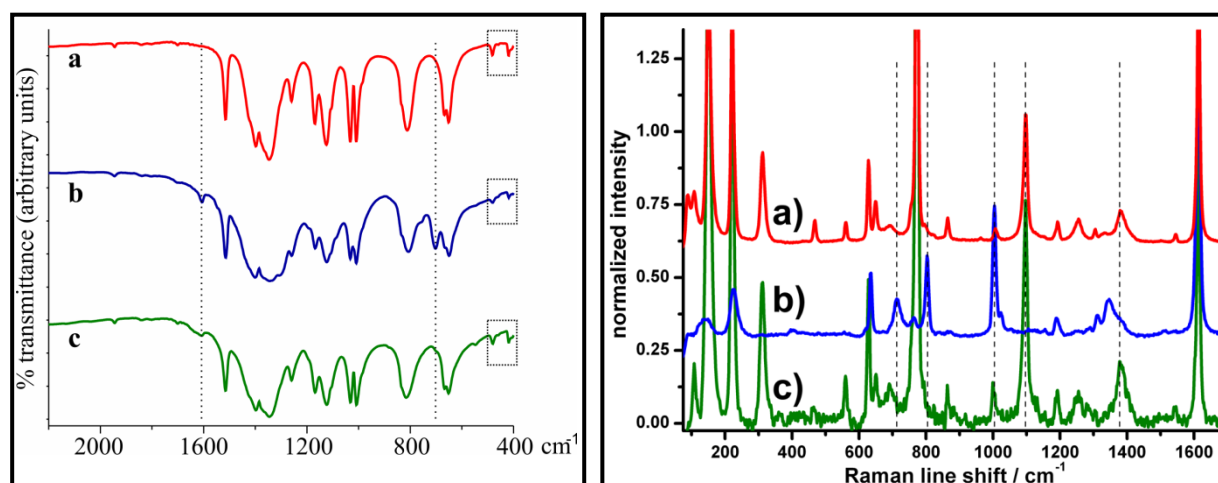


Figure 4.6: For both images: **a)** Untreated BDBA starting material (red curve); **b)** after thermal treatment, *i.e.* pre-polymerized into precursor-COFs (blue curve); **c)** after re-hydrolysis and re-crystallisation of **b)** from H₂O (green curve). **LEFT:** Infrared spectra. The absorption maxima in the IR spectra of thermally treated samples **b)** at 701 cm⁻¹ and 1605 cm⁻¹ were also found for solvothermally synthesized COF-1, and indicate the presence of boroxine rings.¹⁵ **RIGHT:** Raman spectra. The modes at ~1097 cm⁻¹ and at ~1378 cm⁻¹ are only observed for untreated **a)** and re-hydrolyzed **c)** BDBA and can be attributed to a B-O-H rocking mode and B-O stretching vibrations of the free boronic acid groups, respectively.¹⁶⁴ Images taken from reference 161.

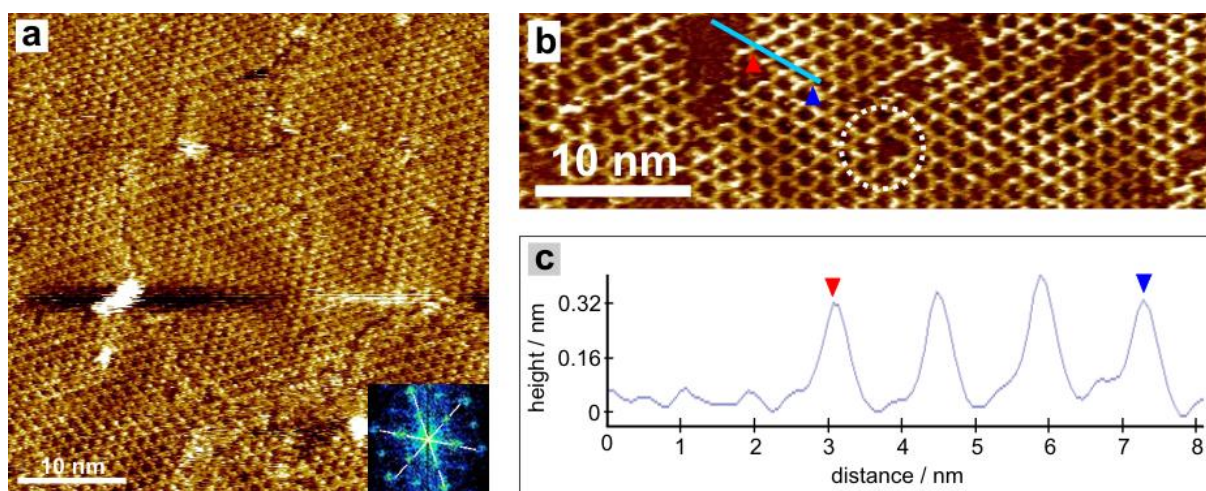


Figure 4.7: **a)** STM image of an extended 2D COF-1 monolayer acquired under dry conditions. The sample was prepared by deposition of precursor-COFs from nonanoic acid and post-processed inside a reactor. The inset depicts the corresponding 2D FFT of the image. The domain size is greatly increased as compared to the precursor-COF monolayer, and all domains in this image have similar azimuthal orientation. Point defects, like missing monomers can be discerned with low density. The STM contrast also exhibits a non-periodic height modulation. **b)** High resolution STM image of a 2D COF-1 monolayer on HOPG prepared similar as the sample in **a)** but using heptanoic acid. Again, point defects like missing monomers can be discerned, a prominent example is marked by the dashed circle. **c)** Line-profile along the blue line indicated in **b)**. The apparent height of the COF monolayer with respect to the uncovered substrate of ~ 0.30 nm indicates monolayer thickness and the lattice parameter corresponds to 1.4 ± 0.1 nm. Images taken from reference 161.

The thermal stability of the surface-supported post-processed 2D COF-1 was probed by exposing them for 14 hours at 200°C under ambient conditions. STM analysis of these samples showed only some degradation of the monolayers. This proves that the 2D COF monolayers stay largely intact. If these monolayers were stabilized only by H-bonds and van der Waals interactions, as typical for self-assembled monolayers (chapter 3), this thermal exposure would have led to their disintegration. To confirm this hypothesis, a self-assembled monolayer, a known system consisting of TMA dissolved in nonanoic acid was tested on HOPG.¹² Exposure of this system to the same temperature (200°C) but only for 1 hour, resulted in the complete desorption of the monolayer.

Additional evidence for the formation of 2D COF-1 is provided by comparing x-ray photoelectron spectra (XPS). These were acquired from a thick film of unreacted BDBA (>100nm) deposited on HOPG by vacuum sublimation and from a post-processed 2D COF-1 monolayer. Spectra are shown in figure 4.8. Comparison of the core level binding energy for O1s, B1s and C1s shows a shift in this energy of O1s from 533.5 eV for unreacted BDBA to 533.0 eV for the COF-1 monolayer. This slight shift towards lower binding energy for COF-1 reveals the change in the oxygen chemical environment when a boroxine ring is formed. This is because in the boronic acid group, O is attached to one H and one B, and in the boroxine ring, O is attached to two B. The electronegativity difference of H and B (H = 2.20, B = 2.04 on the Pauling scale) results in more negative charge in the O atoms in boroxine rings than in boronic acids. Consequently this shows that covalent bonds and hence the 2D COF-1 are formed. No significant change in the B1s and C1s energies are observed, because their direct binding environments do not change in the polymerization reaction. Further information can be found in reference 161.

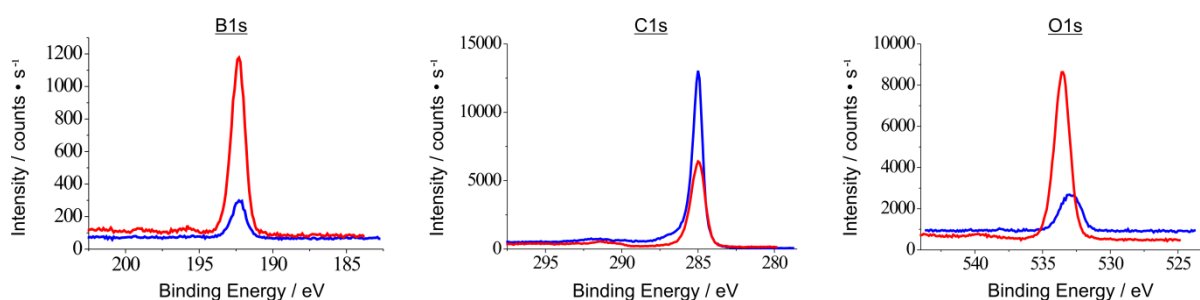


Figure 4.8: XPS measurements of the B1s, C1s, and O1s core level binding energies in a thick BDBA film on HOPG (red) and a 2D COF-1 monolayer on HOPG (blue). O1s spectra of the polymerized 2D COF-1 monolayer exhibit a slight shift to lower binding energy as compared to the film of unreacted BDBA molecules. This can be explained by the change of the oxygen chemical environment from B-O-H in the boronic acid group to B-O-B in the boroxine ring upon condensation. Both the B1s and C1s spectra do not exhibit any significant shifts, because their direct chemical environments are unaffected by the condensation reaction. The high intensity of C1s in the COF-1 monolayer sample originates from the HOPG substrate. Image taken from reference 161.

4.3.2 Synthesis via Direct On-Surface Polymerization

Although the realization of 2D COF-1 monolayers via precursor-COFs is possible and gives valuable information regarding the independent proof of the boroxine ring formation or the reversibility of the process, a more direct and simple synthesis is desirable. To this end, supersaturated solutions containing the precursor BDBA molecules were prepared. Solvents used were the same polar and non-polar ones described above. The supersaturated solutions were deposited directly on the HOPG surface and thermally treated in an oven inside the reactor with the same parameters used to post-process precursor-COFs. STM images obtained from the resulting monolayers were indistinguishable from those prepared through precursor-COFs. Here, a delicate solution concentration balance is essential: On the one side, an excessive supersaturated solution results in a thin insulating film preventing tunneling electrons to flow and hence hampering STM image acquisition. On the other hand, a too diluted solution fails to yield stable monolayers, because these solvents are not able to dissolve enough molecular precursors in order to prevent their complete desorption during polymerization. The choice of solvent does not notably influence the final lateral extension or amount of defects in the 2D COF domains, hinting to a minor solvent influence in this more direct synthetic route.

4.4 Synthesis of Isorecticular 2D COFs

The more direct synthetic route explained in section 4.3.2 allows a simple and fast preparation of 2D COFs. This straightforward method was used to form isorecticular 2D COFs with molecular precursors **II** – **IV**. Their organic backbones consist of σ -bonded phenyl rings that retain the D_{2h} symmetry, as BDBA, yielding regular 2D COFs with increasing hexagonal cavity sizes. Both the lattice parameter and cavity size increased, depending on the precursor used (figure 4.3).¹⁶⁵ **V** was selected to demonstrate that modifying the type and character of the molecular backbone also yields a 2D COF with similar regular hexagonal cavities.¹⁶⁵ This is because the backbone of **V** consists of a pyrene chemical group composed of fused phenyl rings, as compared to the σ -bonded phenyl rings of **II** – **IV**. Calculated (using MM) and experimental lattice parameters are listed in Table 4.1. STM images of the networks attained using molecules **II** – **V** are depicted in Figure 4.9.

Molecules **II**, **III** and **V** yielded regular 2D COF domains of at least $100 \times 100 \text{ nm}^2$ area, achieving almost complete surface coverage. However, 2D COFs of **IV** only partially covered the substrate. In the areas that are not covered by this COF, disordered arrangements of adsorbed **IV** molecules were usually found. This observation can be explained in terms of monomer size: **IV** has the largest size of all diboronic acids presented. Thus, it can be inferred that its lateral mobility along the surface is hampered by a large adsorption energy and by a large influence exerted by the corrugation of the surface potential.^{123,166-168} Hence, this prevents a portion of the already adsorbed

molecules to approach close enough to each other to react. This experimental observation made for **IV** suggests that large diboronic acid molecules must adsorb first on the substrate, and self-condense *on it* at a later stage. This condensation reaction *on the substrate* may be initiated by a rise in the temperature. (See section 4.5.)

In some areas, molecule **V** yielded bilayers of the COF, as shown in figure 4.9g. These layers are stacked in an eclipsed fashion, as already observed in COF bulk crystal synthesized from the same monomer.¹⁵³ This behavior can be rationalized by means of a high π - π interaction arising between pyrene backbones via its delocalized π -electrons. These enhanced interlayer bonds stabilize such an arrangement.

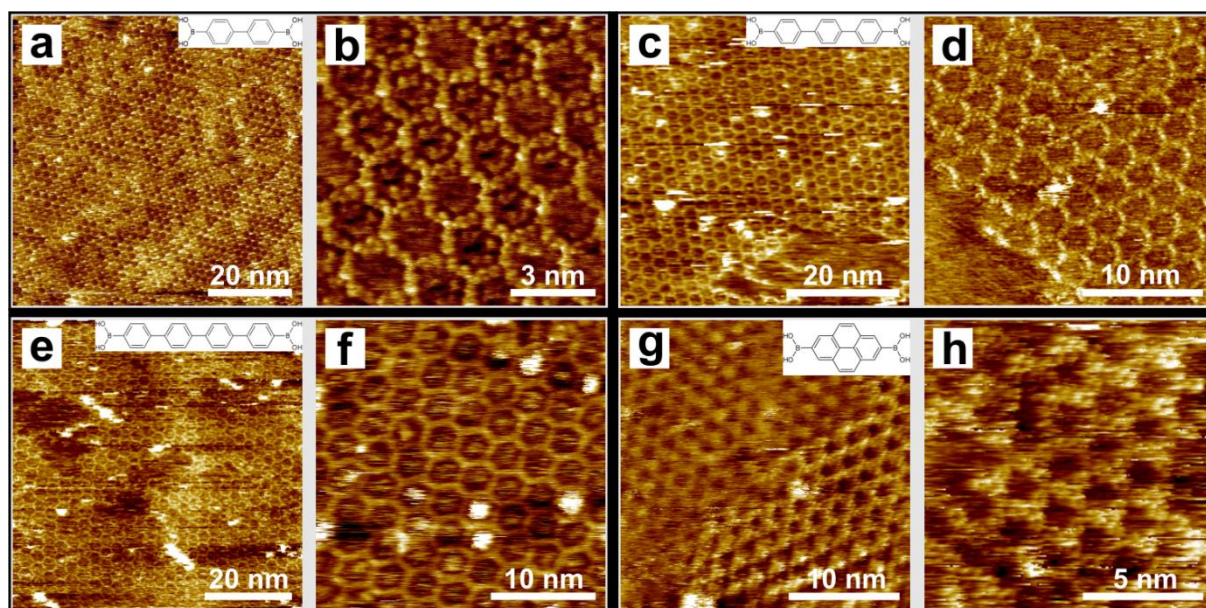


Figure 4.9: Ambient STM images of surface-supported 2D COFs obtained from self-condensation of: **a, b) II**; **c, d) III**; **e, f) IV**; **g, h) V**. The respective monomers are shown in the insets. Image adapted from reference 165.

Table 4.1: Summarized experimental and MM (Dreiding) derived lattice parameters for all 2D COFs. **I + VI** is listed here for the sake of completeness.

| building blocks | experimental lattice parameters | | | Forcefield derived lattice parameters | | | |
|-----------------|---------------------------------|---------------|-----------------------|---------------------------------------|--------|-----------------------|----------------|
| | a (nm) | b (nm) | γ ($^\circ$) | a (nm) | b (nm) | γ ($^\circ$) | pore size (nm) |
| I | 1.4 ± 0.1 | 1.4 ± 0.1 | 60.0 ± 3 | 1.5 | 1.5 | 60 | 1.0 |
| II | 2.1 ± 0.3 | 2.1 ± 0.2 | 58.9 ± 4 | 2.3 | 2.3 | 60 | 1.6 |
| III | 2.9 ± 0.2 | 2.9 ± 0.2 | 57.5 ± 3 | 3.0 | 3.0 | 60 | 2.4 |
| IV | 3.5 ± 0.3 | 3.6 ± 0.3 | 62.0 ± 5 | 3.8 | 3.8 | 60 | 3.2 |
| V | 2.1 ± 0.1 | 2.1 ± 0.1 | 58.9 ± 2 | 2.3 | 2.3 | 60 | 1.4 |
| I + VI | 2.7 ± 0.3 | 2.7 ± 0.3 | 57.1 ± 4 | 3.0 | 3.0 | 60 | 2.4 |

4.5 Activation Temperature for Self-Condensation

Although the molecules **I** – **V** possess the same boronic acid functional groups in the same para-orientation, the activation temperature for the formation of the respective 2D COF monolayers via self-condensation is not necessarily the same. To determine their respective activation temperatures, the molecules were dissolved/suspended in heptanoic acid and drop-cast on HOPG, as explained in section 4.3.2. Then, these systems were thermally treated inside a pre-heated oven for 30 minutes. The temperature of the oven was varied in successive experimental trials. Because not all possible temperatures can be probed, the exact activation temperatures lie in the ranges listed in table 4.2.

Table 4.2: On-surface activation temperature ranges of molecules **I** – **V** to form 2D COFs. If no activation was found at or below 70°C, the activation temperature lies between this number and 107°C, the highest temperature measured inside the reactor. The lowest temperature given is 25°C, the usual ambient temperature in the laboratory.

| Building block | I | II | III | IV | V |
|-----------------------------------|------------------|------------------|------------------|-------------------|-------------------|
| Activation Temperature range [°C] | $25 > T \geq 50$ | $33 > T \geq 50$ | $50 > T \geq 70$ | $70 > T \geq 107$ | $70 > T \geq 107$ |

The activation temperature found for the monolayer formation of BDBA differs from that observed using Thermal Gravimetric Analysis (TGA) of bulk BDBA: Here the condensation starts at ~150°C, at least ~100°C above the experimentally temperature found for the initiation of on-surface condensation.^{141,161} This difference can be explained in part by the known spontaneous dehydration of boronic acids that can occur already at room temperature.¹⁶⁹ At temperatures that are somewhat higher than ambient temperatures (50 – 70°C), this spontaneous reaction becomes vastly accelerated. The substrate may also play a role in promoting the condensation reaction by lowering the activation energy barrier.¹⁴⁸ Hence, temperatures inside the reactor of ~110°C during thermal treatments are more than sufficient for **I** – **V** to yield COF monolayers.

An important result also found during these experiments is that at or below 70°C, molecules **I** – **III** already form small to medium-sized 2D COF domains, whereas **IV** and **V** never formed any observable 2D COF at these temperatures. However, extended monolayers for **I** – **III** were never observed under these reaction conditions outside the reactor. Hence, extended monolayers can only be formed at higher temperatures (above 100°C) and in the presence of a humid atmosphere assuring reaction reversibility.¹⁶⁵

4.6 From Supramolecular Self-Assembly to 2D COF

Boronic acids are known to form hydrogen-bonded self-assembled structures.¹⁷⁰ One example thereof is self-assembly of BDBA on KCl(001).¹⁷¹ Similarly, in the bulk, the crystalline structure of BDBA is known to form H-bonds between individual molecules.¹⁷²

It has already been experimentally observed, that a previous step in the realization of covalently-interlinked monolayers is non-covalent self assembly of its molecular building blocks,^{123,139,146,148,173,174} or the formation of protopolymers on a substrate.^{140,175} Pre-arrangements of precursor structures via the two ways mentioned before could facilitate covalent bond formation between them in a following reaction step. This is because the molecules lie in close proximity to each other, and because their functional groups attain the required steric orientation.

Studies of the formation of 2D COFs on HOPG using **I** – **V** presented also several well-suited opportunities to investigate the supramolecular self-assembly of these same molecular precursor. It was found that in the cases of **I** and **II** dissolved in fatty acids, no supramolecular self-assembly was ever imaged at the solid-liquid interface by means of ambient STM. Either their small adsorption energies, as a consequence of their small size, prevent altogether the stable adsorption on HOPG, or this preceding step is very short-lived, leading rapidly to the formation of more stable 2D COFs at higher temperatures. However, with **III** and **IV**, self-assembled structures were easily observed at temperatures *lower* than those needed for the polymerization into 2D COFs. A case in point is molecule **III**, for which supramolecular self-assemblies and 2D COF domains coexist very close to each other after a 30 minutes treatment at 70°C, or after a thermal treatment inside the reactor at 120°C using dodecane as solvent.¹⁶⁵ According to the experimental STM observations, the proposed self-assembly configuration of **III** brings the boronic acid moieties very close together to one another, as depicted in figure 4.10. Then, upon heating up gently the entire system, the condensation, *i.e.* boroxine formation is activated, yielding 2D COFs. Here, desorption of some **III** molecules from the substrate is necessary to provide enough space for the less dense open-pore network of the COF. In the case of **V**, a well ordered self-assembly of these molecules dissolved in heptanoic acid was never found; instead, only short-range ordered arrangements of adsorbed molecules could be imaged. These arrangement were never experimentally observed to reorganize into a long-range ordered self-assembly, even when heating at 70°C for 1 h.¹⁶⁵

The observations mentioned above, and especially the evidence found for **III** (figure 4.10c) and **IV** (figure 5a in reference 165), point to a conceivable 2D COF reaction mechanism for boronic acids with large enough surface area. In this mechanism, the molecular precursors may form a 2D COF on HOPG, *preceded* by a supramolecular self-assembly step.

In the future, in-situ temperature-controlled STM studies of these surface-supported polymerization processes may shed light on the mechanism of the synthesis of these 2D materials. During these studies, other reaction parameters will also be better understood.

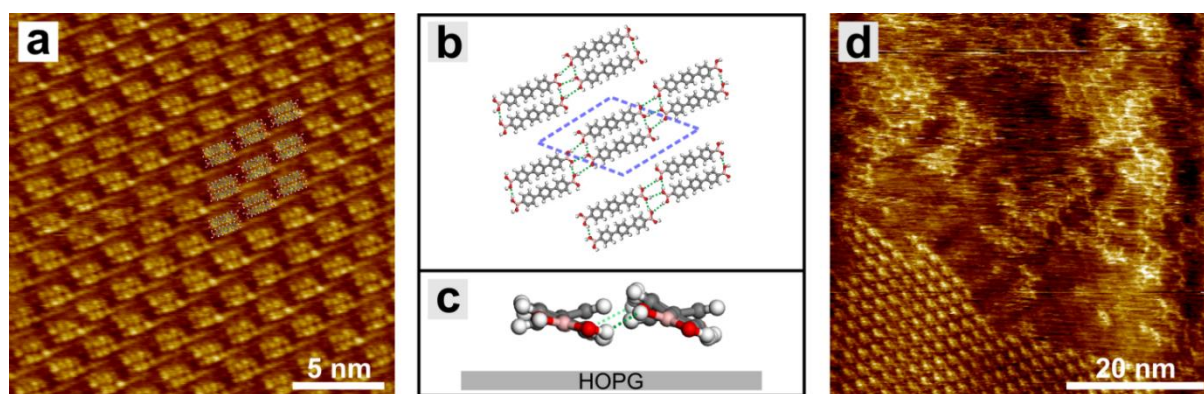


Figure 4.10: **a)** STM image of a self-assembled monolayer of **III** acquired at the liquid-solid interface with heptanoic acid. Overlaid molecules are drawn to scale. **b)** Tentative model as derived from the STM data. Unit cell and hydrogen bonds are indicated by dashed blue and green lines respectively. **c)** Side view of the monolayer illustrating a conceivable tilt of the molecular plane with respect to the substrate. **d)** STM image of a thermally treated sample (70°C, 30 minutes) showing the coexistence of unreacted self-assembled domains (lower left part) and first 2D COFs (upper right part). Image taken from reference 165.

4.7 Stability of the Boroxine Ring

COFs composed of boroxine rings have already shown a high thermal stability when heated in a dry atmosphere,^{137,141,143,176} but show minor stability against water: They undergo relatively fast decomposition back to its original building blocks when exposed to atmospheric humidity.^{177,178} For instance, 2D COFs made from **II** to **IV**, are readily decomposed when left overnight under normal ambient conditions, but survive almost intact when left inside a desiccators for the same time period. This decomposition is driven by the susceptibility to nucleophilic attack by water (a mild nucleophile) at electron-deficient boron sites.^{177,179}

The making and breaking of boroxine rings can be directly observed in successive STM images taken when precursor-COFs were applied onto HOPG. For these observations, heptanoic acid was used as a dispersion medium and the experiments were carried out at a laboratory temperature of 33°C. The observed domains of nanocrystalline precursor-COFs undergo repeated assembly and disassembly, as depicted in the sequence in figure 4.11. The assembly/disassembly behavior is most probably induced by the scanning tip. This finding can be explained by the interplay of several aspects: The interaction of the scanning tip with the adsorbants,^{144-147,180} the nucleophilicity of the boroxine ring explained above, the presence of small quantities of water in heptanoic acid that help the reaction to go forward or backward, and the relatively small enthalpy change associated with the boroxine formation. This formation enthalpy, from free boronic acid to yield boroxine rings, has been calculated to be between 28 and 51 kcal/mol,¹⁸¹ pointing to *only a moderate* strength of the B–O covalent bonds within boroxine rings. Even though these estimated values were not calculated for any of the molecules presented here, it explains then why these bonds are susceptible to interact with the scanning tip.

It is important to highlight the ability of heptanoic acid to dissolve some water, albeit in very limited quantities.¹⁸² Water can originate from the condensation reaction or from atmospheric humidity, being apparently enough to guaranty the reversible reaction conditions.

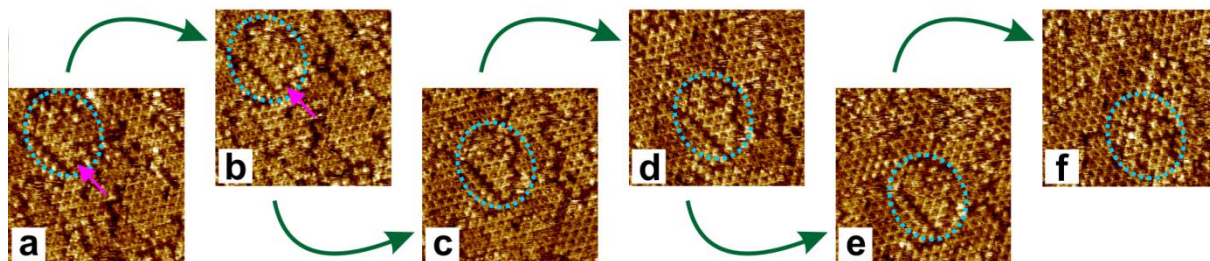


Figure 4.11: STM images depicting the successive making and breaking of boroxine rings. The blue ellipse highlights the growth of a small 2D COF-1 domain. Starting with a linear array of hexagonal cavities (**a** and **b**, arrow), the domain reacts with nearby molecules, growing laterally (**b** to **e**) towards a triangular shape. This domain later disappears by partially coalescing with a neighboring domain (**f**). All images were scanned at a room temperature of 33°C. Time span between successive images: ~1.5 minutes. All images: 23 × 23 nm².

The STM images in figure 4.11 also reveal the presence of small tripodal units, constituting the smallest polymerized aggregates that are regularly observable. These aggregates are constructed by 3 BDBA molecules condensed into one boroxine ring, as depicted in figure 4.1a. Smaller units were seldomly, if at all, experimentally observed, hinting towards a minimum size required by the building blocks to adsorb flat on the substrate for a long enough residence time to be observed. This is not achieved with just a single BDBA (**I**) or **II** molecule.

4.8 Heteromeric 2D COF via Boronic Ester Formation

So far, realization of single-component 2D COFs interconnected by boroxine ring moieties (figure 4.1a) has been demonstrated under ambient^{161,165,183} and UHV¹⁴¹ conditions. Greater long-range order was achieved under ambient conditions than under UHV, because the UHV environment does not promote reversible reaction conditions. Attempts to synthesize a two-component 2D COF under UHV conditions with BDBA (**I**) + HHTP (**VI**), interconnected by boronic ester moieties (figure 4.1b), resulted in short-range ordered networks only.^{141,173}

The synthesis of 2D COFs with the same two constituents mentioned above has been attempted but under ambient conditions. Its bulk equivalent is the COF-5, synthesized by Yagui and co-workers¹⁵ in the year 2005. For this purpose, stoichiometric amounts of the components (2 HHTP : 3 BDBA) were weighed, dissolved in warm water, slowly recrystallized, and grounded to attain homogeneity. The mixture was then treated in an oven for 2 hours at 200°C to yield precursor-COFs. Again, during this procedure a humid environment was maintained. In a last step, this precursor-COFs were dispersed in heptanoic acid, applied onto a freshly cleaved HOPG substrate, and thermally

treated inside the reactor for 1 hour at 120°C. Once again, under the same humid condition as explained before for single-component 2D COFs.

A representative STM image of the successful trials is shown in figure 4.12, along with a line profile. This profile proves the formation of two monolayers stacked in an eclipsed fashion via the periodic repetition of peaks and troughs at basically two different heights. This evidence is in good agreement with the stacking fashion found for the bulk COF formed from these same components.¹⁵ Table 4.1 shows the experimental and MM derived unit cell parameters for this 2D COF. They agree very well with the experimental unit cell lattice parameters of 3.0 nm found for the bulk COF-5.¹⁵

Although in principle it is demonstrated here that it is possible to realize this class of two-component 2D COF with long-range order domains, it was not possible to reliably reproduce these results. Also, slight changes in preparation parameters, for instance, using a longer thermal treatment, or applying more water inside the reactor, resulted in no observable improvement. Only shifting the stoichiometric BDBA:HHTP ratio towards more HHTP and less BDBA, slightly improved the success rate.

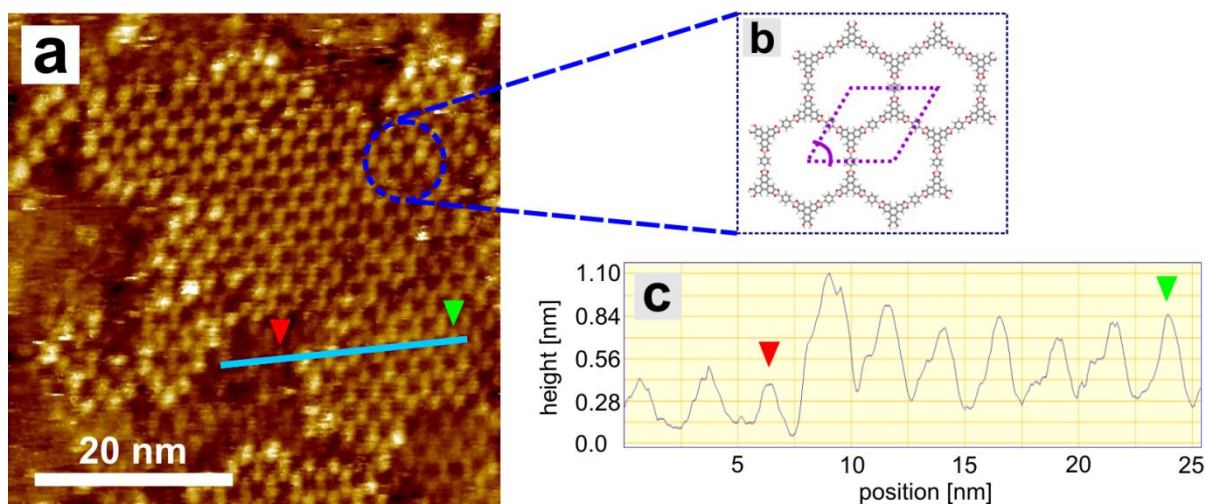


Figure 4.12: **a)** Representative ambient STM image of a two-component 2D COF realized with BDBA (**I**) and HHTP (**VI**), by forming boronic ester linkages. **b)** Molecular representation of 4 rings of this COF. The unit cell parameters are $a = b = 3.0$ nm; $\gamma = 60^\circ$. **c)** Line profile along the light-blue line indicated in **a)**. The apparent step height from one monolayer to two monolayers with respect to the uncovered substrate indicates one or two monolayer thickness.

4.9 Summary

In this chapter, it has been shown that covalent bond formation under reversible conditions yields long-range ordered networks held together by these strong bonds. The ideal reaction conditions will certainly depend on the system of interest, *i.e.* the parameters should not be considered universal. For instance, the conditions attained inside the reactor are very well suited for the formation of extended 2D COFs of **I – III** and **V**, but are not good enough for long-range ordered COFs made from **IV** or **I + VI**.

The reversibility of the boroxine formation reaction, by condensation and rehydrolysis from boronic acid, was demonstrated here with complementary analytical methods, like IR, Raman and PXRD. This characteristic also allows boronic acids to self-repair during the formation of COFs, yielding a very regular structure, provided they are prompted to make and break covalent bonds during the formation process.

It has also been shown here, that the unit cell parameter, and hence the respective cavity size, can be tuned by selecting the appropriate para-diboronic acid precursors. The unit cell parameters spanned from 1.5 nm using **I** up to 3.8 nm using **IV**. This last size should not be taken as an upper limit to the upwards scalability of the unit cell parameters. However, it seems that with larger molecules, a consequently larger adsorption enthalpy hinders molecular mobility on the substrate. This suggests a change in the reaction conditions if 2D COFs with larger cavities are going to be prepared. Altogether the feasibility of formation of isorecticular 2D COF has been demonstrated.

The supramolecular self-assembly of some diboronic acids was also tested here. Results showed that under the applied experimental conditions, small monomers as **I** and **II** do not self-assemble on the graphite substrate, **III** and **IV** do self-assemble, whereas **V** forms a disordered structure. This may imply that self-assembly, at least for **III** and **IV**, is a preceding step in the process of 2D COF formation. Currently this is an open research question, suggesting the possibility of an in-situ study of this process in the future.

The viability of heteromeric 2D COFs has also been proved here. However, reaction parameters must be improved to obtain regular and extended 2D COFs from molecular precursors **I** + **VI**.

5

Conclusions

In this work, the realization of surface supported monolayers of supramolecular self-assemblies and two-dimensional covalent organic frameworks has been presented. Suitable organic linkers, mostly dissolved in organic solvents, were the starting materials for both syntheses. STM was the main analytical tool used to investigate the structures on the surfaces. STM provided very precise, and highly resolved detailed images, from which structural parameter were derived and used for modeling.

The first subject presented here, the self-assembly of tricarboxylic acids, is a spontaneous process occurring under ambient conditions mediated by reversible hydrogen bonds. Although the formation of these ordered structures reduces the entropy of the system, they can only form if the overall entropy of the universe increases. When formed, these structures are in thermodynamic equilibrium with further molecules in the supernatant solution. This equilibrium enables the formation of very regular and extended molecular networks by allowing error correction and filling of voids.

Thermodynamical parameters have been estimated by considering the enthalpic and entropic contributions for self-assembly. Enthalpic contributions were deduced from molecular mechanics, whereas entropic changes were estimated using adapted models for rotational and vibration contributions. The values obtained from these two factors were combined to obtain the change in Gibbs free energy upon self-assembly for several different polymorphs found. This free energy analysis explained why the self-assembly was a thermodynamically favored process, and thus spontaneous. Other parameters influencing self-assembly were also presented in this thesis. These are molecular structure, like shape, size, and functional groups of the adsorbates; intermolecular forces, mainly hydrogen bonds of different strengths; interaction of the adsorbates with the substrate, via van der Waals forces; solvent; concentration; and possible structural changes induced by potential molecular guests.

Depending on the solvent used and the solute concentration, one large tricarboxylic acid yielded at least four different polymorphs. However, none of them was the expected open-pore network stabilized solely by cyclic two-fold strong intermolecular hydrogen bonds. This implies that knowledge of the above mentioned factors, gathered taking into account the information presented here and in many other studies, is not yet enough to predict in advance the final supramolecular self-assembly. This means experimentation is still an indispensable requirement.

The second main topic presented here is the formation of extended, regular, surface-supported two-dimensional covalent organic frameworks (2D COFs). For this aim, boronic acid-functionalized

molecules were employed. When boronic acids react via a condensation reaction, they form boroxine rings (B_3O_3), held together by covalent bonds. In this reaction, water is released as a by-product.

To realize 2D COFs, two methods were used. In a first method, 1,4-benzenediboronic acid was pre-polymerized in an oven under a humid atmosphere. This process yielded bulk precursor-COF nanocrystals. When dispersed in organic solvents and drop-cast on graphite, these nanocrystals readily adsorbed on the graphite substrate. In a second step, these samples were post-processed by a thermal treatment under reversible conditions inside a reactor with a small amount of water added. If enough water is supplied during the reaction, the making and breaking of covalent bonds is promoted. Thus, structural errors that may arise during the polymerization are efficiently corrected, yielding 2D COF networks with the energetically most favorable configuration, and exhibiting relatively large domains.

In a second method, the same thermal treatment inside a reactor as explained above was undertaken with graphite substrates containing, instead of precursor-COFs, dispersed 1,4-benzenediboronic acid molecules in organic solvents. That is, the pre-polymerization step was completely skipped. The 2D COFs yielded by this one-step procedure were very similar in regularity and lateral extension to those realized with precursor-COFs.

These two procedures, using the comparatively small monomer 1,4-benzenediboronic acid, provided the proof of principle. The second and simpler process was later extended to yield isotopological frameworks with larger unit cell parameters, tuned in size by a previous selection of the appropriate molecular precursor. For this purpose, para-diboronic acids with molecular backbones consisting of phenyl rings σ -bonded or fused were always used. For all monomers, isotopological networks with a regular and extended covalent structure were obtained.

Thermal stability of the 2D COFs was tested by heating for a long period of time under atmospheric conditions, and subsequent examination with the ambient STM. After this rather harsh treatment, 2D COF were still present on the substrate. Also, the reversibility of the boroxine ring formation reaction to the boronic acid precursor was proven by means of rehydrolysis of precursor-COFs. This demonstrated the error correction properties required for the formation of regular 2D COF networks.

The viability of the formation of a heteromeric 2D COF was also demonstrated. By boronic ester formation, again a covalently bound structural unit formed by means of the condensation reaction of a boronic acid and a diol. This was realized under the same reversible reaction conditions inside the reactor as already employed for boroxine ring formation.

To summarize the present work, the possibility of controlled formation of nanoscale molecular patterns has been shown. However, at the present stage, not all parameters affecting molecular self-assembly or 2D COF formation are fully understood, and probably other factors still lack a detailed study. Hence, it is still a long way before conclusive results are achieved, which will permit the large scale fabrication of molecular monolayers with very specific characteristics that were defined in advance. Also here, the realization of regular and extended 2D COFs has been demonstrated. This may

be a first step towards the understanding of the reaction conditions, among other factors, needed for large-scale production of free-standing 2D polymers, much resembling a single graphene sheet. Before 2D polymers free of a supporting substrate are available, there are other possible applications and experiments that may be achievable using surface-supported 2D COFs. For example, the transfer of a 2D COF layer from the original supporting graphite surface to another different substrate by bringing the two surfaces together may be possible. This would provide a method to functionalize a substrate where the 2D COF of interest cannot form under the known reaction conditions. Also, the cavities found in the 2D COFs may be used as a template to host and position guest molecules at specific locations. These guest molecules may possess chemical groups directed to react only with each other and yield a new and different 2D network. Afterwards, by dissolving the original 2D COF with a solvent that leaves intact the new network of guest molecules –probably just water–, a newly functionalized surface may be formed. All of these would certainly open a new world of possibilities in material science.

Appendix 1

Preparation of Ultra Flat Gold (111) Surfaces by Physical Vapor Deposition (PVD) as Substrate for Supramolecular Self-Assembly

Vacuum evaporation of metals onto different substrates is a popular method to produce inexpensive surfaces for STM experiments. Glass, silicon (Si) and calcium fluoride (CaF_2) have been used as substrates with good results,¹⁸⁴ but in particular, mica (muscovite, or common mica; chemical formula $\text{KA}_2(\text{AlSi}_3\text{O}_{10})(\text{OH})_2$) has become one of the most common substrates used for the deposition of gold. This is because it is atomically flat, cheap, and easy to cleave with adhesive tape through the (001) plane of K atoms. Upon cleavage, these atoms are distributed equally between the two newly created surfaces, so each cleaved face would contain half a monolayer of K atoms.¹⁸⁵ Figure A1.1 shows a schematic representation of the mica structure. The gold deposited on mica via PVD is (111) terminated. There is a large collection of literature dealing with the different parameters for the deposition of gold on mica; a brief overview can be found in the publication of M. Levin *et al.*¹⁸⁶

In this work, freshly cleaved mica (with adhesive tape; reminiscent of the HOPG cleaving procedure) was used as a substrate without any further ex-situ treatment. It was outgassed in the vacuum chamber described in figure A1.2, at 350 - 400°C for ~12 hours. Only the best commercially available class of muscovite was used, the so-called V-1 type.

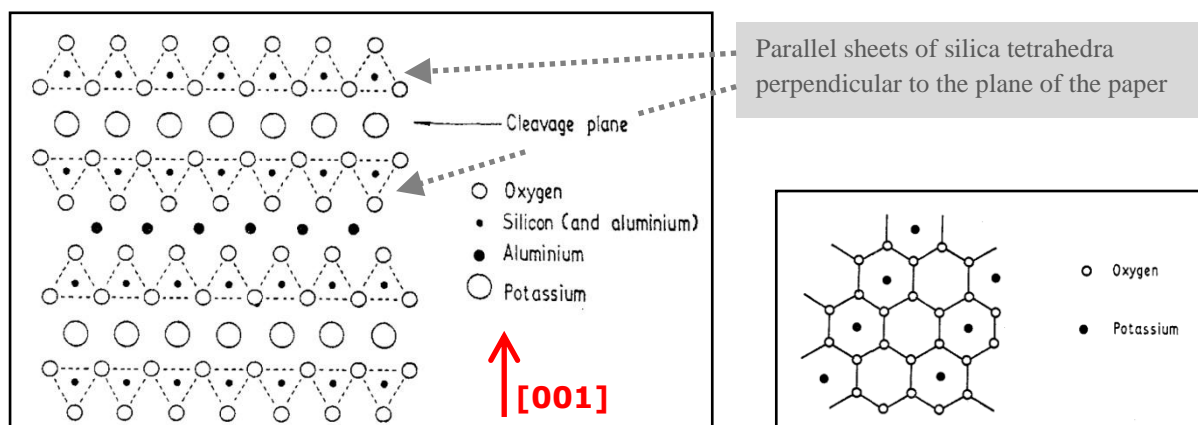


Figure A1: Left: Schematic illustration of the mica structure. Cleavage occurs along the (001) plane, where monolayers of hexagonally arrayed potassium ions separate the sheets. A layer of hexagonally arrayed oxygen ions lies beneath this surface. Right: Surface structure of cleaved (001) mica.¹⁸⁵ Images reproduced with permission from IOPscience.

Gold films deposited via PVD onto mica yield a gold substrate (111) terminated. This surface termination suggests that the crystallographic order of the mica substrate influences significantly that of gold due to some matching degree between the two materials at the interface.¹⁸⁷ In general, when a film is deposited on a substrate, the interfacial energy is minimized by maximizing the

density of appropriate bonds across the interface in an attempt to merge the symmetries of both. If it is energetically favorable for the film material to match the substrate's crystallography, then it will grow epitaxially. The degree of matching between substrate and film can be defined by f , the fraction mismatch in the atomic periodicities of the two materials along the surface, given in the following equation:¹⁸⁷

$$f = \frac{a_e - a_s}{(a_e + a_s)/2} \approx \frac{a_e - a_s}{a_s}, \quad (\text{A1.1})$$

where a_e and a_s are the lattice parameters along equivalent directions in the film and substrate surface, respectively. Generally, if $f < 0.1$, epitaxy ensues, but if $f > 0.1$ few of the interfacial bonds are well aligned and therefore there is little reduction in the interfacial energy.¹⁸⁷ The distance of the O atoms in mica's SiO_4 tetrahedra is 0.255 – 0.286 nm, whereas face-centered cubic (fcc) Gold crystallizes with 0.288 nm as the smallest distance between nearest neighbor Au atoms. These data would give f values of ~ 0.1 at the most, thus ensuring epitaxial growth of Au(111) on mica.¹⁸⁸

The high vacuum chamber shown in figure A1.2 was used to deposit gold. It was pumped by a turbomolecular pump with a rotary forepump, achieving a final pressure of 2.7×10^{-8} mbar. An oil trap was inserted between the two pumps to prevent oil backstreaming into the chamber. Customized components were added to the chamber: A substrate (mica) holder/heater made of ceramic, together with a W mask with nine windows to mount the mica; a water-cooled quartz crystal micro balance; a Ta shutter; and an integrated W-coil + alumina crucible gold evaporator with variable positioning. To minimize thermal losses, the ceramic heater and the crucible were doubly shielded with 0.2 mm thick Ta housings. Tests were carried out with the configuration shown in figure A1.2 to ensure the functionality of all parts. For deposition of gold films, the crucible was heated with a current of 22.5 A to a temperature of, $\sim 900^\circ\text{C}$, high enough to evaporate the gold at the desired rate. The flux of Au atoms can be blocked by the shutter, thereby accurately controlling the deposition time. The pressure in the chamber during the evaporation was normally 2.7×10^{-7} mbar. Up to 9 samples per run could be prepared using the flexible W mask with nine windows.

The deposition rate was tested in several experimental runs. A final applied current of 21 to 22.5 A to the heater resulted in reasonable gold evaporation rates. These rates were found to be constant throughout the experiments, as long as the current was also kept constant. Readouts of the quartz crystal micro balance against time are depicted in figure A1.3 for several different currents applied to the W-coil + alumina crucible containing gold.

In the first experiments, the W-coil + alumina crucible was incrementally heated for 9 minutes, before the shutter was opened. Although this did not alter the final gold surface, it was found to be too harsh for the ceramic crucible, destroying it after several trials. A slower heating rate, taking 18 minutes until the final required current was reached, preserved the crucible. After several tests, a

current of 22.5 A was selected for regular runs of gold deposition, producing films of ~300 nm thickness in 31 minutes.

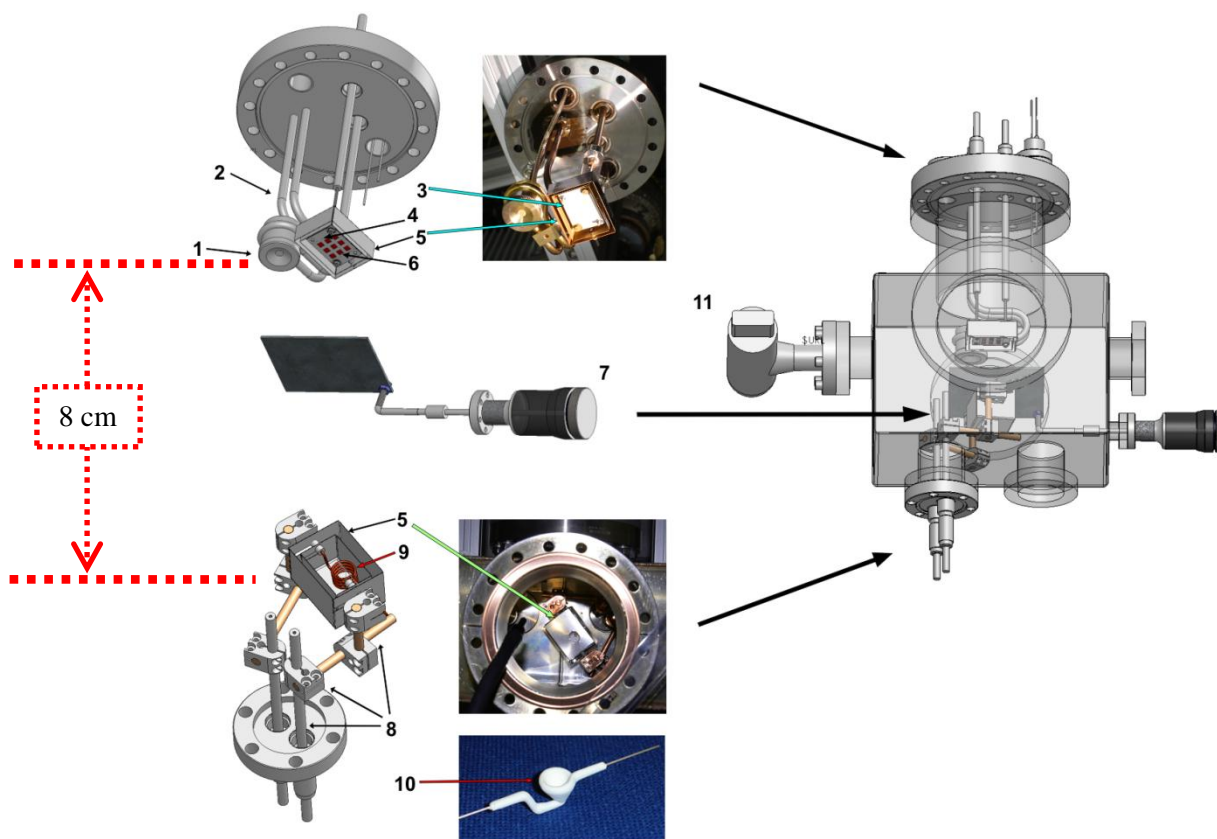


Figure A1.2: Components of the gold evaporator and mica mounting assembly: **1)** Water-cooled quartz crystal micro balance; **2)** balance holder and water cooling feedthrough; **3)** ceramic heater; **4)** sample holder with nine windows to mount the mica; **5)** two-fold Ta thermal radiation shields; **6)** position of the mica sandwiched between ceramic heater and evaporation mask; **7)** shutter to block the gold beam; **8)** flexible arrangement of copper conductors to position the crucible; **9)** W-coil with an **10)** integrated alumina crucible for efficient heating of the evaporant; **11)** pressure gauge. The right hand side of the picture shows the location of each component inside the high vacuum chamber. When assembled, the distance separating the gold evaporator and the sample holder is 8 cm.

To measure the film thickness, a Nanosurf® easyScan Atomic Force Microscope (AFM) was used. An area at the gold film boundary was scanned where clean mica and gold-covered mica surfaces could be imaged at the same time. A representative example is depicted in figure A1.4. The analysis of the AFM image yields a thickness of 300 nm. With this information, and taking 31 minutes deposition time into account, it is possible to calculate the deposition rate of gold on mica for the chosen conditions as follows:

$$\text{Rate of gold deposition} = \frac{\text{gold film thickness}}{\text{deposition time}} = \frac{300 \text{ nm}}{1860 \text{ s}} = 0.16 \text{ nm/s}$$

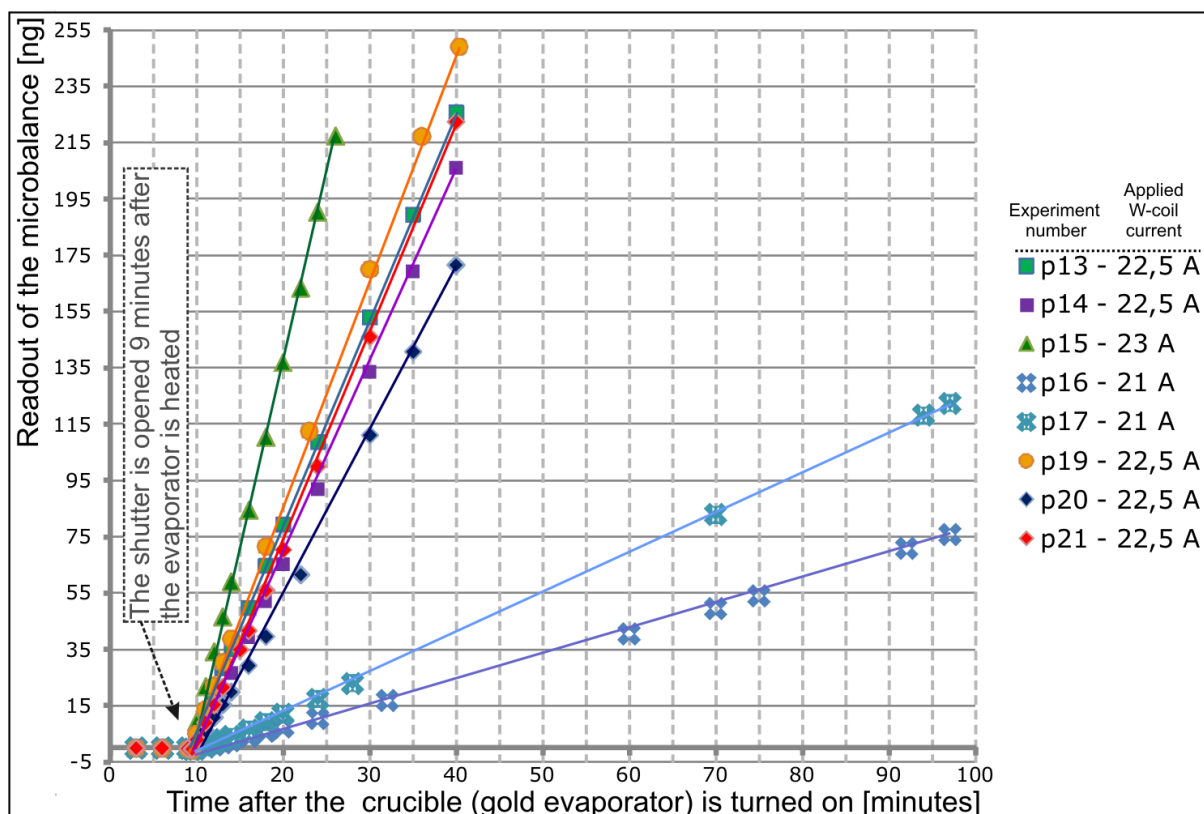


Figure A1.3: Quartz crystal micro balance readout versus time. The deposition rate of the gold, as observed in the straight lines connecting the dots in the graph, is constant for constant heating current. The slight variations are caused by different positions of the evaporator relative to the quartz balance.

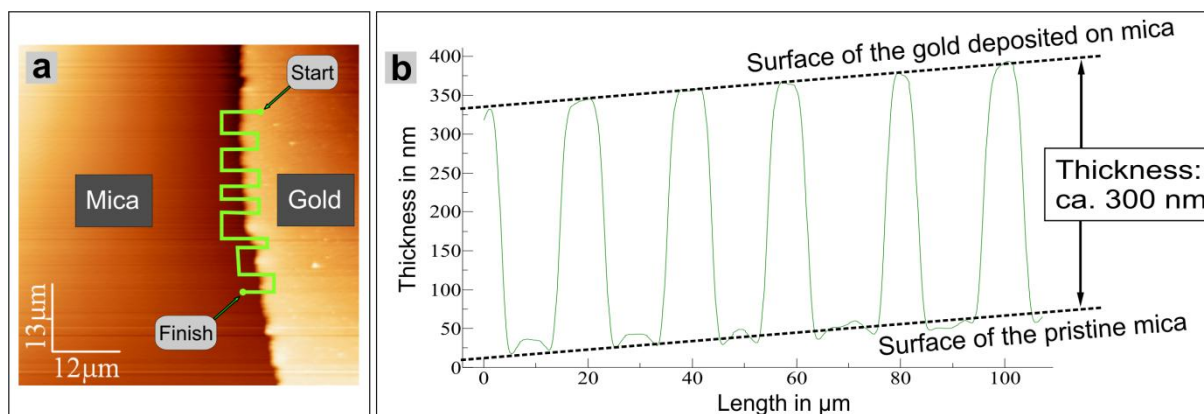


Figure A1.4: **a)** $64 \times 64 \mu\text{m}^2$ AFM (false color) image of the gold film boundary deposited on mica. **b)** Analysis of the green line-profile plotted on the AFM image in **a)**. The dotted lines are drawn to compensate the slope and allow for a precise measurement of the gold film thickness. The steep slopes indicate the boundary between the Au film and mica in **a)**, and *vice versa*; the plateaus are either on the gold film or mica substrate. The AFM image was analyzed with the WSxM Scanning Probe Microscopy Software.¹⁸⁹

The gold surfaces were studied using the ambient STM with mechanically cut Pt/Ir (90/10) tips. Before flame annealing, the surfaces do not exhibit a recognizable (111) termination. This is shown in figure A1.5. After $3 \times$ flame annealing, the surfaces exhibit recognizable triangular shapes, with step edges intersecting under 60° or 120° , which is a clear indication of (111) termination.

Terraces are flat and large enough to be used in further STM experiments. This is depicted in figure A1.6.

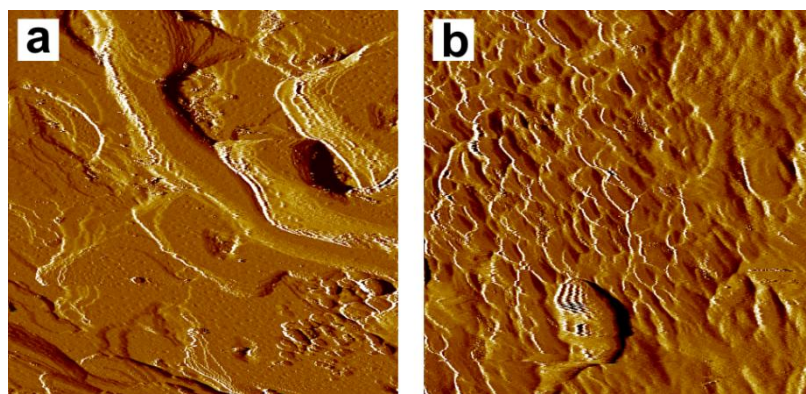


Figure A1.5: STM topography of the gold surfaces *before* flame annealing. They are rough and do not exhibit a recognizable (111) termination. **a)** $446 \times 446 \text{ nm}^2$; **b)** $279 \times 279 \text{ nm}^2$.

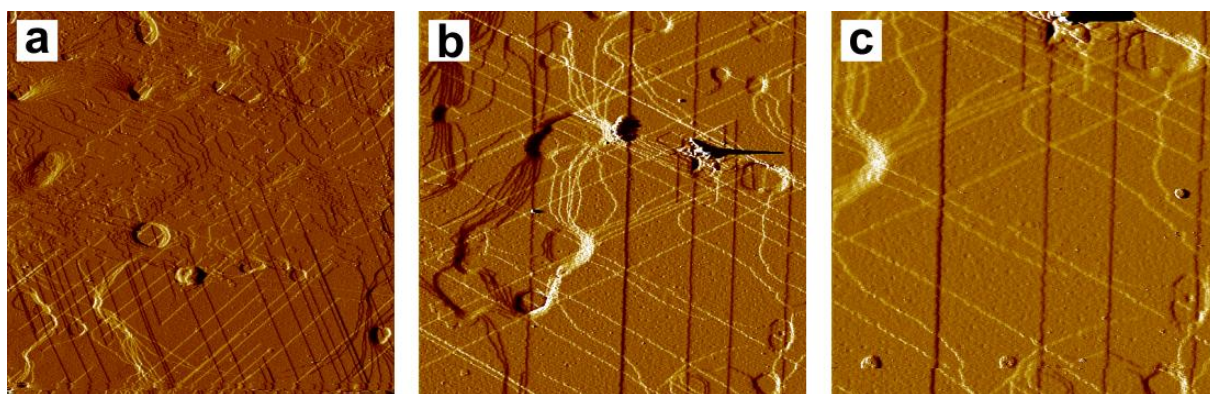


Figure A1.6: STM topography of the gold surfaces *after* $3\times$ flame annealing, exhibiting triangular shapes. These are step edges that intersect under 60° , which is a clear indication of (111) termination. Terraces are flat and large enough to be used in further STM experiments. **a)** $1160 \times 1160 \text{ nm}^2$; **b)** $640 \times 640 \text{ nm}^2$; **c)** $402 \times 402 \text{ nm}^2$.

Flame annealing is a required step to yield (111) terminated gold surfaces. Flame annealing affects the gold surface in several ways: by removing adsorbed molecules (contaminants),¹⁸⁶ by dehydroxylating the mica substrate (evolution of water from the interior of the mica),¹⁸⁶ and by causing the grain boundaries to diffuse across the individual grains, forming larger flat surfaces by coalescence.¹⁹⁰ For flame annealing, a butane torch is used, heating slightly the gold films for 30 seconds until a dark red color is observed. This is done preferably under subdued light or in complete darkness. After the elapsed time, the mica is left on a copper surface for another 30 seconds to cool down. For best results, this procedure is done right after the gold films are taken out of the vacuum chamber, and repeated three times. Figure A1.7 shows the difference in substrate finishing after $1\times$ or $3\times$ repetitions of the annealing procedure, proving that $3\times$ yield surfaces with larger flat terraces. Flame annealing can also remove some Au atoms from the surface.

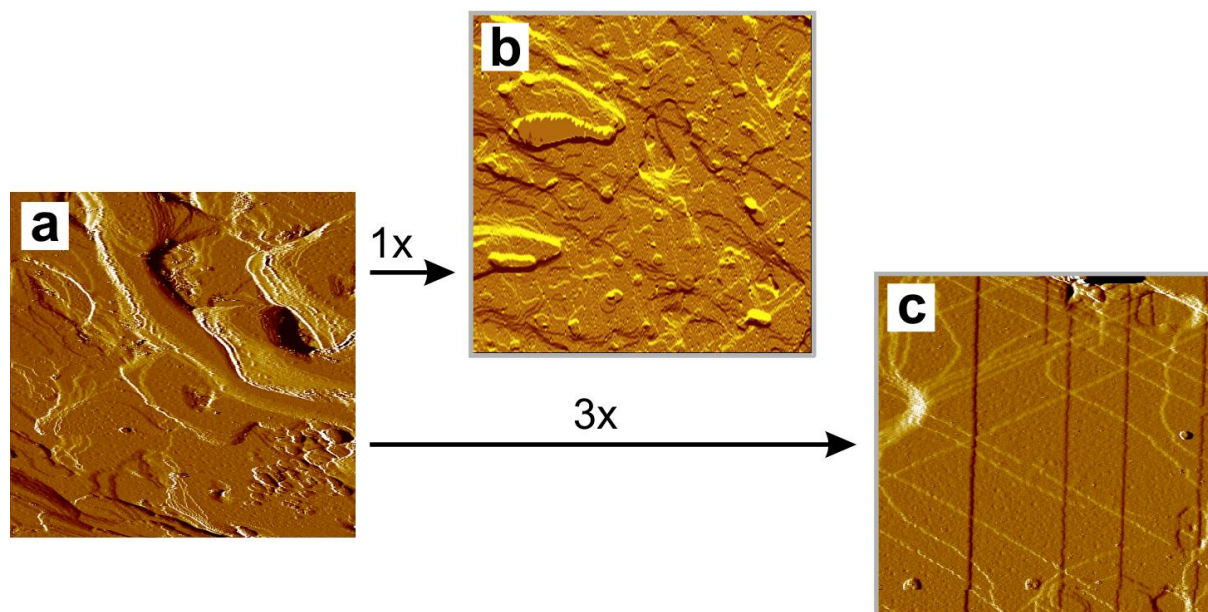


Figure A1.7: **a)** STM topographs of the gold surfaces *before* flame annealing ($446 \times 446 \text{ nm}^2$), **b)** after 1× flame annealing ($581 \times 581 \text{ nm}^2$), and **c)** after 3× flame annealing ($402 \times 402 \text{ nm}^2$). Annealing at least 3 times is necessary to yield flat and large Au(111) defect-free surfaces of at least $50 \times 50 \text{ nm}^2$.

To independently confirm the emergence of ultraflat Au(111) surfaces after flame annealing, Low Electron Energy Diffraction (LEED) was used. Samples with and without annealing were compared. The LEED patterns (112 eV) presented in figure A1.8 reveal the (111) surface of the gold films in both samples; however, the presence of sharper defined diffraction spots in the annealed sample (figure A1.8b) proves larger (111) crystalline domains than in the untreated sample.

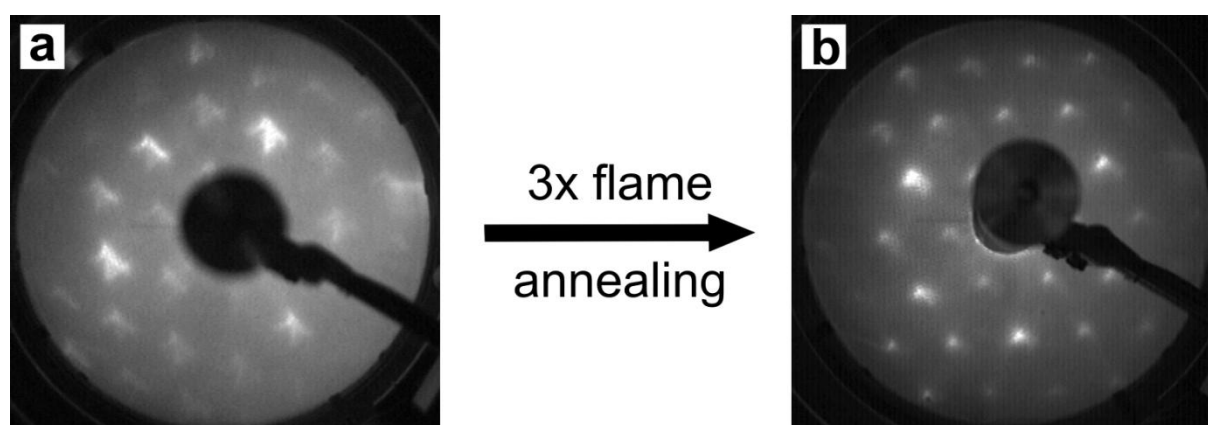


Figure A1.8: LEED patterns revealing the (111) surface termination of the gold films (112 eV). **a)** Samples before and **b)** after flame annealing. The more clearly defined and sharper spots in **b)** indicate the presence of larger (111) crystalline domains. LEED Images obtained by Georg Eder and Hermann Walch.

In order to investigate self-assembly of long chain alcohols into two-dimensional monolayers, a drop of 1-decanol was directly applied to freshly flame annealed gold surfaces. For STM experiments a mechanically cut Pt/Ir (90/10) tip was immersed into a liquid film on the surface.

Typically, 100 mV bias voltage and tunneling current setpoints around 70 pA were used for image acquisition. Examples of the self-assemblies observed are depicted in figure A1.9.

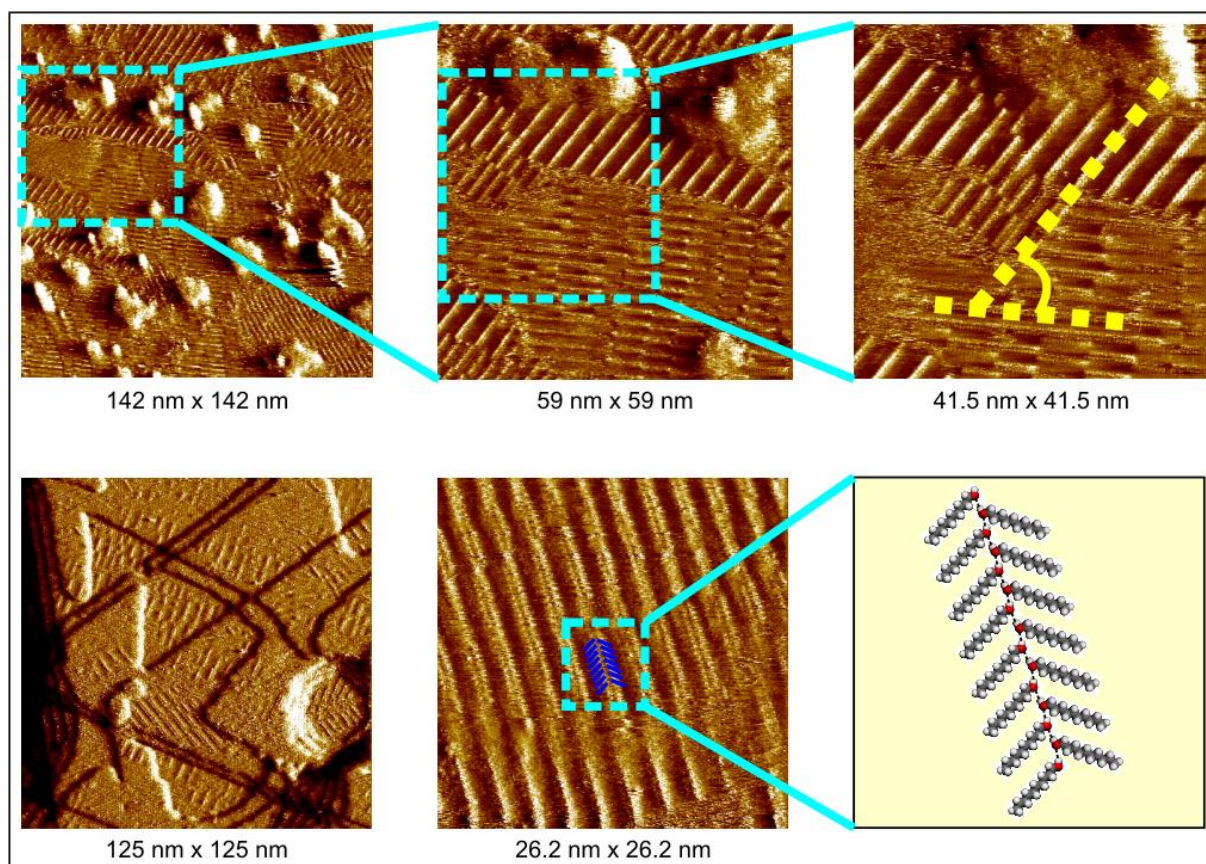


Figure A1.9: STM topographs of 1-decanol self-assembly on flame annealed Au(111) substrates. The images above depict a boundary between two rotational domains (54.7°) of the 1-decanol monolayer. Some unidentified (dirt) particles are also present. Images below depict: left hand side: ordered alcohol molecules on terraces of the gold surface; center: details of ordered rows of molecules; right hand side: tentative model of the molecular assembly. Intermolecular hydrogen bonds are the main driving force for the self-assembly.¹⁹¹

Appendix 2

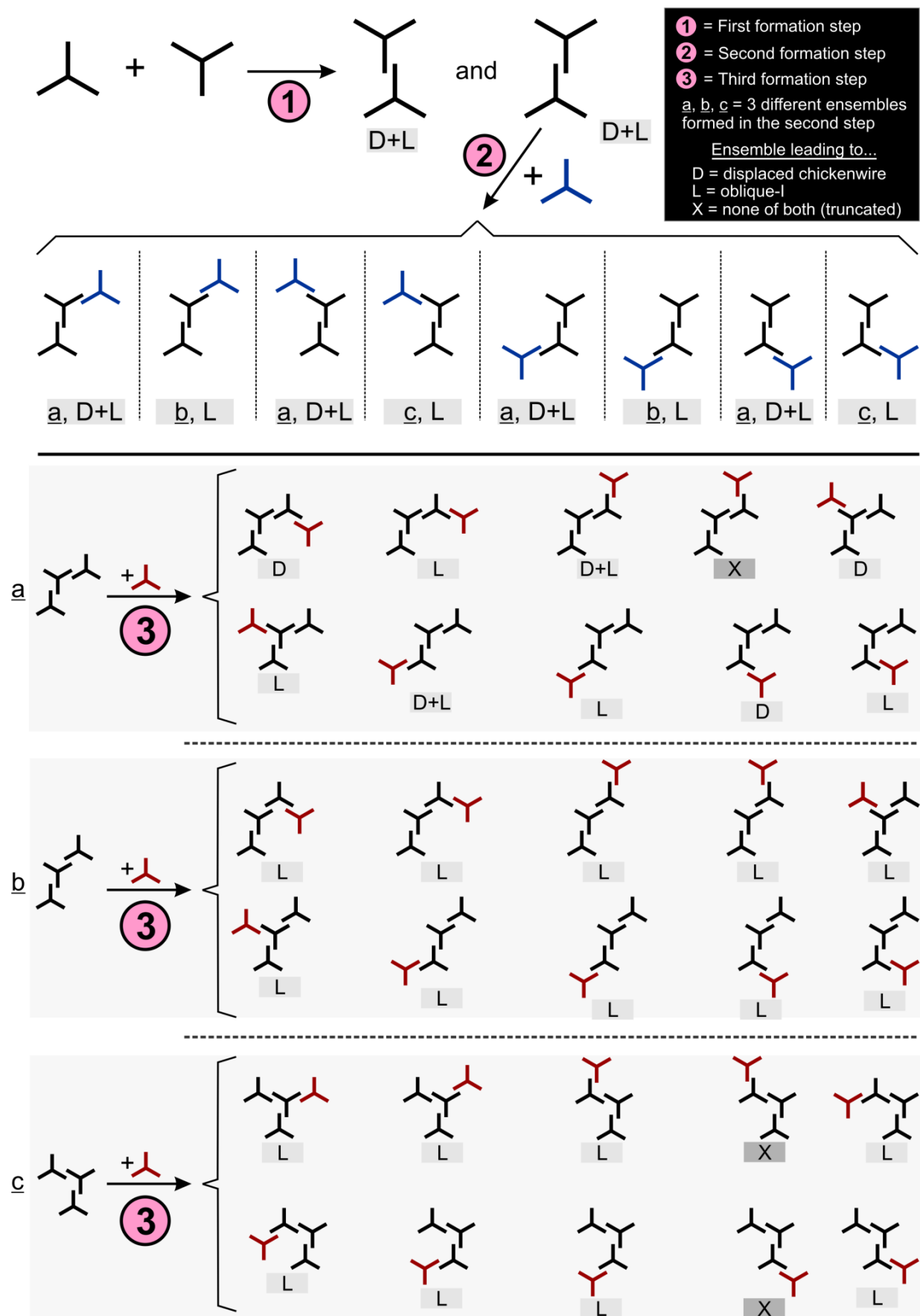
Stepwise Assembly Scheme and Evaluation of Formation Probabilities for Two Different Polymorphs from TCBPB

Figure A.1 presents a step by step (molecule by molecule) assembly scheme for the formation of ensembles leading to the formation of oblique-I (L), displaced chickenwire (D), or none of both (X). Every tripod represents a TCBPB molecule. Notice that an ensemble is **not** yet a stable nucleus, but an aggregate of molecules with pre-defined relative positions. An ensemble can be converted into a stable nucleus only if it becomes thermodynamically stable. The relationships between L, D and X are given in table 3.2 (chapter 3), reproduced here.

Table 3.2: Relationships found among TCBPB ensembles at the 1st, 2nd, 3rd, and 4th step of their formation. Only ensembles leading to the formation of oblique-I, displaced chickenwire, or none of both were considered.

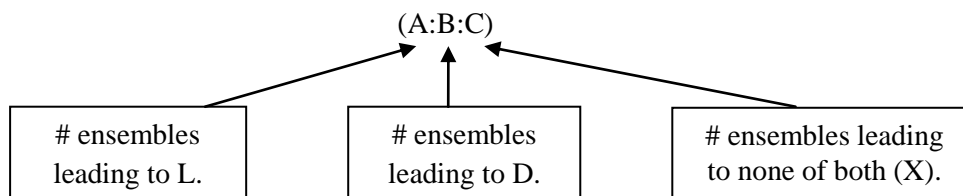
| Ensemble formation step | Number of molecules involved | Probabilistic relationships | | |
|-------------------------|------------------------------|--------------------------------|--|--|
| | | Ensembles leading to oblique-I | Ensembles leading to displaced chickenwire | Ensembles <i>unable</i> to lead to any of both |
| 1 st | 2 | 1 | 1 | 0 |
| 2 nd | 3 | 2 | 1 | 0 |
| 3 rd | 4 | 3 | 1 | 0.4 |
| 4 th | 5 | 4 | 1 | 2.3 |

Figure A2.1: Step by step assembly scheme for the formation of ensembles leading to the formation of oblique-I (L), displaced chickenwire (D), or none of both (X).



Calculation of the formation probabilities of the arrangements presented in table 3.2:

Notation:



Calculation procedure:

1st step: There are 6 possible ensemble configurations; 3 of them being geometrically equivalent. That reduces itself to 2 different dimeric configurations. The dimer is a common motif of both structures and does not preselect any polymorph. Hence, a dimer *has* the same chances to lead to both assemblies. So the chances are: $2 \times (1:1:0) = (2:2:0)$. It can be simplified to $(1:1:0)$.

2nd step: Any of the two different dimers in the 1st step yields the same number of possible ensembles in the second step, so only one half are calculated. The other half is made of mirror images.

There are 8 possible ensembles originating from every dimeric configuration in the 1st step: $4 \times \underline{a}$; $2 \times \underline{b}$; and $2 \times \underline{c}$.

\underline{a} can yield both structures, hence it is labeled “D + L”; \underline{b} and \underline{c} can only yield oblique-I, thus they are labeled “L”. At this stage, there are no ensembles that lead to none of both (X).

Therefore, the number of ensembles that *can* lead to L is 8, and those that *can* lead to D is 4. So, number of ensembles leading to L vs. number of ensemble leading to D = $2 \times (8:4:0) = (16:8:0)$. Simplifying: $(2:1:0)$.

3rd step: Each of the 8 ensembles in the 2nd step yields 10 ensembles in the 3rd.

\underline{a} yields 6 ensembles that *can* lead to L, 5 to D, and 1 to none (X). This relationship has to be multiplied by the number of possible \underline{a} structures in the 2nd step, which is 4, and the number of total structures in the first, which is 2. Hence for \underline{a} : $4 \times 2 \times (6:5:1) = (48:40:8)$.

\underline{b} yields only 10 ensembles that *can* lead to L, hence $2 \times 2 \times (10:0:0) = (40:0:0)$.

\underline{c} forms 8 ensembles that *can* lead to L, and 2 that lead to none (X), hence $2 \times 2 \times (8:0:2) = (32:0:8)$.

Adding up all three ensembles gives: $(48:40:8) + (40:0:0) + (32:0:8) = (120:40:16)$.

This can be simplified to $(15:5:2)$. For the ease of comparison with the previous relationships, it can be further simplified to $(3:1:\frac{2}{5})$, or $(3:1:0.4)$.

4th step: Every ensemble in the 3rd step yields 12 ensembles in the 4th. For the evaluation of the probabilities in this step, those ensembles marked with X in the 3rd step are not evaluated here. This is because they are supposed to already be ensembles unable to lead to L or D in the 4th step. The fact that in hundreds of STM images of the self-assembly of TCBPB, not even one misplaced adsorbate was observed, as is depicted in the ensembles marked with X, can be understood on the basis of the reversibility of the self-assembly process: If an adsorbate is misplaced, it can be corrected by desorption and resorption of the same or other molecular adsorbates in the right position. This process implies going back one step, so the probabilities belong to the preceding step, and not to this step. However, taking or not into consideration the probabilities for further growth of X ensembles in the 4th step do not alter the final L:D ratio. The 4th step is not graphically represented in figure A2.1.

The majority of the 9 ensembles of the 3rd step of a (not considering 1 X) yield 44 ensembles that *can* lead to L, 30 to D, and 38 to X. This relationship has to be multiplied by the number of possible a structures in the 2nd step, and by the number of dimers in the first step. Thus for the 4th step: $4 \times 2 \times (44:30:38) = (352:240:304)$.

For the case of b, there are none X ensembles in the 3rd step. There are 84 ensembles that can lead to L, and 36 to X. There are none that can lead to D. This relationship is multiplied by the number of possible b structures in the 2nd step, which are 2, and by the number of dimers in the first step. Hence for this step: $2 \times 2 \times (84:0:36) = (336:0:144)$.

The 3rd step of c has 2 ensembles marked as X, so they are not counted in the following evaluation. There are in total 68 ensembles that *can* lead to L, 28 to X, and none to D. Thus, multiplying by the number of possible c structures in the second step, and again by those in the first step, gives the following result: $2 \times 2 \times (68:0:28) = (272:0:112)$.

Adding up gives: $(352:240:304) + (336:0:144) + (272:0:112) = (960:240:560)$.

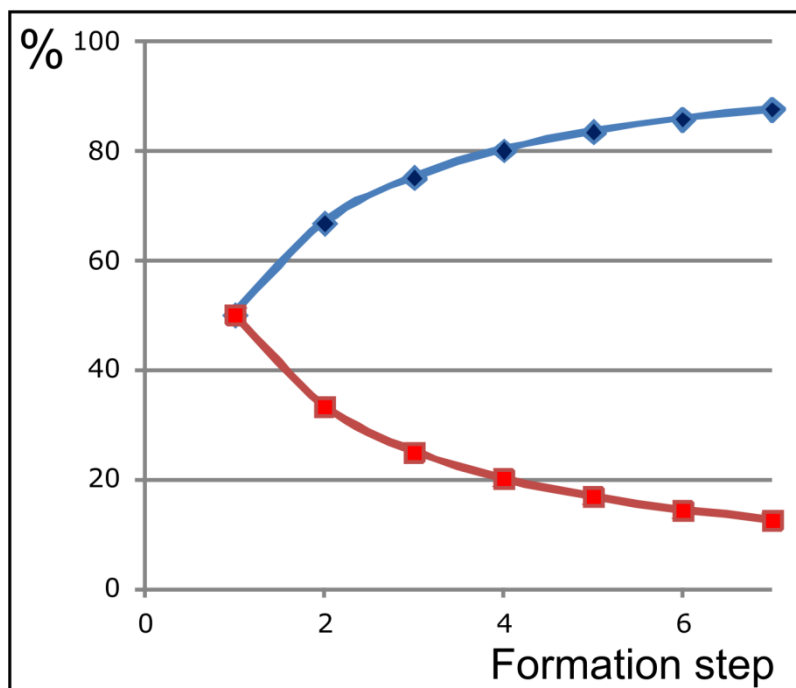
Simplifying: $(4:1:2\frac{1}{3})$.

For the ease of comparison with the previous relationships: (4:1:2.3)

Table A2.1: Relationships found in table 3.2, given in %, and calculated only for ensembles leading to oblique-I and to displaced chickenwire.

| Ensemble formation step | Number of molecules involved | Probabilistic relationships | |
|-------------------------|------------------------------|--------------------------------|--|
| | | Ensembles leading to oblique-I | Ensembles leading to displaced chickenwire |
| 1 st | 2 | 50 | 50 |
| 2 nd | 3 | 66.7 | 33.3 |
| 3 rd | 4 | 75 | 25 |
| 4 th | 5 | 80 | 20 |

Figure A2.2: Graphical representation of the probabilities given in table A.1. Evaluated from $n = 2$ up to the 7th formation step ($n = 8$), calculated using equation 3.8. **Blue** = oblique-I; **red** = displaced chickenwire. It can be observed that the probability of forming oblique-I approaches asymptotically the 100% value; whereas for displaced chickenwire, it approaches the zero line.



Publications

List of publications that were published as part of this dissertation in chronological order.

- 1. Reversible Phase Transitions in Self-Assembled Monolayers at the Liquid-Solid Interface: Temperature-Controlled Opening and Closing of Nanopores**
Rico Gutzler, Thomas Sirtl, Jürgen F. Dienstmaier, Kingsuk Mahata, Wolfgang M. Heckl, Michael Schmittel, and Markus Lackinger
J. Am. Chem. Soc. **2010**, *132*, 5084–5090.
- 2. On the Scalability of Supramolecular Networks – High Packing Density vs Optimized Hydrogen Bonds in Tricarboxylic Acid Monolayers**
Jürgen F. Dienstmaier, Kingsuk Mahata, HermannWalch, Wolfgang M. Heckl, Michael Schmittel and Markus Lackinger
Langmuir, **2010**, *26* (13), 10708-10716.
- 3. Extended Two-Dimensional Metal Organic Frameworks Based on Thiolate Copper Coordination Bonds**
Hermann Walch, Jürgen Dienstmaier, Georg Eder, Rico Gutzler, Stefan Schlögl, Kalpataru Das, Michael Schmittel, and Markus Lackinger
J. Am. Chem. Soc. **2011**, *133*, 7909-7915.
- 4. Synthesis of Well-Ordered COF Monolayers: Surface Growth of Nanocrystalline Precursors versus Direct On-Surface Polycondensation**
Jürgen F. Dienstmaier, Alexander M. Gigler, Andreas J. Goetz, Paul Knochel, Thomas Bein, Andrey Lyapin, Stefan Reichmaier, Wolfgang M. Heckl, and Markus Lackinger
ACS Nano **2011**, *5* (12), 9737-9745.
- 5. Isorecticular Two-Dimensional Covalent Organic Frameworks Synthesized by On-Surface Condensation of Diboronic Acids**
Jürgen F. Dienstmaier, Dana D. Medina, Mirjam Dogru, Paul Knochel, Thomas Bein, Wolfgang M. Heckl, and Markus Lackinger,
ACS Nano **2012**, *6* (8), 7234-7242.

Reversible Phase Transitions in Self-Assembled Monolayers at the Liquid–Solid Interface: Temperature-Controlled Opening and Closing of Nanopores

Rico Gutzler,^{*,†} Thomas Sirtl,[†] Jürgen F. Dienstmaier,[†] Kingsuk Mahata,[‡] Wolfgang M. Heckl,[#] Michael Schmittel,[‡] and Markus Lackinger^{*,†}

Department of Earth and Environmental Sciences and Center for NanoScience (CeNS), Ludwig-Maximilians-University, Theresienstrasse 41, 80333 Munich, Germany, Center of Micro and Nanochemistry and Engineering, Organische Chemie I, University Siegen, Adolf-Reichwein-Strasse 2, 57068 Siegen, Germany, Deutsches Museum, Museumsinsel 1, 80538 Munich, Germany, and Department of Physics, TUM School of Education, Technical University Munich, Schellingstrasse 33, 80333 Munich, Germany

Received October 19, 2009; E-mail: rico.gutzler@lrz.uni-muenchen.de; markus@lackinger.org

Abstract: We present a variable-temperature study of monolayer self-assembly at the liquid–solid interface. By means of *in situ* scanning tunneling microscopy (STM), reversible phase transitions from a nanoporous low-temperature phase to a more densely packed high-temperature phase are observed. The occurrence of the phase transition and the respective transition temperature were found to depend on the type of solvent and solute concentration. Estimates of the entropic cost and enthalpic gain upon monolayer self-assembly suggest that coadsorption of solvent molecules within the cavities of the nanoporous structure renders this polymorph thermodynamically stable at low temperatures. At elevated temperatures, however, desorption of these relatively weakly bound solvent molecules destabilizes the nanoporous polymorph, and the densely packed polymorph becomes thermodynamically favored. Interestingly, the structural phase transition provides external control over the monolayer morphology and, for the system under discussion, results in an effective opening and closing of supramolecular nanopores in a two-dimensional molecular monolayer.

Introduction

Self-assembly of ordered monolayers at the liquid–solid interface has been proven to be well suited for functionalizing surfaces and, thus, has become a topic of elaborate research.^{1–5} Especially porous networks, which can be utilized as supramolecular host systems for defined coadsorption of nanoscopic guests, have received broad interest.^{6–11} Tailoring morphology, size, and functionalization of porous networks thus remains a

topic of fundamental interest in nanotechnology. The monolayer morphology is primarily governed by the structure and functional groups of the molecule,^{12–14} but can also depend on the type of solvent,^{15–18} concentration,^{5,19–21} substrate,²² substrate-mediated interactions,²³ and other factors. Among all important parameters for self-assembly at the liquid–solid interface, temperature is probably the one least studied, and only a few examples are reported in the literature.^{21,24–30} For instance, English and Hipps use STM to reveal the progressive desorption of coronene from Au(111) between room temperature and 55 °C (*in situ*, up to 105 °C *ex-situ*).²⁷ However, in many variable-temperature studies samples are just conditioned at elevated temperatures, while measurements are still conducted at room temperature.

Although temperature is a vital parameter for any self-assembly because it directly affects both thermodynamics and kinetics, little is known about its influence on physisorbed

[†] Ludwig-Maximilians-University.

[‡] University Siegen.

[#] Deutsches Museum and Technical University Munich.

- (1) Barth, J. V.; Costantini, G.; Kern, K. *Nature* **2005**, *437* (7059), 671–679.
- (2) De Feyter, S.; De Schryver, F. C. *J. Phys. Chem. B* **2005**, *109* (10), 4290–4302.
- (3) Elemans, J. A. A. W.; De Feyter, S. *Soft Matter* **2009**, *5* (4), 721–735.
- (4) Kühnle, A. *Curr. Opin. Colloid Interface Sci.* **2009**, *14* (2), 157–168.
- (5) Yang, Y. L.; Wang, C. *Curr. Opin. Colloid Interface Sci.* **2009**, *14* (2), 135–147.
- (6) Kudernac, T.; Lei, S. B.; Elemans, J. A. A. W.; De Feyter, S. *Chem. Soc. Rev.* **2009**, *38* (2), 402–421.
- (7) Madueno, R.; Raisanen, M. T.; Silien, C.; Buck, M. *Nature* **2008**, *454* (7204), 618–621.
- (8) Theobald, J. A.; Oxtoby, N. S.; Phillips, M. A.; Champness, N. R.; Beton, P. H. *Nature* **2003**, *424* (6952), 1029–1031.
- (9) Stepanow, S.; Lingenfelder, M.; Dmitriev, A.; Spillmann, H.; Delvigne, E.; Lin, N.; Deng, X. B.; Cai, C. Z.; Barth, J. V.; Kern, K. *Nat. Mater.* **2004**, *3* (4), 229–233.
- (10) Griessl, S. J. H.; Lackinger, M.; Jamitzky, F.; Markert, T.; Hietschold, M.; Heckl, W. M. *Langmuir* **2004**, *20* (21), 9403–9407.

- (11) Kühne, D.; Klappenberger, F.; Decker, R.; Schlickum, U.; Brune, H.; Klyatskaya, S.; Ruben, M.; Barth, J. V. *J. Am. Chem. Soc.* **2009**, *131* (11), 3881–3883.
- (12) Tahara, K.; Furukawa, S.; Uji-I, H.; Uchino, T.; Ichikawa, T.; Zhang, J.; Mamdouh, W.; Sonoda, M.; De Schryver, F. C.; De Feyter, S.; Tobe, Y. *J. Am. Chem. Soc.* **2006**, *128* (51), 16613–16625.
- (13) Kampschulte, L.; Werblowsky, T. L.; Kishore, R. S. K.; Schmittel, M.; Heckl, W. M.; Lackinger, M. *J. Am. Chem. Soc.* **2008**, *130* (26), 8502–8507.
- (14) Gutzler, R.; Lappe, S.; Mahata, K.; Schmittel, M.; Heckl, W. M.; Lackinger, M. *Chem. Commun.* **2009**, (6), 680–682.

monolayers at the liquid–solid interface. For 1,3,5-tris(4-carboxyphenyl)benzene (BTB, cf. Figure 1a) monolayers, temperature-dependent structural phase transitions were observed under vacuum conditions on the Ag(111) surface.³¹ Yet, most likely driven by a stepwise deprotonation of the carboxylic groups, these phase transitions are not reversible.

Herein we demonstrate how the morphology of BTB monolayers at the carboxylic acid/graphite interface specifically can be switched bidirectionally by lowering and raising the temperature. As detailed below, interfacial BTB monolayers show a fully reversible temperature-driven structural phase transition, changing from an open pore network to a nonporous, densely packed structure. Accordingly, nanopores can be closed at slightly elevated temperatures and opened again by cooling the sample below the transition temperature. Such a reversible process opens venues for various applications in which guest coadsorption is controlled by temperature, as a densely packed structure in contrast to an open-pore structure does not facilitate coadsorption of molecular guests.

Our experimental findings can be explained and are rationalized by thermodynamic considerations, where the free energies of adsorption of both polymorphs are evaluated from a molecule-based estimation of enthalpic gains and entropic costs.

Results and Discussion

Solvent Dependence. Three different carboxylic acids served as solvents, namely heptanoic (7A), octanoic (8A), and nonanoic acid (9A). At room temperature with 7A as solvent, BTB

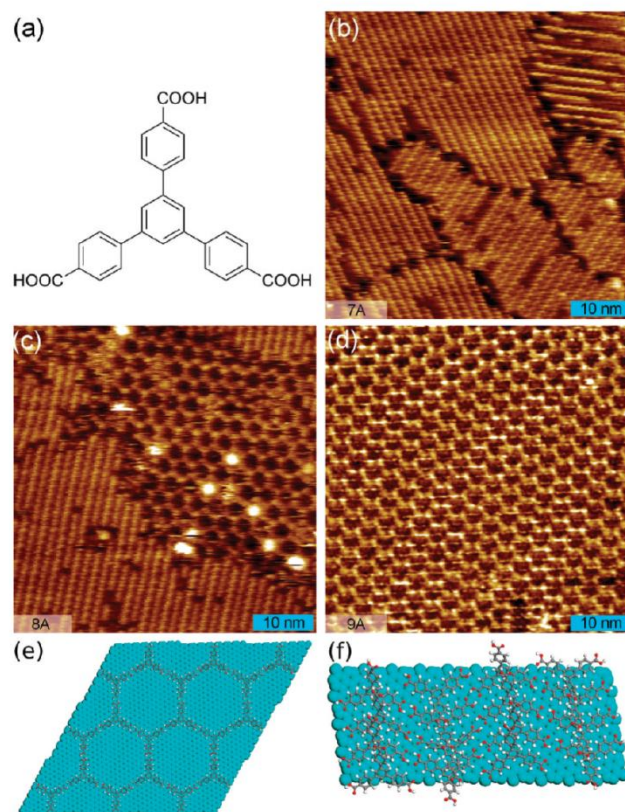


Figure 1. (a) Chemical structure of 1,3,5-tris(4-carboxyphenyl)benzene (BTB). STM topographs of BTB monolayers at the (b) heptanoic acid/graphite ($V_{\text{bias}} = 0.80$ V, $I_T = 77$ pA), (c) octanoic acid/graphite ($V_{\text{bias}} = 1.10$ V, $I_T = 92$ pA), and (d) nonanoic acid/graphite interface ($V_{\text{bias}} = 1.15$ V, $I_T = 71$ pA). In all cases saturated solutions were used and topographs were recorded at room temperature. (e) Ball-and-stick model of a chicken-wire BTB monolayer on graphite; nine unit cells are depicted (cyan: graphite substrate, gray: carbon, white: hydrogen, red: oxygen). (f) Top view of a ball-and-stick model of the row structure of BTB on graphite; eight unit cells are depicted. Adjacent rows are interconnected via hydrogen bonds.

furnishes a previously unobserved densely packed row structure on HOPG with striped appearance (Figure 1b). In 8A, the row structure is found in coexistence with the chicken-wire structure, a hexagonal, less dense open-pore network (Figure 1c) that is quite common for other 3-fold symmetric tricarboxylic acids as well.^{14,32} At room temperature, 9A as solvent exclusively yields the chicken-wire structure (Figure 1d). Models of the respective polymorphs are presented in Figure 1e,f.

Temperature Dependence. A home-built heatable sample stage facilitates STM measurements at the liquid–solid interface from room temperature up to ~ 70 °C. Heating the BTB/7A system to over 60 °C did not result in any change of the monolayer morphology. At all intermediate temperatures, exclusively the row structure was observed. In 8A, the coexistence of both phases prevailed up to ~ 43 °C. Above this temperature the sample was entirely covered with the row structure. Similarly, in 9A the chicken-wire structure was stable up to ~ 55 °C, while at temperatures above only the row structure could be observed. In order to verify the reversibility of the BTB phase transition, several heat–cool cycles were conducted in 8A and 9A, where images were repeatedly acquired below as well as above the respective transition temperature

- (15) Kampschulte, L.; Lackinger, M.; Maier, A. K.; Kishore, R. S. K.; Griessl, S.; Schmittl, M.; Heckl, W. M. *J. Phys. Chem. B* **2006**, *110* (22), 10829–10836.
- (16) Mamdouh, W.; Uji-i, H.; Ladislav, J. S.; Dulcey, A. E.; Percec, V.; De Schryver, F. C.; De Feyter, S. *J. Am. Chem. Soc.* **2006**, *128* (1), 317–325.
- (17) Li, Y. B.; Ma, Z.; Qi, G. C.; Yang, Y. L.; Zeng, Q. D.; Fan, X. L.; Wang, C.; Huang, W. *J. Phys. Chem. C* **2008**, *112* (23), 8649–8653.
- (18) Zhang, X.; Chen, Q.; Deng, G. J.; Fan, Q. H.; Wan, L. J. *J. Phys. Chem. C* **2009**, *113* (36), 16193–16198.
- (19) Lei, S. B.; Tahara, K.; De Schryver, F. C.; Van der Auweraer, M.; Tobe, Y.; De Feyter, S. *Angew. Chem., Int. Ed.* **2008**, *47* (16), 2964–2968.
- (20) So, C. R.; Tamerler, C.; Sarikaya, M. *Angew. Chem., Int. Ed.* **2009**, *48* (28), 5174–5177.
- (21) Palma, C. A.; Bjork, J.; Bonini, M.; Dyer, M. S.; Llanes-Pallas, A.; Bonifazi, D.; Persson, M.; Samorì, P. *J. Am. Chem. Soc.* **2009**, *131*, 13062–13071.
- (22) Klappenberger, F.; Cañas-Ventura, M. E.; Clair, S.; Pons, S.; Schlickum, U.; Qu, Z. R.; Strunskus, T.; Comisso, A.; Wöll, C.; Brune, H.; Kern, K.; De Vita, A.; Ruben, M.; Barth, J. V. *ChemPhysChem* **2008**, *9* (17), 2522–2530.
- (23) Wang, Y. F.; Ge, X.; Manzano, C.; Korger, J.; Berndt, R.; Hofer, W. A.; Tang, H.; Cerda, J. *J. Am. Chem. Soc.* **2009**, *131* (30), 10400–10402.
- (24) Valiokas, R.; Ostblom, M.; Svedhem, S.; Svensson, S. C. T.; Liedberg, B. *J. Phys. Chem. B* **2000**, *104* (32), 7565–7569.
- (25) Azzam, W.; Bashir, A.; Terfort, A.; Strunskus, T.; Wöll, C. *Langmuir* **2006**, *22* (8), 3647–3655.
- (26) Bleger, D.; Kreher, D.; Mathevet, F.; Attias, A. J.; Schull, G.; Huard, A.; Douillard, L.; Fiorini-Debuschert, C.; Charra, F. *Angew. Chem., Int. Ed.* **2007**, *46* (39), 7404–7407.
- (27) English, W. A.; Hips, K. W. *J. Phys. Chem. C* **2008**, *112* (6), 2026–2031.
- (28) Kong, X. H.; Deng, K.; Yang, Y. L.; Zeng, Q. D.; Wang, C. *J. Phys. Chem. C* **2007**, *111* (26), 9235–9239.
- (29) Li, C. J.; Zeng, Q. D.; Liu, Y. H.; Wan, L. J.; Wang, C.; Wang, C. R.; Bai, C. L. *ChemPhysChem* **2003**, *4* (8), 857–859.
- (30) Yamada, R.; Wano, H.; Uosaki, K. *Langmuir* **2000**, *16* (13), 5523–5525.
- (31) Ruben, M.; Payer, D.; Landa, A.; Comisso, A.; Gattinoni, C.; Lin, N.; Collin, J. P.; Sauvage, J. P.; De Vita, A.; Kern, K. *J. Am. Chem. Soc.* **2006**, *128* (49), 15644–15651.

- (32) Lackinger, M.; Griessl, S.; Heckl, W. M.; Hietschold, M.; Flynn, G. W. *Langmuir* **2005**, *21* (11), 4984–4988.

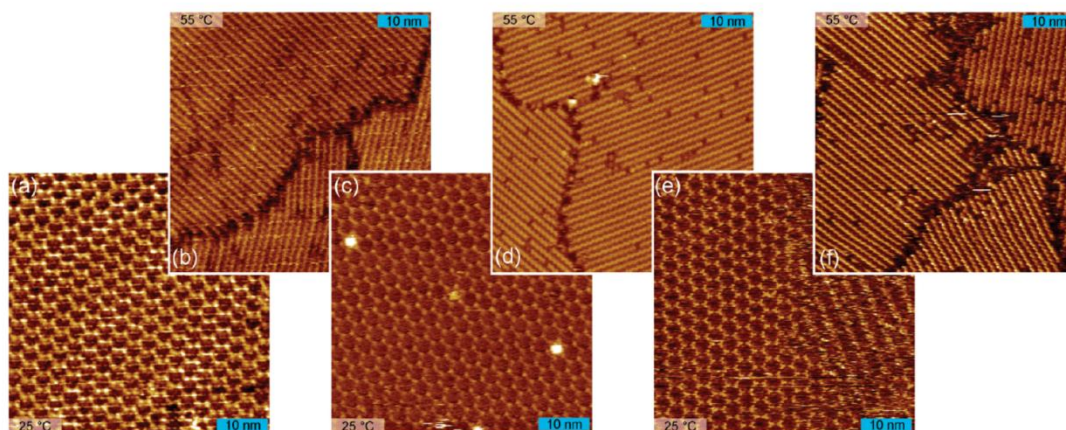


Figure 2. STM topographs as acquired during repeated heat–cool cycles of saturated BTB in nonanoic acid solutions demonstrating the reversibility of the phase transition. The respective temperature is stated in the lower (upper) left corner of each image. The cycle starts at the lower left image (a) at room temperature ($V_{\text{bias}} = 1.15$ V, $I_T = 71$ pA) and is continued (b) at 55 °C ($V_{\text{bias}} = 1.15$ V, $I_T = 72$ pA) → (c) at 25 °C ($V_{\text{bias}} = 1.15$ V, $I_T = 65$ pA) → (d) at 55 °C ($V_{\text{bias}} = 1.15$ V, $I_T = 73$ pA) → (e) at 25 °C ($V_{\text{bias}} = 1.15$ V, $I_T = 77$ pA) → (f) at 55 °C ($V_{\text{bias}} = 1.15$ V, $I_T = 79$ pA).

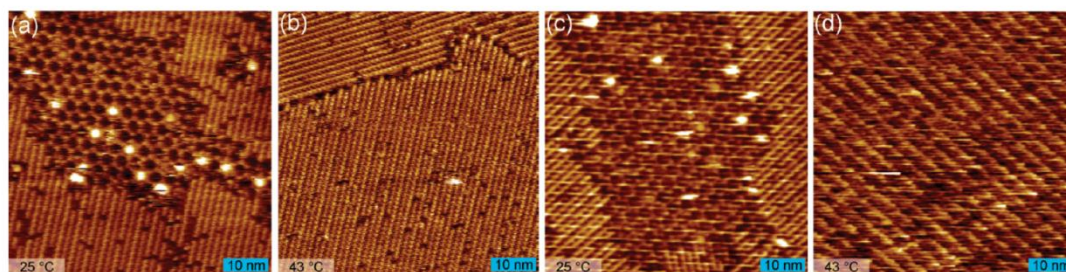


Figure 3. STM topographs as obtained from repeated heat–cool cycles of saturated BTB in octanoic acid solutions demonstrating the reversibility of the phase transition. The respective temperature is stated in the lower left corner of each image. The series starts at the left image (a) at room temperature ($V_{\text{bias}} = 1.10$ V, $I_T = 92$ pA) and is continued (b) at 43 °C ($V_{\text{bias}} = 1.10$ V, $I_T = 78$ pA) → (c) at 25 °C ($V_{\text{bias}} = 1.10$ V, $I_T = 56$ pA) → (d) at 43 °C ($V_{\text{bias}} = 1.10$ V, $I_T = 85$ pA).

(cf. Figures 2 and 3). In both solvents, the chicken-wire structure reappears below the temperature thresholds of ~ 43 °C (**8A**) and ~ 55 °C (**9A**), respectively. In some cases in **9A** small patches of the row structure emerged after the first cycle.

Concentration Dependence. While all studies described above were conducted with saturated solutions, further experiments were carried out with diluted solutions. Solubilities of BTB are 0.77 mM in **7A**, 0.75 mM in **8A**, and 0.50 mM in **9A**; thus all saturated solutions exhibit comparable concentrations. At BTB concentrations in **7A** of about 50% saturation, the row structure assembled on the surface coexisting with the chicken-wire structure. For more diluted solutions, at concentrations around 10% saturation, the chicken-wire structure is the dominating polymorph, emphasizing the importance of solute concentration in molecular self-assembly. Concentration-induced polymorphism, where the less densely packed polymorphs emerge for more diluted solutions, was found for various other systems.^{18,19,33} As concluded from thermodynamic considerations, the observation of coexistence of both polymorphs over a wide concentration range can be taken as an indication that their free energies are very similar.¹⁹ As a singular experiment we explored possible phase transitions in 50% saturated solution of BTB in **9A**. However, at temperatures up to ~ 70 °C no phase transition

was observable, therefore pointing toward a relation between concentration and transition temperature.

Discussion

With respect to the adsorption geometry of BTB molecules and adsorbate–substrate and intermolecular interactions, the row and chicken-wire polymorphs are entirely different. In the chicken-wire structure BTB molecules adsorb planar on the surface and are interconnected by linear double O–H \cdots O hydrogen bonds between carboxylic groups, as thoroughly discussed elsewhere.¹⁵ The hexagonal unit cell ($a = 3.2$ nm) contains two molecules. Likewise, the unit cell of the row structure (unit cell parameters: $a = 3.3$ nm, $b = 0.7$ nm, 82° angle) contains two molecules, but its relatively small area readily indicates nonplanar adsorption. The row structure is also comparable to the monolayer morphology found for a slightly larger tricarboxylic acid,¹⁴ in which molecules are stacked face-to-face along columns parallel to the substrate. The monolayer is then comprised of densely packed parallel rows. In the row structure molecules adsorb nearly upright; thus the molecule–substrate interaction is diminished as compared to planar adsorption. However, intermolecular van der Waals and π – π interactions stabilize the structure. BTB molecules adsorb with two carboxylic groups on the substrate, while the third carboxylic group points off the surface into the solution. According to our structural model, inter-row O–H \cdots O hydrogen bonds are feasible, yet their unfavorable geometry and the absence of resonance effects that stabilize cyclic hydrogen bonds render

(33) Meier, C.; Roos, M.; Künzel, D.; Breitruck, A.; Hoster, H. E.; Landfester, K.; Gross, A.; Behm, R. J.; Ziener, U. *J. Phys. Chem. C* **2010**, *114* (2), 1268–1277.

Table 1. Comparison of Packing Density, Enthalpic Gain (Δh_{eff}), Entropic Cost ($-\Delta s$), and Free Energy of Adsorption (Δg) per Unit Area of the Two Polymorphs at Two Reference Temperatures of 300 and 350 K^a

| | packing density (10^{14} cm^{-2}) | Δh_{eff} ($\mu\text{J cm}^{-2}$) | $-\Delta s$ (@300 K) ($\mu\text{J cm}^{-2}$) | $-\Delta s$ (@350 K) ($\mu\text{J cm}^{-2}$) | $\Delta g = \Delta h_{\text{eff}} - T\Delta s$ (@300 K) ($\mu\text{J cm}^{-2}$) | $\Delta g = \Delta h_{\text{eff}} - T\Delta s$ (@350 K) ($\mu\text{J cm}^{-2}$) |
|--|--|---|---|---|--|--|
| chicken-wire (without solvent coadsorption) | 0.23 | -5.8 | +3.9 | +4.6 | -1.9 | -1.2 |
| chicken-wire (with $8 \times \mathbf{9A}$ solvent molecules coadsorbed) | 0.23 (BTB) 0.90 ($\mathbf{9A}$) | -23.7 | +14.6 | +17.1 | -9.1 | -6.6 |
| row | 0.87 | -18.5 | +14.8 | +17.3 | -3.7 | -1.2 |

^a Stabilizing enthalpic contributions are assumed to be temperature independent. Δh_{eff} refers to values derived from molecular mechanics calculations; Δs is calculated using eqs 1 and 2.

them energetically inferior as compared to the double hydrogen bonds of the chicken-wire structure. Based on STM-derived unit cell parameters, the packing densities of the polymorphs amount to 0.23 molecules nm^{-2} for the chicken-wire and 0.87 molecules nm^{-2} for the row structure, respectively.

Thermodynamics. In the following we discuss whether the experimentally observed structure always represents the thermodynamically most stable polymorph at the respective temperature, i.e., the polymorph that yields the lowest Gibbs free energy. For monolayer self-assembly at the liquid–solid interface the whole system including the solution needs to be considered to evaluate all thermodynamic contributions. From an entropic point of view, adsorption and self-assembly of molecules from solution is unfavorable because molecules lose degrees of freedom and thus entropy upon aggregation. On the other hand, favorable enthalpic contributions arise from attractive molecule–substrate and molecule–molecule interactions. A balance of both contributions (entropy and enthalpy) steers self-assembly, and renders it a thermodynamically driven process. In order to gain insight into the thermodynamic properties of the two BTB polymorphs, the various entropic contributions were partitioned and estimated according to a method proposed by Whitesides and co-workers and similarly employed by Krissinel and Henrick.^{34,35} When molecules assemble into supramolecular complexes, the entropic penalty mainly arises from losses in translational, rotational, conformational, and vibrational entropy, $\Delta S_{\text{tot}} = \Delta S_{\text{trans}} + \Delta S_{\text{rot}} + \Delta S_{\text{conf}} + \Delta S_{\text{vib}}$. Since BTB molecules do not possess significant internal degrees of freedom, conformational entropy losses can be neglected. Because of their relatively high energy in comparison to thermal energy, intramolecular vibrations do not significantly contribute to the entropy and can also be neglected.³⁴ The following equations provide reasonable estimates for the two relevant entropy terms for soluted molecules:

$$S_{\text{trans}} = R \ln [c^{-1} (2\pi m k_{\text{B}} T e^{5/3} / h^2)^{3/2}] \quad (1)$$

$$S_{\text{rot}} = R \ln [\pi^{1/2} / \gamma (8\pi^2 k_{\text{B}} T e / h^2)^{3/2} (I_1 I_2 I_3)^{1/2}] \quad (2)$$

Here, h is Planck's constant, k_{B} the Boltzmann constant, R the gas constant, and T the absolute Temperature, while e is Euler's number, m is the solute's mass, and c is the solute

concentration. Furthermore, γ considers the symmetry of the molecule, and I_1 , I_2 , and I_3 are its principle moments of inertia. In order to avoid overestimation of translational entropy, concentrations are related to the free volume of the solvent as proposed by Whitesides and co-workers. The free volume of a solvent can be estimated by the hard cube approximation³⁴ and is significantly smaller than the actual volume, e.g., $\sim 32 \text{ mL}$ for 1 L of heptanoic acid. It is assumed that upon adsorption molecules entirely lose their translational and rotational entropy, consequently eqs 1 and 2 allow estimating the entropic loss for adsorption of a single BTB molecule from solution. In the same manner, the entropic losses for coadsorbed solvent molecules can be estimated.

In order to compare the entropic costs for the two polymorphs, contributions from rotational and translational entropy were calculated assuming saturated solutions. For all three solvents, the entropic cost for BTB adsorption has a similar value of $-0.190 \text{ kJ mol}^{-1} \text{ K}^{-1}$ for translational and $-0.152 \text{ kJ mol}^{-1} \text{ K}^{-1}$ for rotational entropy. In order to estimate the entropic cost per unit area for self-assembly of a pure monolayer of the respective polymorph, the total entropy loss of $-0.342 \text{ kJ mol}^{-1} \text{ K}^{-1}$ was then combined with STM-derived molecular packing densities. Numbers for the entropic contribution to the free energy at 300 K (room temperature) and 350 K respectively are provided in Table 1. It can be clearly seen that the row structure is entropically far less favorable than the chicken-wire structure, due to its 3.8-fold higher packing density. The entropic cost becomes even more pronounced at elevated temperatures. However, the situation is altered when solvent coadsorption within the cavities of the chicken-wire structure is taken into account. Although coadsorbed solvent molecules have not been directly observed in this study, probably due to their low stabilization energy and short residence times, coadsorption of guest molecules within open-pore networks was observed experimentally^{14,16,18,21} and has been recognized as an important stabilizing contribution.^{12,13,19,33,36} For instance, coadsorption of coronene as molecular guest in the cavities of an open-pore dehydrobenzoannulene polymorph stabilizes this host–guest network thermodynamically in comparison to the densely packed polymorph.³⁶

In the present case, up to eight solvent molecules ($\mathbf{8A}$ or $\mathbf{9A}$) can be coadsorbed in each cavity of the chicken-wire structure

(34) Mammen, M.; Shakhnovich, E. I.; Deutch, J. M.; Whitesides, G. M. *J. Org. Chem.* **1998**, *63* (12), 3821–3830.

(35) Krissinel, E.; Henrick, K. *J. Mol. Biol.* **2007**, *372* (3), 774–797.

(36) Furukawa, S.; Tahara, K.; De Schryver, F. C.; Van der Auweraer, M.; Tobe, Y.; De Feyter, S. *Angew. Chem., Int. Ed.* **2007**, *46* (16), 2831–2834.

(cf. Supporting Information Figure S4). Coadsorbed **9A** solvent molecules cause a translational entropy loss of $-0.102 \text{ kJ mol}^{-1} \text{ K}^{-1}$ and a rotational entropy loss of $-0.132 \text{ kJ mol}^{-1} \text{ K}^{-1}$. Comparison of these values with the entropic losses for BTB adsorption points out that the total entropic cost increases more steeply with the number of adsorbed molecules rather than with the size and molecular weight of adsorbates. Since solvent coadsorption drastically increases the number of adsorbed molecules, the associated entropic cost of the chicken-wire structure becomes significantly enhanced. The relatively large entropic contributions to Gibbs free energy of both solute and solvent molecules (cf. Table 1) underline the fact that entropy considerations have to be taken into account for thermodynamics of monolayer self-assembly.

A quantitative comparison of the stabilizing enthalpic contributions between the two polymorphs is more difficult because different types of interactions (i.e., hydrogen bonds vs van der Waals and π - π interactions) need to be compared. Molecular mechanics (MM) simulations are well suited to evaluate the energetics of van der Waals interactions. However, standard force fields seriously underestimate the strength of cyclic resonance stabilized hydrogen bonds.³⁷ In order to make a valid comparison of binding enthalpies, MM results using the Dreiding force field for the chicken-wire polymorph are combined with the experimentally and theoretically well-established binding enthalpy of -60 kJ mol^{-1} for the 2-fold O-H \cdots O hydrogen bond between two carboxylic groups.³⁸

According to the proposed method, the average binding enthalpy of BTB molecules in the chicken-wire structure amounts to -332 kJ mol^{-1} . This value originates from the combination of a MM-derived molecule-substrate interaction of -242 kJ mol^{-1} with the binding enthalpy due to intermolecular hydrogen bonds of $-90 \text{ kJ mol}^{-1} = 3 \times 0.5 \times -60 \text{ kJ mol}^{-1}$. In the chicken-wire structure all three carboxylic groups of each molecule form 2-fold intermolecular hydrogen bonds, while the factor 0.5 corrects for overcounting of pairwise interactions.

The row structure is predominantly stabilized by van der Waals interactions, and the average binding enthalpy was evaluated by MM computations, which yield a value of -308 kJ mol^{-1} (cf. Supporting Information for details). As anticipated, the adsorbate-substrate binding is inferior in the row structure (-176 kJ mol^{-1}), but due to the high packing density and mutual molecular arrangement the intermolecular van der Waals and π - π interactions are superior.

Last, the stabilizing effect of coadsorbed solvent molecules within the cavities of the chicken-wire structure is calculated. Coadsorption of eight **9A** solvent molecules in one cavity of the chicken-wire structure yields an enthalpic contribution of -940 kJ mol^{-1} per unit cell (cf. Supporting Information for a structural model and details of the calculation).

Binding enthalpies obtained from the above methods refer to isolated, geometry-optimized molecules under vacuum. Yet, the appropriate reference state for these considerations is dissolved and solvated solute molecules.³⁹ Solvation enthalpies lower the effective binding enthalpies significantly. In comparison to experiments under ultra-high-vacuum conditions,

desorption barriers are substantially lower at the solid-liquid interface, which gives rise to an effective adsorption-desorption equilibrium even for comparatively large compounds.^{13,18,36} Corrections of the adsorption enthalpy due to solvation were included by assuming that the interaction of dissolved solute molecules in solution is governed by intermolecular solvent-solute or solute-solute hydrogen bonds, where each of the three carboxylic groups of BTB forms a 2-fold hydrogen bond with a binding enthalpy of -60 kJ mol^{-1} . Consequently, solvation lowers the effective binding enthalpy of each molecule by at least $+180 \text{ kJ mol}^{-1}$.

On the basis of the estimates of both entropic cost and enthalpic gain, the free energies of adsorption of each polymorph were evaluated for two reference temperatures. Since in all experiments the surface coverage is close to unity, we will refer to Gibbs free energy of adsorption per unit area A : $\Delta g = \Delta G/A = \Delta H/A - T\Delta S/A = \Delta h - T\Delta s$ (note that Δh and Δs , i.e., enthalpy and entropy changes per unit area upon monolayer self-assembly, are both negative). The results are summarized in Table 1. For the chicken-wire polymorph two scenarios were considered, with and without coadsorption of solvent (**9A**).

For room temperature the figures in Table 1 indicate that the row structure is thermodynamically favored over the pure chicken-wire polymorph, i.e., when solvent coadsorption is neglected. However, despite its large entropic cost, solvent coadsorption still stabilizes the chicken-wire polymorph at room temperature and even renders this bimolecular monolayer the thermodynamically most stable polymorph in **9A**. At elevated temperature, the free energy gain associated with self-assembly of a monolayer row structure becomes comparable to the chicken-wire structure without coadsorbed solvent due to the increased entropic cost of the more densely packed polymorph. On the basis of these estimates of Δg , the following explanation for the reversible phase transition is proposed: With the aid of solvent coadsorption, the chicken-wire polymorph is the thermodynamically most stable polymorph at room temperature in **9A**. Upon increasing the temperature, coadsorbed solvent molecules start to desorb first, while the chicken-wire network is still stable. Coadsorbed solvent molecules are less tightly bound than BTB molecules, as the latter—due to their size—have increased interaction with the substrate and are additionally stabilized by six hydrogen bonds. Once the chicken-wire structure lacks the stabilizing contribution from solvent coadsorption, the free energy of adsorption of the row structure becomes comparable, giving rise to the phase transition. The proposed model also consistently explains the solvent dependence of the transition temperature. The binding enthalpies of fatty acid molecules on graphite increase approximately linearly with their aliphatic chain length. Accordingly, the desorption temperature of **8A** solvent molecules is lower than that of **9A** molecules. In the thermodynamic competition between chicken-wire and row structure, easier desorption leads to a lower transition temperature in **8A** than in **9A** solutions or a transition temperature even below room temperature as observed for **7A**.

Although in the present case a molecule-based evaluation of thermodynamic quantities yields the correct trends, a word of caution is appropriate. The Gibbs free energies of adsorption and the relative thermodynamical stabilities of these polymorphs sensitively depend on the subtle balance of adsorbate-adsorbate, adsorbate-substrate, and solute-solvent interactions. A quantitative thermodynamic discussion of the complex situation of monolayer self-assembly at the liquid-solid interface is challenging primarily because of inaccuracies in the evaluation of

(37) Martsinovich, N.; Troisi, A. *J. Phys. Chem. C* **2010**, *114* (10), 4376–4388.

(38) Neuheuser, T.; Hess, B. A.; Reutel, C.; Weber, E. *J. Phys. Chem.* **1994**, *98* (26), 6459–6467.

(39) Meier, C.; Landfester, K.; Künzel, D.; Markert, T.; Gross, A.; Ziener, U. *Angew. Chem., Int. Ed.* **2008**, *47* (20), 3821–3825.

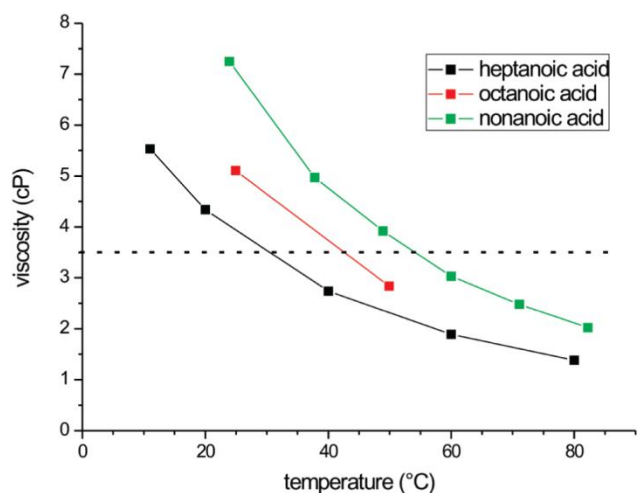


Figure 4. Viscosities of pure heptanoic (7A), octanoic (8A), and nonanoic acid (9A) as a function of temperature,⁴¹ depicting the inverse dependence of viscosity on temperature. The dashed line indicates a value of 3.5 cP.

both entropic and enthalpic contributions, but also due to hardly assessable contributions, as for instance from solvation. Also, for solvent coadsorption precise structural data are not available.

Nevertheless, established methods to estimate entropic costs and evaluation of binding energies based on molecular mechanics and experimental values for hydrogen bond energies allow at least a semiquantitative evaluation of Gibbs free energies of adsorption of competing monolayer polymorphs. Although the exact prediction of crossing points as a function of concentration or temperature is hardly possible, at least a qualitative understanding of trends can be obtained. On the other hand, kinetic effects might also play an important role for monolayer self-assembly. From basic considerations, we conclude that the adsorption rate of solute molecules is proportional to c/η , where c stands for the solute concentration and η for the solvent viscosity (cf. Supporting Information). Interestingly, the viscosities of all three solvents in this study are considerably different at room temperature and crucially depend on temperature as depicted in Figure 4. Also, the viscosities of 7A, 8A, and 9A, and thus the adsorption rate, correlate inversely with temperature and vary appreciably within the relevant temperature interval.

Further interesting aspects are topological and epitaxial similarities between chicken-wire and row structure: As illustrated in Figure 5, STM topographs of both coexisting polymorphs clearly show a structurally well-defined heterointerface. Moreover, the direction of the rows is aligned with the cavities of the chicken-wire polymorph. Both facts indicate that a morphological transition from chicken-wire to row polymorph might be initiated by filling of empty cavities of the chicken-wire structure with excess BTB molecules. Under conditions where the row structure becomes thermodynamically favored, this phase transition can also be understood as a cross nucleation event, i.e., a special case of heterogeneous nucleation where a thermodynamically more

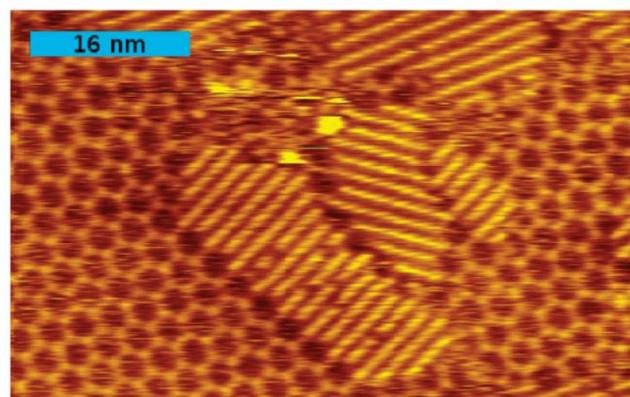


Figure 5. STM topograph of a BTB monolayer in nonanoic acid (9A) after heating and cooling. Patches of the row structure are observable and coexist with the chicken-wire structure. The lower left phase boundary exemplifies a general observation: the rows are aligned with the chicken-wire structure. Every other row is connected to molecules from the chicken-wire polymorph; rows in between end in cavities.

stable polymorph nucleates on a preexistent metastable modification.⁴⁰

De Feyter et al. discussed and modeled the concentration dependence of bimorphic monolayer self-assembly in detail.¹⁹ Similarly, by means of a slightly different model, Meier et al. conclude that densely packed polymorphs become thermodynamically preferred at higher solute concentrations.³³ In both cases, at low concentrations, an open-pore structure is favored over a densely packed structure, just as in the present case for BTB in 7A. The thermodynamic model proposed by de Feyter et al. also includes a temperature-dependent term, which results in a diminished coverage ratio of open-pore to densely packed polymorph at elevated temperatures. Consequently, their model seems generally applicable and can also explain the temperature-dependent phase transition, provided that the chemical potential of BTB molecules in the row structure is sufficiently large.

Conclusions and Outlook

By means of STM reversible temperature-driven phase transitions have been observed for BTB monolayers at the liquid–solid interface. Carboxylic acids were used as solvents, and transition temperatures were found to depend on type of solvent and concentration. The two polymorphs differ significantly in packing density, arrangement of molecules, and intermolecular interactions. Both morphologies are known, and analogues have previously been reported for other tricarboxylic acids.^{14,15} Estimates of the entropic cost and enthalpic gain upon monolayer self-assembly of both polymorphs suggest that a thermodynamic explanation for the phase transition in view of Gibbs free energy of adsorption is only appropriate when solvent coadsorption is taken into account. Solvent coadsorption within the cavity voids of the nanoporous chicken-wire structure has a high entropic cost because the number of adsorbed molecules is large. However, this entropic cost is still outweighed by the associated enthalpic gain. In order to explain the phase transition, we propose that desorption of coadsorbed solvent molecules

(40) Yu, L. *CrystEngComm* **2007**, *9* (10), 847–851.

(41) Landolt-Börnstein *Tabellenwerk Zahlenwerte und Funktionen aus Physik, Chemie, Astronomie, Geophysik und Technik*; Springer: Berlin, **2002**; Vol. 18 B.

eventually destabilizes the chicken-wire polymorph and leads to the emergence of the row structure. This purely thermodynamic model inherently explains the reversibility of the phase transition. However, the kinetics of adsorption and desorption can also determine the experimental observations. For instance, the row structure patches that were occasionally observed in **9A** after the first heat-cool cycle might be attributed to a slow desorption kinetics of BTB molecules in the row structure. Mostly because of the strong temperature dependence of solvent viscosity, also the adsorption kinetics changes significantly with temperature.

There is one particularly intriguing aspect to the phase transition from chicken-wire to row structure: it closes supramolecular cavities. This effect may be utilized for the controlled release of molecular guests with conceivable medical and life-science applications. With this in mind, it would be highly interesting to explore whether adsorption

of deliberate molecular guests other than coadsorbed solvent molecules within the pores of the chicken-wire structure hampers the phase transition, thus leading to increased transition temperatures or even suppression of the phase transition.

Acknowledgment. Financial support by the Deutsche Forschungsgemeinschaft (Sonderforschungsbereich 486, FOR 516), the Bayerische Forschungsförderung, and the Nanosystems Initiative Munich (NIM) is gratefully acknowledged.

Supporting Information Available: Experimental details, kinetic considerations, additional STM topographs, and details of molecular mechanics simulations. This material is available free of charge via the Internet at <http://pubs.acs.org>.

JA908919R

Supporting Information

Reversible phase transitions in monolayer self-assembly at the liquid-solid interface –
temperature controlled opening and closing of nanopores

Rico Gutzler^{*†}, *Thomas Sirtl*[†], *Jürgen F. Dienstmaier*[†], *Kingsuk Mahata*[‡], *Wolfgang M.
Heckl*[#], *Michael Schmittel*[‡], and *Markus Lackinger*^{*†}

[†] Department of Earth and Environmental Sciences and Center for NanoScience (CeNS),
Ludwig-Maximilians-University, Theresienstrasse 41, 80333 Munich, Germany; [‡] Center of
Micro and Nanochemistry and Engineering, Organische Chemie I, University Siegen, Adolf-
Reichwein-Strasse 2, 57068 Siegen, Germany; [#] Deutsches Museum, Museumsinsel 1, 80538
Munich and Department of Physics, TUM School of Education, Technical University
Munich, Schellingstrasse 33, 80333 Munich, Germany

1. Experimental details
2. Kinetic considerations
3. Additional STM topographs
4. Details on molecular mechanics + additional results
5. References

1. Experimental details

All solvents were used as received from Sigma Aldrich and 1,3,5-tris(4-carboxyphenyl)benzene was synthesized according to literature-known procedures.¹ Solutions were prepared by dissolving BTB until saturation in the respective carboxylic acid. Subsequently, solutions were centrifuged in order to avoid supersaturation effects. Droplets of ~2.5 μ L saturated solution were applied onto the basal plane of freshly cleaved highly oriented pyrolytic graphite (HOPG). STM experiments were carried out with a home-built STM driven by RHK control electronics. The STM tip was immersed into solution during image acquisition. All images were recorded in constant current mode and were processed by line wise levelling only, except for some topographs recorded in 8A where a Gaussian filter was applied. For details on the heatable sample stage and STM measurements at elevated temperature cf. Walch et al.²

BTB solubilities in all solvents were determined by UV-Vis absorption spectroscopy conducted with a USB4000 UV-Vis spectrometer from Ocean Optics.

2. Kinetic considerations

Two main kinetic factors influence monolayer formation on surfaces: the adsorption rate of molecules on the surface, the flux F , and transport of adsorbates across the surface, i.e. surface diffusion as described by the diffusivity D . When the ratio of surface diffusion to adsorption rate F/D is small, the resulting surface structure represents the thermodynamic equilibrium. On the other hand, when the ratio F/D becomes large, kinetic effects become increasingly important.

According to Fick's laws of diffusion, the flux F of dissolved molecules impinging on a surface is given by:

$$F = -d (\partial c / \partial z), \quad (1)$$

where d is the bulk diffusivity in solution (not to be confused with the surface diffusivity D), c the concentration in solution and z the spatial coordinate perpendicular to the surface.

The chemical potential μ of an ideal solution as a function of temperature T and concentration c is given by:

$$\mu = \mu_0 + RT \ln c \quad (2)$$

with R being the gas constant and μ_0 the chemical potential under standard conditions.

Accordingly equation (1) can be rewritten as:

$$F = -dc / RT (\partial \mu / \partial z). \quad (3)$$

The flux F of molecules impinging on the surface is thus driven by a gradient in the chemical potential perpendicular to the surface. This gradient is build up by a difference between chemical potential on the surface with respect to the bulk (solution) and is non-zero until the monolayer growth has been completed. In thermodynamical equilibrium, when the gradient is zero, the net flux F likewise becomes equal to zero. As a coarse approximation, the bulk diffusivity d , i.e. the mobility of solute molecules in solution, can be approximated by the Stokes-Einstein equation:

$$d = k_B T / 6\pi r \eta(T). \quad (4)$$

Consequently, the flux becomes:

$$F \propto - c / \eta(T) (\partial\mu / \partial z). \quad (5)$$

In equations (4) and (5), r is the radius of a spherical particle and $\eta(T)$ the solvent viscosity, which in the case of fatty acids strongly depends on temperature in the range 25 °C to 50 °C. From equation (5), the ratio solute concentration to solvent viscosity c/η is identified as the critical parameter for the flux F .

3. Additional STM Topographs

Concentration dependence (heptanoic acid):

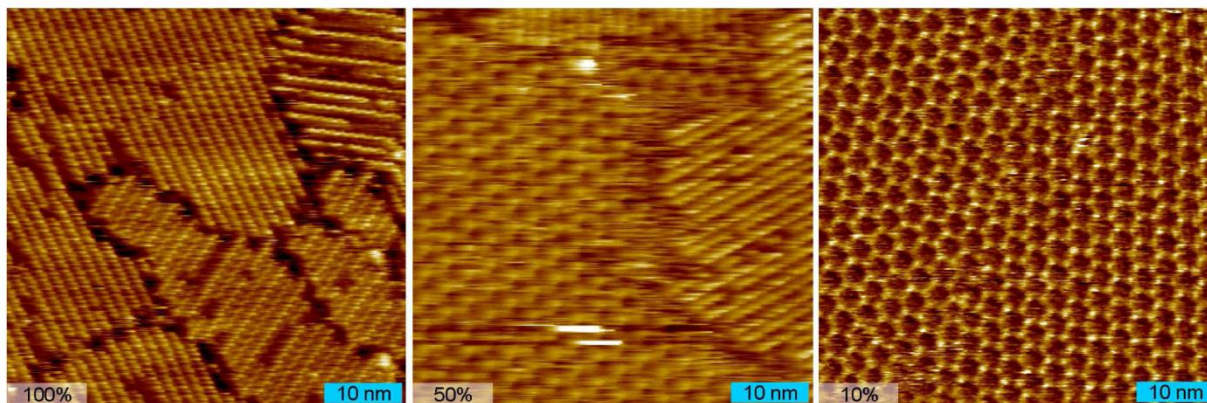


Fig. S1. Left: Saturated solution of BTB in heptanoic acid ($V_{\text{bias}} = 0.80$ V, $I_{\text{T}} = 77$ pA). Exclusively the row structure is observed. Center: 50% saturated solution ($V_{\text{bias}} = 0.84$ V, $I_{\text{T}} = 90$ pA).; row and chickenwire structure coexist. Right: 10% saturated solution ($V_{\text{bias}} = 0.96$ V, $I_{\text{T}} = 73$ pA); almost solely the chickenwire structure is formed.

Intermediate temperatures (nonanoic acid)

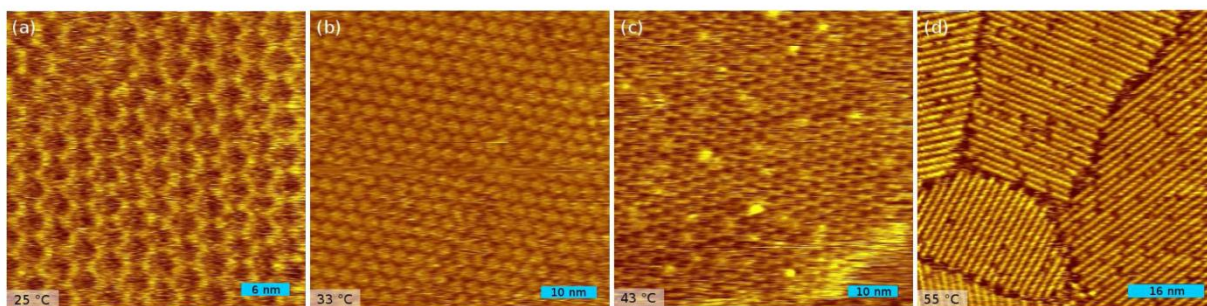


Fig. S2: STM topographs of BTB in nonanoic acid for intermediate temperatures: (a) at room temperature ($V_{\text{bias}} = 1.05 \text{ V}$, $I_{\text{T}} = 90 \text{ pA}$), (b) at $\sim 33 \text{ }^\circ\text{C}$ ($V_{\text{bias}} = 1.05 \text{ V}$, $I_{\text{T}} = 57 \text{ pA}$), (c) at $\sim 43 \text{ }^\circ\text{C}$ ($V_{\text{bias}} = 1.05 \text{ V}$, $I_{\text{T}} = 95 \text{ pA}$), and (d) at $\sim 55 \text{ }^\circ\text{C}$ ($V_{\text{bias}} = 1.04 \text{ V}$, $I_{\text{T}} = 69 \text{ pA}$). At temperatures below the transition temperature only the chickenwire polymorph can be observed.

4. Details on molecular mechanics + additional results

Molecular mechanics based on the Dreiding force field as implemented in the Cerius² (Version 4.5, MSI) software package was utilized for a structural refinement and estimation of binding energies. Periodic boundary conditions were employed with the experimental unit cells as constraints. The graphite substrate was approximated by two layers and atomic positions in the second layer were fixed. Values for the unit cell parameters were deduced from split images,³ where one part of the image depicts the adsorbate layer and in the other part the graphite substrate was atomically resolved. Molecules were arranged on the surface without further constraints. An energy difference of < 0.001 kcal/mol and a force difference < 0.5 kcal/mol/Å between single steps served as convergence criteria. For the hexagonal structure, nine unit cells were used as the basic building unit (cell parameters in matrix notation referring to the graphite lattice vectors: $U = (21 \ 45 \ 0)$ $V = (45 \ 24 \ 0)$). The basic unit for the row structure consisted of eight unit cells ($U = (4 \ 12 \ 0)$ $V = (30 \ 10 \ 0)$). Binding energies were calculated by extracting one molecule from the optimized structure and performing a single point energy calculation.

The average binding enthalpy $\Delta H_{\text{BTB-row}}$ of a single BTB molecule in the row structure was evaluated in the following way:

(1) Evaluate energy ΔE_{total} to remove a single BTB molecule from the row structure:

- optimize complete structure (including all BTB molecules on the surface) $\rightarrow E_1$
- delete one molecule from the structure and calculate energy (without further geometry optimization) $\rightarrow E_2$
- calculate energy of a single geometry optimized BTB molecule $\rightarrow E_3$
- $\Delta E_{\text{total}} = E_1 - E_2 - E_3$

(2) Evaluate binding energy of a single BTB molecule in the row structure

to graphite $\Delta E_{\text{mol-sub}}$:

- optimize complete row structure (including all BTB molecules on the surface)
- delete all molecules from the structure except one and calculate energy (no geometry optimization in between) $\rightarrow E_1$
- calculate energy of pristine graphite, i.e. without BTB molecules adsorbed $\rightarrow E_2$
- calculate energy of a single geometry optimized BTB molecule $\rightarrow E_3$
- $\Delta E_{\text{mol-sub}} = E_1 - E_2 - E_3$

(3) Average binding enthalpy $\Delta H_{\text{BTB-row}}$ of BTB molecules in the row structure:

- evaluate average intermolecular binding energy $\Delta E_{\text{mol-mol}}$:

$$\Delta E_{\text{mol-mol}} = (\Delta E_{\text{total}} - \Delta E_{\text{mol-sub}}) / 2$$

since pairwise interactions are equally shared by two bonding partners, only 50% count for the average intermolecular binding energy per molecule

- $\Delta H_{\text{BTB-row}} = \Delta E_{\text{mol-mol}} + \Delta E_{\text{mol-sub}}$

Binding enthalpy ΔH_{solv} of coadsorbed solvent molecules ΔH_{coads} :

- optimize full BTB network with one cavity filled with eight 9A molecules $\rightarrow E_1$
- calculate energy of empty, geometry optimized BTB network $\rightarrow E_2$
- calculate energy of one single optimized 9A molecule $\rightarrow E_3$
- $\Delta H_{\text{solv}} = E_1 - E_2 - 8 \times E_3$

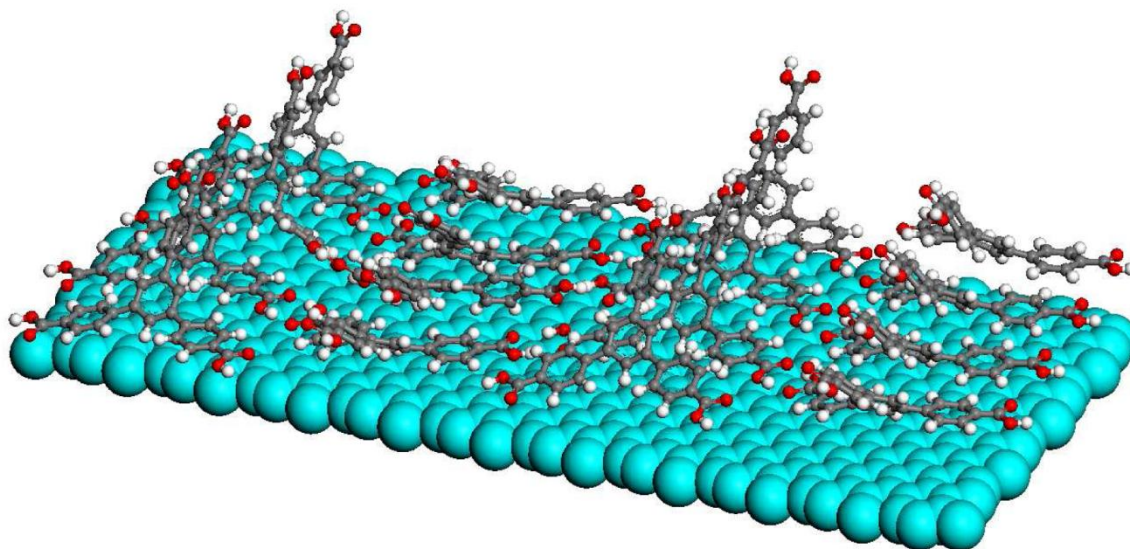


Fig. S3: Inclined view of a ball-and-stick model of the row structure, eight unit cells are depicted. Adjacent rows are tilted in opposite directions. (cyan: graphite substrate, grey: carbon, white: hydrogen, red: oxygen)

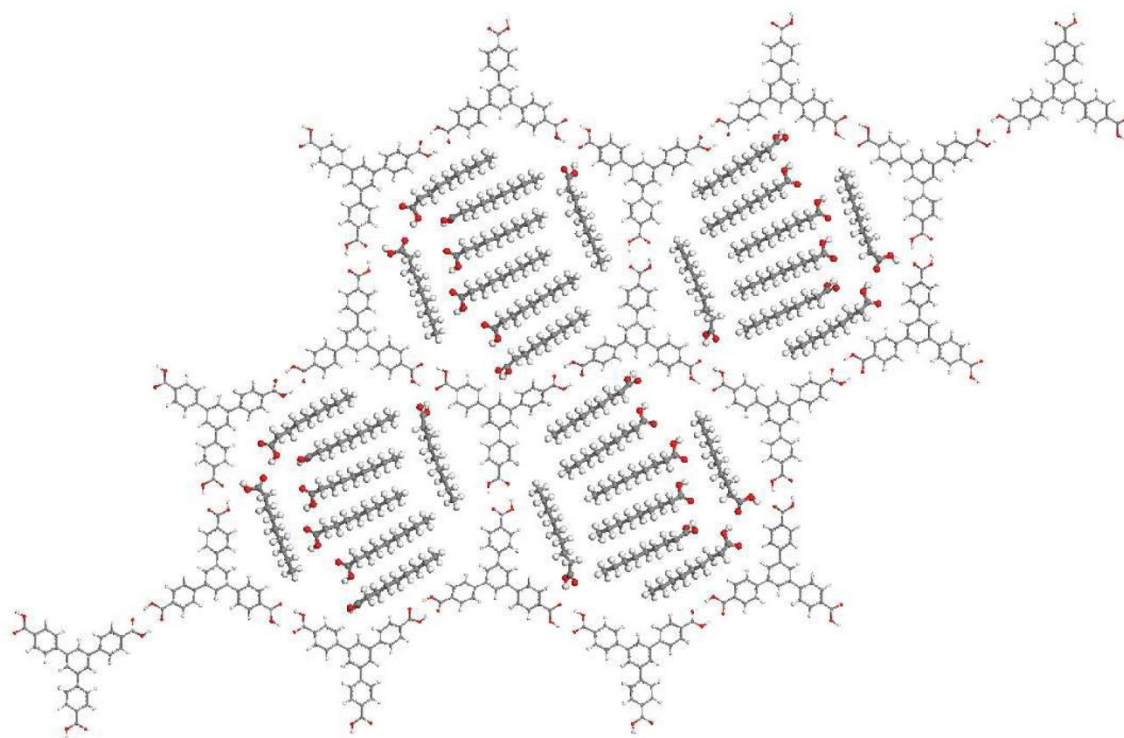


Fig. S4: Ball-and-stick model of the chickenwire structure with coadsorbed nonanoic acid molecules. 8 solvent molecules fit within one cavity;

5. References

1. Weber, E.; Hecker, M.; Koepp, E.; Orlia, W.; Czugler, M.; Csoregh, I., *J. Chem. Soc., Perkin Trans. 2* **1988**, (7), 1251-1257.
2. Walch, H.; Maier, A. K.; Heckl, W. M.; Lackinger, M., *J. Phys. Chem. C* **2009**, 113 (3), 1014-1019.
3. Lackinger, M.; Heckl, W. M., *Langmuir* **2009**, 25 (19), 11307-11321.

On the Scalability of Supramolecular Networks – High Packing Density vs Optimized Hydrogen Bonds in Tricarboxylic Acid Monolayers

Jürgen F. Dienstmaier,^{*,†} Kingsuk Mahata,[‡] Hermann Walch,[†] Wolfgang M. Heckl,^{§,⊥}
Michael Schmittl,[‡] and Markus Lackinger^{*,†}[†]Department for Earth- and Environmental Sciences and Center for NanoScience (CeNS), Ludwig-Maximilians-University, Theresienstrasse 41, D-80333 Munich, Germany, [‡]Center of Micro and Nanochemistry and Engineering, Organische Chemie I, Universität Siegen, Adolf-Reichwein-Strasse 2, D-57068 Siegen, Germany, [§]Deutsches Museum, Museumsinsel 1, D-80538 Munich, Germany, and [⊥]Department of Physics, TUM School of Education, Technical University Munich, Schellingstrasse 33, D-80333 Munich, Germany

Received October 21, 2009

We present a scanning tunneling microscopy (STM) based study of 1,3,5-tris[4'-carboxy(1,1'-biphenyl-4-yl)]benzene (TCBPB) monolayers at the liquid–solid interface. In analogy to smaller aromatic 3-fold symmetric tricarboxylic acids, this compound was aimed to yield two-dimensional nanoporous networks with large cavities. Depending on the solute concentration, three crystallographically distinct phases with pores of different size and shape were observed on graphite (001) with heptanoic acid as solvent. All three phases have the same dimer motif as basic building block in common. Yet, as opposed to other carboxylic acid assemblies, these dimers are not interconnected by 2-fold O–H···O hydrogen bonds as anticipated, but by two energetically inferior C–H···O hydrogen bonds. Instead of the common head-to-head arrangement, this bonding pattern results in displaced dimers, which allow for higher packing density, and due to their lower symmetry give rise to chiral polymorphs. In accordance with studies of comparable systems, a positive correlation between solute concentration and average surface packing density is identified and rationalized by thermodynamic arguments.

1. Introduction

Scalability of structures is an interesting and intriguing aspect of material science, and isoreticular metal organic frameworks (IRMOFs) represent a particularly nice and well-known example thereof.¹ A widely open and definitely system-specific question is to what extent building blocks can be scaled up, while the underlying structure is still retained. In the case of porous systems, up-scaling of building blocks may lead to increased pore size which opposes nature's affinity for dense packing. The strength of directional interactions as hydrogen or coordination bonds remains nearly independent of molecular size, whereas the omnipresent van der Waals interactions gain in magnitude with increasing sizes of molecules. As a consequence, up-scaling definitely alters the balance of interactions. For that very reason, the existence of an upper limit for the pore size is predicted for surface supported 2D nanoporous supramolecular systems.² The present study aims to expand the pore size as compared to those of previously studied hexagonal open pore networks formed by 3-fold symmetric aromatic tricarboxylic acids. The smallest representative is trimesic acid (TMA, Figure 1a) which consists of a central phenyl ring, symmetrically substituted with three carboxylic groups. Already for this comparatively small building block, different polymorphic structures were revealed at the liquid-

graphite interface depending on the solvent applied.^{3,4} Moreover, a whole series of systematically varying TMA monolayer structures with increasing packing density was reported on Au(111).⁵ These observations already indicate that self-assembly is not exclusively dictated by the building block, but depends to a large extent on the type of surface, conditions, and environment.^{3,6–8} This apparent drawback, however, can be turned into the advantage of having a handle on self-assembly, provided that underlying processes are understood on a molecular level. The next larger tricarboxylic acid investigated is 1,3,5-benzenetricarboxylic acid (BTB, Figure 1b), where three phenyl rings have been added as conformationally rigid spacers between the central phenyl ring and each peripheral carboxylic group. Similar to TMA, BTB also exhibits polymorphism both at the liquid–solid interface⁷ and under vacuum conditions.⁹ Moreover, for BTB, reversible temperature dependent phase transitions have been observed at the liquid–solid interface, and are explained by a thermodynamic model.¹⁰ With phenylethyne units as even larger spacers (Figure 1c), either complete methylation of the inner phenyl ring or use of aprotic aromatic solvents were required to obtain planar adsorption of molecules followed by self-assembly into hexagonal networks.¹¹ Herein, we would like to present our

*Corresponding authors. E-mail: (M.L.) markus@lackinger.org.

(1) Doonan, C. J.; Morris, W.; Furukawa, H.; Yaghi, O. M. *J. Am. Chem. Soc.* **2009**, *131*, 9492.

(2) Weber, U. K.; Burlakov, V. M.; Perdigão, L. M. A.; Fawcett, R. H. J.; Beton, P. H.; Champness, N. R.; Jefferson, J. H.; Briggs, G. A. D.; Pettifor, D. G. *Phys. Rev. Lett.* **2008**, *2008*, 156101.

(3) Lackinger, M.; Griessl, S.; Heckl, W. M.; Hietschold, M.; Flynn, G. W. *Langmuir* **2005**, *21*, 4984.

(4) MacLeod, J. M.; Ivasenko, O.; Perepichka, D. F.; Rosei, F. *Nanotechnology* **2007**, *18*, 424031.

(5) Ye, Y.; Sun, W.; Wang, Y.; Shao, X.; Xu, X.; Cheng, F.; Li, J.; Wu, K. *J. Phys. Chem. C* **2007**, *111*, 10138.

(6) Yang, Y.; Wang, C. *Curr. Opin. Colloid. Interface Sci.* **2008**, *14*, 135.

(7) Kampschulte, L.; Lackinger, M.; Maier, A.; Kishore, R. S. K.; Griessl, S.; Schmittl, M.; Heckl, W. M. *J. Phys. Chem. B* **2006**, *110*, 10829.

(8) Leigh, D. F.; Nörenberg, C.; Cattaneo, D.; Owen, J. H. G.; Porfyrikis, K.; Li Bassi, A.; Ardavan, A.; Briggs, G. A. D. *Surf. Sci.* **2007**, *601*, 2750.

(9) Ruben, M.; Payer, D.; Landa, A.; Comisso, A.; Gattinoni, C.; Lin, N.; Collin, J.; Sauvage, J.; De Vita, A.; Kern, K. *J. Am. Chem. Soc.* **2006**, *128*, 15644.

(10) Gutzler, R.; Sirtl, T.; Dienstmaier, J. F.; Mahata, K.; Heckl, W. M.; Schmittl, M.; Lackinger, M. *J. Am. Chem. Soc.* **2010**, *132*, 5084.

(11) Gutzler, R.; Lappe, S.; Mahata, K.; Schmittl, M.; Heckl, W. M.; Lackinger, M. *Chem. Commun.* **2009**, *2009*, 680.

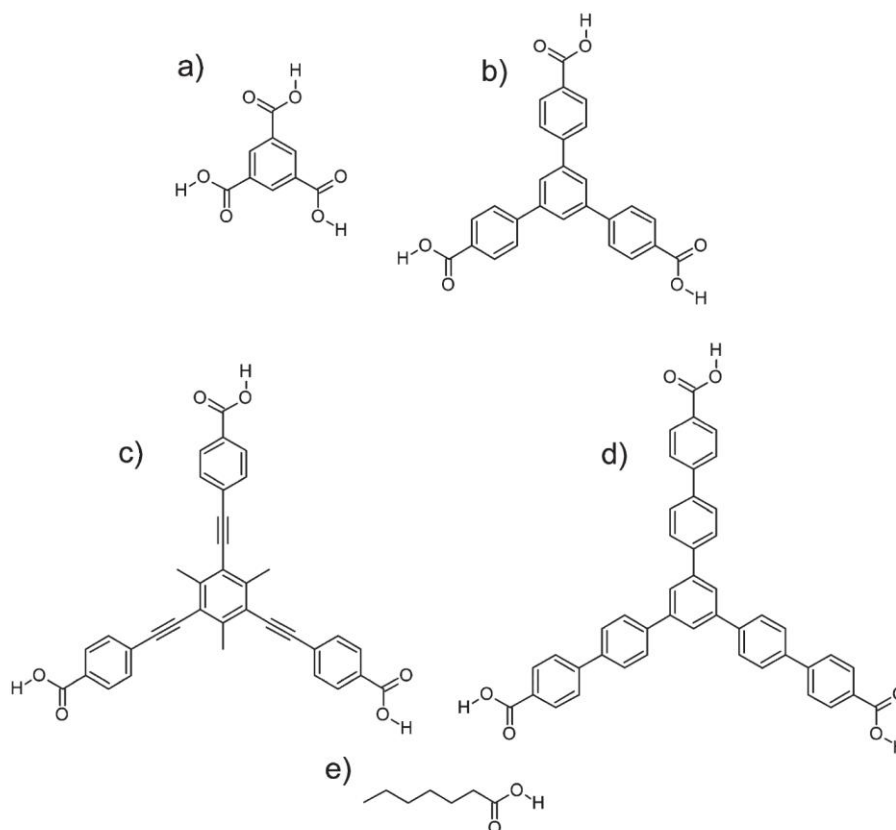


Figure 1. Chemical structures of tricarboxylic acids investigated in the present and previous studies: (a) trimesic acid (TMA), (b) 1,3,5-benzenetribenzoic acid (BTB), (c) (4-{2-[3,5-bis[2-(4-carboxyphenyl)-1-ethynyl]-2,4,6-trimethyl-phenyl]-1-ethynyl})-1,3,5-tris[4'-carboxy(1,1'-biphenyl-4-yl)]benzoic acid (TCBPB), and (e) heptanoic acid, utilized as solvent.

results on the next larger homologue, the 1,3,5-tris[4'-carboxy-(1,1'-biphenyl-4-yl)]benzene (TCBPB, Figure 1d), which contains a biphenyl spacer. The results reveal that the enlarged tricarboxylic acid does not yield the anticipated well-known isotopological hexagonal networks, but other monolayer structures with nonideal intermolecular hydrogen bond patterns.

2. Experimental Section

TCBPB (1,3,5-tris[4'-carboxy(1,1'-biphenyl-4-yl)]benzene) was synthesized in two steps via trimerization of 1-(4'-bromobiphenyl-4-yl)ethanone followed by carboxylation using *n*-BuLi/CO₂ (cf. Supporting Information).¹² Prior to dissolving TCBPB, the hygroscopic compound was desiccated at 150 °C for 48 h in high vacuum in order to completely remove residual water. Heptanoic acid (Fluka, purity ≥99%, Figure 1e), nonanoic acid (Aldrich, purity 96%), 1-nonanol (Merck, purity ≥98%), 1-undecanol (Sigma-Aldrich, purity ≥99%), dodecane (Fluka, purity ≥99%) were used as solvents without further purification. Saturated solutions served as stock solutions for successive dilutions. Those were prepared by dissolving the solute until sedimentation, sonication for 15 min, and subsequent centrifugation for 15 min at 5000 rpm. The solubility of TCBPB in heptanoic acid was determined by UV–vis absorption spectroscopy conducted with a USB4000 UV–vis spectrometer from Ocean Optics and amounts to $49.3 \pm 5.3 \mu\text{M}$.

Molecular monolayers were imaged in situ at the liquid–solid interface under ambient conditions with a home-built STM operated by an ASC 500 Scanning Probe Microscopy Controller from attocube systems AG. For all experiments, STM tips were mechanically cut from a Pt/Ir (90/10) wire and used without

further insulation. Constant current topographs were obtained with tunneling voltages around +0.8 V applied to the tip and set point currents in the order of 50 pA for fatty acid solvents, and 200–800 pA for alcohols. Prior to the STM experiments, small droplets (~5 μL) of the respective solution were applied to the freshly cleaved basal plane (5 × 5 mm²) of highly oriented pyrolytic graphite (HOPG).

3. Results and Discussion

TCBPB is comprised of seven phenyl rings and functionalized with three carboxylic acid groups in a 3-fold symmetric manner. Its structure is depicted in Figure 1d and can be regarded as a central phenyl ring which is symmetrically substituted with three 4-biphenylcarboxylic acid entities.

Polymorphic Structures. In a series of STM experiments with varying TCBPB concentration in heptanoic acid, three crystallographically different monolayer polymorphs could be distinguished. Representative high resolution STM topographs of all three polymorphic modifications (oblique-I, oblique-II, and displaced chickenwire) are depicted in Figure 2. Unit cell parameters, as accurately determined by the so-called “split-image” technique, as well as number and type of intermolecular hydrogen bonds are summarized in Table 1. Tentative models of all polymorphic structures based on STM data are depicted in Figure 3. During the experimental time span neither phase transitions nor ripening were observed. As further discussed below, a clear correlation between surface structure and solute concentration is evident, albeit for diluted solutions (<10%) only coexistence of several structures was found.

(12) Sun, D.; Xe, Y.; Mattox, T. M.; Parkin, S.; Zhou, H. *Inorg. Chem.* **2006**, *45*, 7566.

(13) Lackinger, M.; Heckl, W. M. *Langmuir* **2009**, *25*, 11307–11321.

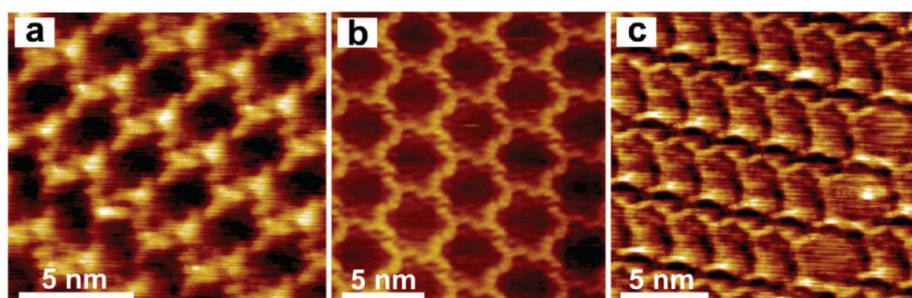


Figure 2. High resolution STM topographs of all three TCBPB monolayer polymorphs distinguished in this study: (a) oblique-I; (b) displaced chickenwire (drift corrected); (c) oblique-II intergrown with a single row of displaced chickenwire.

Table 1. Summarized Unit Cell Parameters and Overview over Number and Type of Intermolecular Hydrogen Bonds (per Unit Cell) for Each Polymorphic Structure^a

| structure | <i>a</i> (nm) | <i>b</i> (nm) | γ (deg) | area (nm ²) | packing density (nm ⁻²) | C–H···O hydrogen bonds | O–H···O hydrogen bonds |
|-----------------------|---------------|---------------|----------------|-------------------------|-------------------------------------|------------------------|------------------------|
| oblique-I | 3.6 | 2.5 | 81.8 | 9.0 | 0.22 | 6 | 2 |
| oblique-II | 3.8 | 2.4 | 78.3 | 9.0 | 0.22 | 4 | 2 |
| displaced chickenwire | 4.2 | 3.8 | 59.2 | 13.7 | 0.15 | 6 | 0 |

^a All three structures incorporate two molecules per unit cell.

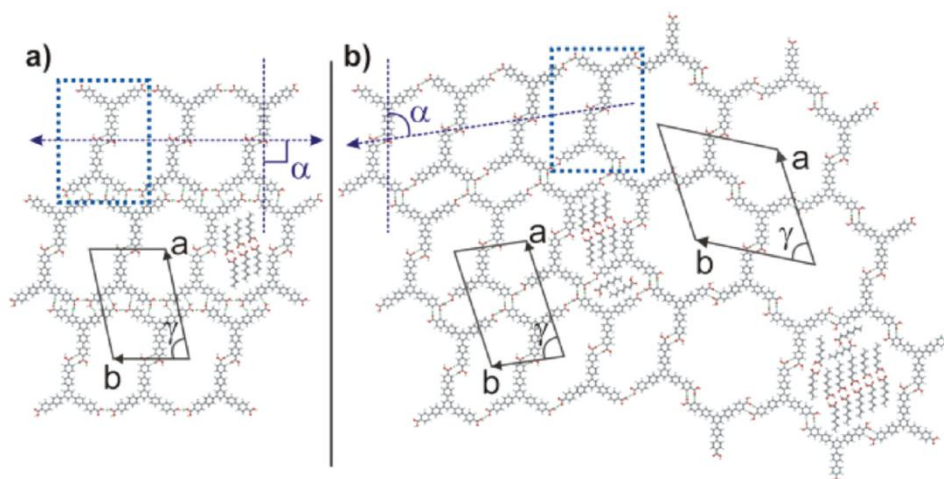


Figure 3. Proposed models of the three polymorphs (all models are to scale) with unit cells indicated. In addition, possible configurations for solvent coadsorption (based on dimerization) within the cavity voids are depicted. The dotted rectangle highlights the displaced TCBPB dimer motif, the basic unit of all three structures. Dashed purple lines with arrows indicate the row direction and the definition of the dimer axis, respectively (a) oblique-I structure ($\alpha \approx 90^\circ$); (b) oblique-II (left-hand side, $\alpha \approx 81^\circ$) and displaced chickenwire (right-hand side). This model illustrates the perfect structural match between oblique-II and displaced chickenwire, and the possibility of the two structures to deliberately intergrow.

In order to check for the generality of the observed concentration-induced polymorphism, a series of different solvents was tested: In dodecane no self-assembled TCBPB monolayers were observed at all, in full agreement with its solubility being even below the detection limit of the UV–vis spectrometer. On the other hand, STM experiments with nonanoic acid and 1-nonanol as solvents exclusively yielded the oblique-I polymorph, and no concentration-induced polymorphism was observed for dilutions down to 10% and 5% saturation, respectively. Below these concentrations self-assembly of TCBPB was not observed anymore. Interestingly, for concentrations down to 35% saturation 1-undecanol as solvent resulted either in isolated small patches of the oblique-I polymorph or disordered but stable molecular aggregates (cf. Supporting Information Figure S4). For lower concentrations adsorbed molecules could not be observed anymore. Concentration dependent emergence of three distinct monolayer structures was *exclusively* observed with heptanoic acid as solvent.

As anticipated, the large aromatic system of TCBPB results in planar adsorption on graphite. Single molecules can be identified by means of their 3-fold symmetry and the size match between STM image and molecular geometry. Planar adsorption is common to all three polymorphic structures with a dimer, as highlighted in Figure 3, being the basic motif of all structures. Yet, in contrast to the commonly encountered head-to-head dimer motifs of carboxylic acids, the observed TCBPB dimer is bound in a displaced geometry. These untypical dimers are associated via two C–H···O hydrogen bonds, rather than by two equivalent O–H···O hydrogen bonds as for the commonly encountered configuration. According to the model which was derived from the STM topographs, the carbon–oxygen distance in the dimer amounts to ~ 0.25 nm, and hence lies well within the range of C–H···O hydrogen bonds.^{14,15}

(14) Scheiner, S.; Kar, T.; Gu, Y. *J. Biol. Chem.* **2001**, *276*, 9832.

(15) Desiraju, G. R. *Acc. Chem. Res.* **1996**, *59*, 441.

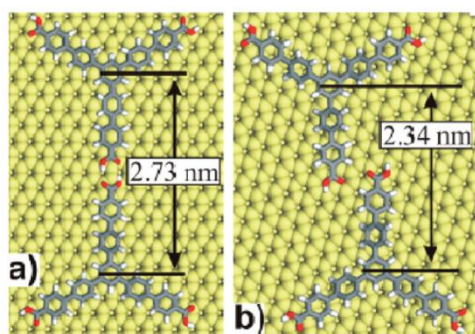


Figure 4. Molecular mechanics simulations of both isolated ideal and displaced dimers with their corresponding dimensions. Ideal dimers form two cyclic O–H···O hydrogen bonds, while displaced dimers are associated via two C–H···O hydrogen bonds.

The association motif described above is not so common for carboxylic acids, albeit bulk crystal structures of carboxylic acids do not always necessarily feature the cyclic 2-fold O–H···O hydrogen bond between COOH groups. For instance in acetic acid crystals, the COOH hydroxyl groups form O–H···O hydrogen bonds, whereas the corresponding carbonyl oxygen atoms take part in C–H···O hydrogen bonds.^{16–19} Another example is given by crystalline pyrazinic acid, where the carbonyl oxygen atoms preferentially take part in heteronuclear C–H···O hydrogen bonds.²⁰ Although, the formation probability of 2-fold cyclic O–H···O hydrogen bonds is very high for carboxylic acids, different bonding patterns may still arise.¹⁵ It is also known that C(sp²)-H groups can act as weak hydrogen bond donors, because their acidity is sufficiently enhanced,²¹ and in particular cyclic synthons emerge for this moiety.²² Moreover, the acidity of H atoms in the *ortho* position of benzoic acid is enhanced.²³

As compared to the more common head-to-head dimer, the displaced dimer exhibits nonideal hydrogen bonds, but on the other hand allows for a higher packing density of molecules on the surface. Also, the displaced dimer gives rise to chiral monolayers, an important difference in comparison to the head-to-head dimer. Accordingly, both enantiomeric forms have been observed for all three polymorphs. Interestingly, a very similar tricarboxylic acid of comparable size resulted in monolayers with head-to-head dimers at the octanoic acid–graphite interface.^{24,25}

Molecular mechanics simulations of both, ideal and displaced dimers along with the corresponding dimensions are depicted in Figure 4. According to *ab initio* calculations the binding enthalpy for the cyclic 2-fold O–H···O hydrogen bond between two carboxylic groups amounts to -60 kJ mol^{-1} (slightly dependent on functional and basis set^{26–28}) whereas a single C–H···O hydrogen bond contributes only -4 to -8 kJ mol^{-1} .^{23,29} Because

- (16) Jones, R. E.; Templeton, D. H. *Acta Crystallogr.* **1958**, *11*, 484.
 (17) Nahrungbauer, I. *Acta Chem. Scand.* **1970**, *24*, 453.
 (18) Jönsson, P. G. *Acta Crystallogr.* **1971**, *B27*, 893.
 (19) Turi, L.; Dannenberg, J. J. *J. Phys. Chem.* **1993**, *97*, 12197.
 (20) Takusagawa, F.; Higuchi, T.; Shimada, A.; Tamura, C.; Sasada, Y. *Bull. Chem. Soc. Jpn.* **1974**, *47*, 1409.
 (21) Steiner, T.; Desiraju, G. R. *Chem. Commun.* **1998**, *1998*, 891.
 (22) Nangia, A. *Cryst. Eng.* **2001**, *4*, 49.
 (23) Vishweshwar, P.; Nangia, A.; Lynch, V. M. *J. Org. Phys.* **2002**, *67*, 556.
 (24) Ma, Z.; Wang, Y.; Wang, P.; Huang, W.; Li, Y.; Lei, S.; Yang, Y.; Fan, X.; Wang, C. *ACS Nano* **2007**, *1*, 160.
 (25) Li, Y.; Ma, Z.; Qi, G.; Yang, Y.; Zeng, Q.; Fan, X.; Wang, C.; Huang, W. *J. Phys. Chem. C* **2008**, *112*, 8649.
 (26) Zhao, J.; Khalizov, A.; Zhang, R.; McGraw, R. J. *Phys. Chem. A* **2009**, *113*, 680.
 (27) Neuheuser, T.; Hess, B. A.; Reutel, C.; Weber, E. *J. Phys. Chem.* **1994**, *98*, 6459.
 (28) Winkler, A.; Mehl, J. B.; Hess, P. *J. Chem. Phys.* **1994**, *100*, 2717.
 (29) Desiraju, G. R. *Acc. Chem. Res.* **1991**, *24*, 290.

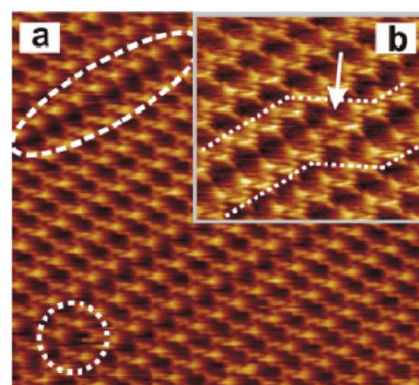


Figure 5. STM topographs of oblique-I obtained at 10% saturation illustrating commonly observed defects. (a) This topograph ($46 \times 41 \text{ nm}^2$) demonstrates how the chirality of the displaced dimer can switch within one row (dotted circle) without major disturbance of the surrounding network. The dashed oval highlights a row of molecules self-assembled in a head-to-head configuration, instead of the commonly found displaced geometry. (b) Close-up ($21 \times 18 \text{ nm}^2$) of the head-to-head row of dimers showing how this defect propagates from one row to the adjacent row, by means of two molecules (highlighted by the arrow) which acquire intermediate positions.

the strength of a 2-fold cyclic O–H···O hydrogen bond is considerably enhanced by cooperative effects, a phenomenon known in the literature as resonance-assisted hydrogen bonding (RAHB),³⁰ the binding energy of the 2-fold cyclic hydrogen bond is significantly larger than twice the binding energy of a single O–H···O hydrogen bond. RAHB is well established for cyclic O–H···O hydrogen bonds between two carboxylic groups, but this cooperative effect is in principle also conceivable for the two cyclic C–H···O hydrogen bonds of the displaced dimer (cf. Supporting Information, Figure S5 for a detailed bonding scheme).^{31,32} Nevertheless, it can be stated that the association strength of ideal straight dimers is considerably higher than for the displaced geometry.

The three observed polymorphs differ in the mutual arrangement of the dimers, their unit cell parameters, packing densities, and hydrogen bond patterns. In the following discussion, the numbers of hydrogen bonds refer to the primitive unit cells.

In the oblique-I structure, dimers are aligned along rows with their axis (as defined in Figure 3a) almost perpendicular to the row. Unit cell parameters of the oblique-I structure amount to $3.6 \pm 0.2 \times 2.5 \pm 0.2 \text{ nm}^2$ with an angle of $81.8^\circ \pm 4^\circ$. According to the tentative model each dimer is associated with its intrarow neighbor through two single O–H···O hydrogen bonds. The binding strength of such a single, nonlinear hydrogen bond is estimated to be in the order of -8.4 kJ mol^{-1} .^{33,34} Adjacent rows of dimers are interconnected by networks of four comparatively weak C–H···O hydrogen bonds, with each bond adding ~ -4 to -8 kJ mol^{-1} to the binding enthalpy.^{23,29}

Two different types of defects as illustrated in Figure 5 are commonly observed in the oblique-I structure. The white dotted circle highlights an area where within a row the dimer chirality

- (30) Gilli, G.; Gilli, P. *J. Mol. Struct.* **2000**, *552*, 1.
 (31) Steiner, T. *Chem. Commun.* **1997**, *1997*, 727.
 (32) Castellano, R. K. *Curr. Org. Chem* **2004**, *8*, 845.
 (33) The binding enthalpy of a single straight O–H···O hydrogen bond amounts to -11 kJ mol^{-1} ; common force fields approximate the angular dependence of the binding energy with a cosine function; in this case the angle is $\sim 40^\circ$, consequently the binding energy of this nonlinear hydrogen bond is reduced to -8.4 kJ mol^{-1} .
 (34) Beck, J. F.; Mo, Y. *J. Comput. Chem.* **2006**, *28*, 455.

changes. Another interesting defect is the occurrence of an intermingled row of head-to-head dimers. The origin of this defect is not entirely clear: it may be a consequence of an antiphase domain boundary or may also result from the continuation of a point defect. Both types of defects can easily be incorporated into the structure without major disturbances or stress imposed on the surrounding network. Figure 5b shows how the head-to-head arrangement propagates from one row to the adjacent row. In order to facilitate this transition, the two molecules marked by the arrow, occupy intermediate positions.

The second polymorph distinguished in this study is the displaced chickenwire structure as depicted in Figure 2b. This structure can either occur as a single row, as observed in Figure 2c, or self-assemble into larger domains. The displaced chickenwire structure is hexagonal within the experimental error and belongs to the two-dimensional space group *P6* which does not exhibit any mirror or glide planes. The unit cell parameters amount to $4.2 \pm 0.2 \times 3.8 \pm 0.2 \text{ nm}^2$ with an angle of $59^\circ \pm 2^\circ$ and a tentative model is depicted in Figure 3b. Each TCBPB molecule is interconnected to three adjacent molecules through in total six C–H···O hydrogen bonds in a 3-fold symmetric manner. The number of C–H···O hydrogen bonds per unit cell also amounts to six. The displaced chickenwire structure encompasses approximately circular cavities with an inner diameter of 3.5 nm. The space group *P6* is chiral, and correspondingly, both enantiomeric forms of the displaced chickenwire structure have been observed on the surface. It is highly likely that growth of a nucleus into a chirally pure domain is promoted, since only attachment of homochiral dimers allows for translational symmetry.^{35,36}

The third structure observed for TCBPB is oblique-II with unit cell parameters $3.8 \pm 0.2 \times 2.4 \pm 0.2 \text{ nm}^2$ and an angle of $78^\circ \pm 4.5^\circ$. Figure 2c exemplifies the close relation between oblique-II and displaced chickenwire. In fact, oblique-II cannot exist independently from the displaced chickenwire structure (vide infra). Oblique-I and -II are very similar to each other, with both structures consisting of linearly aligned dimers. Equally, their packing densities are nearly identical. Besides all similarities, there are important differences: In oblique-II, the angle between the dimer axis (cf. Figure 3 for a definition) and row axis amounts to $\sim 81^\circ$, while in oblique-I it is perpendicular. Second, while the TCBPB dimers in oblique-I form hydrogen bonds with six adjacent dimers, in oblique-II, dimers form hydrogen bonds with only four adjacent dimers. In oblique-II, dimers are interconnected by two O–H···O hydrogen bonds within the rows, whereas in between the rows interaction is mediated by two C–H···O hydrogen bonds. These differences in hydrogen bonding also result in important morphological differences: While oblique-I exhibits one larger cavity per unit cell, oblique-II contains both a larger and a smaller cavity per unit cell which can be understood as the opening of voids in between the rows, as evident from Figure 3. Yet, since the packing densities of both structures are so similar, the summed cavity area of oblique-II has to be similar to the cavity area of oblique-I. Finally, in contrast to oblique-I, we have never observed defects in oblique-II, where adjacent dimers within the same row exhibit different chirality. The reason is most likely that in oblique-II such a defect would seriously disturb or even interrupt the network. Because in oblique-II the dimer axis is no longer perpendicular to the row direction, the rows cannot be continued anymore if one of the dimers exhibits opposite chirality. The same holds true for the

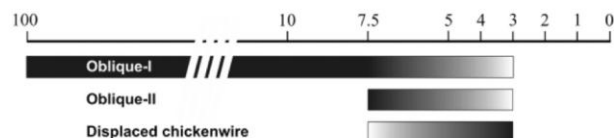


Figure 6. Dependence between solute concentration and emergence of the various interfacial monolayer phases of TCBPB in heptanoic acid (dark colors imply a large weight of the respective phase). The percentage refers to saturated solutions, where the solubility in heptanoic acid amounts to $49.3 \pm 5.3 \mu\text{M}$. Only for concentrations between 10% and 100% oblique-I was observed as single phase, otherwise phase mixtures were observed, where the relative weight depends on concentration. For concentrations below 3% saturation interfacial monolayers could not be observed anymore. Tested concentrations are 100% (saturation), 50, 20, 10, 7.5, 5, 4, 3, 2, and 1%.

displaced chickenwire, where only homochiral domains have been observed. Moreover, also at the interface of intergrown chickenwire and oblique-II the chirality is preserved. In contrast to oblique-I and displaced chickenwire, no unattached domains of oblique-II were found in numerous independent experimental runs. Each oblique-II domain was always associated with at least one row of the displaced chickenwire structure. As evident from the model in Figure 3(b) there is an ideal structural match between oblique-II and displaced chickenwire. The two structures can intergrow without strain, provided that the chirality is maintained across the interface. The fact that pure extended domains of displaced chickenwire have regularly been observed without any indications of oblique-II suggests that the latter phase cannot exist independently of the displaced chickenwire acting as a nucleus. In the light of the similarity in packing densities of oblique-I and -II and the perfect match between oblique-II and chickenwire, oblique-II may be considered as an intermediate phase.

Concentration Dependence. The occurrence of the three distinct phases can be controlled by solute concentration in solution. The concentration dependence is graphically summarized in Figure 6: from 100% down to 10% saturation, oblique-I self-assembles exclusively. At a concentration of 7.5%, both oblique-II and displaced chickenwire start to appear on the surface, yet in coexistence with oblique-I. With increasing dilution, i.e. in the range between 7.5% and 3% saturation, the equilibrium shifts toward the displaced chickenwire structure, while the percentage of the two oblique phases diminishes. At a concentration of 5%, oblique-II still dominates over the two other polymorphs, while at 3% displaced chickenwire is observed almost exclusively. At concentrations below $\sim 3\%$ saturation, no self-assembled monolayers could be detected anymore. It is noteworthy that at these low concentrations, the number of dissolved molecules in the liquid phase becomes already comparable to the number of molecules in the monolayer (cf. Supporting Information Figure S6 for details). Albeit below 10% saturation none of the phases has been observed exclusively, a clear correlation between solute concentration and dominance of one of the monolayer phases has been found: the higher the solute concentration in solution, the higher the packing density of molecules on the surface. A more gradual increase of average surface packing density becomes possible through the coexistence of various phases. For instance, as illustrated in Figure 7, parts a and b, for concentrations of 5% and 3%, respectively the coexistence of chickenwire and oblique-II was found. Yet, for the higher solute concentration of 5% the dominant phase is densely packed oblique-II, whereas for the lower concentration of 3% the less dense displaced chickenwire structure dominates. It can clearly be seen that the intergrown arrangement of displaced chickenwire

(35) Miura, A.; Jonkheijm, P.; De Feyter, S.; Schenning, A. P. H. J.; Meijer, E. W.; De Schryver, F. C. *Small* **2005**, *1*, 131.

(36) De Feyter, S.; De Schryver, F. C. *J. Phys. Chem. B* **2005**, *109*, 4290.

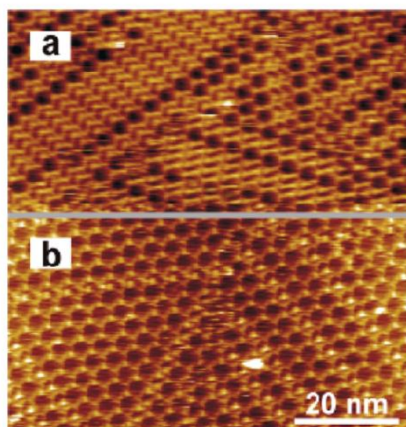


Figure 7. STM topographs acquired at (a) 5%, and (b) 3% TCBPB concentration. By means of controlling the solute concentration the relative amount of adsorbed monolayer phases can be influenced. The more diluted solution yielded a higher amount of the less densely packed chickenwire structure, whereas for the higher concentration oblique-II dominates. The scale bar applies to both images. Parts a and b exhibit opposite chirality.

and oblique-II retains the same chirality. Apparently, by varying the surface content of the two phases the system can continuously adjust any average surface concentration of molecules between the packing densities of both structures.

Solvent Coadsorption. Since nanoporous networks expose pristine substrate to solution, coadsorption of either solute or solvent molecules within the cavities is to be expected and was concluded also for other nanoporous systems.^{10,11,25} Especially in the displaced chickenwire structure six free hydroxyl groups of bordering molecules point into each cavity, resulting in “sticky cavities”. Hence the host–guest interaction is enhanced, which could promote coadsorption of guests with hydrogen bond acceptors. This coadsorption is manifested in the reproducible observation of contrast features within the cavities, as also observed for other nanoporous systems at the liquid–solid interface.⁷ A representative example of internal contrast in the cavities of the chickenwire structure is depicted in Figure 2c. Contrast features are not unique for the chickenwire structure, but were also observed within the cavities of both oblique structures, as shown in Figure 8 for oblique-I. Because in the oblique structures the internal contrast features have a striped appearance which is consistent with the lamella characteristics observed for alkane derivatives³⁷ or carbamates with long aliphatic chains,^{38,39} they could be readily associated with assemblies of heptanoic acid solvent molecules²⁵ rather than with TCBPB molecules. Although, a single stabilizing O–H···O hydrogen bond between a coadsorbed solvent molecule and the free hydroxyl groups in the cavity wall is conceivable, it is more favorable for heptanoic acid solvent molecules to adsorb dimerized in the cavities of the three structures as shown in the tentative models in Figure 3. The proposed adsorption geometry is also in agreement with the contrast features depicted in Figure 8. Interaction between the free hydroxyl groups of the TCBPB network with heptanoic acid molecules in a more upright geometry is still possible. Yet, such an arrangement is difficult to verify by STM imaging.

(37) Giancarlo, L. C.; Fang, H.; Rubin, S. M.; Bront, A. A.; Flynn, G. W. *J. Phys. Chem. B* **1998**, *102*, 10255.

(38) Kim, K.; Plass, K. E.; Matzger, A. J. *Langmuir* **2003**, *19*, 7149.

(39) Kim, K.; Plass, K. E.; Matzger, A. J. *Langmuir* **2005**, *21*, 647.

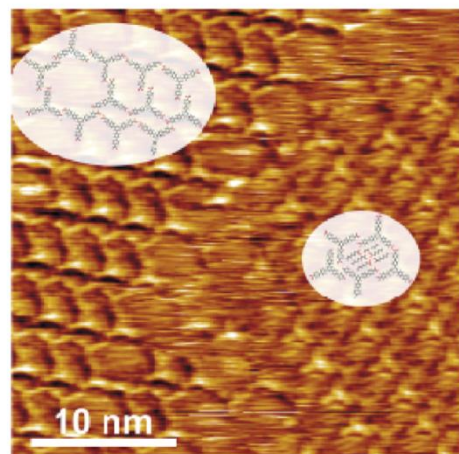


Figure 8. A representative example of internal contrast features found within in the cavities of oblique-I with a tentative model of coadsorbed heptanoic acid molecules. This image was obtained at 4% concentration. Notice that the three structures can coexist at this concentration.

Thermodynamics. In view of the self-assembled structures of smaller analogous tricarboxylic acids an important question arises: Why has the common ideal chickenwire structure based on head-to-head dimers never been observed for TCBPB molecules, but only the displaced chickenwire structure? Since many studies on 2D interfacial self-assembly conclude that the monolayers are in thermodynamical equilibrium with the supernatant solution,^{40–43} in the following it is argued that thermodynamics favors the displaced rather than the ideal chickenwire structure for this large aromatic tricarboxylic acid. In general, the driving force for self-assembly is the associated minimization of Gibbs free energy which in this case is composed of an enthalpic gain and an entropic loss. The enthalpic gain arises from attractive adsorbate–substrate and adsorbate–adsorbate interactions, while entropy is generally diminished when molecules associate or adsorb on a surface.

Estimates of the enthalpic gain per molecule ΔH were obtained from a combination of molecular mechanics (MM) simulations based on the Dreiding force field with literature values for intermolecular interaction energies. The molecule–substrate interaction was estimated by MM, while for intermolecular hydrogen bonds literature values were considered. According to MM results, the enthalpy of adsorption of a single TCBPB molecule on graphite amounts to -392 kJ mol^{-1} . In the displaced chickenwire structure each molecule is interconnected with three adjacent molecules by in total six hydrogen bonds, where each bond adds about -6 kJ mol^{-1} when a possible RAHB stabilization is not taken into account.^{23,29} Consequently the total average molar binding enthalpy in the displaced chickenwire structure amounts to $\Delta H = -392 \text{ kJ mol}^{-1} + 0.5 \times 6 \times -6 \text{ kJ mol}^{-1} = -410 \text{ kJ mol}^{-1}$, where the factor 0.5 corrects for double counting of pairwise intermolecular interactions. The same procedure provides ΔH for oblique-I ($-418.4 \text{ kJ mol}^{-1}$), oblique-II (-415 kJ mol^{-1}), and ideal chickenwire (-482 kJ mol^{-1}). For the latter

(40) Kampschulte, L.; Werblösky, T. L.; Kishore, R. S. K.; Schmittel, M.; Heckl, W. M.; Lackinger, M. *J. Am. Chem. Soc.* **2008**, *130*, 8502.

(41) Lei, S.; Tahara, K.; De Shryver, F. C.; Van der Auweraer, M.; Tobe, Y.; De Feyter, S. *Angew. Chem., Int. Ed.* **2008**, *47*, 2964.

(42) Stabel, A.; Heinz, R.; Schryver, F. C.; Rabe, J. P. *J. Phys. Chem.* **1995**, *99*, 205.

(43) Eichhorst-Gerner, K.; Stabel, A.; Moessner, G.; Declercq, D.; Valiyaveetil, S.; Enkelmann, V.; Müllen, K.; Rabe, J. P. *Angew. Chem., Int. Ed. Engl.* **1996**, *13-14*, 1492.

Table 2. Comparison of Molecular Packing Densities, Entropic Costs Δs , Enthalpic Gains Δh , and Free Energies Δg per Unit Area of the Three Experimentally Observed and One Hypothetical TCBPB Polymorphs for Two Different Concentrations (Saturated Solution vs Diluted Solution at 4% Saturation)^a

| structure | packing density (10 ¹⁴ cm ⁻²) | $-T\Delta s$ ($\mu\text{J cm}^{-2}$) saturated ^b | $-T\Delta s$ ($\mu\text{J cm}^{-2}$) 4% saturated ^b | Δh ($\mu\text{J cm}^{-2}$) | $\Delta g = \Delta h - T\Delta s$ ($\mu\text{J cm}^{-2}$) saturated | $\Delta g = \Delta h - T\Delta s$ ($\mu\text{J cm}^{-2}$) 4% saturation |
|-----------------------|---|--|---|---|--|--|
| displaced chickenwire | 0.15 | +2.88 (+2.91) | +3.08 (+3.13) | -10.21 | -7.33 (-7.30) | -7.13 (-7.08) |
| ideal chickenwire | 0.10 | +1.92 (+1.97) | +2.05 (+2.11) | -8.00 | -6.08 (-6.03) | -5.95 (-5.89) |
| oblique-I | 0.22 | +4.22 (+4.22) | +4.52 (+4.59) | -15.28 | -11.06 (-11.06) | -10.77 (-10.69) |
| oblique-II | 0.22 | +4.22 (+4.22) | +4.52 (+4.59) | -15.16 | -10.94 (-10.94) | -10.64 (-10.57) |

^aThe entropic contribution to the free energy $-T\Delta s$ was evaluated at room temperature (300 K) and considers translational and rotational entropy. The total binding enthalpy Δh contains contributions from molecule–molecule and molecule–substrate interactions. For molecule–molecule interactions only hydrogen bonds were considered and van der Waals contributions neglected. Area normalized values were derived by multiplying molar quantities with molecular packing densities as obtained from STM (displaced chickenwire, oblique-I and -II) or MM data (ideal chickenwire). ^bFor values in parentheses the concentration change upon self-assembly has been included (cf. Supporting Information), whereas for the other values the loss of translational entropy has been estimated based on eq 1.

structure the *ab initio* value of -60 kJ mol^{-1} was employed for the binding enthalpy of straight 2-fold O–H···O hydrogen bonds.^{27,28} The packing density of this hypothetical polymorph was estimated by MM simulations of a single six membered ring which result in a hexagonal lattice with $a = 4.7 \text{ nm}$, and consequently a packing density of 0.10 nm^{-2} .

In the following a molecule based approach proposed by Whitesides et al. is used to estimate the entropic loss of self-assembly.⁴⁴ Upon adsorption from solution, molecules completely lose their rotational and translational entropy. For conformationally rigid molecules like TCBPB, the loss of conformational entropy can be neglected. Likewise, vibrational entropy does not change significantly during self-assembly and can also be ignored. Translational and rotational entropy of soluted molecules can be estimated by the following equations:⁴⁴

$$S_{\text{trans}} = R \ln \left[\frac{1}{c} \left(\frac{2\pi m k_B T e^{5/3}}{h^2} \right)^{3/2} \right] \quad (1)$$

$$S_{\text{rot}} = R \ln \left[\frac{\pi^{1/2}}{\gamma} \left(\frac{8\pi^2 k_B T e}{h^2} \right)^{3/2} (I_1 I_2 I_3)^{1/2} \right] \quad (2)$$

Here, R is the gas constant, T the temperature, k_B is Boltzmann's, and h Planck's constant while e is Euler's number, m denotes the solute's mass, and c is its concentration. In order to avoid overestimation of translation entropy, the concentration refers to the free volume of the solvent (32 mL for 1 L of heptanoic acid) as obtained by the hard cube approximation.⁴⁴ Furthermore, γ is related to the symmetry of the solute molecule, while I_1 , I_2 , and I_3 are its principle moments of inertia. According to the equations above, the loss of rotational entropy per adsorbed molecule is independent of concentration, whereas the loss of translational entropy per molecule as derived from the Sackur–Tetrode equation depends inversely logarithmic on concentration. Consequently, the total entropy change per adsorbed molecules, as given by the sum of rotational and translational entropy, depends on concentration and increases with dilution.

Because of the relatively low solubility of TCBPB in heptanoic acid, the amount of dissolved molecules in $5 \mu\text{L}$ becomes comparable to the amount of molecules in $5 \times 5 \text{ mm}^2$ of a monolayer, especially for diluted solutions. Thus, the concentration can already decrease significantly upon self-assembly of a monolayer, and eq 1 underestimates the loss of translational

entropy per molecule. A more accurate expression for loss of translational entropy which also includes changes of the concentration upon self-assembly is provided in the Supporting Information (eqs S1 and S2). However, as evident from Table 2, concentration changes during self-assembly result only in minor corrections.

Since the surface coverage in these experiments is always close to unity, we refer to the free energy per unit area $\Delta g = \Delta G/A$. Combining the total entropic cost $\Delta S = \Delta S_{\text{trans}} + \Delta S_{\text{rot}}$ with STM derived molecular packing densities allows to estimate entropic cost per unit area $\Delta s = \Delta S/A$. Similarly, multiplication of ΔH with packing density allows to estimate the enthalpic gain per unit area $\Delta h = \Delta H/A$. Summation of $-T\Delta s$ with Δh results in the free energy per unit area Δg . Values for the three experimentally observed structures and the hypothetical ideal chickenwire structure are provided in Table 2 for two different solute concentrations.

According to these estimates of Δg , the experimentally observed displaced chickenwire polymorph is thermodynamically more stable than the anticipated hypothetical ideal chickenwire structure. The decisive reason is that for such a large aromatic molecule as TCBPB the interaction with the substrate becomes relatively strong, and a higher packing density facilitates significantly larger Δh from adsorption. This major enthalpic advantage cannot be compensated by the comparatively small enthalpic advantage offered by formation of two ideal O–H···O hydrogen bonds which would lead to a significantly lower packing density. From this pure enthalpic consideration the displaced chickenwire structure is more favorable. But even when the increased entropic cost of the displaced chickenwire structure due to its higher packing density is taken into account, it still remains thermodynamically more stable than the ideal chickenwire structure.

Similarly, Δg values were evaluated for both oblique structures. According to this consideration, the oblique-I structure should be the thermodynamically most stable independent phase, consistent with the experimental observation for higher concentrations. From Table 2 it becomes also obvious that at lower concentrations, the increased translational entropy cost diminishes Δg of the densely packed oblique structures more seriously than for the less densely packed chickenwire structures. Yet, according to these estimates even for dilute solutions, Δg of oblique-I remains more favorable than for the displaced chickenwire structure, posing the question, how can the emergence of the displaced chickenwire polymorph be explained by this thermodynamical model.

In general, coexistence of different monolayer polymorphs over a wide concentration range is a clear experimental indication for similarity of the respective Δg values.⁴¹ In order to rationalize the thermodynamical stability of the displaced chickenwire

(44) Mammen, M.; Shakhnovich, E. I.; Deutch, J. M.; Whitesides, G. M. *J. Org. Chem.* **1998**, *63*, 3821.

structure, further contributions to Δg have to be included. One conceivable additional contribution arises from cooperative effects of cyclic 2-fold C–H···O hydrogen bonds as already discussed above. The cyclic arrangement of the two C–H···O hydrogen bonds allows for resonance assisted hydrogen bonds, similar to the cyclic O–H···O hydrogen bond between carboxylic groups, and RAHB has also been theoretically predicted for weaker C–H···O hydrogen bonds.^{31,32} The fact that all observed structures share the displaced dimer as basic unit can be seen as experimental indication for a relatively high stability of this arrangement. Since the displaced chickenwire structure features three pairs of possibly RAHB stabilized C–H···O hydrogen bonds per unit cell, consideration of this cooperative effect increases the thermodynamic stability of displaced chickenwire with respect to oblique-I.

Second, additional enthalpic contributions from solvation significantly affect the Δg values, and therefore the relative stabilities of distinct monolayer phases. The reference state for our enthalpy estimates are single isolated molecules in vacuum. Yet, upon self-assembly of interfacial monolayers, solute molecules adsorb from the liquid phase where they are dissolved and solvated. The associated solvation enthalpy considerably lowers the effective binding enthalpy, however, this additional enthalpic contribution is very difficult to assess. For tricarboxylic acids dissolved in fatty acid solvents, it is reasonable to assume that each carboxylic group of the solute molecules is saturated by a 2-fold hydrogen bond. Thus, a lower limit for solvation enthalpy is -180 kJ mol^{-1} , i.e. three times the binding enthalpy of a 2-fold O–H···O hydrogen bond. Since solvation significantly reduces the effective enthalpy of adsorption per molecule, this additional contribution weakens the enthalpic gain of densely packed structures more seriously than that of less densely packed structures. Consequently, inclusion of the solvation enthalpy further increases the thermodynamical stability of the displaced chickenwire structure with respect to oblique-I.

Both RAHB of cyclic C–H···O hydrogen bonds and enthalpic contributions from solvation are in principle able to explain the concentration dependent crossover between oblique-I and displaced chickenwire on thermodynamic grounds, while both polymorphs still remain thermodynamically more stable than the ideal chickenwire structure. It is noteworthy, that the applied method of molecule based estimation of enthalpic gains and entropic losses is not sufficiently precise to exactly reproduce concentration dependent crossovers. Nevertheless, our results reproduce a generally observed trend for concentration induced monolayer polymorphism at the liquid solid interface: higher solute concentrations lead to more densely packed monolayer polymorphs. In two recent works by de Feyter et al. and Behm et al. this trend could likewise be explained by thermodynamic models.^{41,45}

Although it is rather complex and challenging to establish a rigid quantitative thermodynamic model for monolayers at the liquid–solid interface, the proposed method at least allows understanding and reproducing trends. In the present case the thermodynamical preference of more densely packed polymorphs over a structure where specifically the intermolecular hydrogen bonds are optimized can be explained.

4. Conclusion

In this work, three different monolayer polymorphs emerged upon adsorption of the enlarged tricarboxylic acid TCBPB from heptanoic acid solution on a graphite surface. All three polymorphs share the same dimer motif as building block and are

nanoporous; i.e., they exhibit a periodic arrangement of cavities. Contrary to monolayer structures observed for smaller tricarboxylic acids, here the dimers are not associated through two strong cyclic O–H···O hydrogen bonds but by two weaker C–H···O hydrogen bonds. This results in a displaced geometry and gives rise to chirality, a phenomenon which has not been encountered before for monolayers of aromatic tricarboxylic acids. Also, the displaced dimer geometry is definitely suboptimal in terms of intermolecular hydrogen bonds, but facilitates higher packing density, and thus a larger contribution from stabilizing molecule–substrate interactions.

During the course of concentration dependent experiments a positive correlation between solute concentration and average surface packing density could clearly be established. For any concentration below 10% saturation only coexistence of all phases was observed, yet, the relative weight of each phase depends on concentration. Interestingly, the two oblique polymorphs exhibit almost identical packing density whereas the displaced chickenwire structure is significantly less dense. Oblique-I is an independent phase, whereas oblique-II was only observed in conjunction with the chickenwire polymorph. The latter two phases feature perfect structural match and can intergrow without strain, thereby providing a possibility to continuously tune the average packing density between those of the pure phases.

The preference of the observed displaced chickenwire structure over the hypothetical ideal chickenwire structure can be understood on thermodynamical grounds: Gibbs free energies per unit area Δg were evaluated for all polymorphs. The entropic cost arises from losses of translational and rotational entropy, and was evaluated by established methods. The enthalpic gain was estimated by combining literature values for intermolecular hydrogen bond energies with a molecular mechanics derived adsorption energy. According to these estimates the hypothetical ideal chickenwire is thermodynamically less favorable than the experimentally observed displaced chickenwire structure. Yet, both densely packed oblique structures are thermodynamically more stable than the displaced chickenwire structure, even at lower concentrations, where the cost due to translational entropy is increased. However, if enthalpic contributions from solvation and cooperative effects of cyclic C–H···O hydrogen bonds are included, the displaced chickenwire can become the thermodynamically favored polymorph at low concentrations. Thermodynamics of molecular monolayers at the liquid–solid interface is a complex problem. For the complete picture, the solution definitely needs to be included. For that reason this problem is difficult to address by atomistic simulations because of the large system size. Nevertheless, semiquantitative considerations as applied in the present case have the potential to at least provide a basic understanding of the main contributions to Gibbs free energy of adsorption and their dependence on external parameters as concentration and temperature.

A major lesson to be learnt from this study is that structure prediction cannot exclusively be based on formation of ideal intermolecular hydrogen bonds. In particular, for larger compounds, the relative enthalpic weight of other contributions as molecule–surface interactions becomes increasingly important and formation of ideal hydrogen bond patterns is not the most important criterion.

Acknowledgment. We gratefully acknowledge financial support by the DFG within the Sonderforschungsbereich 486 and FOR 516 as well as by the cluster of excellence Nanosystems-Initiative-Munich (NIM) and the Bayerische Forschungsförderung.

(45) Meier, C.; Roos, M.; Künzel, D.; Breitruck, A.; Hoster, H. E.; Landfester, K.; Gross, A.; Behm, R. J.; Ziener, U. *J. Phys. Chem. C* **2010**, *114*, 1268.

Note Added after ASAP Publication. This article was published ASAP on June 10, 2010. A new reference (13) has been added to the reference list. The correct version was published on June 15, 2010.

Supporting Information Available: Text discussing the synthesis and NMR characterization of TCBPB, additional STM topographs, detailed hydrogen bonding

scheme, comparison of number of molecules in solution and for monolayer, and translational entropy for concentration changes, including a scheme showing the synthesis and figures showing the NMR spectra, STM topography, bonding patterns, and plot of the number of TCBPB molecules vs relative concentration. This material is available free of charge via the Internet at <http://pubs.acs.org>.

On the Scalability of Supramolecular Systems – High Packing Density vs.

Optimized Hydrogen Bonds in Tricarboxylic Acid Monolayers

Jürgen F. Dienstmaier, Kingsuk Mahata, Wolfgang M. Heckl, Michael Schmittel,

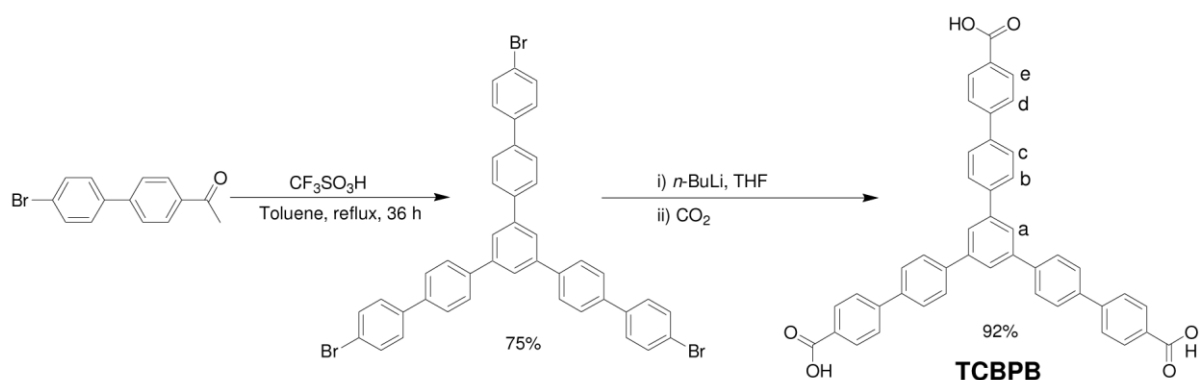
*and Markus Lackinger**

Supporting Information

- (1) Synthesis of 1,3,5-tris[4'-carboxy(1,1'-biphenyl-4-yl)]benzene (TCBPB)**
- (2) Additional STM topographs**
- (3) Hydrogen Bond Pattern for displaced Dimers**
- (4) Number of molecules in solution vs. monolayer**
- (5) Translational entropy loss for changing concentrations**

(1) Synthesis of 1,3,5-tris[4'-carboxy(1,1'-biphenyl-4-yl)]benzene (TCBPB)

^1H NMR and ^{13}C NMR were recorded on a Bruker Avance 400 MHz spectrometer using the deuterated solvent as the lock and residual solvent as the internal reference. NMR measurements were carried out at 298 K. The following abbreviations were utilized to describe peak patterns: s = singlet and d = doublet. The numbering of the carbon atoms of the molecular formula shown in the experimental section is only used for the assignments of the NMR signal and is not in accordance with the IUPAC nomenclature rules. The melting point was measured on a Büchi SMP-20 and the infrared spectrum recorded using a Varian 1000 FT-IR instrument. Elemental analysis measurement was done using a EA 3000 CHNS.



Scheme S1. Synthesis of 1,3,5-tris[4'-carboxy(1,1'-biphenyl-4-yl)]benzene (TCBPB).

1,3,5-Tris(4'-bromobiphenyl-4-yl)benzene was synthesized according to a known procedure.¹

Synthesis of 1,3,5-Tris[4'-carboxy(1,1'-biphenyl-4-yl)]benzene (TCBPB): In an oven-dried three-neck round-bottomed flask 1,3,5-tris(4'-bromobiphenyl-4-yl)benzene (2.01 g, 2.61 mmol) was loaded under nitrogen atmosphere. After addition of dry THF (120 mL), $n\text{-BuLi}$ (6.30 mL, 15.8 mmol) was added slowly at $-60\text{ }^\circ\text{C}$ to $-70\text{ }^\circ\text{C}$ over a period of 30 min. The resultant green solution was stirred for another 6 h at the same temperature. CO_2 gas was passed through the reaction mixture over a period of 30 min maintaining the temperature unchanged. Thereafter, the reaction mixture was allowed to warm up to room temperature with slow purging of CO_2 gas. Excess of $n\text{-BuLi}$ was neutralized using water. The salts were acidified using acetic acid furnishing a clear solution. After removal of THF under reduced pressure a white precipitate was obtained which was filtered off and was dried inside a desiccator. Yield 92%; mp $> 260\text{ }^\circ\text{C}$; ^1H NMR (400 MHz, $\text{THF-}d_6$) δ 7.82 (d, $^3J = 8.4\text{ Hz}$, 6 H,

d-H), 7.86 (d, $^3J = 8.4$ Hz, 6 H, [b/c]-H), 7.95 (d, $^3J = 8.4$ Hz, 6 H, [b/c]-H), 8.03 (s, 3 H, a-H), 8.12 (d, $^3J = 8.4$ Hz, 6 H, e-H); ^{13}C NMR (100 MHz, THF- d_8) δ 125.7, 127.5, 128.4, 128.6, 130.9, 131.1, 140.2, 141.6, 142.8, 145.5, 167.4; IR (KBr) ν 3330-2400, 1683, 1606, 1420, 1271, 1179, 1101, 1004, 822, 772 cm^{-1} ; Anal. Calcd. for $\text{C}_{45}\text{H}_{30}\text{O}_6 \cdot \text{H}_2\text{O}$: C, 78.93; H, 4.71. Found: C, 78.94; H, 4.34.

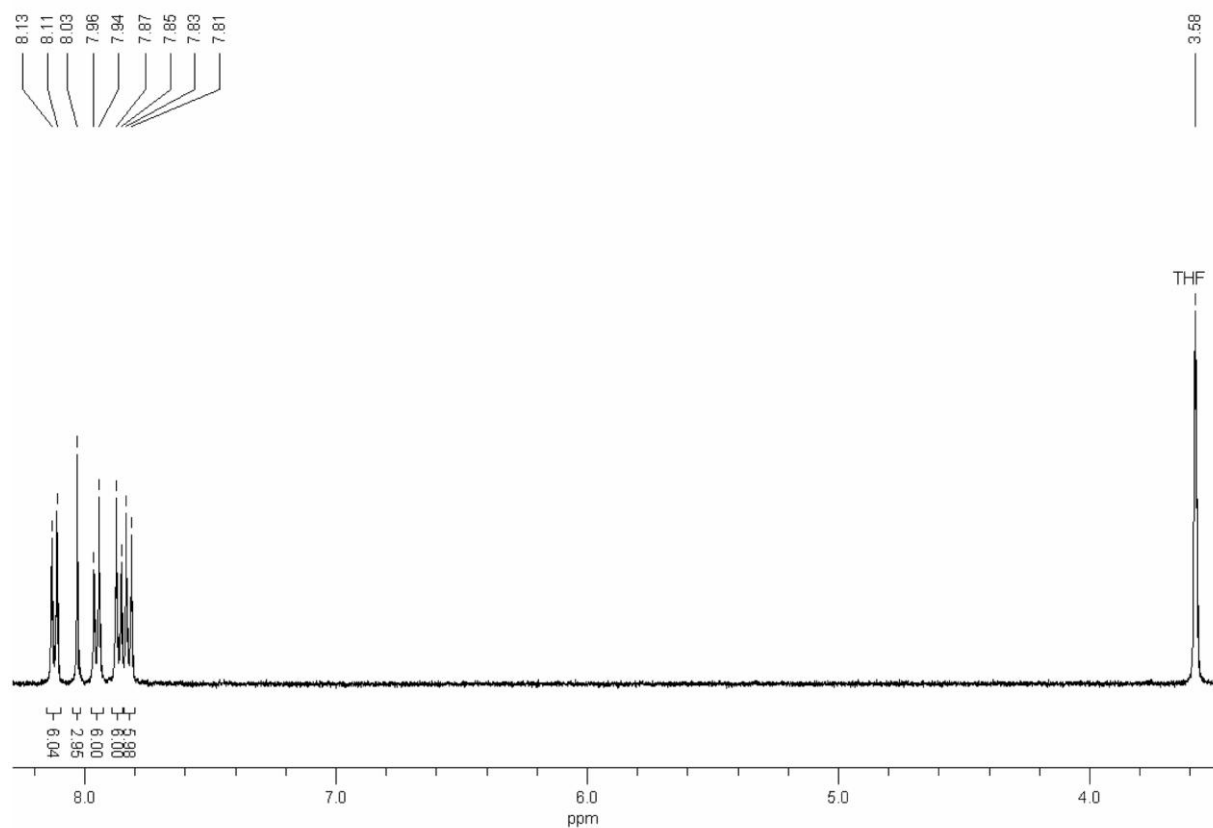


Figure S2. ^1H NMR spectrum (400 MHz, THF- d_8 , 298 K) of TCBPB

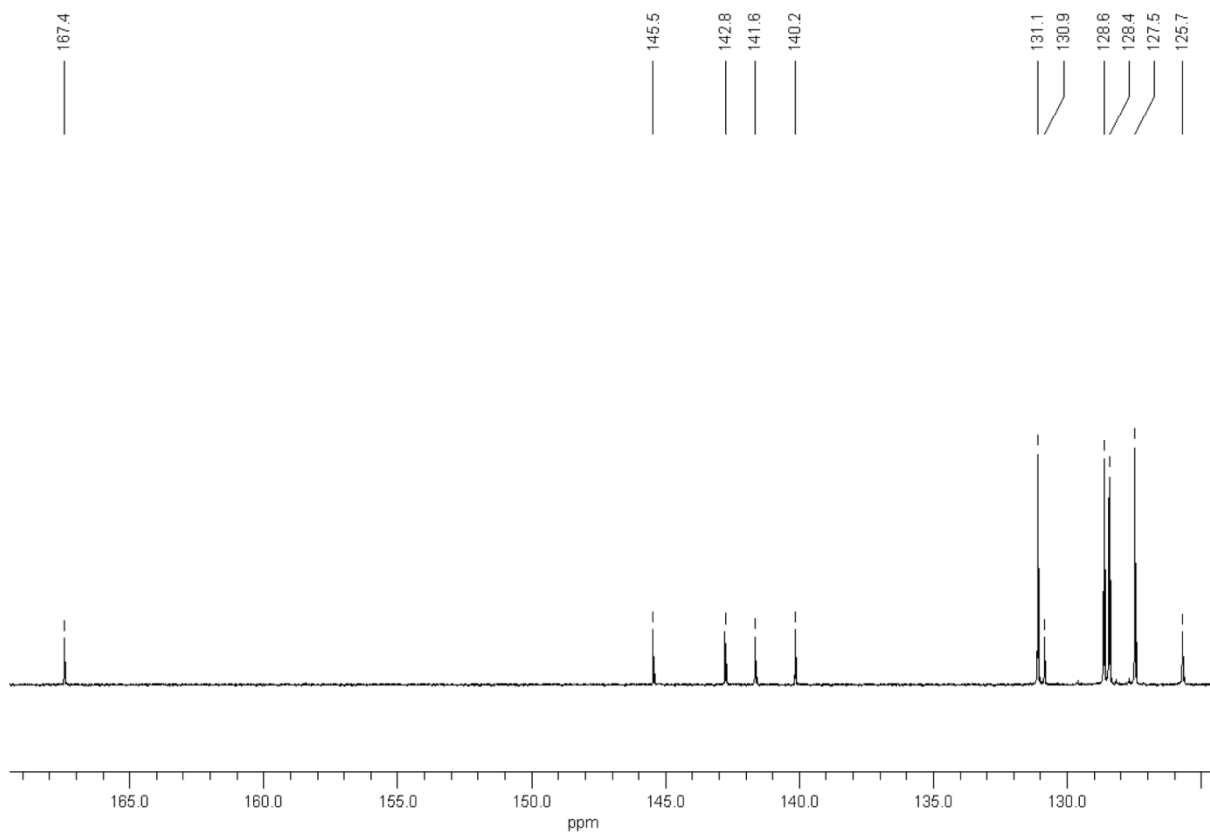


Figure S3. ^{13}C NMR spectrum (100 MHz, $\text{THF-}d_8$, 298 K) of TCBPB.

(2) Additional STM topographs

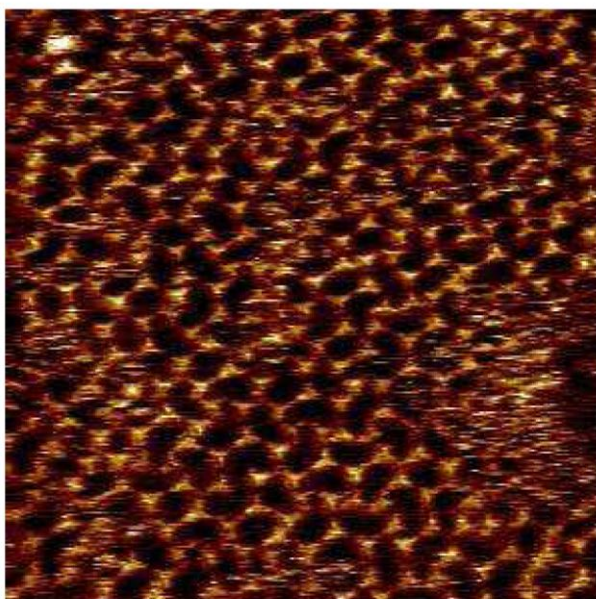


Figure S4 Representative STM topograph ($40 \times 40 \text{ nm}^2$) of the disordered structure found for concentrations between 100% and 35% saturation in 1-undecanol solutions. This image was obtained at a concentration of 35% saturation.

(3) Hydrogen Bond Pattern for displaced Dimers

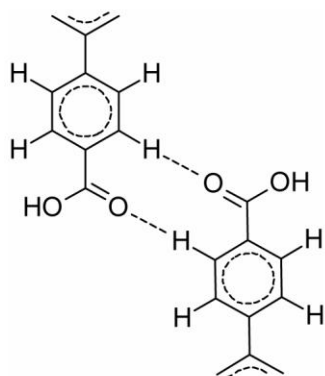


Figure S5 Bonding pattern of the cyclic two-fold C-H...O hydrogen bond between displaced TCBPB dimers. By a cooperative effect known in the literature as “resonance assisted hydrogen bond” (RAHB), the binding energy of cyclic hydrogen bonds is significantly enhanced as compared to twice the binding energy of a single hydrogen bond.

(4) Number of molecules in solution vs. monolayer

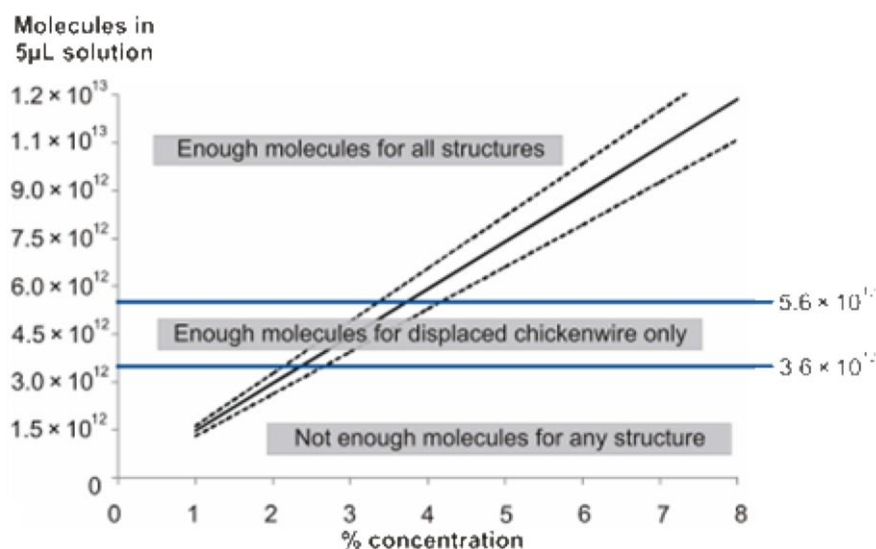


Figure S6 Number of TCBPB molecules in 5 µL TCBPB in heptanoic acid solution as a function of relative concentrations between 1 % and 8 % saturation. For full coverage of a 5×5 mm² HOPG crystal surface, oblique-I and -II require 5.6×10^{12} molecules, whereas displaced chickenwire requires only 3.6×10^{12} molecules. Accordingly, if all dissolved molecules were adsorbed on the surface, for concentrations above ~ 3.7 %, the oblique phases should have been observed exclusively. However, between 3 % and 7.5 %, all three phases were found in coexistence. The dashed lines indicate the experimental error of the concentration measurement. Notice that below ~ 2.5 %, no self-assembled structure of TCBPB was found, although the number of dissolved molecules would still be sufficient to at least partly cover the surface.

(5) Translational entropy loss for changing concentrations

The following expression allows evaluation of the loss of translational entropy for the case that the solute concentration changes markedly upon self-assembly:

$$\Delta S_{trans} = k_B \cdot \int_{N_0}^{N_0 - \Delta N} dN \cdot \ln \left[\frac{V}{N} \left(\frac{2\pi \cdot m \cdot k_B T \cdot e^{\frac{5}{3}}}{h^2} \right)^{\frac{3}{2}} \right] \quad (S1)$$

$$\Delta S_{trans} = k_B \cdot \left(\begin{aligned} & (N_0 - \Delta N) \cdot \ln \left[\frac{V}{N_0 - \Delta N} \left(\frac{2\pi \cdot m \cdot k_B T \cdot e^{\frac{5}{3}}}{h^2} \right)^{\frac{3}{2}} \right] - \Delta N \\ & - N_0 \cdot \ln \left[\frac{V}{N_0} \left(\frac{2\pi \cdot m \cdot k_B T \cdot e^{\frac{5}{3}}}{h^2} \right)^{\frac{3}{2}} \right] \end{aligned} \right) \quad (S2)$$

Here N_0 denotes the number of molecules in solution before self-assembly, ΔN the number of molecules adsorbed during self-assembly of a monolayer, and the actual concentration c is expressed as number of molecules N in the solution volume V , i.e. $c = N/V$.

For instance self-assembly of an oblique-I monolayer (5 μL solution on 0.25 cm^2 substrate) causes a rotational entropy loss of 0.168 kJ K^{-1} , whereas the loss of translational entropy amounts to 0.217 kJ K^{-1} for saturated solution and increases to 0.244 kJ K^{-1} for a diluted solution at 4% saturation.

[1] J. Lu, Y. Tao, M. D'iorio, Y. Li, J. Ding, M. Day, *Macromolecules* **2004**, 37, 2442.

Extended Two-Dimensional Metal–Organic Frameworks Based on Thiolate–Copper Coordination Bonds

Hermann Walch,[†] Jürgen Dienstmaier,[†] Georg Eder,[†] Rico Gutzler,^{†,‡} Stefan Schlögl,[†] Thomas Sirtl,[⊥] Kalpataru Das,[‡] Michael Schmittl,[‡] and Markus Lackinger^{*,†,§,⊥}

[†]Department for Earth and Environmental Sciences and Center for NanoScience, Ludwig-Maximilians-Universität, Theresienstrasse 41, 80333 München, Germany

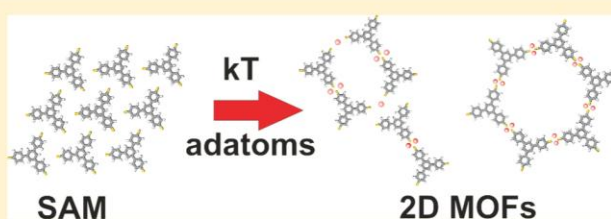
[‡]Center of Micro and Nanochemistry and Engineering, Organische Chemie I, Universität Siegen, Adolf-Reichwein-Strasse 2, 57068 Siegen, Germany

[§]Deutsches Museum, Museumsinsel 1, 80538 München, Germany

[⊥]Technical University Munich, TUM School of Education, Schellingstrasse 33, 80799 München, Germany

S Supporting Information

ABSTRACT: Self-assembly and surface-mediated reactions of 1,3,5-tris(4-mercaptophenyl)benzene—a three-fold symmetric aromatic trithiol—are studied on Cu(111) by means of scanning tunneling microscopy (STM) under ultrahigh-vacuum (UHV) conditions. In order to reveal the nature of intermolecular bonds and to understand the specific role of the substrate for their formation, these studies were extended to Ag(111). Room-temperature deposition onto either substrate yields densely packed trigonal structures with similar appearance and lattice parameters. Yet, thermal annealing reveals distinct differences between both substrates: on Cu(111) moderate annealing temperatures (~ 150 °C) already drive the emergence of two different porous networks, whereas on Ag(111) higher annealing temperatures (up to ~ 300 °C) were required to induce structural changes. In the latter case only disordered structures with characteristic dimers were observed. These differences are rationalized by the contribution of the adatom gas on Cu(111) to the formation of metal–coordination bonds. Density functional theory (DFT) methods were applied to identify intermolecular bonds in both cases by means of their bond distances and geometries.



INTRODUCTION

In the past years a great structural and chemical variety of surface-supported metal–organic networks has been demonstrated by combining appropriately functionalized organic building blocks with various coordinating metals.¹ While some of the coordination complexes utilized for surface-confined systems were already well-known from bulk systems, other coordination numbers and geometries are unique to surface-supported networks. Concerning the intermolecular bond strength, and thus the overall stability of the structures, metal–organic networks occupy an intermediate position between hydrogen-bonded networks and covalent organic frameworks.^{1a} Yet, since metal–coordination bonds are reversible under commonly applied growth conditions, the preparation of long-range ordered networks becomes feasible. The motivation of this work is to extend the tool box of functional groups for the design of surface-supported metal–organic networks to thiol groups and understand the formation kinetics and topological properties of thiolate–metal complexes. To this end we designed and synthesized a highly symmetric aromatic trithiol molecule and studied its self-assembly and surface-supported reactions by means of scanning tunneling microscopy on a Cu(111) surface, which is known to inherently supply copper coordination centers from

its free adatom gas.² To clarify the specific role of the substrate, similar experiments were also conducted on Ag(111). Thiolate–copper coordination bonds are of particular interest because of their electronic conjugation which allows electronically coupling of molecular units by thiolate–copper–thiolate bonds.³ One conceivable application of copper–thiolate complexes hence lies in the field of molecular electronics, where reliable tools are required for interconnection of molecular entities in an atomically defined manner without perturbing or interrupting electronic conjugation.

EXPERIMENTAL DETAILS

All samples were prepared and characterized in an ultrahigh-vacuum chamber (base pressure $< 5 \times 10^{-10}$ mbar) equipped with an Omicron VT scanning tunneling microscope (STM). Cu(111) single crystals were prepared by subsequent cycles of Ar⁺-ion sputtering and annealing at 820 K. Additional low energy electron diffraction (LEED) experiments for further characterization of the precursor structure were carried out in a separate UHV system equipped with standard preparation facilities and LEED optics from Omicron. LEED measurements were

Received: February 8, 2011

Published: May 02, 2011

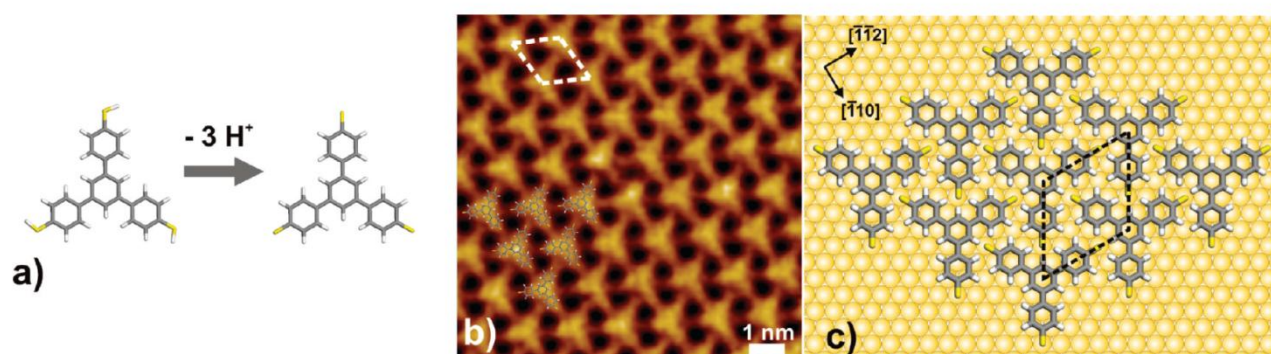


Figure 1. (a) TMB fully deprotonates upon room temperature adsorption on reactive copper surfaces forming a surface-anchored trithiolate. (b) STM topograph of as-deposited TMB on Cu(111) acquired at room temperature ($I_T = 185$ pA, $U_T = 0.79$ V, 10×10 nm², $a = b = 1.30$ nm, $\gamma = 120^\circ$, unit cell indicated by dashed white lines). The densely packed trigonal structure contains one molecule per unit cell. (c) Tentative model of the densely packed trithiolate structure including the Cu(111) substrate. While the azimuthal orientation of the TMB-derived trithiolates with respect to the substrate directions can be inferred from the experiment, the precise adsorption site is not known.

carried out at a sample temperature of ~ 50 K maintained by a closed-cycle helium cryostat. 1,3,5-Tris(4-mercaptophenyl)benzene (TMB) was thermally evaporated from a home-built Knudsen cell with crucible temperatures around 145°C . During deposition and STM imaging the substrate was held at room temperature. STM images were acquired at room temperature and processed by line-wise leveling and 3×3 Gaussian filtering.

RESULTS AND DISCUSSION

In this work, adatom-mediated coordination of TMB (cf. Figure 1a) on Cu(111) into two-dimensional (2D) metal–organic networks based on thiolate–copper coordination bonds is presented. Bulk synthesis already yielded copper–thiolate metal–organic frameworks (MOF)³ and linear polymeric structures.⁴ While surface-confined coordination networks based on copper–carboxylate coordination bonds have been reported by several groups,^{1d,2b,5} to our knowledge, this type of interlinking chemistry has not been utilized for surface-supported 2D systems. We demonstrate that upon thermal annealing an initial precursor structure is converted into copper–thiolate coordinated networks mediated by the free-adatom gas of the Cu(111) surface. Interestingly, the thiolate–copper complexes found in this study contain copper dimers which coordinate two thiolates. In bulk MOFs, interconnects typically consist of single metal atoms as coordination centers. In the proposed system the coordinating metal dimers are additionally stabilized by adsorption on the surface, possibly rendering them unique for surface-confined systems.

In a first preparation step TMB is deposited by thermal sublimation under ultrahigh-vacuum (UHV) conditions on Cu(111) at room temperature and characterized by means of *in situ* STM and LEED. Figure 1b depicts an STM topograph of the resulting self-assembled densely packed trigonal structure with an STM-derived lattice parameter of (1.30 ± 0.05) nm. Accompanying LEED measurements (cf. Supporting Information) aid to identify the monolayer as a commensurate $3\sqrt{3} \times 3\sqrt{3}$ R30° superstructure. Upon adsorption on reactive metal surfaces thiols deprotonate and become thiolates which are anchored by sulfur–metal bonds.⁶ Both the size of the unit cell and the three-fold symmetric appearance of adsorbed TMB in STM topographs substantiate the assumption that TMB fully

deprotonates on Cu(111) and forms three covalent S–Cu bonds with the substrate; a tentative model of the precursor structure is depicted in Figure 1c. However, the formation of a densely packed monolayer indicates a non-negligible contribution from intermolecular interactions for structure formation. While the azimuthal orientation of TMB within the unit cell and with respect to the substrate can be inferred from STM topographs, its absolute adsorption position with respect to the copper substrate remains unknown. Interestingly, the TMB-derived trithiolate molecule is also commensurate with the substrate; i.e. for its actual azimuthal orientation all sulfur atoms reside on similar adsorption sites and can thus simultaneously optimize their interaction with the substrate. Covalent anchoring by three peripheral sulfur groups stabilizes a planar adsorption geometry of TMB on Cu(111), whereas monothiolates tend to adsorb upright,^{6d,7} or inclined, as it is the case for halogen-substituted thiophenols.⁸

In a second preparation step, thermal annealing at 160 – 200°C for ~ 10 min converts the self-assembled trithiolate monolayers into two polymorphs which are both identified as metal–organic coordination networks. STM topographs of both metal-coordinated polymorphs are depicted in Figure 2. Conversion of the initial precursor structure into 2D metal-coordinated networks is accompanied by substantial reorientation and repositioning of TMB molecules, but most importantly by introducing intermolecular copper–thiolate coordination bonds.

The effect of annealing is 2-fold: First lateral mobility of the trithiolate species is enhanced. Second, the area density of the free copper adatom gas is greatly increased, whereby a sufficient amount of highly mobile coordination centers is supplied.

The influence of a 2D adatom gas has been recognized as an important contribution to the surface chemistry of metals.⁹ The adatom gas originates from a temperature-dependent evaporation/condensation equilibrium at step-edges. At lower temperatures, processes with lower activation energies are dominant, i.e. mass transport along step-edges. For higher temperatures mass exchange between step-edges and terraces is the dominant process¹⁰ leading to a drastic increase of the free adatom concentration already at moderate temperatures of ~ 500 K.¹¹ Conversion of initially intermolecular hydrogen-bonded networks into metal–organic networks on Cu(111) in this temperature range have similarly been reported by Matena^{2b}

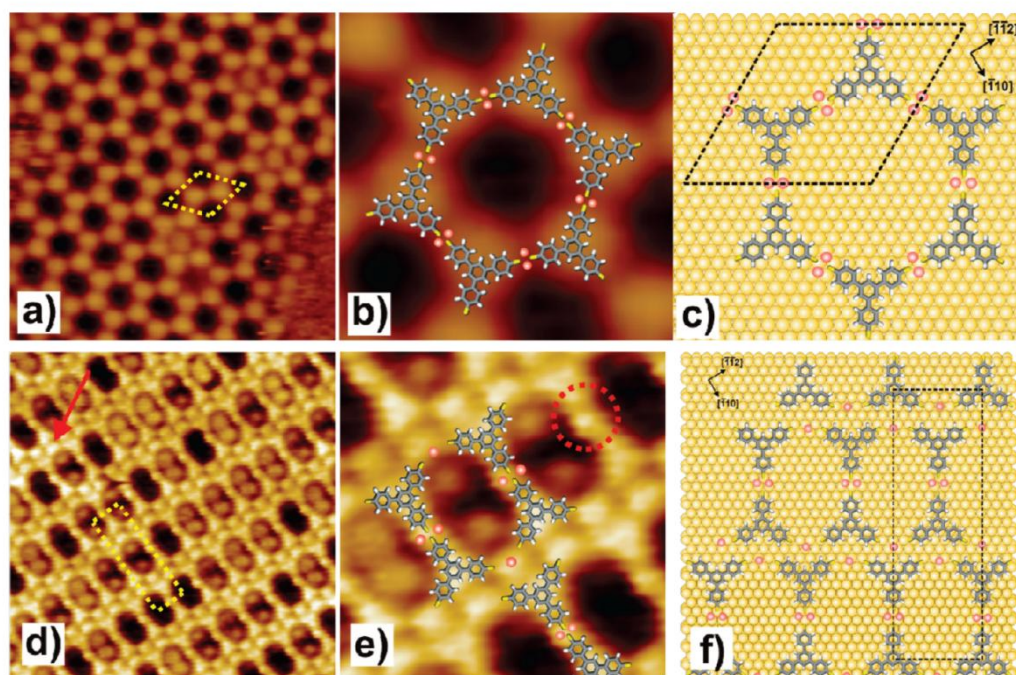


Figure 2. (a) STM topograph of honeycomb structure with unit cell indicated ($U_T = -1.0$ V, $I_T = 67$ pA, 24×24 nm², $a = b = 3.4$ nm, $\gamma = 120^\circ$) and (b) close-up (6.5×6.5 nm²) of honeycomb structure with molecular model. (c) Tentative model of the honeycomb structure including the substrate; the hexagonal unit cell is indicated by black dashed lines. (d) STM topograph of dimer row structure with unit cell indicated ($U_T = -0.8$ V, $I_T = 121$ pA, 18×18 nm², $a = 2.2$ nm, $b = 6.6$ nm, $\gamma = 90^\circ$) and (e) close-up (6.9×6.9 nm²) of dimer row structure with molecular model. Protruding features are observed in the STM contrast at the center of a dimer (marked by the dashed circle) and hint toward metal coordination. (f) Tentative model of the dimer row structure including the substrate; the rectangular unit cell is indicated by black dashed lines.

and Pawin.^{2a} In the latter work, annealing at lower temperatures leads to a partially hydrogen-bonded and partially metal-coordinated polymorph. As already mentioned above for TMB, two different metal-coordinated networks, a hexagonal honeycomb and a centered rectangular dimer row structure emerge. In both structures copper adatoms coordinate TMB molecules via their thiolate groups.

The hexagonal honeycomb structure (Figure 2a–c) has a lattice parameter of 3.4 nm and belongs to the plane space group $p6mm$. The second structure is less symmetric ($c2mm$) and is composed of rows of dumbbell-shaped dimers (Figure 2e–f). Adjacent dimer rows are offset by exactly half a lattice parameter exactly along the row axes, resulting in a rectangular centered nonprimitive unit cell. During the conversion of the densely packed precursor structure into the porous networks, entrapment of excess TMB molecules within the pores occurs frequently and gives rise to additional contrast features within the pores as evident from Figure 2. This observation is in accord with other experiments on periodic and irregular porous surface-supported networks where molecules, either deposited in excess, captured during structure formation,^{12,13} or additionally deposited¹⁴, were likewise trapped within the pores.

The honeycomb and dimer row structure were observed in coexistence as shown in Figure 3. The relative ratio of both phases slightly depends on the initial coverage of the precursor structure, with a preference for the more densely packed dimer row structure at higher coverages. It is noteworthy that the morphology of the two metal-coordinated TMB polymorphs resembles those of rubrene monolayers both on (110) and (111) copper surfaces¹⁵ and Au(111).¹⁶ Yet, despite the similar appearance of rubrene vs TMB monolayers in STM topographs, their

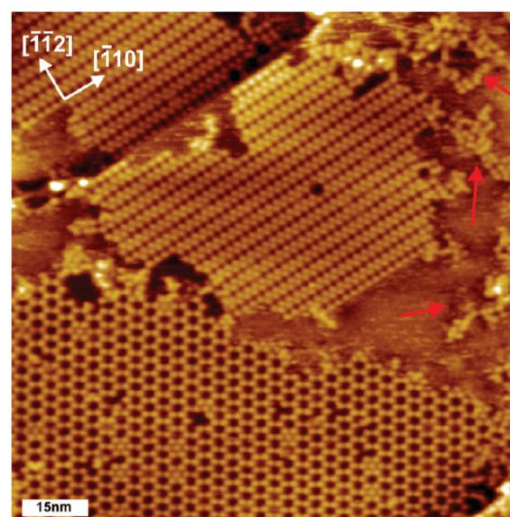


Figure 3. Overview STM topograph illustrating the coexistence of both phases ($U_T = -1.64$ V, $I_T = 66$ pA, 116×116 nm²) on Cu(111). Red arrows indicate first occurrence of degraded molecules starting to appear at annealing temperatures around 220 °C. White arrows indicate crystallographic directions of the substrate.

self-assembly is notably different. In the gas phase rubrene is highly nonplanar and even remains nonplanar after adsorption. TMB, on the other hand, is slightly nonplanar in the gas phase due to an out-of-plane rotation of its peripheral mercaptophenyl units with respect to the phenyl ring at the center. However, the

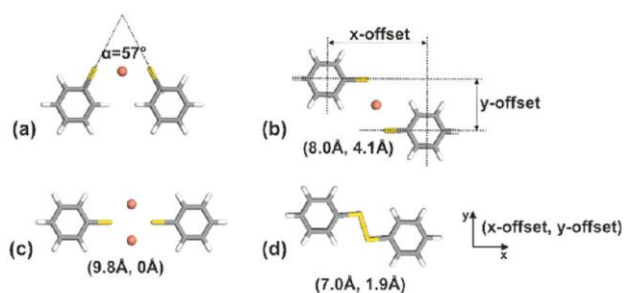


Figure 4. DFT geometry optimized intermolecular bonding schemes for interconnected phenylthiolates via (a) one-center *trans*-coordination *syn*-conformation ($\alpha = 57^\circ$), (b) one-center *trans*-coordination *anti*-conformation (x -offset = 8.0 Å, y -offset = 4.1 Å), (c) two-center coordination bond (x -offset = 9.8 Å, no y -offset), (d) covalent coupling via disulfur-bridge (x -offset = 7.0 Å, y -offset = 1.9 Å). For all bonds, the center-to-center distance of the phenyl groups (x -offset) and the perpendicular axial offset (y -offset) respectively are given in parentheses.

mirror symmetric STM appearance of TMB in all observed structures suggests that it becomes planar upon adsorption due to interactions with the substrate. Also the pronounced chirality of rubrene affects its self-assembly and leads to the expression of chiral structures and aggregates,¹⁷ while no indication of chirality is discernible in any of the TMB structures. Lastly, the interactions which drive self-assembly are distinctly different for rubrene and TMB. In the precursor structure of TMB, covalent bonds between sulfur and copper play an important role, whereas after the phase transition metal coordination becomes the predominant interaction. On the other hand, these types of interactions are absent in rubrene self-assembly, where van der Waals interactions, higher multipole electrostatic interactions, and substrate-mediated interactions govern structure formation.¹⁸

For a fundamental understanding of the thiolate–copper coordination bonds, DFT calculations (cf. Supporting Information for details) have been performed of the connecting nodes, modeled by two phenylthiolates and corresponding copper centers. Four different intermolecular bonding schemes were considered: metal-coordination bonds mediated by one or two copper atoms, and a covalent disulfur bridge. Motivated by experimental results on thiolate–gold complexes¹⁹ both *syn*–*trans* and *anti*–*trans* arrangements were taken into account for the one-center coordination bonds. To reduce the computational cost only the outer phenylthiolate parts were simulated, and for ease of calculations the explicit substrate influence has been neglected in this first approximation. Typically, intermolecular bond lengths of adsorbed systems are altered in comparison to the gas phase, but these differences are normally small and, especially for large entities, often below the accuracy of STM measurements. DFT results on these simplified model systems are depicted in Figure 4. Major findings can be summarized as follows. Only two-center coordination bonds facilitate linear interconnection. One-center coordination bonds and covalent disulfur bridges both result in lateral offsets perpendicular to the bond axis.

The one-center *anti* conformational arrangement and the disulfur bridge result in a lateral bond offset of ~ 4.1 Å and ~ 1.9 Å, respectively. These lateral offsets are sufficiently large to be identifiable in STM topographs. In the one-center *syn* conformational assembly the molecular axes include an angle of 57° , which is significantly larger than the 35° reported for

Au-coordinated methylthiolate by Voznyy and co-workers.¹⁹ This can readily be explained by steric repulsion, being more pronounced for the bulky phenyl ligands as compared to that for methyl groups.

According to DFT results, the total binding energy of two-center coordination complexes is strongest with a value of 555 kJ/mol. Total binding energies of *trans*–*syn* (394 kJ/mol) and *trans*–*anti* (397 kJ/mol) one-center coordination complexes are comparable, but notably lower than for the two-center complex. The covalent disulfur bridge is the weakest bond with a strength of 151 kJ/mol. Covalent S–S bonds exhibit a certain variability of bond angles and energies,²⁰ with the latter value being within the typical range.

Both the honeycomb and the dimer row structure contain dumbbell shaped TMB dimers as basic structural motif. High resolution STM images of both polymorphs occasionally show protruding features between dimers; an example is marked in Figure 2e. An additional STM topograph of the honeycomb structure very clearly showing protruding contrast features at the center position between adjacent molecules is provided in the Supporting Information (cf. Figure S2). Although these contrast features hint toward intermolecular bonds through metal-coordination, they do not allow to unambiguously infer the exact number of metal-coordination centers per bond. Yet, since no lateral displacement occurs along the dimer axis, the DFT calculations suggest coordination of the thiolate groups by two copper atoms as depicted in Figure 4c. This conclusion is further substantiated by comparison of experimental and theoretical bond lengths. STM data yield a center-to-center distance of $2.0 (\pm 0.2)$ nm between two TMB molecules in the dimer. DFT results in combination with the intramolecular distance between central and outer phenyl rings in TMB (0.46 nm for a geometry optimized isolated molecule) postulate a dimer center-to-center distance of 1.90 nm. Accordingly, the experimental lattice parameter of the honeycomb structure (3.4 nm) is in good agreement with the anticipated lattice parameter from the two-center coordination interconnect (3.3 nm), while both the one-center coordination scenario (2.9 nm) and the covalent disulfur bridge (2.8 nm) would yield notably smaller lattice parameters. From the $p6mm$ symmetry it can be concluded that all intermolecular bonds in the honeycomb structure are equivalent. A complete model of the honeycomb structure is overlaid in the STM topograph depicted in Figure 2b, and a tentative structural model including the substrate is separately presented in Figure 2c.

Yet, due to its lower symmetry the dimer row structure cannot consistently be explained solely on the basis of two-center coordination bonds. Thus, a bonding scheme is proposed involving different types of intermolecular bonds. Both appearance and center-to-center distance of dimers (~ 2.0 nm) within the rows are similar to the honeycomb structure. Also in both structures the dimers have the same orientation with respect to the Cu(111) substrate, i.e. their axes are oriented along the $\langle 1\bar{1}2 \rangle$ direction. This registry points toward a distinct epitaxial relation between the dimers and the Cu(111) substrate. Hence, it is concluded that also the dimers within the dimer row structure are similarly interconnected by two-center coordination bonds. These dimers assemble in parallel rows, where adjacent rows are shifted half a lattice parameter with respect to the row direction. STM topographs exhibit protruding contrast features directly above and below intrarow neighbors (marked in Figure 2d by a red arrow) which point toward a *trans*–*syn* arrangement, as implemented in the models in e and f of Figure 2, where the

former is overlaid to the STM image and the latter model includes the substrate. Since coordinating copper atoms cannot be resolved separately, as is also the case for the two atoms coordinating the dimers, dimer–dimer coordination by more than one Cu atom cannot be excluded. Polynuclear copper–thiolate coordination bonds are common,²¹ where coordinating copper clusters are further stabilized by cuprophilicity.²² For instance, coordination by Cu₃ clusters has also been observed previously for bulk systems.³

Since the doubly copper-coordinated dimer is the structural motif of both the honeycomb and the dimer row structure, its adsorption geometry on the Cu(111) substrate is of particular interest. A tentative model which takes both the STM-derived orientation with respect to the substrate and the DFT-derived atomic configuration of the interconnect into account is provided in Figure 5. This model illustrates that both coordinating copper atoms could indeed adsorb at similar sites, for instance as tentatively shown in three-fold hollow sites (yellow: substrate atoms).

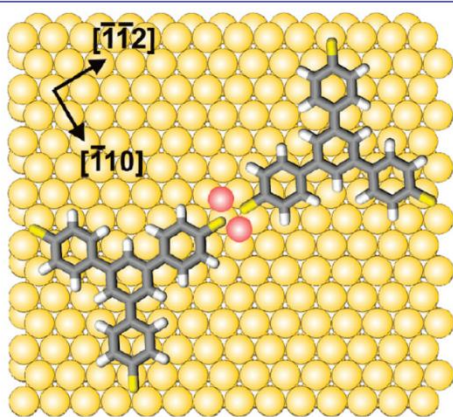


Figure 5. Tentative model of the adsorption geometry of a doubly copper coordinated TMB dimer including the Cu(111) substrate. Both coordinating copper atoms (colored red) could adsorb on similar lattice sites to simultaneously optimize their adsorption energy, e.g. as shown on three-fold hollow sites (yellow: substrate atoms).

surface-confined metal-coordination complexes range most likely between the two extreme values, i.e. 2.87 Å as derived from our DFT calculations for a fully neglected and 2.55 Å—the Cu(111) lattice parameter—for a fully effective substrate influence. Therefore, in summary the actual Cu–Cu distance might result from a compromise and interplay between the periodic potential of the substrate which favors the smaller Cu–Cu spacing closer to the lattice constant and the gas phase Cu–Cu spacing which is more influenced by the orbital configuration and hybridization of the thiolate and the copper centers.

In order to reveal the specific role of the Cu(111) substrate for the phase transition and to shed light on the chemical properties and reactivity of copper adatoms, the same type of experiments with similar sample preparation protocols were conducted on Ag(111). Room-temperature deposition of TMB on Ag(111) also yields a densely packed trigonal structure (cf. Figure 6a, $a = 1.35 \pm 0.05$ nm). Since the lattice parameter of the trigonal structure on Ag(111) is similar to the value obtained on Cu(111) within experimental error, the precursor structure on Ag(111) is also identified as densely packed deprotonated trithiolates which are covalently anchored to the substrate through three peripheral thiolate–metal bonds. While the initial TMB precursor structures appear similar on both substrates, the response to thermal annealing is distinctly different on Ag(111): annealing up to 250 °C for ~1 h did not result in a phase transition; however, after the sample annealed at 300 °C for ~1 h, disordered glassy networks were observed in coexistence with remnants of the precursor structure; a typical STM topograph is depicted in Figure 6b. Nonperiodic glassy organic networks have recently gained substantial interest. Particularly nice examples include metal-coordination networks of nonlinear, prochiral ditopic organic linkers with cobalt atoms²³ and hydrogen-bonded cytosine networks on Au(111).^{13b,24} Further, structurally comparable irregular organic networks have also been observed, when halogenated precursor molecules were polymerized by surface-mediated reactions into covalent networks.²⁵ While the irregularity of the glassy metal-coordination and hydrogen-bonded networks arises from the low symmetry of the building blocks in combination with the energetic equivalence of various different basic intermolecular bond motifs, the degree of disorder typically

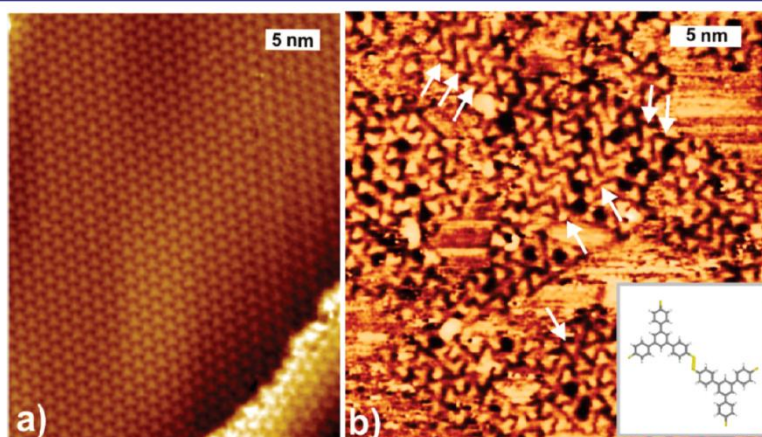


Figure 6. STM topographs of TMB deposited on Ag(111) (a) as-deposited at room temperature ($U_T = -0.33$ V, $I_T = 44$ pA, 30×39 nm²) and (b) after annealing to 300 °C for ~1 h ($U_T = -0.98$ V, $I_T = 85$ pA, 30×30 nm²). The precursor structure on Ag(111) appears similar to Cu(111) with a similar lattice parameter of (1.35 ± 0.05) nm. Annealing of as-deposited samples at conditions which would already result in irreversible deterioration of the networks on Cu(111), yields a glassy disordered network on Ag(111). Within the disordered networks interconnected dimers can be discerned (marked by white arrows); their dimensions are consistent with formation of covalent disulfur bridges.

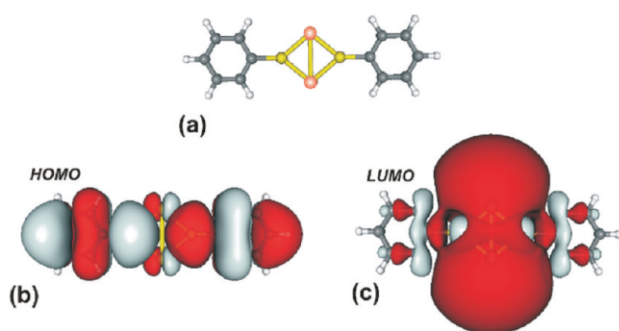


Figure 7. DFT results of structure and frontier molecular orbitals of a two-center coordination bond interconnecting two phenylthiolates (a) geometry, (b) HOMO, (c) LUMO of the complex.

observed for covalent networks is owed to the irreversibility of the covalent molecular interlinks under the growth conditions, which inhibits postcorrection of topological defects. A closer look at the disordered TMB structures on Ag(111) reveals dimers with a distinct lateral offset to the interconnecting axis; examples are marked in Figure 6b by white arrows. The lateral offset is consistent with DFT-derived values for disulfur bridges; consequently, we propose that the dimers observed after a thermal treatment of the precursor structure on Ag(111) are covalently interlinked.

An interesting, not entirely solved question is why adatom-mediated formation of metal-coordination networks was observed for the same TMB molecules on Cu(111) but not on Ag(111). On both substrates, the densely packed precursor structures obtained upon room temperature deposition are structurally quite similar, and differences in their precise epitaxial relations between both substrates can hardly account for the absence of metal-coordination networks on Ag(111). Also the temperature dependent densities of the adatom gases on both surfaces are comparable²⁶ ruling out adatom availability as a decisive criterion. Even more so, since tempering the Ag(111) samples up to significantly higher temperatures should have provided a sufficient amount of adatoms. Nevertheless, silver coordinated TMB metal-organic networks have never been observed, but only irregular networks. The absence of metal-coordination networks on Ag(111) is best explained by a different affinity of Cu vs Ag adatoms to form metal-coordination bonds with thioliates. This hypothesis is in accord with experimental findings on the adatom-mediated formation of carboxylate-based metal-coordination networks on Cu(111) vs Ag(111). While metal-coordination networks of trimesic acids were readily observed on Cu(111), their formation was again absent on Ag(111).⁹ Interestingly, preceding deposition of copper onto Ag(111) promoted the formation of trimesic acid metal-coordination networks also on this substrate. These results are consistently explained by the assumption that copper deposition on Ag(111) introduces a copper adatom gas which is in equilibrium with the deposited copper islands. The higher reactivity of this artificially introduced, extrinsic copper adatom gas is the driving force for formation of copper metal-coordination networks.

Moreover, the present results on covalently interlinked TMB molecules on Ag(111) indicate that the lateral offset of disulfur-bridged molecules can clearly be resolved in STM and hence indirectly prove that the porous TMB networks on Cu(111) are not built up by disulfur-bridged molecules.

In order to illustrate the electronic properties of the copper-thiolate metal-coordination interlink, DFT derived frontier molecular orbitals are depicted in Figure 7. Evidently, both HOMO and LUMO of bicoordinated phenylthiolates exhibit intensity at the bond site. The LUMO appears to be more localized at the bond, whereas the HOMO is evenly distributed across the metal-coordination complex. Such delocalization allows for coherent electron transport through the metal-coordination bond, rendering this interconnection chemistry a suitable candidate for interlinking single molecules into more complex molecular electronics circuitry.

SUMMARY

In summary, adatom-mediated 2D metal-organic networks were synthesized on Cu(111) by thermal annealing of a self-assembled precursor structure. The two observed metal-organic networks are based on metal-coordination bonds between thioliates and either one or two copper adatoms. Comparison between DFT-derived and experimental bond lengths and geometries aided in the identification of intermolecular coordination bonds. In contrast, deposition on Ag(111) resulted in a similar precursor structure, but annealing at higher temperatures only resulted in irregular structures, where monomers are interconnected by covalent disulfur bridges. These pronounced differences between both surfaces are explained by a higher affinity of copper adatoms as compared to silver adatoms to form metal-coordination bonds with thioliates.

As suggested by the spatial distributions of their frontier molecular orbitals, copper-thiolate complexes are fully electronically conjugated. This intriguing feature renders copper-thiolate coordination bonds particularly interesting for organic conductors and molecular electronics. Especially the envisioned molecular electronics applications not only require precise electronic function within a single molecule but also equally directional communication between molecules. Yet, up to now the issue of interconnecting single-molecule devices into more complex circuits is not satisfactorily addressed. Numerous studies concluded that, for contacts and interconnects, bond topology on the atomic level is of utmost importance due to the coherent nature of electron transport in molecular electronics. Hence, means to interconnect molecular entities in an atomically defined manner without perturbing or interrupting electronic conjugation are urgently required. Thiol groups in combination with copper coordination centers are ideally suited as “solder” for molecular electronics due to their electronic conjugation, their relatively high stability, and not at least due to their compatibility with self-assembly bottom-up fabrication techniques.

ASSOCIATED CONTENT

S Supporting Information. Synthesis and calculational details, additional LEED and STM results. This material is available free of charge via the Internet at <http://pubs.acs.org>.

AUTHOR INFORMATION

Corresponding Author
markus@lackinger.org

Present Address

[#]Institut National de la Recherche Scientifique, Université du Québec, 1650 boulevard Lionel-Boulet, Varennes, QC, J3X 1S2 Canada.

ACKNOWLEDGMENT

Financial support by the Deutsche Forschungsgemeinschaft (DFG) within the Nanosystems-Initiative Munich (NIM) and with FOR 516 (Siegen) is gratefully acknowledged. St.S. and G.E. are particularly grateful for support by the Elitenetzwerk Bayern and the Hanns-Seidel Stiftung. T.S. acknowledges support by the Fonds der Chemischen Industrie.

REFERENCES

- (1) (a) Barth, J. V. *Annu. Rev. Phys. Chem.* **2007**, *58*, 375–407. (b) Stepanow, S.; Lin, N.; Barth, J. V. *J. Phys.: Condens. Matter* **2008**, *20*, 184002. (c) Stepanow, S.; Lingenfelder, M.; Dmitriev, A.; Spillmann, H.; Delvigne, E.; Lin, N.; Deng, X. B.; Cai, C. Z.; Barth, J. V.; Kern, K. *Nat. Mater.* **2004**, *3*, 229–233. (d) Barth, J. V.; Weckesser, J.; Lin, N.; Dmitriev, A.; Kern, K. *Appl. Phys. A* **2003**, *76*, 645–652. (e) Ruben, M.; Rojo, J.; Romero-Salguero, F. J.; Uppadine, L. H.; Lehn, J. M. *Angew. Chem., Int. Ed.* **2004**, *43*, 3644–3662.
- (2) (a) Pawin, G.; Wong, K. L.; Kim, D.; Sun, D. Z.; Bartels, L.; Hong, S.; Rahman, T. S.; Carp, R.; Marsella, M. *Angew. Chem., Int. Ed.* **2008**, *47*, 8442–8445. (b) Matena, M.; Stöhr, M.; Riehm, T.; Bjork, J.; Martens, S.; Dyer, M. S.; Persson, M.; Lobo-Checa, J.; Müller, K.; Enache, M.; Wadepohl, H.; Zegenhagen, J.; Jung, T. A.; Gade, L. H. *Chem.—Eur. J.* **2010**, *16*, 2079–2091.
- (3) He, J.; Yang, C.; Xu, Z. T.; Zeller, M.; Hunter, A. D.; Lin, J. H. *J. Solid State Chem.* **2009**, *182*, 1821–1826.
- (4) Che, C. M.; Li, C. H.; Chui, S. S. Y.; Roy, V. A. L.; Low, K. H. *Chem.—Eur. J.* **2008**, *14*, 2965–2975.
- (5) (a) Lin, N.; Dmitriev, A.; Weckesser, J.; Barth, J. V.; Kern, K. *Angew. Chem., Int. Ed.* **2002**, *41*, 4779–4783. (b) Perry, C. C.; Haq, S.; Frederick, B. G.; Richardson, N. V. *Surf. Sci.* **1998**, *409*, 512–520. (c) Dougherty, D. B.; Maksymovych, P.; Yates, J. T. *Surf. Sci.* **2006**, *600*, 4484–4491.
- (6) (a) Driver, S. M.; Woodruff, D. P. *Surf. Sci.* **2000**, *457*, 11–23. (b) Ferral, A.; Paredes-Olivera, P.; Macagno, V. A.; Patrito, E. M. *Surf. Sci.* **2003**, *525*, 85–99. (c) Keller, H.; Simak, P.; Schrepp, W.; Dembowski, J. *Thin Solid Films* **1994**, *244*, 799–805. (d) Konopka, M.; Turansky, R.; Dubecky, M.; Marx, D.; Stich, I. *J. Phys. Chem. C* **2009**, *113*, 8878–8887. (e) Maksymovych, P.; Sorescu, D. C.; Yates, J. T. *Phys. Rev. Lett.* **2006**, *97*, 146103. (f) Sardar, S. A.; Syed, J. A.; Ikenaga, E.; Yagi, S.; Sekitani, T.; Wada, S.; Taniguchi, M.; Tanaka, K. *Nucl. Instrum. Methods Phys. Res., Sect. B* **2003**, *199*, 240–243.
- (7) Di Castro, V.; Bussolotti, F.; Mariani, C. *Surf. Sci.* **2005**, *598*, 218–225.
- (8) Wong, K. L.; Lin, X.; Kwon, K. Y.; Pawin, G.; Rao, B. V.; Liu, A.; Bartels, L.; Stolbov, S.; Rahman, T. S. *Langmuir* **2004**, *20*, 10928–10934.
- (9) Lin, N.; Payer, D.; Dmitriev, A.; Strunskus, T.; Woll, C.; Barth, J. V.; Kern, K. *Angew. Chem., Int. Ed.* **2005**, *44*, 1488–1491.
- (10) Giesen, M. *Surf. Sci.* **1999**, *442*, 543–549.
- (11) Giesen, M. *Prog. Surf. Sci.* **2001**, *68*, 1–153.
- (12) Griessl, S.; Lackinger, M.; Edelwirth, M.; Hietschold, M.; Heckl, W. M. *Single Mol.* **2002**, *3*, 25–31.
- (13) (a) Ruben, M.; Payer, D.; Landa, A.; Comisso, A.; Gattinoni, C.; Lin, N.; Collin, J. P.; Sauvage, J. P.; De Vita, A.; Kern, K. *J. Am. Chem. Soc.* **2006**, *128*, 15644–15651. (b) Otero, R.; Lukas, M.; Kelly, R. E. A.; Xu, W.; Laegsgaard, E.; Stensgaard, I.; Kantorovich, L. N.; Besenbacher, F. *Science* **2008**, *319*, 312–315. (c) Kühne, D.; Klappenberger, F.; Decker, R.; Schlickum, U.; Brune, H.; Klyatskaya, S.; Ruben, M.; Barth, J. *J. Phys. Chem. C* **2009**, *113*, 17851–17859.
- (14) (a) Stöhr, M.; Wahl, M.; C.H., G.; Riehm, T.; Jung, T. A.; Gade, L. H. *Angew. Chem., Int. Ed.* **2005**, *44*, 7394–7398. (b) Stöhr, M.; Wahl, M.; Spillmann, H.; Gade, L. H.; Jung, T. A. *Small* **2007**, *3*, 1336–1340.
- (15) (a) Miwa, J. A.; Cicoira, F.; Bedwani, S.; Lipton-Duffin, J.; Perepichka, D. F.; Rochefort, A.; Rosei, F. *J. Phys. Chem. C* **2008**, *112*, 10214–10221. (b) Miwa, J. A.; Cicoira, F.; Lipton-Duffin, J.; Perepichka, D. F.; Santato, C.; Rosei, F. *Nanotechnology* **2008**, *19*, 424021.
- (16) Pivetta, M.; Blüm, M.-C.; Patthey, F.; Schneider, W.-D. *Angew. Chem., Int. Ed.* **2008**, *47*, 1076–1079.
- (17) Blüm, M.-C.; Cavar, E.; Pivetta, M.; Patthey, F.; Schneider, W.-D. *Angew. Chem., Int. Ed.* **2005**, *44*, 5334–5337.
- (18) Tomba, G.; Stengel, M.; Schneider, W.-D.; Baldereschi, A.; De Vita, A. *ACS Nano* **2010**, *4*, 7545–7551.
- (19) Voznyy, O.; Dubowski, J. J.; Yates, J. T.; Maksymovych, P. *Angew. Chem., Int. Ed.* **2009**, *131*, 12989–12993.
- (20) Steudel, R. *Angew. Chem., Int. Ed. Engl.* **1975**, *14*, 655–664.
- (21) Ahte, P.; Palumaa, P.; Tamm, T. *J. Phys. Chem. A* **2009**, *113*, 9157–9164.
- (22) Hermann, H. L.; Boche, G.; Schwerdtfeger, P. *Chem.—Eur. J.* **2001**, *7*, 5333–5342.
- (23) Marschall, M.; Reichert, J.; Weber-Bargioni, A.; Seufert, K.; Auwärter, W.; Klyatskaya, S.; Zoppellaro, G.; Ruben, M.; Barth, J. V. *Nature Chem.* **2010**, *2*, 131–137.
- (24) Kelly, R. E. A.; Lukas, M.; Kantorovich, L. N.; Otero, R.; Xu, W.; Mura, M.; Laegsgaard, E.; Stensgaard, I.; Besenbacher, F. *J. Chem. Phys.* **2008**, *129*, 184707.
- (25) (a) Gutzler, R.; Walch, H.; Eder, G.; Kloft, S.; Heckl, W. M.; Lackinger, M. *Chem. Commun.* **2009**, 4456–4458. (b) Walch, H.; Gutzler, R.; Sirtl, T.; Eder, G.; Lackinger, M. *J. Phys. Chem. C* **2010**, *114*, 12604–12609.
- (26) Zhang, J. M.; Song, X. L.; Zhang, X. J.; Xu, K. W.; Ji, V. *Surf. Sci.* **2006**, *600*, 1277–1282.

Supporting Information

Extended Two-Dimensional Metal-Organic Frameworks Based on Thiolate-Copper

Coordination Bonds

Hermann Walch, Jürgen Dienstmaier, Georg Eder, Rico Gutzler, Stefan Schlögl,

*Thomas Sirtl, Kalpataru Das, Michael Schmittel, and Markus Lackinger**

Synthesis of TMB

Synthesis of TMB:[24] Solid NaSMe (0.395 g, 5.64 mmol) was added in one portion to a solution of 1,3,5-tris(4-bromophenyl)benzene (1.00 g, 1.84 mmol) in dry DMF (35 mL). The reaction mixture was stirred for 1 h at 150 °C. Additional NaSMe (0.395 g, 5.64 mmol) was added, heating was continued for 1 h, and then a third portion of NaSMe (0.395 g, 5.64 mmol) was added to the reaction. The mixture was heated at 150 °C for another 6 h, cooled to 40 °C, and diluted with acetic acid (1.30 mL) and water (39.0 mL). The product forms as a pale gray precipitate, which was filtered, washed with water, and dried in vacuum to afford pure 1,3,5-tris(4-mercaptophenyl)benzene (0.650 g, 88%), mp 179-180 °C (uncorrected). IR (film / cm⁻¹): 3055 (m), 2987 (w), 2306 (w), 1422 (m), 1264 (s), 896 (m), 751 (s); ¹H NMR (CD₂Cl₂, 400 MHz): δ 7.71 (s, 3H), 7.58 (d, J = 8.3 Hz, 6H), 7.38 (d, J = 8.3 Hz, 6H), 3.62 (s, 3H). ¹³C NMR (CD₂Cl₂, 100 MHz): δ 141.8, 138.5, 131.0, 129.9, 128.2, 124.7. Elemental anal. for C₂₄H₁₈S₃: Calcd. C 71.60, H 4.51, S 23.89; found C 71.46, H 4.49, S 24.27.

Computational Details

DFT calculations were conducted with the Gaussian 03 software package. The B3LYP hybrid functional was used in combination with the 6-31+G* basis set for the elements hydrogen, carbon, and sulfur, and the TZVP basis set for copper. Geometries were optimized for neutral assemblies with atom positions fixed in a plane, allowing equilibration of atomic coordinates only within this plane. Standard convergence criteria were applied. Total binding energies were calculated as the difference between energies of the geometry optimized complexes and the summed energies of all individually geometry optimized single entities, i.e. phenylthiolate and copper species. Counterpoise correction as included in the Gaussian 03 package did not yield significantly different values, with differences being less than 5 kJ/mol.

Although these simplified model calculations only roughly approximate the substrate's influence by enforced planarity, tendencies concerning association topology and binding energies of the different bonding schemes can be identified. In addition, DFT derived bond lengths can be applied to estimate lattice parameters of resulting metal-organic networks.

Additional LEED measurements

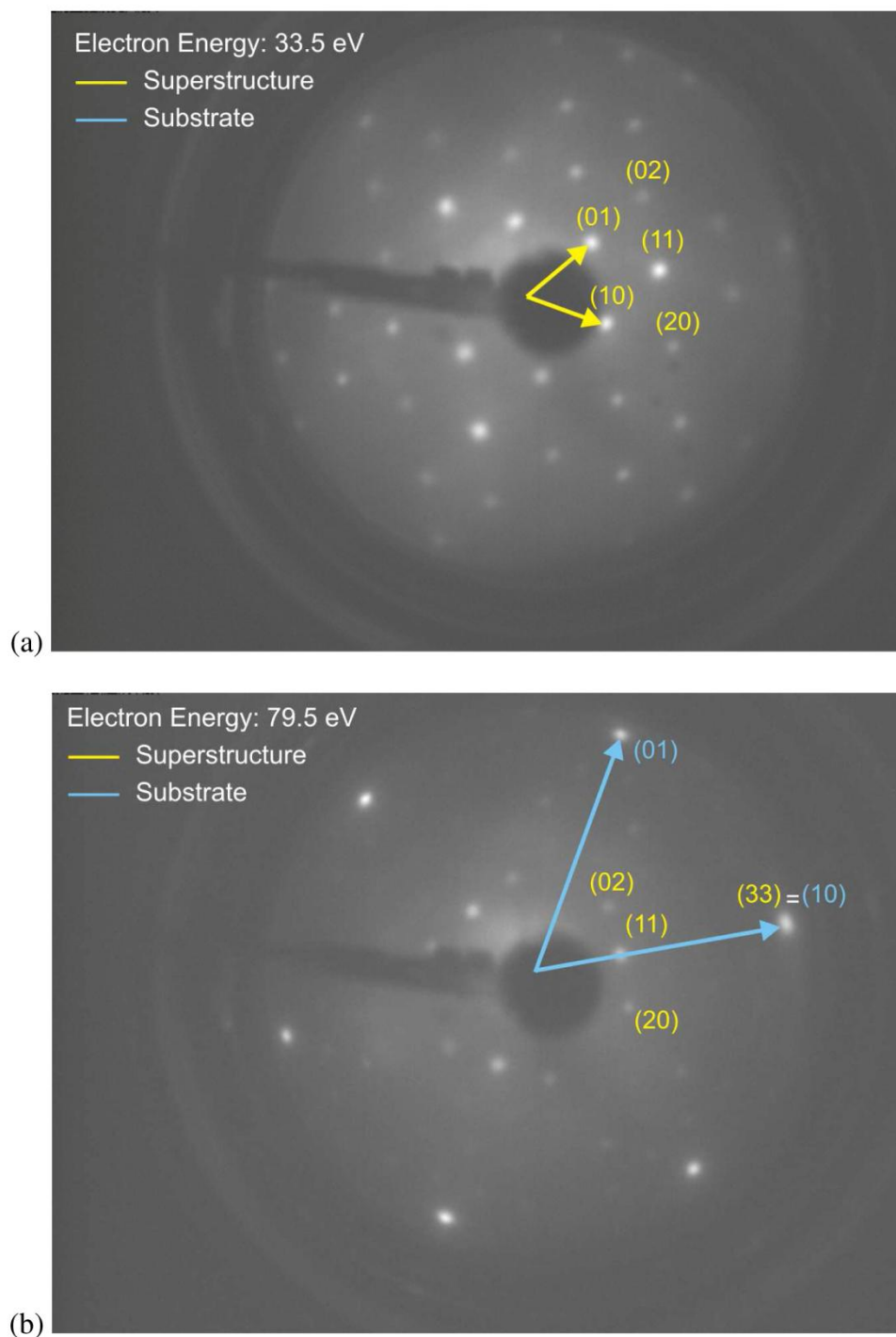


Fig. S1 LEED diffraction patterns of the trigonal densely packed precursor structure. The sample was prepared by room temperature deposition of TMB on Cu(111) and LEED patterns were acquired at sample temperatures of ~ 50 K with electron energies of a) 33.5 eV and b) 79.5 eV. The (hk) values refer to the reflection indices, yellow colors denote superstructure reflections, blue colors substrate reflections. These diffraction experiments reveal the TMB room temperature structure as a commensurate $3\sqrt{3}\times 3\sqrt{3}$ $R30^\circ$ superstructure. This is evident in the LEED pattern acquired at higher electron energy, where the (33) superstructure and (10) substrate reflections coincide.

Additional STM topograph

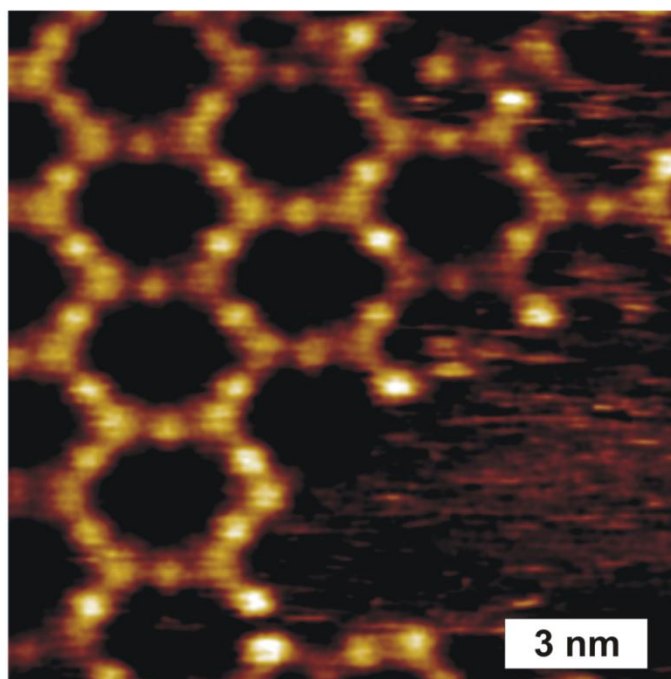


Fig. S2 Additional STM topograph of the metal-coordinated honeycomb polymorph on Cu(111) ($I_T = 83$ pA, $U_T = -1.95$ V, 14×14 nm²). Although the hexagonal structure appears slightly distorted due to thermal drift, apparent protrusions are clearly discernable at the middle of each side of each hexagon, i.e. midst between two adjacent TMB molecules. This peculiar STM contrast was occasionally observed and is attributed to special imaging properties of the STM tip. The protrusions are interpreted as metal-coordination centers and further support the hypothesis of intermolecular bonding through adatom mediated metal coordination.

Synthesis of Well-Ordered COF Monolayers: Surface Growth of Nanocrystalline Precursors *versus* Direct On-Surface Polycondensation

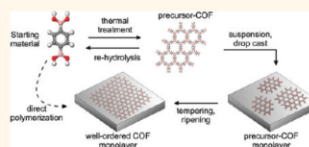
Jürgen F. Dienstmaier,^{†,*} Alexander M. Gigler,[‡] Andreas J. Goetz,[‡] Paul Knochel,[§] Thomas Bein,[§] Andrey Lyapin,[⊥] Stefan Reichmaier,[⊥] Wolfgang M. Heckl,[†] and Markus Lackinger^{†,*}

[†]Deutsches Museum, Museumsinsel 1, 80538 Munich, Germany, TUM School of Education, Technische Universität Munich, Schellingstrasse 33, 80799 Munich, Germany, and Center for NanoScience (CeNS), [‡]Department for Earth- and Environmental Sciences and Center for NanoScience (CeNS), Ludwig-Maximilians-University, Theresienstrasse 41, 80333 Munich, Germany, [§]Department of Chemistry and Center for NanoScience (CeNS), Ludwig-Maximilians-University, Butenandtstrasse 11 (E), 81377 Munich, Germany, and [⊥]Physical Electronics GmbH, Fraunhoferstr. 4, 85737 Ismaning, Germany

Great chemical and structural variety of surface-supported two-dimensional porous molecular networks has been demonstrated over the past decade.^{1,2} Formation and stabilization of porous monolayers can be mediated by various types of intermolecular interactions, most prominently by hydrogen bonding³ and metal–ligand coordination,⁴ but also by comparatively weak and nondirectional van der Waals interactions.⁵ Owing to the weak to intermediate strength of these bond types, intermolecular links become reversible during network formation; hence, defect correction is possible and long-range-ordered structures are frequently obtained. Porous monolayers are highly interesting from a basic science perspective but also auspicious for nanotechnological applications, for instance, as nanoreactors for the synthesis of nanoparticles,¹ as templates for nanopatterning,⁶ as well as for organic electronics.^{7,8} However, many of the above applications or related processing steps demand higher stability of the networks, which ultimately leads to the requirement of strong intermolecular bonds, as realized in 2D polymers and covalent organic frameworks (COFs). Previously reported bulk COFs have been synthesized by various reactions such as self-condensation of boronic acids or co-condensation with polyols,^{9,10} imine bond formation,¹¹ trimerization of nitriles,¹² and most recently, by means of hydrazine bond formation.¹³ Bulk COFs have attracted considerable interest due to their porosity and low density in combination with the extraordinary stability of a covalent material.

ABSTRACT Two different straightforward synthetic approaches are presented to fabricate long-range-ordered monolayers of a covalent organic framework (COF) on an inert, catalytically inactive graphite surface.

Boronic acid condensation (dehydration) is employed as the polymerization reaction. In the first approach, the monomer is prepolymerized by a mere thermal treatment into nanocrystalline precursor COFs. The precursors are then deposited by drop-casting onto a graphite substrate and characterized by scanning tunneling microscopy (STM). While in the precursors monomers are already covalently interlinked into the final COF structure, the resulting domain size is still rather small. We show that a thermal treatment under reversible reaction conditions facilitates on-surface ripening associated with a striking increase of the domain size. Although this first approach allows studying different stages of the polymerization, the direct polymerization, that is, without the necessity of preceding reaction steps, is desirable. We demonstrate that even for a comparatively small diboronic acid monomer a direct thermally activated polymerization into extended COF monolayers is achievable.



KEYWORDS: 2D COF · surface COF · COF-1 · boronic acid · condensation · STM · surface chemistry

Moreover, COF structures can be tailored *via* rational design of appropriate building blocks.^{9,10,14–19}

Similarly, the challenging synthesis of surface-supported covalent nanostructures and 2D COFs has recently gained substantial interest.²⁰ As polymerization reactions, radical addition,^{21–27} condensation,^{28–34} tip- and electron-beam-induced polymerization,³⁵ and alternative reactions^{36–38} have been employed, first under ultrahigh vacuum (UHV) conditions, but meanwhile also under ambient conditions³⁹ or at the liquid–solid interface.⁴⁰

* Address correspondence to markus@lackinger.org.

Received for review August 24, 2011 and accepted October 31, 2011.

Published online October 31, 2011
10.1021/nn2032616

© 2011 American Chemical Society

Since most of the boronic-acid-derived bulk COFs exhibit a layered structure that consists of π - π stacked covalent sheets, single layers of the corresponding bulk structure can serve as promising model systems for 2D COFs. The pioneering examples in this respect are the self-condensation of 1,4-benzenediboronic acid (BDDBA) and the co-condensation of BDDBA with 2,3,6,7,10,11-hexahydroxytriphenylene (HHTP) on Ag(111) under UHV conditions.²⁹ These experiments yielded monolayer equivalents of so-called COF-1 (self-condensation of BDDBA) and COF-5 (co-condensation of BDDBA + HHTP), whereby we refer to a nomenclature introduced by Yaghi and co-workers for bulk COFs.⁹ However, nonreversible reaction conditions during the on-surface condensation polymerization resulted in high densities of topological defects that inhibited the emergence of long-range order as recently studied in more detail for different coinage metal surfaces and preparation conditions.⁴¹ As an intermediate state between bulk crystals and monolayers, both COF-1 and COF-5 multilayers supported on a graphene substrate were recently demonstrated by a solvothermal approach.⁴²

The objective of the present study is to explore the potential of straightforward synthetic approaches for the reliable and facile preparation of long-range-ordered surface-supported COF monolayers. In order to promote efficient synthesis, the proposed method is conducted under ambient conditions, hence does not require costly and time-consuming vacuum techniques, while it relies on reversible reaction conditions to facilitate long-range order. The targeted structure is a single layer of COF-1, synthesized by self-condensation of BDDBA. Bulk crystals of COF-1 were first obtained by Yaghi and co-workers *via* solvothermal synthesis.⁹ This approach avoids the “crystallization problem”, that is, the absence of defect correction mechanisms during growth due to the irreversibility of covalent interlinks, by maintaining slightly reversible reaction conditions.^{43,44} Self-condensation of boronic acids releases H₂O; consequently, the presence of small amounts of water in solution facilitates slightly reversible reaction conditions. A further aim of this study is to demonstrate polymerization on inert surfaces, in order to become independent of catalytic substrate properties, as they are indispensable for polymerization through radical addition.⁴⁵ Surface-mediated polymerization requires activation in order to break existent bonds and form new bonds. The self-condensation of boronic acids typically requires either reactive surfaces^{29,41} or moderately elevated temperatures in the range of 80–100 °C as in the solvothermal synthesis. Yet, thermal activation can be crucial for on-surface reactions because desorption as a competing, likewise thermally activated, process may inhibit the surface-bound reaction. The BDDBA monomer is comparatively small and features a low desorption barrier;

hence, first a method is proposed where the monomers are prepolymerized into larger entities that already exhibit the COF-1 structure and owing to their size a larger desorption barrier. Although this approach allows control and characterization of single reaction steps, nonetheless, methods for direct polymerization, such as without intermediate reaction steps, are highly desirable. First we describe the prepolymerization of BDDBA into nanocrystalline COF-1 precursors. Adsorbed monolayer structures are characterized in real space by high-resolution scanning tunneling microscopy (STM), whereas their covalent nature is independently verified by photoelectron spectroscopy and by demonstrating their thermal stability. In the last part, we also demonstrate a synthetic approach for the straightforward, direct polymerization of BDDBA.

RESULTS AND DISCUSSION

The BDDBA starting material and the reaction scheme are illustrated in Figure 1. Interestingly, ditopic BDDBA monomers yield 2D covalently cross-linked sheets. The reason is the energetically preferred formation of boroxine rings (B₃O₃) through cyclocondensation of three monomers. In the 2D structure, both boronic acid groups of each BDDBA monomer take part in boroxine rings, resulting in a hexagonal structure with *p6mm* symmetry and a lattice parameter of 1.525 nm, according to DFT geometry optimization.²⁹ COF-1-derived monolayers are porous and feature a hexagonal arrangement of approximately 1.0 nm wide pores.

Two different synthetic approaches are evaluated for the preparation of 2D COF-1 monolayers in this work. First, BDDBA is prepolymerized into nanocrystalline COF-1 precursors, drop-cast on a graphite surface, and the domain size is increased by postprocessing. Second, a BDDBA-containing solution is directly deposited onto the surface, and the condensation is thermally activated. The first synthetic approach allows one to carefully characterize important reaction parameters and intermediate states in order to understand fundamental processes in COF monolayer formation, whereas the second approach is straightforward and efficient for the routine preparation of 2D COF monolayers. In the following, we will describe the procedures for each synthesis route and the characterization of COF monolayers and intermediate states.

Synthesis *via* Prepolymerization into Nanocrystalline Precursor-COFs. COF-1 nanocrystals were synthesized by a mere thermal treatment of the BDDBA starting material without any aid of solvent, yet under reversible reaction conditions (see Materials and Methods for experimental details). Thermally prepolymerized BDDBA will be referred to as precursor-COF in the following. The prepolymerization was monitored by thermal gravimetric analysis (TGA), and COF-1 nanocrystals were characterized by powder X-ray diffraction (PXRD), IR,

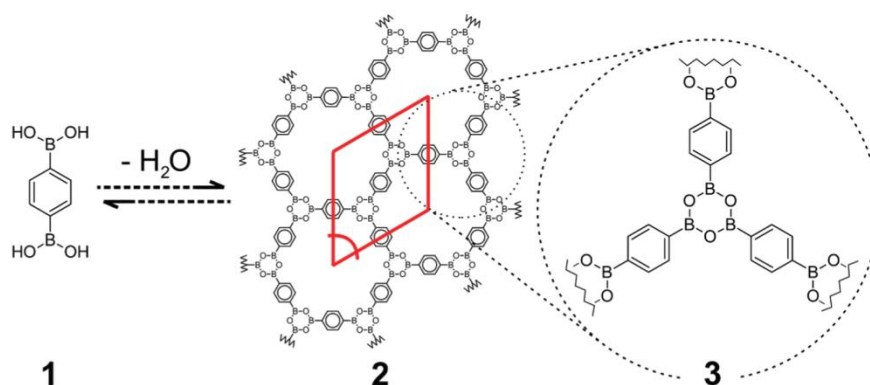


Figure 1. Reaction scheme for the self-condensation of BDDBA from monomers (1) into single 2D COF-1 layers (2). During the condensation, H_2O is released, thus the presence of water facilitates reversible reaction conditions which promote growth of long-range-ordered networks. A unit cell of the 2D COF is marked by red lines, theoretical unit cell parameters from DFT geometry optimization of this hexagonal system amount to $a = b = 1.53 \text{ nm}$ and $\gamma = 60^\circ$.²⁹ (3) Close-up of a boroxine ring resulting from the cyclocondensation of three BDDBA monomers.

and Raman spectroscopy (see Supporting Information for data and spectra). Both Raman and IR spectra of thermally treated BDDBA (*i.e.*, precursor-COFs) exhibit clear signatures of boroxine rings, while spectra of the untreated starting material clearly indicate free boronic acid groups. The IR spectra of precursor-COFs are also in excellent agreement with the results reported for solvothermally synthesized bulk COF-1.⁹ PXRD exhibits rather broad reflections that are also consistent with the previously published COF-1 structure.⁹ The large widths of the reflections originate from the finite sizes of COF-1 nanocrystals, while the presence of $l \neq 0$ reflections indicates stacking in the [001] direction, with a layer separation (*i.e.*, half the lattice parameter) of 0.335 nm. Estimates of the average crystal size were derived from a Rietveld refinement *via* the line broadening model based on the Scherrer equation and amount to 7.8 nm in the lateral direction and 1.0 nm along the [001] stacking direction, that is, about three single layers only (*cf.* Supporting Information).^{46,47} In the TGA measurements, the weight loss sets in at $\sim 150^\circ\text{C}$ and is 94% completed at 300°C . The measured total weight loss of 20.4% is in good agreement with the theoretical expectation for full condensation (21.7%). The slight discrepancy might be caused by unreacted boronic acid groups at the surface of nanocrystals or by the presence of residual unreacted material. From these TGA results, we conclude that a prepolymerization temperature of 250°C is well suited for thermal synthesis and should facilitate full condensation without degradation of precursor-COFs. The amount of residual unreacted BDDBA after thermal treatment is extremely low, as characterized by means of a quartz crystal microbalance (*cf.* Supporting Information for details).

The full reversibility of the polycondensation is demonstrated through rehydrolyzing the precursor-COFs by boiling them in distilled water and recrystallization.

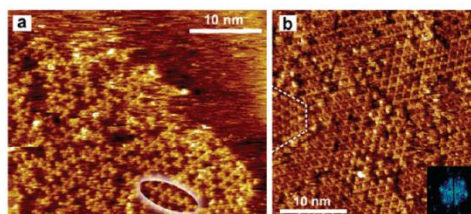


Figure 2. STM images of precursor-COFs on HOPG prepared by drop-casting of thermally treated BDDBA, showing (a) chains that represent fragments of the COF-1 in-plane structure (a representative example is highlighted by the ellipse) and (b) 2D domains, with lateral extensions of typically $<10 \text{ nm}$ and internally hexagonal structure. The inset depicts the 2D FFT of the STM image. Both samples were prepared using heptanoic acid. The STM images were acquired at the liquid–solid interface with the tip immersed in the liquid. Most domains have similar azimuthal orientations, and an example for an occasionally observed exception is marked by dashed lines.

Data from all methods obtained with the rehydrolyzed precipitate were essentially similar to the untreated BDDBA starting material, thereby proving the reversibility of the self-condensation reaction.

After thermal treatment, a small amount ($\sim 5 \text{ mg}$) of the prepolymerized precursor-COF was dispersed in 1.5 mL of various organic solvents (heptanoic acid, nonanoic acid, 1-undecanol, and dodecane). Experiments were conducted with different solvents in order to reveal possible solvent influences. Precursor-COFs were deposited by drop-casting $5 \mu\text{L}$ of the respective suspension onto a freshly cleaved surface of highly oriented pyrolytic graphite (HOPG). Structural characterization of the drop-cast layers was carried out under ambient conditions by high-resolution STM directly at the interface between the graphite substrate and the suspension. STM experiments reveal nearly full coverage of the surface. Predominantly chains and small domains of a hexagonal structure were observed on the surface; representative images are depicted in

Figure 2a,b. Areas between domain boundaries in Figure 2b are covered with smaller chain-like aggregates. The inset of Figure 2b depicts the corresponding 2D fast Fourier transform (2D FFT) of the image and clearly demonstrates the hexagonal symmetry of the domains. Averaging the values of about 40 independent images acquired with a thoroughly calibrated STM after drift and piezo creep have settled down yields lattice parameters of $a = b = 1.4 \pm 0.1$ nm and $\gamma = 60.0 \pm 2.5^\circ$, which are in excellent agreement with both the in-plane lattice parameters reported for COF-1 (1.5 nm)⁹ and with DFT values (1.525 nm) obtained for the 2D analogue.²⁹ However, boronic acids are also known to self-assemble *via* intermolecular hydrogen bonds.⁴⁸ In order to test the robustness of the postulated covalent structural model against competing noncovalent structures, a hypothetical hydrogen-bonded network was simulated by molecular mechanics (MM, *cf.* Supporting Information). Any reasonable structural model must fulfill the experimentally observed $p6mm$ symmetry. In the STM data, connecting nodes between three molecules are clearly observed that would most likely be stabilized by cyclic hydrogen bonds in a noncovalent structure. However, the related MM geometry-optimized structure yields a significantly larger lattice parameter of 2.05 nm and can thus be excluded on experimental grounds. Similar STM experiments on drop-cast precursor-COF layers were carried out with different solvents, where comparable monolayers with similar hexagonal structure and lattice parameters were observed in heptanoic acid and nonanoic acid. However, no precursor-COF monolayers were observed in 1-undecanol and dodecane. These observations can be rationalized by the capability of the carboxylic acid moiety of the fatty acid solvents to stabilize the precursor-COFs in solution *via* strong hydrogen bonds with unreacted boronic acid groups that are prevalent at the edges. This additional favorable hydrogen bond stabilization is not as pronounced in 1-undecanol and entirely absent in the aprotic solvent dodecane, thereby lowering the achievable precursor-COF concentrations. Since usage of two different fatty acid solvents with different chain lengths did not affect the observed monolayer, solvent incorporation into the structures is excluded.

On the basis of careful analysis of structural parameters, we propose that the domains observed after drop-casting precursor-COF suspension are 2D covalent networks which structurally correspond to a single layer of COF-1. The STM image and the corresponding 2D FFT also indicate a preferred azimuthal orientation of the precursor-COF domains with respect to the underlying graphite lattice, pointing toward a substrate templating effect. In most images, a single orientation is prevalent, but domains with deviating azimuthal orientations are also observed occasionally; an example is marked in Figure 2b. This preferred

epitaxial relation hints toward an extremely low thickness of the precursor-COF layer, and their uniform height, where steps have never been observed, indicates a spatially homogeneous thickness. In addition, the apparent height of the precursor-COF layer with respect to the bare graphite substrate as measured at domain boundaries corresponds to 0.30 ± 0.05 nm, which is extremely close to the geometric expectation. From these experimental observations, it is concluded that the STM measurements indeed show a single monolayer of precursor-COFs. However, STM imaging requires electrically conductive samples, and we can thus not fully exclude that the drop-cast deposition could also locally yield higher layer thicknesses, which is not observable by STM. We also note that the lateral extension of the domains below 10 nm in the STM data below 10 nm is consistent with the PXRD results on precursor-COFs.

In order to explore possibilities for increasing the domain size of the highly polycrystalline precursor-COF monolayers by postprocessing, samples were exposed to higher temperatures in a humid atmosphere (see Materials and Methods for details). Drop-cast samples were mounted in the reactor as prepared, that is, with remnants of the volatile solvents. Post-processed samples were characterized after cooling by ambient STM under dry conditions, without solvent on the samples; results are depicted in Figure 3. While the internal hexagonal structure is similar to the precursor-COF monolayer (*cf.* close-up and line profile in Figure 3b,c), a clear increase in domain size well above 40 nm is evident from the overview image. This can only be explained by on-surface ripening of the nanocrystalline precursor-COF domains. The apparent height of the 2D COF-1 adlayer with respect to the substrate as measured at domain boundaries corresponds to 0.30 ± 0.05 nm, proving that the STM observations indeed show a single monolayer of 2D COF-1. Also, the pores appear empty in the STM images, suggesting that residual solvent and monomers were entirely removed during the thermal treatment. While precursor-COF monolayers could only be imaged at the liquid–solid interface with heptanoic and nonanoic acid, extended COF-1 monolayers were also observed after thermal treatment using 1-undecanol and dodecane. This apparent contradiction can be explained by a low, but not vanishing, precursor-COF concentration in dodecane and 1-undecanol. Since the solvents completely evaporate at an early stage of the thermal treatment, all of the previously dispersed precursor-COFs in the entire solvent volume precipitate at the surface. Even so, the precursor-COF concentration in 1-undecanol and dodecane is too low to promote adsorption at the liquid–solid interface; it is apparently sufficient to feature COF monolayers after a thermal treatment.

Although the 2D COFs feature extremely low defect density, occasional point defects like missing building

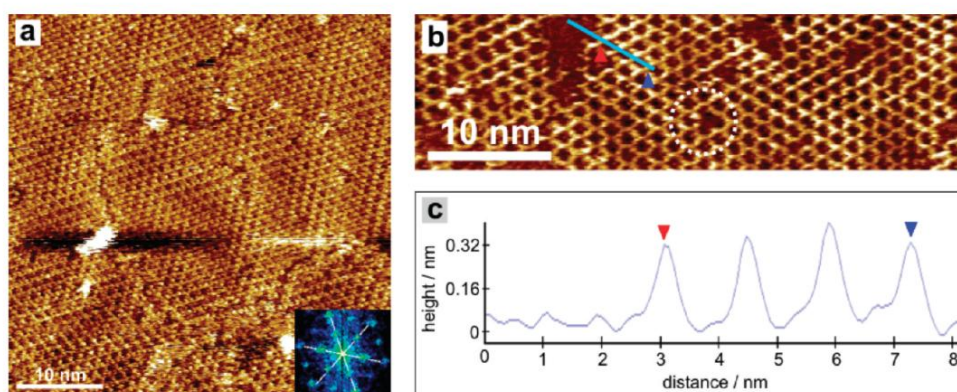


Figure 3. (a) STM image (acquired under dry conditions) of an extended 2D COF-1 monolayer. The sample was prepared by deposition of precursor-COFs from nonanoic acid and postprocessing by a thermal treatment. The inset depicts the corresponding 2D FFT of the image. The domain size is greatly increased as compared to the precursor-COF monolayer, and all domains in this image have similar azimuthal orientation. Point defects, like missing monomers, can be discerned with low density. The STM contrast also exhibits a nonperiodic height modulation. (b) High-resolution STM image of a 2D COF-1 monolayer on HOPG prepared similar as the sample in (a) but using heptanoic acid. Again, point defects like missing monomers can be discerned, and a prominent example is marked by the dashed circle. (c) Line profile along the blue line indicated in (b). The apparent height of the COF monolayer with respect to the uncovered substrate of ~ 0.30 nm indicates monolayer thickness, and the lattice parameter corresponds to 1.4 ± 0.1 nm.

blocks were also observed (*cf.* Figure 3a,b). It is noteworthy that the presence of water in the reactor is also extremely important for the on-surface ripening process. Postprocessing without adding water to the reactor did not result in an increase of the domain size but in a decrease of coverage due to the onset of desorption.

The contrast modulation discernible in Figures 3a, 4, and S2 (Supporting Information) is another interesting feature of the extended 2D COF monolayers. In general, STM contrast results from a convolution of electronic and geometric sample properties, and it can be difficult to discriminate between both. For instance, Moiré patterns are often observed in STM images of hydrogen-bonded organic monolayers on graphite^{49,50} or graphene on HOPG and other substrates,^{51–53} due to the higher (*i.e.*, over a larger integer number of lattice vectors) commensurability of adsorbate and superstructure lattice. However, Moiré patterns give rise to a periodic contrast modulation, whereas here the contrast modulation is not periodic. Whether this is a hint toward slight nonplanarity will be addressed in further experiments.

Additional Independent Evidence for Formation of COF-1 Monolayers. So far, the formation of COF-1 monolayers was concluded based on a comparison of STM-derived lattice parameters with experimental lattice parameters from bulk COF-1 and theoretical values from DFT calculations. Yet, verification of high thermal stability and photoelectron spectroscopy provide additional complementary evidence that actually covalent monolayers were formed.

In order to explore the thermal stability of these monolayers, postprocessed samples were exposed to a relatively high temperature of 200 °C for almost 14 h

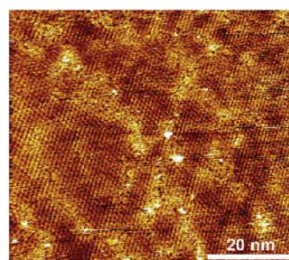


Figure 4. STM image (acquired under dry conditions) of an extended 2D COF-1 monolayer acquired under dry conditions. The sample was prepared by applying solutions of unreacted BDBA in nonanoic acid directly onto the substrate and thermal postprocessing under humid conditions. This sample is similar to the postprocessed precursor-COF monolayers with regard to lattice parameter, domain size, and defect density. Also, a nonperiodic contrast modulation is discernible here.

under ambient conditions and subsequently characterized by STM (*cf.* Supporting Information). Even after such rather harsh treatment for organic monolayers, hexagonal monolayers with similar lattice parameters could still be imaged by STM. If the monolayers were only stabilized by comparatively weak van der Waals interactions or even stronger hydrogen bonds, such a thermal treatment would result in desorption of the monolayer from the weakly interacting graphite substrate. As a reference, the thermal stability of trimesic acid (TMA) monolayers⁵⁴ that are stabilized by a fully cross-linked network of relatively strong double hydrogen bonds between carboxylic acid groups was studied by the same method. However, for this non-covalently stabilized TMA monolayer, annealing at 200 °C for 1 h already caused complete desorption. Consequently, the high thermal stability of the BDBA-derived monolayers can only be explained by formation of covalently interlinked networks. Yet, the

thermally treated COF-1 monolayers show a slight decrease in coverage, possibly hinting toward the onset of degradation.

In addition, the covalent character of the monolayers is also verified by comparative X-ray photoelectron spectra (XPS) that were acquired from both a thick film (>100 nm) of unreacted BDBA deposited by vacuum sublimation onto graphite and a postprocessed COF-1 monolayer. XPS data of O1s, B1s, and C1s core levels from both samples are depicted in Figure 5. Comparison reveals a slight shift of the O1s binding energy from 533.5 eV for the reference sample (unreacted BDBA) to 533.0 eV for the COF-1 monolayers. This slight shift toward lower binding energy for thermally treated samples is in accordance with the change of the oxygen chemical environment through condensation of boronic acid groups into boroxine rings and serves as further evidence for the polymerization. In the boronic acid moieties of unreacted BDBA monomers, oxygen is bound to both boron and hydrogen atoms, while in the boroxine rings of a COF-1 monolayer, oxygen is bound to two boron atoms. Since hydrogen is slightly more electronegative than boron (2.20 for H vs 2.04 for B on the Pauling scale), oxygen atoms become more negative in the boroxine rings, resulting in a slightly lower O1s binding energy in the COF-1 monolayer. Unfortunately, values for directly comparable compounds are not available in the literature, but for boron trioxide (B_2O_3), an O1s binding energy of 533.0 eV was reported,⁵⁵ whereas for boric acid ($B(OH)_3$), the O1s binding energy amounts to 533.5 eV.⁵⁶ As anticipated, both the B1s and C1s binding energies do not exhibit significant shifts because the direct binding partners of boron and carbon do not change through the condensation. The B1s peak at 191.7 eV coincides well with previously reported values for a chlorine-substituted phenyl boronic acid.⁵⁷ Yet, both intensity and line shape of the C1s peak are different between the BDBA film and COF monolayer: the BDBA film exhibits a symmetric main peak at 284.4 eV and a shakeup satellite at a higher binding energy of about 291 eV that is characteristic for aromatic molecules.^{58,59} In the C1s spectrum of the COF-1 monolayer, this characteristic appearance is still discernible, but in addition, the signature from the graphite substrate with a narrow and asymmetric peak shape also contributes to the spectrum.⁶⁰

Synthesis via Direct On-Surface Polymerization of BDBA. Introduction of precursor-COFs as the intermediate state for the synthesis of COF monolayers bears advantages for the fundamental understanding of the polymerization. For instance, we could show that on-surface ripening, that is, a significant increase in domain size, is feasible through thermal treatment under reversible reaction conditions. Also, additional analyses of IR and Raman spectroscopy could be applied to precursor-COFs but were inconclusive for monolayers. However,

direct polymerization of the unreacted monomers on the surface would be advantageous in terms of easier and more efficient preparation protocols. In order to address the question, whether direct polycondensation of BDBA on the surface is also feasible, supersaturated BDBA solutions were directly deposited onto graphite and annealed in the reactor under humid conditions. Parameters for this thermal treatment were similar to the postprocessing of precursor-COF monolayers, and samples were again characterized by STM (*cf.* Supporting Information). STM data of directly polymerized COF-1 monolayers were indistinguishable from monolayers that were fabricated *via* ripening of drop-cast precursor-COFs. Not only lattice parameters were similar, but also domain size and point defect density were comparable. Similarly, a nonperiodic height modulation on the 10 nm length scale is again pointing toward a slightly nonplanar character. As an independent proof of the covalent nature of directly prepared COF-1 monolayers, their thermal stability was verified according to the previous procedure. Direct BDBA polymerization was also accomplished in different aliphatic solvents (heptanoic acid, nonanoic acid, 1-undecanol, and dodecane), suggesting a minor solvent influence. Experiments with different BDBA concentrations in nonanoic acid clearly show that the direct polymerization is only possible at higher concentrations (*i.e.*, supersaturations).

In summary, we demonstrate that even when the BDBA monomers were not prepolymerized into larger entities, their thermally activated polymerization is feasible and yields similar results as on-surface ripening of precursor-COF monolayers. From these experiments, we conclude that either desorption is not the dominating thermally activated process or is suppressed in the critical stage of the polycondensation. Hence, direct polymerization of the ditopic boronic acid linker is the most straightforward method for the reliable and efficient preparation of extended, well-ordered COF-1 monolayers under ambient conditions.

CONCLUSION AND OUTLOOK

In summary, we have demonstrated the potential of straightforward synthetic approaches to prepare surface-confined 2D COFs with single-crystalline domains having lateral extensions above 40 nm. In a first synthetic route, nanocrystalline precursor-COFs were synthesized by thermally annealing the bisboronic acid building blocks in a humid atmosphere, drop-cast deposition of a monolayer, and a thermally activated ripening of initially very small domains into extended domains. The covalent nature of the network was proven by comparison of experimental structural parameters with DFT calculations, augmented by XPS and verification of the anticipated high stability

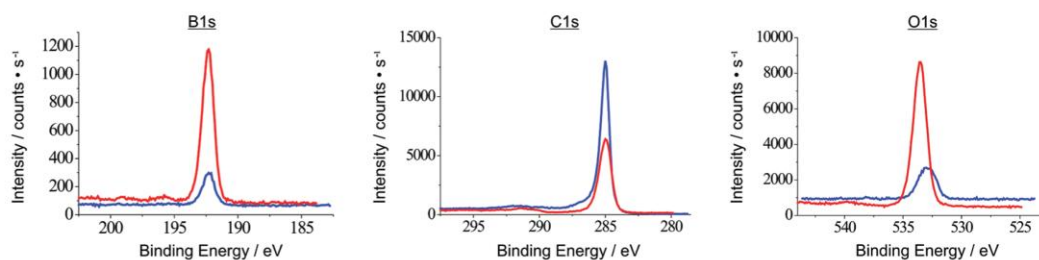


Figure 5. XPS measurements of the B1s, C1s, and O1s core level binding energies in a thick BDBA film on HOPG (red) and a 2D COF-1 monolayer on HOPG (blue). O1s spectra of the polymerized 2D COF-1 monolayer exhibit a slight shift to lower binding energy as compared to the film of unreacted BDBA molecules. This can be explained by the change of the oxygen chemical environment from B–O–H in the free boronic acid group to B–O–B in the boroxine ring upon condensation. Both the B1s and C1s spectra do not exhibit any significant shifts because their direct chemical environments are not affected by the condensation reaction. The high intensity of C1s in the COF-1 monolayer sample originates from the HOPG substrate.

through a thermal treatment. While this stepwise synthesis allows one to characterize reaction intermediates and to demonstrate that on-surface ripening of COF-1 monolayers is possible, the controllable direct synthesis from not previously treated monomers would facilitate significantly easier preparation protocols. We show that a direct polymerization is also feasible, by deposition of a solution containing the unreacted BDBA monomer and a thermal treatment under reversible reaction conditions. COF-1 monolayers prepared by either method were indistinguishable in STM measurements and both exhibit high thermal stability.

The novel synthetic approaches presented here avoid elaborate vacuum deposition techniques and should in principle be scalable to larger surface areas.

MATERIALS AND METHODS

Thermal Synthesis of Nanocrystalline Precursor-COFs. BDBA (Sigma-Aldrich, 98.1% purity) was used without further purification. For the thermally induced polymerization, a small amount of BDBA (~0.2 g) was exposed to a temperature of 250 °C for 2 h in a preheated oven (volume = 4.3 L) under ambient conditions. Thereafter, the powdery product was removed and allowed to cool to room temperature without special precautions. An additional crucible with water (~65 mL) in the oven guaranteed a high humidity throughout the process. Similar thermal treatment of BDBA in a dry atmosphere yielded only small aggregates that were not suited for further processing (*cf.* Supporting Information). We find that the solvent-free condensation does not require exact adjustment of the H₂O partial pressure during the thermal treatment, as long as water is present at all. The powdery product obtained after the prepolymerization has a slight yellowish tinge, presumably due to char formation or unexpected reactions with impurities.⁶¹ Different organic solvents were used both for BDBA monomers and precursor-COFs: heptanoic acid (Fluka, purity ≥98%), nonanoic acid (SAFC, purity ≥96%), 1-undecanol (Aldrich, purity 99%), and dodecane (Sigma-Aldrich, anhydrous, purity ≥99%).

Postprocessing of Precursor-COF Monolayers. Drop-cast samples were positioned inside a stainless steel reactor (7.7 cm³) that was placed in a preheated oven at 120 °C for ~60 min. Samples were mounted face down, and 50–100 μL of H₂O were added to the bottom of the reactor, but not in direct contact with the sample. Varying the amount of water in this range does not have any observable effect on the final structures. The reactor can be sealed off with a valve (Swagelok, SS Bellows sealed

As for solvothermal methods, the presence of water is important for the polycondensation of BDBA in both the direct synthesis and the stepwise synthesis *via* prepolymerization and ripening, in order to facilitate the slight reversibility required for successful crystallization. While the proposed synthetic approaches are facile and reliable, the next challenge is to adapt the preparation protocol to accomplish structural versatility. Here, the proof of principle has been demonstrated by means of a relatively simple one-component system. Significantly greater structural and chemical diversity can be achieved, however, by combining two building blocks as demonstrated for the solvothermal synthesis of several bulk COFs. Thus, adaptation of the proposed method to the combination of several more complex building blocks is the next important step.

valve), which was, however, kept slightly open during the postprocessing to allow gas exchange with the ambient environment and to ensure that the interior always remained at atmospheric pressure. In this experiment, the precise moment of complete disappearance of the liquid water is not known. We anticipate that when water is not present anymore, bond reversibility and thus domain ripening come to an end. In order to track the temperature during cooling and heating times, the temperature inside the reactor was monitored with a thermocouple. The maximum temperature in the 60 min period was 107 °C; a full temperature profile is reproduced in the Supporting Information.

Analytics. Raman spectra were acquired with a confocal Raman microscope (alpha300 R; WITec GmbH, Ulm, Germany) using excitation at $\lambda = 785$ nm. Single spectra were acquired at several positions on each sample averaging 10 spectra with 5 s integration time each at a laser power of 50 mW. For optimum signal efficiency, a 100× microscope objective with a numerical aperture of 0.9 was used. IR spectra were acquired with a Bruker Equinox 55 instrument. Small amounts of the samples (untreated, thermally treated, and rehydrolyzed BDBA) were mixed with dry KBr (previously dehydrated for ~1 week), compressed into pellets, and immediately analyzed. TGA was performed with a Netzsch STA 449 C instrument, with a heating rate of 10 °C/s and an original weight of 11.4 mg of BDBA. PXRD characterization was performed on an Oxford Diffraction diffractometer equipped with a 2D Atlas detector, operating at 100 mm sample to detector distance and using Mo K_{α1} radiation (HOPG monochromator). The data obtained by recording several frames of Debye–Scherrer rings on the 2D detector were integrated to one-dimensional intensity *versus* 2 θ data by the

diffractometer software (CRYSTALIS PRO). The scattering from the mylar foil and the instrumental background were subtracted during the postprocessing. General Structure Analysis System (GSAS) software with the graphical front-end EXPGUI was used for the estimation of the coherent domain size via an anisotropic line broadening model using the Scherrer equation.^{46,47} In nanocrystalline materials, the coherent domain size can be assumed to be equal to the crystallite size. The previously reported structure of COF-1 was used as a model.⁹ The atomic positions were fixed during the simulation, and texture effects were corrected with a March-Dollase model assuming a preferred orientation of 0.5 for 001. The final χ^2 distribution was found to be 3.145.

STM images were acquired with a home-built drift-stable scanning probe microscope operated by an ASC500 scanning probe microscopy controller from attocube systems AG. STM measurements were conducted either directly at the liquid–solid interface (precursor-COF monolayer) or under dry conditions (after postprocessing). Constant current images were obtained with tunneling voltages between +0.3 and +0.9 V applied to the tip and set point currents between 50 and 90 pA.

XPS analysis was performed with a PHI 5000 VersaProbe spectrometer (Physical Electronics) equipped with a 180° spherical energy analyzer and a multichannel detection system with 16 channels. Spectra were acquired at a base pressure of 5×10^{-7} Pa using a focused scanning monochromatic Al K α source (1486.68 eV) with spot size of 200 μ m and beam power of 50 W. The instrument was run in the FAT analyzer mode with electrons emitted at 45° to the surface normal. Dual beam charge neutralization was applied throughout the analysis. High-resolution scans of the B1s, C1s, and O1s energy spectra were taken with a pass energy of 23.5 eV. Data were analyzed using the program MultiPak.

Acknowledgment. Financial support from the Nano Systems Initiative Munich (NIM) and the Bayerische Forschungsstiftung is gratefully acknowledged. We also would like to thank WITec GmbH for granting the Raman measurements, Johanna Eichhorn, Dr. Kai-Uwe Hess for their assistance with effusion cell BDBA deposition rates and TGA measurements, and Prof. Stefan Sotier for initial XPS measurements.

Supporting Information Available: Additional STM images, PXRD, IR, Raman, TGA data, sublimation curves for BDBA, molecular mechanics simulation of hypothetical self-assembled BDBA monolayers, and temperature profile inside the reactor during the thermal activation. This material is available free of charge via the Internet at <http://pubs.acs.org>.

REFERENCES AND NOTES

- Lei, S. B.; Tahara, K.; Adisoewjoso, J.; Balandina, T.; Tobe, Y.; De Feyter, S. Towards Two-Dimensional Nanoporous Networks: Crystal Engineering at the Solid–Liquid Interface. *CrystEngComm* **2010**, *12*, 3369–3381.
- De Feyter, S.; Elemans, J. A. A. W.; Lei, S. B. Molecular and Supramolecular Networks on Surfaces: From Two-Dimensional Crystal Engineering to Reactivity. *Angew. Chem., Int. Ed.* **2009**, *48*, 7298–7332.
- Lackinger, M.; Griessl, S.; Heckl, W. M.; Hietschold, M.; Flynn, G. W. Self-Assembly of Trimesic Acid at the Liquid–Solid Interface—A Study of Solvent-Induced Polymorphism. *Langmuir* **2005**, *21*, 4984–4988.
- Shi, Z.; Lin, N. Porphyrin-Based Two-Dimensional Coordination Kagome Lattice Self-Assembled on a Au(111) Surface. *J. Am. Chem. Soc.* **2009**, *131*, 5376–5377.
- Lei, S.; Tahara, K.; De Schryver, F. C.; Van der Auweraer, M.; Tobe, Y.; De Feyter, S. One Building Block, Two Different Supramolecular Surface-Confined Patterns: Concentration in Control at the Solid–Liquid Interface. *Angew. Chem., Int. Ed.* **2008**, *47*, 2964–2968.
- Joo, S. H.; Choi, S. J.; Oh, I.; Kwak, J.; Liu, Z.; Terasaki, O.; Ryoo, R. Ordered Nanoporous Arrays of Carbon Supporting High Dispersions of Platinum Nanoparticles. *Nature* **2001**, *412*, 169–172.
- Spitler, E. L.; Dichtel, W. R. Lewis Acid-Catalysed Formation of Two-Dimensional Phthalocyanine Covalent Organic Frameworks. *Nat. Chem.* **2010**, *2*, 672–677.
- Jiang, D. L.; Wan, S.; Guo, J.; Kim, J.; Ihee, H. A Belt-Shaped Blue Luminescent, and Semiconducting Covalent Organic Framework. *Angew. Chem., Int. Ed.* **2008**, *47*, 8826–8830.
- Cote, A. P.; Benin, A. I.; Ockwig, N. W.; O’Keeffe, M.; Matzger, A. J.; Yaghi, O. M. Porous, Crystalline, Covalent Organic Frameworks. *Science* **2005**, *310*, 1166–1170.
- Cote, A. P.; El-Kaderi, H. M.; Furukawa, H.; Hunt, J. R.; Yaghi, O. M. Reticular Synthesis of Microporous and Mesoporous 2D Covalent Organic Frameworks. *J. Am. Chem. Soc.* **2007**, *129*, 12914–12915.
- Uribe-Romo, F. J.; Hunt, J. R.; Furukawa, H.; Klock, C.; O’Keeffe, M.; Yaghi, O. M. A Crystalline Imine-Linked 3-D Porous Covalent Organic Framework. *J. Am. Chem. Soc.* **2009**, *131*, 4570–4571.
- Kuhn, P.; Antonietti, M.; Thomas, A. Porous, Covalent Triazine-Based Frameworks Prepared by Ionothermal Synthesis. *Angew. Chem., Int. Ed.* **2008**, *47*, 3450–3453.
- Uribe-Romo, F. J.; Doonan, C. J.; Furukawa, H.; Oisaki, K.; Yaghi, O. M. Crystalline Covalent Organic Frameworks with Hydrazone Linkages. *J. Am. Chem. Soc.* **2011**, *133*, 11478–11481.
- Korich, A. L.; Iovine, P. M. Boroxine Chemistry and Applications: A Perspective. *Dalton Trans.* **2010**, *39*, 1423–1431.
- Nishiyabu, R.; Kubo, Y.; James, T. D.; Fossey, J. S. Boronic Acid Building Blocks: Tools for Self Assembly. *Chem. Commun.* **2011**, *47*, 1124–1150.
- Tilford, R. W.; Gemmill, W. R.; zur Loye, H. C.; Lavigne, J. J. Facile Synthesis of a Highly Crystalline, Covalently Linked Porous Boronate Network. *Chem. Mater.* **2006**, *18*, 5296–5301.
- El-Kaderi, H. M.; Hunt, J. R.; Mendoza-Cortes, J. L.; Cote, A. P.; Taylor, R. E.; O’Keeffe, M.; Yaghi, O. M. Designed Synthesis of 3D Covalent Organic Frameworks. *Science* **2007**, *316*, 268–272.
- Campbell, N. L.; Clowes, R.; Ritchie, L. K.; Cooper, A. I. Rapid Microwave Synthesis and Purification of Porous Covalent Organic Frameworks. *Chem. Mater.* **2009**, *21*, 204–206.
- Wan, S.; Guo, J.; Kim, J.; Ihee, H.; Jiang, D. A Photoconductive Covalent Organic Framework: Self-Condensed Arene Cubes Composed of Eclipsed 2D Polypyrene Sheets for Photocurrent Generation. *Angew. Chem., Int. Ed.* **2009**, *48*, 5439–5442.
- Sakamoto, J.; van Heijst, J.; Lukin, O.; Schluter, A. D. Two-Dimensional Polymers: Just a Dream of Synthetic Chemists? *Angew. Chem., Int. Ed.* **2009**, *48*, 1030–1069.
- Bieri, M.; Blankenburg, S.; Kivala, M.; Pignedoli, C. A.; Ruffieux, P.; Müllen, K.; Fasel, R. Surface-Supported 2D Heterotriangulene Polymers. *Chem. Commun.* **2011**, *47*, 10239–10241.
- Blunt, M. O.; Russell, J. C.; Champness, N. R.; Beton, P. H. Templating Molecular Adsorption Using a Covalent Organic Framework. *Chem. Commun.* **2010**, *46*, 7157–7159.
- Grill, L.; Dyer, M.; Lafferentz, L.; Persson, M.; Peters, M. V.; Hecht, S. Nano-architectures by Covalent Assembly of Molecular Building Blocks. *Nat. Nanotechnol.* **2007**, *2*, 687–691.
- Gutzler, R.; Walch, H.; Eder, G.; Kloft, S.; Heckl, W. M.; Lackinger, M. Surface Mediated Synthesis of 2D Covalent Organic Frameworks: 1,3,5-Tris(4-bromophenyl)benzene on Graphite(001), Cu(111), and Ag(110). *Chem. Commun.* **2009**, 4456–4458.
- Cai, J.; Ruffieux, P.; Jaafar, R.; Bieri, M.; Braun, T.; Blankenburg, S.; Muoth, M.; Seitsonen, A. P.; Saleh, M.; Feng, X.; Müllen, K.; Fasel, R. Atomically Precise Bottom-Up Fabrication of Graphene Nanoribbons. *Nature* **2010**, *466*, 470–473.
- Lipton-Duffin, J. A.; Ivasenko, O.; Perepichka, D. F.; Rosei, F. Synthesis of Polyphenylene Molecular Wires by Surface-Confined Polymerization. *Small* **2009**, *5*, 592–597.
- Lipton-Duffin, J. A.; Miwa, J. A.; Kondratenko, M.; Ciccoira, F.; Sumpster, B. G.; Meunier, V.; Perepichka, D. F.; Rosei, F. Step-by-Step Growth of Epitaxially Aligned Polythiophene by Surface-Confined Reaction. *Proc. Natl. Acad. Sci. U.S.A.* **2010**.

28. Schmitz, C. H.; Schmid, M.; Gärtner, S.; Steirück, H.-P.; Gottfried, J. M.; Sokolowski, M. Surface Polymerization of Poly(*p*-phenylene-terephthalamide) on Ag(111) Investigated by X-ray Photoelectron Spectroscopy and Scanning Tunneling Microscopy. *J. Phys. Chem. C* **2011**, *115*, 18186–18194.
29. Zwaneveld, N. A. A.; Pawlak, R.; Abel, M.; Catalin, D.; Gimes, D.; Bertin, D.; Porte, L. Organized Formation of 2D Extended Covalent Organic Frameworks at Surfaces. *J. Am. Chem. Soc.* **2008**, *130*, 6678–6679.
30. Treier, M.; Richardson, N. V.; Fasel, R. Fabrication of Surface-Supported Low-Dimensional Polyimide Networks. *J. Am. Chem. Soc.* **2008**, *130*, 14054–14055.
31. Jensen, S.; Greenwood, J.; Früchtel, H. A.; Baddeley, C. J. STM Investigation on the Formation of Oligoamides on Au(111) by Surface-Confined Reactions of Melamine with Trimesoyl Chloride. *J. Phys. Chem. C* **2011**, *115*, 8630–8636.
32. Schmitz, C. H.; Ikononov, J.; Sokolowski, M. Two-Dimensional Polyamide Networks with a Broad Pore Size Distribution on the Ag(111) Surface. *J. Phys. Chem. C* **2011**, *115*, 7270–7278.
33. Weigelt, S.; Busse, C.; Bombis, C.; Knudsen, M. M.; Gothelf, K. V.; Lægsgaard, E.; Besenbacher, F.; Linderoth, T. R. Surface Synthesis of 2D Branched Polymer Nanostructures. *Angew. Chem., Int. Ed.* **2008**, *47*, 4406–4410.
34. Treier, M.; Fasel, R.; Champness, N. R.; Argent, S.; Richardson, N. V. Molecular Imaging of Polyimide Formation. *Phys. Chem. Chem. Phys.* **2009**, *11*, 1209–1214.
35. Clair, S.; Ourdjini, O.; Abel, M.; Porte, L. Tip- or Electron Beam-Induced Surface Polymerization. *Chem. Commun.* **2011**, *47*, 8028–8030.
36. Abel, M.; Clair, S.; Ourdjini, O.; Mossoyan, M.; Porte, L. Single Layer of Polymeric Fe-Phthalocyanine: An Organometallic Sheet on Metal and Thin Insulating Film. *J. Am. Chem. Soc.* **2011**, *133*, 1203–1205.
37. In't Veld, M.; Iavicoli, P.; Haq, S.; Amabilino, D. B.; Raval, R. Unique Intermolecular Reaction of Simple Porphyrins at a Metal Surface Gives Covalent Nanostructures. *Chem. Commun.* **2008**, 1536–1538.
38. Matena, M.; Riehm, T.; Stöhr, M.; Jung, T. A.; Gade, L. H. Transforming Surface Coordination Polymers into Covalent Surface Polymers: Linked Polycondensed Aromatics through Oligomerization of N-Heterocyclic Carbene Intermediates. *Angew. Chem., Int. Ed.* **2008**, *47*, 2414–2417.
39. Beton, P. H.; Russell, J. C.; Blunt, M. O.; Garfitt, J. M.; Scurr, D. J.; Alexander, M.; Champness, N. R. Dimerization of Tri(4-bromophenyl)benzene by Aryl–Aryl Coupling from Solution on a Gold Surface. *J. Am. Chem. Soc.* **2011**, *133*, 4220–4223.
40. Tanoue, R.; Higuchi, R.; Enoki, N.; Miyasato, Y.; Uemura, S.; Kimizuka, N.; Stieg, A. Z.; Gimzewski, J. K.; Kunitake, M. Thermodynamically Controlled Self-Assembly of Covalent Nanoarchitectures in Aqueous Solution. *ACS Nano* **2011**, *5*, 3923–3929.
41. Ourdjini, O.; Pawlak, R.; Abel, M.; Clair, S.; Chen, L.; Bergeon, N.; Sassi, M.; Olson, V.; Debierre, J.-M.; Coratger, R.; Porte, L. Substrate-Mediated Ordering and Defect Analysis of a Surface Covalent Organic Framework. *Phys. Rev. B* **2011**, *84*, 125421.
42. Colson, J. W.; Woll, A. R.; Mukherjee, A.; Levendorf, M. P.; Spittler, E. L.; Shields, V. B.; Spencer, M. G.; Park, J.; Dichtel, W. R. Oriented 2D Covalent Organic Framework Thin Films on Single-Layer Graphene. *Science* **2011**, *332*, 228–231.
43. Whitesides, G. M.; Grzybowski, B. Self-Assembly at All Scales. *Science* **2002**, *295*, 2418–2421.
44. Perepichka, D. F.; Rosei, F. Extending Polymer Conjugation into the Second Dimension. *Science* **2009**, *323*, 216–217.
45. Walch, H.; Gutzler, R.; Sirtl, T.; Eder, G.; Lackinger, M. Material- and Orientation-Dependent Reactivity for Heterogeneously Catalyzed Carbon–Bromine Bond Homolysis. *J. Phys. Chem. C* **2010**, *114*, 12604–12609.
46. Larson, A. C.; von Dreele, R. B. *General Structure Analysis System (GSAS)*, Los Alamos National Laboratory Report LAUR 86-748, 2000.
47. Toby, B. H. EXPGUI, a Graphical User Interface for GSAS. *J. Appl. Crystallogr.* **2001**, *34*, 210–213.
48. Pawlak, R.; Nony, L.; Bocquet, F.; Olson, V.; Sassi, M.; Debierre, J. M.; Loppacher, C.; Porte, L. Supramolecular Assemblies of 1,4-Benzene Diboronic Acid on KCl(001). *J. Phys. Chem. C* **2010**, *114*, 9290–9295.
49. Edelwirth, M.; Freund, J.; Sowerby, S. J.; Heckl, W. M. Molecular Mechanics Study of Hydrogen Bonded Self-Assembled Adenine Monolayers on Graphite. *Surf. Sci.* **1998**, *417*, 201–209.
50. Thomas, L. K.; Kühnle, A.; Rode, S.; Beginn, U.; Reichling, M. Monolayer Structure of Arachidic Acid on Graphite. *J. Phys. Chem. C* **2010**, *114*, 18919–18924.
51. Zhang, J. F.; Cao, G. Y. STM Study of Moiré Patterns on HOPG. *Chin. J. Chem. Phys.* **2006**, *19*, 197–199.
52. Xhie, J.; Sattler, K.; Ge, M.; Venkateswaran, N. Giant and Supergiant Lattices on Graphite. *Phys. Rev. B* **1993**, *47*, 15835–15841.
53. Wang, B.; Bocquet, M. L.; Marchini, S.; Günther, S.; Wintterlin, J. Chemical Origin of a Graphene Moiré Overlay on Ru(0001). *Phys. Chem. Chem. Phys.* **2008**, *10*, 3530–3534.
54. Griessl, S.; Lackinger, M.; Edelwirth, M.; Hietschold, M.; Heckl, W. M. Self-Assembled Two-Dimensional Molecular Host–Guest Architectures from Trimesic Acid. *Single Mol.* **2002**, *3*, 25–31.
55. Nefedov, V. I.; Gati, D.; Dzburinskii, B. F.; Sergushin, N. P.; Salyn, Y. V. The X-ray Electronic Studies of Oxides of Certain Elements. *Z. Neorg. Khim.* **1975**, *20*, 2307–2314.
56. Brian, R. S. Surface Characterization of Aluminum Foil Annealed in the Presence of Ammonium Fluoborate. *Appl. Surf. Sci.* **1989**, *40*, 249–263.
57. Hendrickson, D. N.; Hollander, J. M.; Jolly, W. L. Core-Electron Binding Energies for Compounds of Boron, Carbon, and Chromium. *Inorg. Chem.* **1970**, *9*, 612–615.
58. Jones, T. S.; Ashton, M. R.; Richardson, N. V.; Mack, R. G.; Unertl, W. N. The Interaction of the Polyimide Precursors PMDA (1,2,4,5-Benzenetetracarboxylic Anhydride) and m-PDA (1,3-Phenylenediamine) with Ni(110). *J. Vac. Sci. Technol., A* **1990**, *8*, 2370–2375.
59. Keane, M. P.; de Brito, A. N.; Correia, N.; Svensson, S.; Lunell, S. Experimental and Theoretical Study of the N1s and C1s Shake-Up Satellites in Pyridine and Aniline. *Chem. Phys.* **1991**, *155*, 379–387.
60. van Attekum, P. M. T. M.; Wertheim, G. K. Excitonic Effects in Core-Hole Screening. *Phys. Rev. Lett.* **1979**, *43*, 1896–1898.
61. Morgan, A. B.; Jurs, J. L.; Tour, J. M. Synthesis, Flame-Retardancy Testing, and Preliminary Mechanism Studies of Nonhalogenated Aromatic Boronic Acids: A New Class of Condensed-Phase Polymer Flame-Retardant Additives for Acrylonitrile-Butadiene-Styrene and Polycarbonate. *J. Appl. Polym. Sci.* **2000**, *76*, 1257–1268.

Synthesis of Well-Ordered COF Monolayers:
Surface Growth of Nanocrystalline Precursors vs.
Direct On-Surface Polycondensation

*Jürgen F. Dienstmaier^{‡,†}, Alexander M. Gigler[†], Andreas J. Goetz[†], Paul Knochel[#], Thomas Bein[#],
Andrey Lyapin[⊥], Stefan Reichlmaier[⊥], Wolfgang M. Heckl[‡], and Markus Lackinger^{‡,*}*

[‡] Deutsches Museum, Museumsinsel 1, 80538 Munich (Germany) and Tech. Univ. Munich, TUM
School of Education, Schellingstrasse 33, 80799 Munich (Germany) and
Center for NanoScience (CeNS)

[†] Department for Earth- and Environmental Sciences and Center for NanoScience (CeNS),
Ludwig-Maximilians-University, Theresienstrasse 41, 80333 Munich (Germany)

[#] Department of Chemistry and Center for NanoScience (CeNS), Ludwig-Maximilians-University,
Butenandtstrasse 11 (E), 81377, Munich (Germany)

[⊥] Physical Electronics GmbH, Fraunhoferstr. 4, 85737 Ismaning, Germany

Content:

Figure S1: STM images of thermally treated BDBA under dry conditions

Figure S2: STM image of post-processed COF-1 monolayer, prepared with nonanoic acid

Figure S3: STM image of a COF-1 monolayer after verification of its thermal stability

Figure S4: PXRD of untreated BDBA, precursor-COFs, and re-hydrolyzed material

Figure S5: Raman spectra of untreated BDBA, precursor-COFs, and re-hydrolyzed material

Figure S6: IR-spectra of untreated BDBA, precursor-COFs, and re-hydrolyzed material

Figure S7: TGA of BDBA

Figure S8: Sublimation of unreacted BDBA

Figure S9: Molecular mechanics simulation of a hypothetical hydrogen bonded BDBA structure

Figure S10: Temperature profile inside the reactor during a thermal treatment

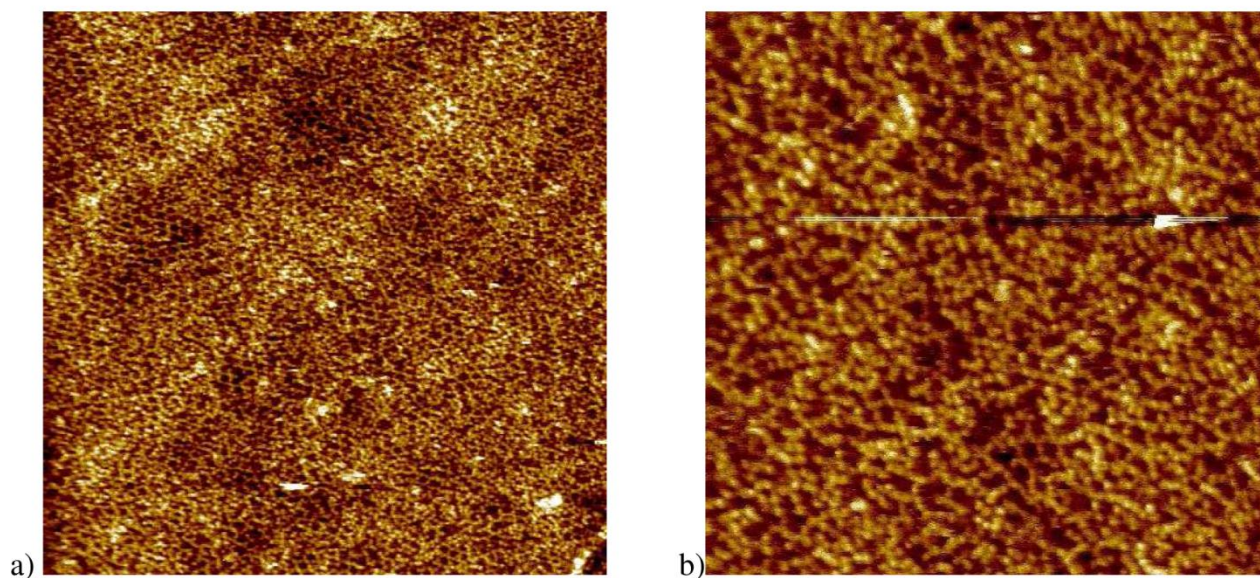


Figure S1 STM images a) ($58 \times 58 \text{ nm}^2$) and b) ($35 \times 35 \text{ nm}^2$) obtained on HOPG after drop-casting a suspension of BDBA that was thermally treated under dry conditions, i.e. in the absence of H_2O . The resulting structures are amorphous and only single polymerized chains and smaller covalent aggregates can be discerned but no extended hexagonal networks.

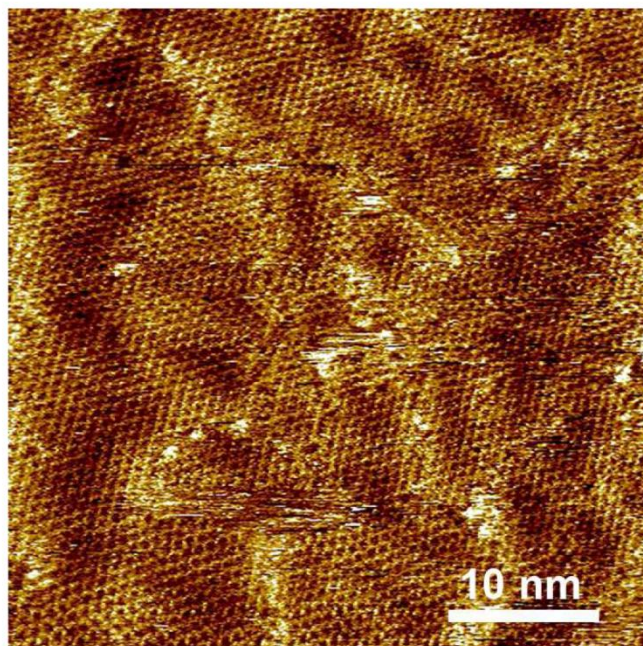


Figure S2 STM image of an extended 2D COF-1 monolayer ($68 \times 68 \text{ nm}^2$) acquired under dry conditions. This monolayer was prepared by drop-casting precursor COFs dispersed in nonanoic acid and post-processing under humid conditions. The surface is fully covered and domains with lateral extension of tens of nanometers can be observed with very few defects, like missing BDBA molecules. Also a non-periodic contrast modulation is clearly discernable.

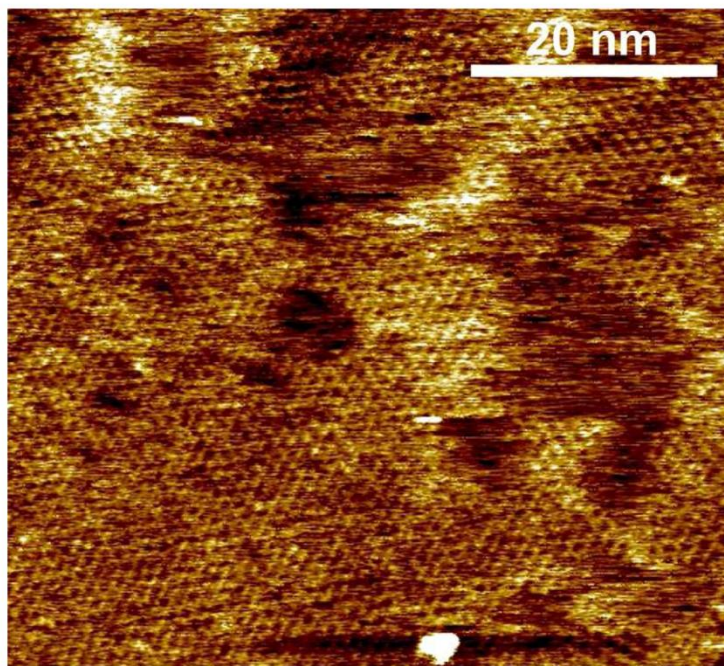


Figure S3 STM image of an extended 2D COF-1 monolayer ($60 \times 60 \text{ nm}^2$) acquired under dry conditions after verification of the thermal stability. To this end, an already post-processed sample was exposed to $200 \text{ }^\circ\text{C}$ for almost 14 h (without supplying additional water). The COF-1 monolayer can clearly be observed, and the thermal stability confirms the covalent nature of intermolecular bonds. Yet, the coverage has slightly decreased, which may indicate a slow degradation.

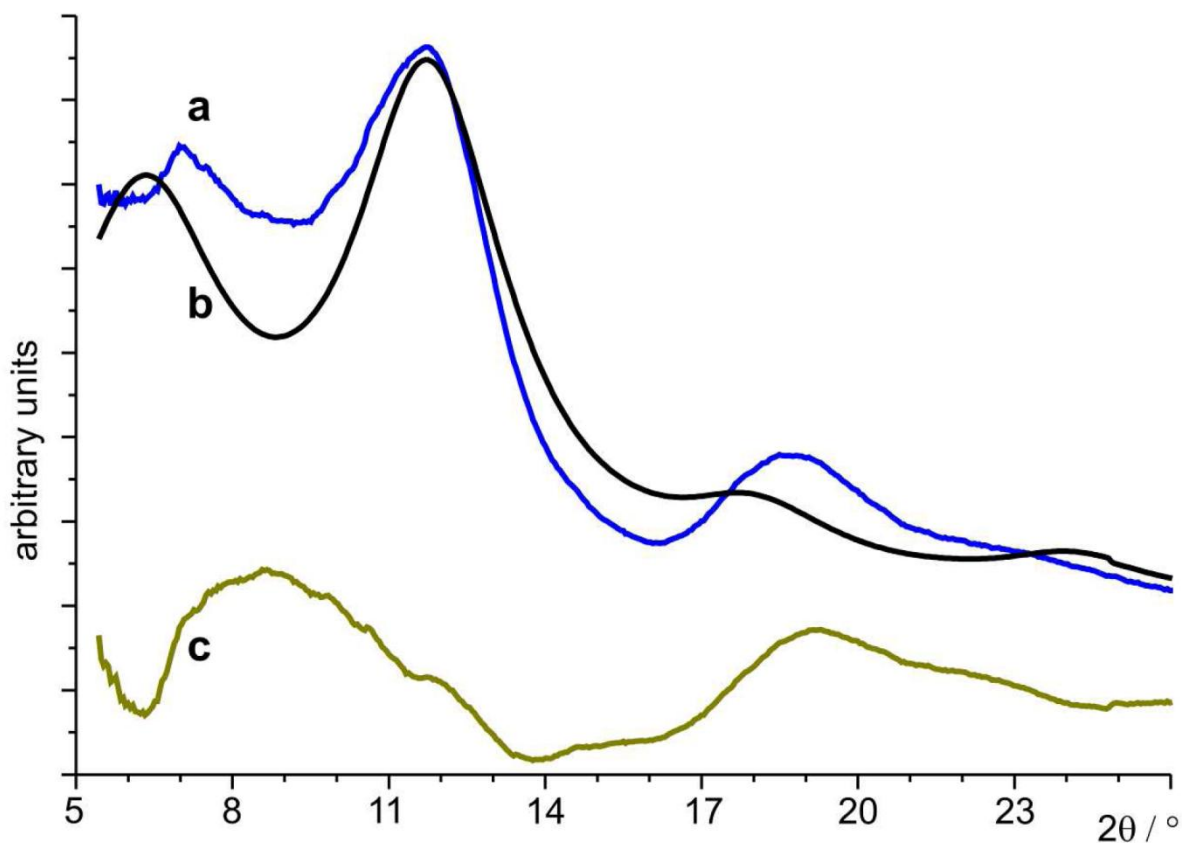


Figure S4 a) Powder X-ray diffractogram ($\text{Mo-K}\alpha_1$) of thermally treated BDBA, i.e. pre-polymerization into precursor-COFs (blue curve) b) Simulated curve of a) based on the previously published COF-1 crystal structure (black curve). The Rietveld refinement allows to estimate a precursor-COF crystal size of 7.8 nm in lateral direction and 1.0 nm along the [001] axis ($\text{Chi}^2 = 3.145$).¹⁻² c) Difference curve between measured and simulated curve, i.e. (a) – (b). The large discrepancy is owed to the extremely small crystal size and the low number of periods especially along the c-axis. Nevertheless, the main features of the experimental diffraction data can be reproduced in the simulation.

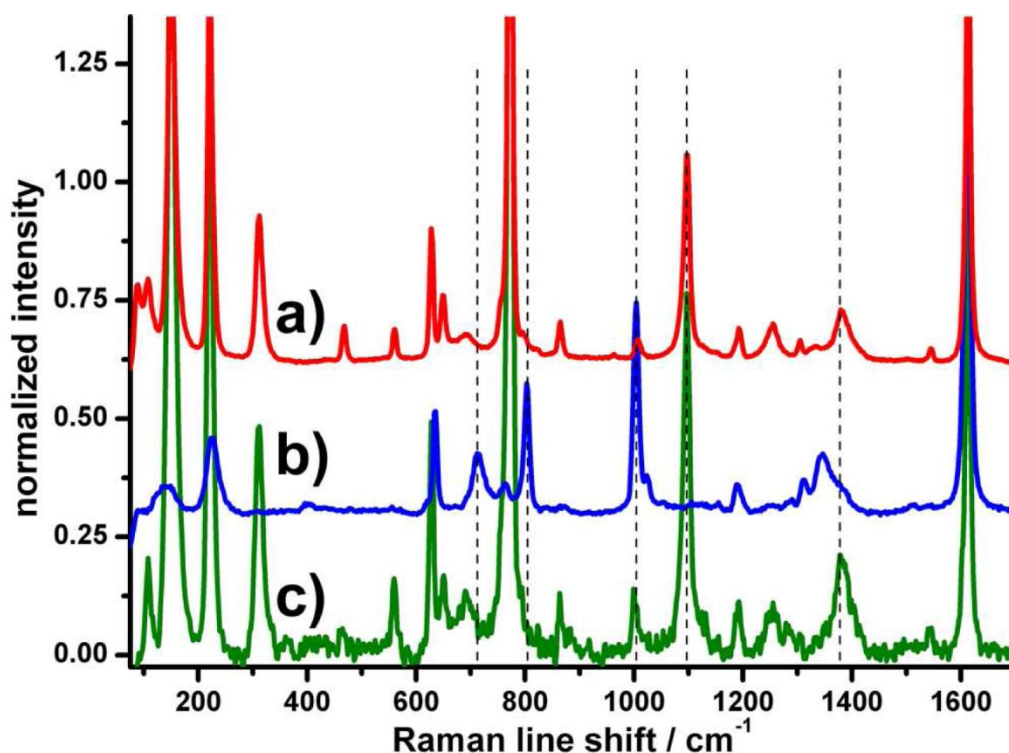


Figure S5 Raman spectra of a) untreated BDBA starting material (red curve), b) after thermal treatment (blue curve), i.e. pre-polymerization into precursor-COFs c) after re-hydrolysis and re-crystallisation of b) from H₂O (green curve). Although not all modes could be assigned, the modes at ~1097 cm⁻¹ and at ~1378 cm⁻¹ are only observed for untreated and re-hydrolyzed BDBA and can be attributed to a B-O-H rocking mode and B-O stretching vibrations of the free boronic acid groups, respectively.³ After thermal treatment the rocking mode at ~1097 cm⁻¹ as well as other, not assigned modes at 770 cm⁻¹ and 310 cm⁻¹ disappear, while new modes at ~713 cm⁻¹, ~804 cm⁻¹, and ~1004 cm⁻¹ appear. The new mode at ~804 cm⁻¹ corresponds to the breathing mode of boroxine rings, and its presence indicates cyclo-condensation of three boronic acid groups.⁴

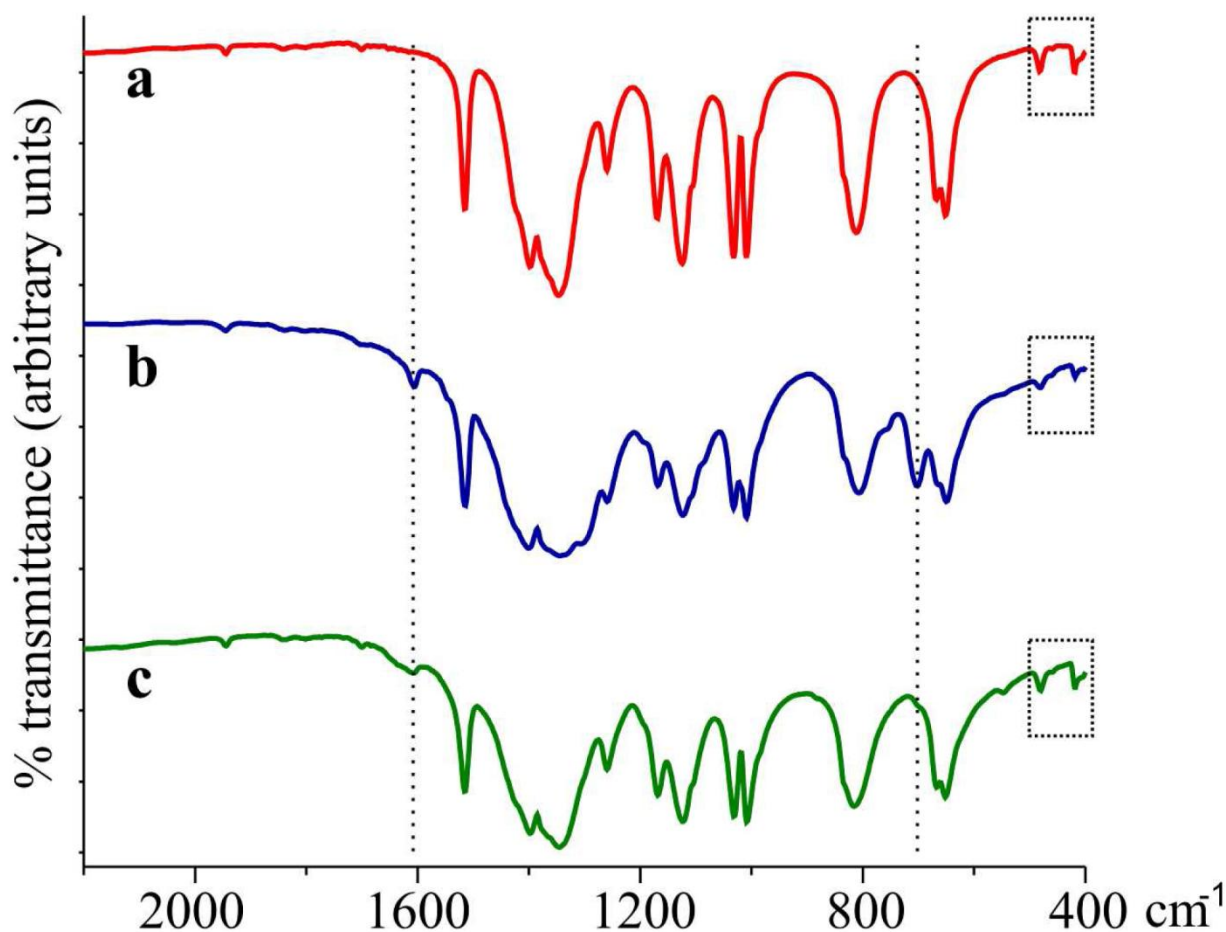


Figure S6 IR spectra of a) untreated BDBA starting material (red curve); b) after thermal treatment, i.e. pre-polymerization into precursor-COFs (blue curve); c) after re-hydrolysis and re-crystallisation of b) from H₂O (green curve). The dotted square marks a region with weak peaks that can be attributed to BO₂ rocking vibrations in the free boronic acid BDBA.⁵ Notice their diminishment in the pre-polymerized sample b). The IR spectrum of the pre-polymerized product is also in excellent agreement with the results reported for solvothermally synthesized COF-1.⁶ In particular, the absorption maxima in the IR spectra of thermally treated samples at 701 cm⁻¹ and 1605 cm⁻¹ were also found for solvothermally synthesized COF-1, and indicate the presence of boroxine rings.⁶ The first mode belongs to out-of-plane deformation of the boroxine unit, and the second mode arises from boronic acid (B(OH)₂) end groups in asymmetrically substituted benzenes. This mode is attributed to free boronic acid groups which are still present on the surface of nanocrystals.

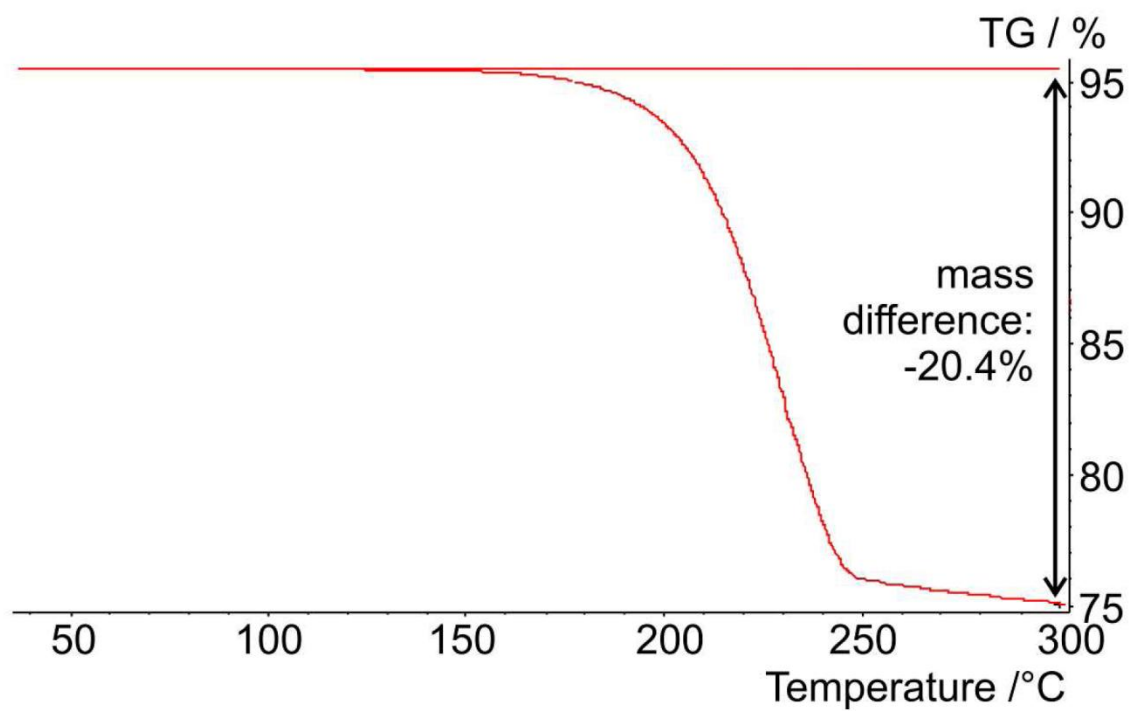


Figure S7 Thermal Gravimetric Analysis (TGA) of previously untreated BDBA (rate: 10 °C / minute, quantity: 11.430 mg). The weight loss due to the condensation is almost completed at ~250 °C. The change of slope at temperatures above 250 °C may indicate the onset of thermal degradation.

Degree of completion of the thermal polymerization

In order to detect the presence of residual unreacted BDBA after thermal treatment, the pre-polymerized product was introduced in an effusion cell operated in high vacuum. The crucible aims at a highly sensitive quartz crystal microbalance (QCMB), thus allowing to measure effusion rates as a function of crucible temperature.⁷ However, heating the precursor-COF up to 200 °C did not result in a detectable deposition of unreacted BDBA monomers on the QCMB chip, although the experiment features monolayer sensitivity. In contrast, the sublimation onset of untreated BDBA starting material can already be detected at ~100 °C, and the sublimation rate increases with temperature according to an Arrhenius law (see below, Figure S8). From these experiments we conclude that the amount of residual unreacted BDBA in the thermally treated material is extremely low.

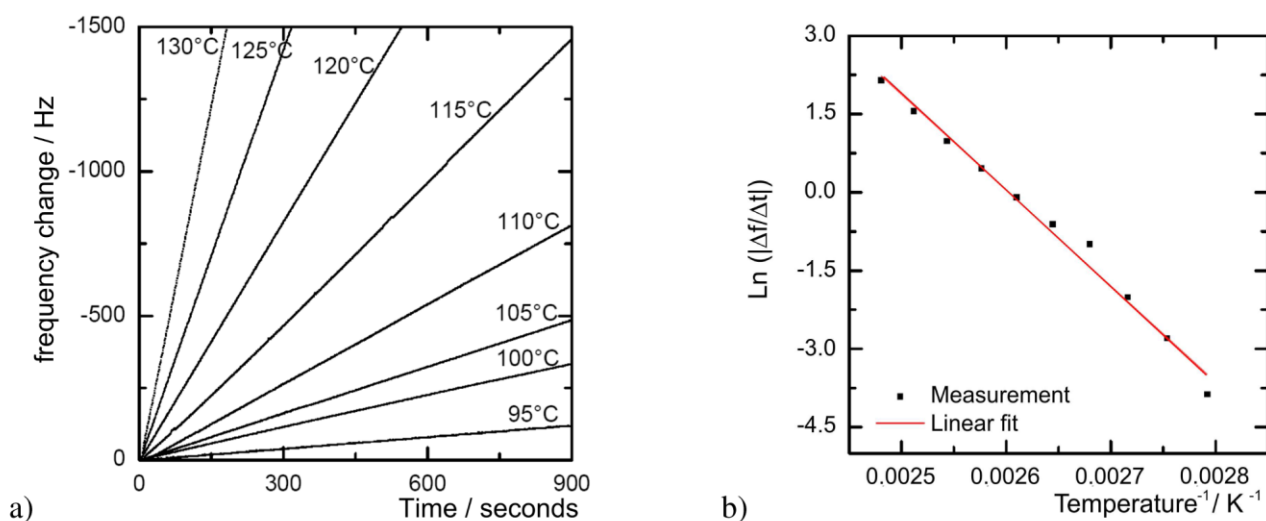


Figure S8 Characterization of the sublimation of untreated BDBA by means of an effusion cell and a Quartz Crystal Micro Balance (QCMB).⁷ a) Frequency shift Δf of the QCMB as a function of time for different crucible temperatures (indicated next to each curve). The linear dependence indicates a constant effusion rate. b) Arrhenius plot of the data in a), where for each crucible temperature T the slope of the respective frequency vs. time curve $|\Delta f/\Delta t|$ was used. These measurements demonstrate that the free boronic acid can be sublimed, whereas from thermally treated BDBA (precursor-COFs) no sublimation could be detected for crucible temperatures up to 200 °C, hinting towards an extremely low amount of unreacted BDBA.

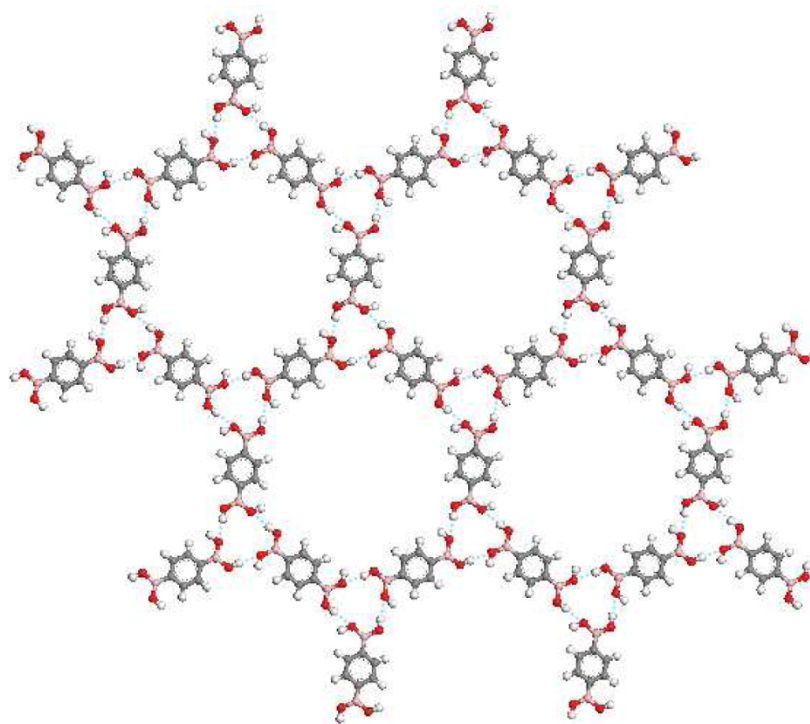


Figure S9 Molecular Mechanics (MM) calculation of a **hypothetic** porous hexagonal BDBA monolayer structure on a graphite substrate (not shown for clarity) based on the Dreiding force field. The graphite substrate was approximated by two layers, and the atomic positions of the second one were fixed. The BDBA molecules were arranged flat on the surface without constraints. The structure is stabilized by cyclic intermolecular hydrogen bonds (indicated by dotted lines). Note that there are no boroxine rings present here. The distance between adjacent pores, i.e. the lattice parameter of this hypothetical self-assembled structure corresponds to 2.05 nm. Colour code: C = gray; B = pink; O = red; H = white.

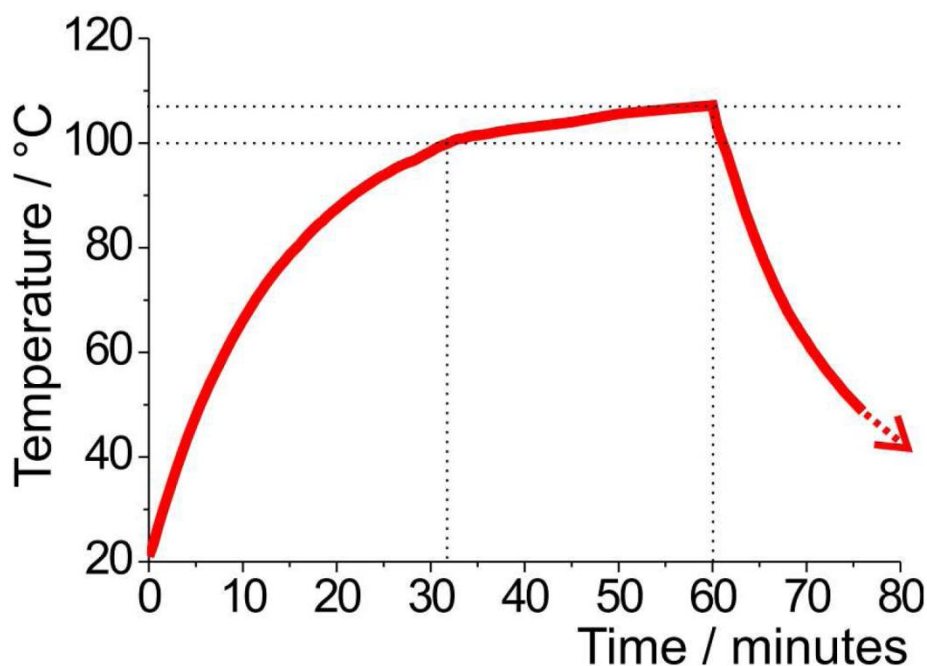


Figure S10 Temperature profile inside the reactor during the thermally induced ripening process of precursor-COF layers into well-ordered 2D COF-1 monolayers with large domains. The oven was pre-heated to 120 °C. While the reactor remained inside the oven for 60 minutes its interior temperature reached 107 °C before it was removed and allowed to cool down. The temperature inside the reactor remained above 100 °C for ~30 minutes.

References

1. Larson, A. C.; von Dreele, R. B., General Structure Analysis System (GSAS), Los Alamos National Laboratory Report LAUR 86-748. **2000**.
2. Toby, B. H., EXPGUI, A Graphical User Interface for GSAS. *J. Appl. Crystallog.* **2001**, *34*, 210 - 213.
3. Krishnan, K., The Raman Spectrum of Boric Acid. *Proc. Indian. Acad. Sci. (Math. Sci.)* **1963**, *57*, 103-108.
4. Goubeau, J.; Keller, H., Raman-Spektren und Struktur von Boroxol-Verbindungen. *Z. Anorg. Allg. Chem.* **1953**, *272* (5-6), 303-312.
5. Faniran, J. A.; Shurvell, H. F., Infrared Spectra of Pheynlboronic Acid (Normal and Deuterated) and Diphenyl Phenylboronate. *Can. J. Chemistry.* **1968**, *46* (12), 2089-2095.
6. Cote, A. P.; Benin, A. I.; Ockwig, N. W.; O'Keeffe, M.; Matzger, A. J.; Yaghi, O. M., Porous, Crystalline, Covalent Organic Frameworks. *Science* **2005**, *310* (5751), 1166-1170.
7. Gutzler, R.; Heckl, W. M.; Lackinger, M., Combination of a Knudsen Effusion Cell with a Quartz Crystal Microbalance: In Situ Measurement of Molecular Evaporation Rates with a Fully Functional Deposition Dource. *Rev. Sci. Instrum.* **2010**, *81* (1), 015108.

Isorecticular Two-Dimensional Covalent Organic Frameworks Synthesized by On-Surface Condensation of Diboronic Acids

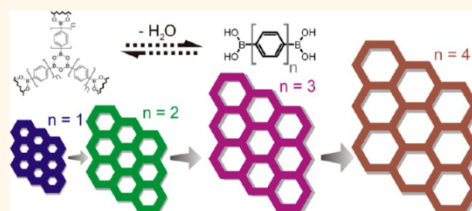
Jürgen F. Dienstmaier,^{†,‡} Dana D. Medina,^{‡,§} Mirjam Dogru,^{‡,§} Paul Knochel,[§] Thomas Bein,^{‡,§} Wolfgang M. Heckl,^{†,‡} and Markus Lackinger^{†,‡,*}

[†]Deutsches Museum, Museumsinsel 1, 80538 Munich, Germany, and TUM School of Education, Technical University of Munich, Schellingstrasse 33, 80799 Munich, Germany, [‡]Center for NanoScience (CeNS), Schellingstrasse 4, 80799 Munich, Germany, and [§]Department of Chemistry, Ludwig-Maximilians-University, Butenandtstrasse 11 (E), 81377 Munich, Germany

Two-dimensional covalent organic structures are a novel class of materials with extraordinary properties rendering them suitable for numerous potential applications in nanotechnology.¹ Especially porous networks, so-called covalent organic frameworks (COF), are of great interest for nanopatterning,² for organic electronics,^{3,4} as nanoreactors,⁵ and for immobilization of functional molecules in size-matched pores.⁶ For the on-surface synthesis of covalent organic structures, different types of chemical reactions were successfully employed, most prominently radical recombination^{7–15} and condensation reactions,^{16–23} or a combination thereof.^{24,25} In particular, the polycondensation of boronic acids on surfaces has already yielded promising results.^{16,24,26,28} Moreover, both mechanisms and thermodynamics of the on-surface condensation of 1,4-benzenediboronic acid were already studied by density functional theory complemented by entropy considerations.²⁹ It was suggested that the surface polycondensation is endothermic and, hence, entropically driven as a result of the elimination and release of water molecules as reaction byproduct. According to Le Chatelier's principle, supplying H₂O offers a way to introduce reversibility in the condensation reaction, a key requirement for the synthesis of long-range-ordered covalent structures.^{1,26,27}

Recently, we demonstrated a novel and straightforward preparation protocol for the synthesis of regular and extended surface-confined 2D COFs based on the polycondensation of 1,4-benzenediboronic acid (cf. **1** in Figure 1) as a model system.²⁷ This

ABSTRACT



On-surface self-condensation of 1,4-benzenediboronic acid was previously shown to yield extended surface-supported, long-range-ordered two-dimensional covalent organic frameworks (2D COFs). The most important prerequisite for obtaining high structural quality is that the polycondensation (dehydration) reaction is carried out under slightly reversible reaction conditions, *i.e.*, in the presence of water. Only then can the subtle balance between kinetic and thermodynamic control of the polycondensation be favorably influenced, and defects that are unavoidable during growth can be corrected. In the present study we extend the previously developed straightforward preparation protocol to a variety of para-diboronic acid building blocks with the aim to tune lattice parameters and pore sizes of 2D COFs. Scanning tunneling microscopy is employed for structural characterization of the covalent networks and of noncovalently self-assembled structures that form on the surface prior to the thermally activated polycondensation reaction.

KEYWORDS: condensation · dehydration · scanning tunneling microscopy · surface chemistry · boronic acid · covalent organic frameworks

diboronic acid building block was also successfully used in the synthesis of COF-1 bulk crystals.³⁰ For the on-surface polymerization, the reaction was pursued in an open system, where an initially added amount of water and eventually the H₂O partial pressure decrease over time. On the other hand, very promising results were also accomplished by Guan *et al.* in a closed system, where H₂O was supplied by the

* Address correspondence to markus@lackinger.org.

Received for review May 29, 2012 and accepted July 9, 2012.

Published online 10.1021/nn302363d

© XXXX American Chemical Society

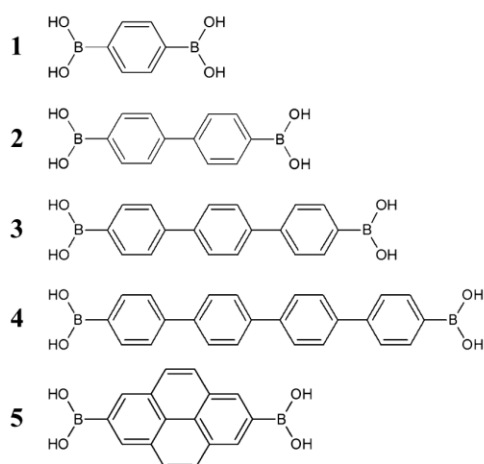


Figure 1. Molecular structures of diboronic acid monomers: **1**, 1,4-benzenediboronic acid (previously studied); **2**, biphenyldiboronic acid; **3**, terphenyldiboronic acid; **4**, quaterphenyldiboronic acid; **5**, pyrene-2,7-diboronic acid.

temperature-dependent and reversible dehydration of $\text{CuSO}_4 \cdot 5\text{H}_2\text{O}$.²⁶ In both sets of experiments graphite (001) served as an inert substrate and is not believed to play a vital chemical role in the polymerization. For 2D COF synthesis according to the first method, **1** was dissolved in an organic solvent (alkanes, aliphatic alcohols, or carboxylic acids) and drop-cast onto the substrate. The polymerization was initiated by a thermal treatment in an open system. The final structure is formed when the water has vanished and covalent interlinks are no longer reversible. The 2D COFs were characterized by scanning tunneling microscopy (STM), and the covalent cross-linking was unambiguously verified by comparison of experimental with theoretical lattice parameters, aided by verification of both the monolayers' high thermal stability and the accompanying chemical changes by X-ray photoelectron spectroscopy.²⁷ The above straightforward synthesis protocol yields full surface coverage with 2D COF-1 featuring domain sizes exceeding $40 \times 40 \text{ nm}^2$.

While in the previous work the proof of principle was demonstrated, we now extend our studies to show that the proposed synthesis protocol can also yield structurally diverse 2D COFs with increased pore dimensions. Adjustable pore sizes are an important prerequisite to specifically design host systems for variably sized guests as large functional molecules.³¹ To this end, we adapt a well-established synthesis strategy of isorecticular organic structures, where the length of an organic spacer group of the monomer is increased by adding conformationally rigid entities as phenyl or ethynyl groups, while maintaining the steric arrangement of linker groups. Yaghi *et al.* and Dichtel *et al.* successfully implemented this principle with para-diboronic acids for bulk COFs.^{30,32,33} Since the linear arrangement of the two boronic acid functionalities is

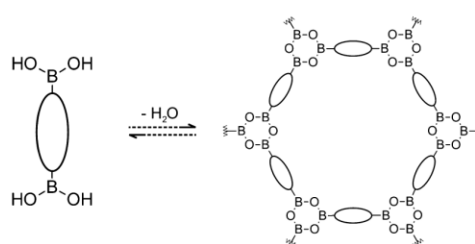


Figure 2. General reaction scheme of diboronic acid self-condensation into hexagonal 2D COFs. The straight organic backbones of the diboronic acids are symbolically represented by ellipses.

maintained, the network topology is not changed. In addition, we demonstrate that not only *p*-polyphenyl diboronic acids but also a para-diboronic acid with an aromatic pyrene backbone are suitable monomers for 2D COFs. While the same pyrene diboronic acid already yielded bulk COFs with a layered structure,³⁴ the synthesis of a single surface-supported 2D COF layer represents a major step toward templated growth.

Since boronic acids are known to form stable hydrogen-bonded structures, we now also study non-covalent self-assembly of the building blocks at the liquid–solid interface. This is important, because hydrogen-bonded complexes of boronic acids were identified as significant intermediate structures in the self-condensation reaction.²⁹ Consequently, self-assembled diboronic acid monolayers may be an important precursor structure for the polycondensation and might also influence 2D COF formation in the subsequent thermal treatment. Self-assembled structures of **1** were already observed upon deposition onto silver and gold surfaces under ultrahigh-vacuum (UHV) conditions.^{35,36} Although the basic experimental conditions between UHV and the liquid–solid interface are fundamentally different and the interaction between monomers and metals is typically stronger, preceding supramolecular phases may play a general role in polymerization reactions of monomers that can also form relatively stable hydrogen-bonded structures.

RESULTS AND DISCUSSION

The cyclic self-condensation of three boronic acids yields planar boroxine rings (B_3O_3), whereby three H_2O molecules per boroxine ring are eliminated.^{26,30,34} Accordingly, self-condensation of diboronic acids can result in fully reticulated planar networks, as has been demonstrated for both 2D and layered 3D systems. The self-condensation of diboronic acids yields covalent sheets with a hexagonal arrangement of boroxine rings that are interconnected by the organic backbone of the diboronic acid monomer. The general reaction scheme of the self-condensation is outlined in Figure 2. Here the polycondensation reaction is carried out in an open system. Reversible reaction conditions are realized by adding a small amount of water to the bottom

TABLE 1. Summarized Experimental and Molecular Mechanics (MM)-Derived Lattice Parameters for All 2D COFs and MM-Derived Adsorption Energies on Graphite for All Diboronic Acid Building Blocks

| building block | experimental lattice parameters | | | MM-derived lattice parameters | | | | MM adsorption energy [kJ/mol] |
|----------------|---------------------------------|---------------|----------------|-------------------------------|---------------|----------------|-----------------------------|-------------------------------|
| | <i>a</i> [nm] | <i>b</i> [nm] | γ [deg] | <i>a</i> [nm] | <i>b</i> [nm] | γ [deg] | pore size ^b [nm] | |
| 1 ^a | 1.4 ± 0.1 | 1.4 ± 0.1 | 60.0 ± 3 | 1.5 | 1.5 | 60 | 1.0 | 254.6 |
| 2 | 2.1 ± 0.3 | 2.1 ± 0.3 | 58.9 ± 4 | 2.3 | 2.3 | 60 | 1.6 | 405.4 |
| 3 | 2.9 ± 0.2 | 2.9 ± 0.2 | 57.5 ± 3 | 3.0 | 3.0 | 60 | 2.4 | 535.8 |
| 4 | 3.5 ± 0.3 | 3.6 ± 0.3 | 62.0 ± 5 | 3.8 | 3.8 | 60 | 3.2 | 685.1 |
| 5 | 2.1 ± 0.1 | 2.1 ± 0.1 | 58.9 ± 2 | 2.3 | 2.3 | 60 | 1.4 | 511.3 |

^a Derived in a previous study.²⁷ ^b Maximum diameter of a disk that fits into a pore in a van der Waals representation of the respective 2D COF.

of the reactor, and the polymerization is initiated by tempering to ~100 °C. During the heating procedure the water evaporates and the chemical equilibrium is eventually fully shifted to the dehydrated state. Details of the protocol can be found in the Materials and Methods section.

Chemical modification of the organic backbone is the strategy pursued to increase the pore size of COFs with the aim to establish an isoreticular series of 2D COFs. This general design principle for organic materials is well known from supramolecular monolayers,^{37,38} isoreticular metal organic frameworks (MOF),³⁹ and 2D metal coordinated networks⁴⁰ and has also been exploited successfully for bulk crystals of various diboronic acid-derived COFs.^{30,34,41,42} The compounds utilized in this study are illustrated in Figure 1: benzene diboronic acid (**1**) as used in the previous study, biphenyldiboronic acid (**2**), terphenyldiboronic acid (**3**), quaterphenyldiboronic acid (**4**), and pyrene-2,7-diboronic acid (**5**). The organic backbones of all diboronic acids are composed of phenyl rings, either σ -bonded (**1–4**) or fused into a pyrene core (**5**). Planar adsorption of these organic backbones is driven by π - π interactions with the graphite substrate, whereby the adsorption energies increase with backbone size. The two boronic acid functional groups are attached in para-position, hence providing straight linkers. Assuming a fully planar geometry of the polyphenyl backbone as known from adsorbed polyphenyls,^{40,43} all building blocks have D_{2h} symmetry. In order to obtain crystallographic reference data for all 2D COFs, their theoretical lattice parameters were calculated by molecular mechanics (MM) calculations; results are listed in Table 1 and compared to experimental data. Additionally, the MM-derived adsorption energies with respect to the gas phase are provided.

Utilizing the standard synthesis procedure, all building blocks yielded well-ordered 2D COFs on graphite; representative STM images of all networks are depicted in Figure 3. In the following the results obtained for the not previously studied diboronic acids (**2–5**) are described in more detail.

Biphenyldiboronic Acid (2). Self-condensation of **2** yields 2D COFs with a domain size of up to 100 × 100 nm² and

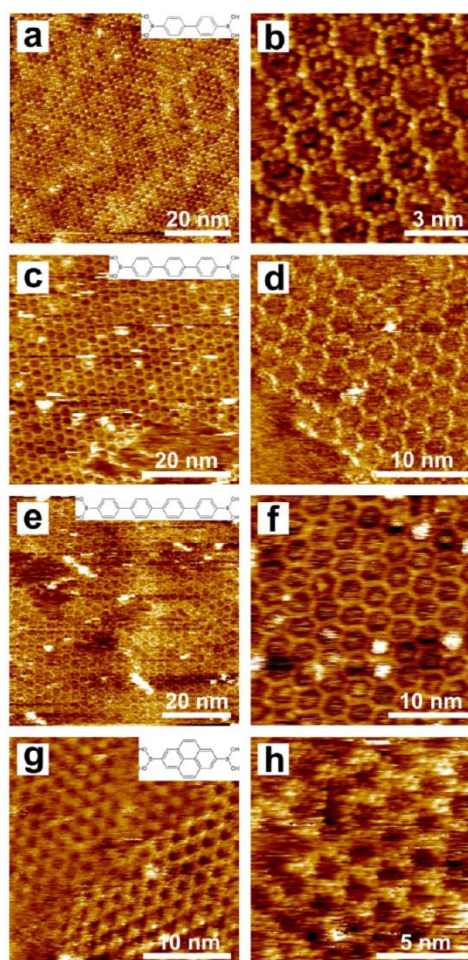


Figure 3. STM images of 2D COFs derived from polycondensation of the following monomers: (a, b) **2**, (c, d) **3**, (e, f) **4**, (g, h) **5**. The respective monomers are depicted in the insets. Details for all 2D COFs can be found in the text.

almost full surface coverage, as illustrated in Figure 3a and b. In the detailed view, contrast features within the pores are clearly discernible and are attributed to either residual solvent molecules or unreacted monomers. The experimental lattice parameter of this $p6mm$

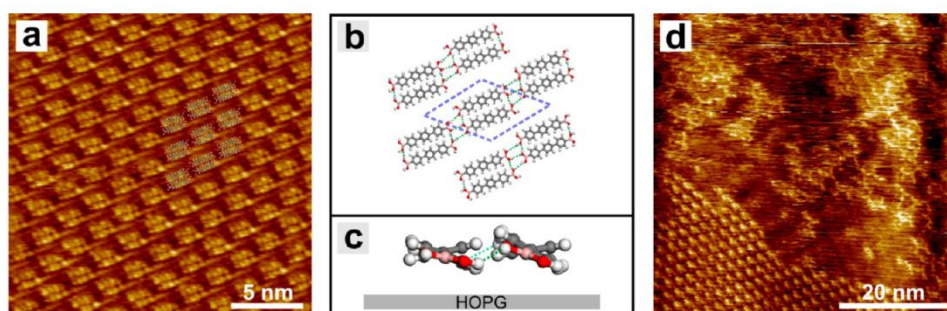


Figure 4. (a) STM image of self-assembled monolayers of terphenyldiboronic acid (**3**) acquired at the liquid–solid interface with heptanoic acid. Overlaid molecules are drawn to scale. (b) Tentative model as derived from the STM data. Unit cell and hydrogen bonds are indicated by dashed blue and green lines, respectively. (c) Side-view of the model with tilted molecular planes with respect to the substrate. Such tilting is suggested by the small inter-row spacing and was similarly found in comparable bulk crystals and monolayers of **1**. (d) STM image of a thermally treated sample (70 °C, 30 min) showing the coexistence of unreacted self-assembled domains (lower left part) and first 2D COFs (upper right part).

symmetric structure of 2.1 ± 0.3 nm agrees well with the theoretical value of 2.3 nm and thereby confirms covalent interlinking into the anticipated network structure. In a recent study, the diboronic acid **2** was likewise polymerized in a closed system, where the hexagonal networks had similar lattice parameters.²⁶ Noncovalent self-assembly of **2** into stable structures could not be observed at the heptanoic acid–graphite interface at room temperature. However, a gentle thermal treatment at temperatures that are significantly lower than the 100 to 150 °C previously used to activate the polymerization on graphite^{26,27} already promotes self-condensation.

Samples were thermally treated at 50 °C for ~30 min (without reactor) and studied *ex situ* after they had cooled to room temperature. Subsequent STM imaging revealed small to intermediate domains of the 2D COF. This indicates that with monomer **2** the reaction can already be initiated at around 50 °C on graphite and that the presence of additional water is not required for the initial growth of small domains. However, without addition of water full surface coverage was never accomplished.

Terphenyldiboronic Acid (3). Domains of a 2D COF with lateral extensions up to 100×100 nm² are routinely obtained through polycondensation of **3** by applying a thermal treatment similar to that for **2** with similar temperatures and exposure times. Almost full surface coverage with only a few voids or missing molecules was achieved, and representative STM images are depicted in Figure 3c and d. Again, the experimental lattice parameter of this *p6mm* symmetric 2D COF of 2.9 ± 0.2 nm agrees well with the MM-derived lattice parameter of 3.0 nm.

Noncovalent Self-Assembly of 3. In contrast to **1** and **2** (diboronic acids with only one or two phenyl rings) the terphenyl diboronic acid **3** was also found to self-assemble into interfacial monolayers that are stabilized by noncovalent interactions. These supramolecular structures were studied on samples without any

previous thermal treatment directly at the heptanoic acid–graphite interface with the STM tip immersed into solution. As evident from the STM images presented in Figure 4a, the supramolecular monolayers almost fully cover the surface. The structure possesses an almost hexagonal lattice with $a = 2.1 \pm 0.1$ nm, $b = 2.2 \pm 0.1$ nm, and $\gamma = 62 \pm 3^\circ$. Single molecules are clearly identified by both their size and shape as well as by their intramolecular contrast with three clearly separated protrusions. These can be assigned to the three individual phenyl rings of the terphenyl backbone.⁴⁴ The unit cell contains two molecules; a tentative model of the structure is shown in Figure 4b. As deduced from the molecular arrangement, the structure is stabilized by five B–O···H–O hydrogen bonds per unit cell. The model suggests that molecules may not adsorb entirely planar, but slightly tilted, as illustrated in Figure 4c. This tilt aids in reducing the steric hindrance of the otherwise too tightly packed polyphenyl backbones of adjacent molecules and, thus, promotes a higher surface packing density. Similar tilting was proposed for **1** both in the sheets of bulk crystals⁴⁵ and in self-assembled 2D structures on a KCl surface.⁴⁶ Interestingly, a comparable thermal treatment to that for **2** at a similar temperature of 50 °C but up to ~1 h was not sufficient to initialize polymerization of **3**. Instead, the self-assembled monolayer persisted. 2D COFs start to nucleate only upon exposure to higher temperatures, around 70 °C, for ~30 min. However, as illustrated in Figure 4d, covalent domains still coexist with self-assembled structures. Again, by means of a simple thermal treatment without H₂O, full surface coverage of a 2D COF was never accomplished.

A solvent dependence was observed for thermal treatment at 120 °C in the reactor with additional water. Using heptanoic acid as solvent, only COFs were observed, but no self-assembled structures anymore. Yet after a similar thermal treatment with dodecane as solvent, COFs and self-assembled supramolecular structures still coexisted. This solvent effect can be

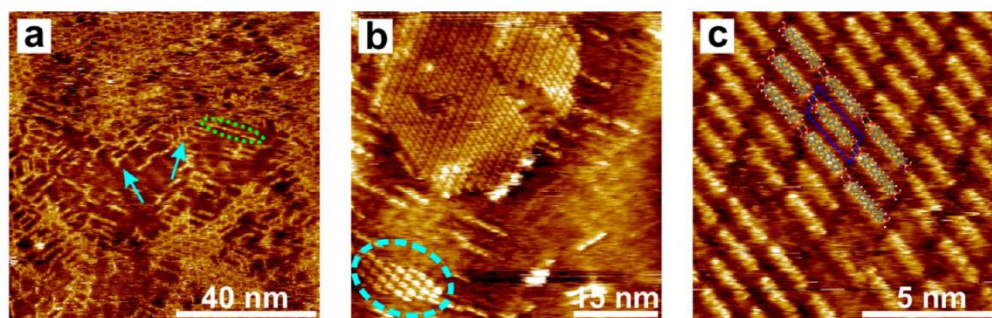


Figure 5. STM images depicting self-assembled and covalently interlinked structures of quaterphenyl diboronic acid (**4**). (a) Example of incomplete polymerization, where hexagonal covalent networks and remainders of the self-assembled structures coexist. The light blue arrows point to tripod structures where single boroxine rings were already formed by condensation of three monomers. The linear arrangements, marked by the dotted oval, are residues of the self-assembled structure. (b) Self-assembled structures of a nontreated sample; two different polymorphs are commonly observed: structure 1 with one molecule per unit cell and lattice parameters $a = 1.1 \pm 0.1$ nm; $b = 2.1 \pm 0.1$ nm; $\gamma = 62 \pm 3^\circ$ (marked by the dashed circle); structure 2 with two molecules per unit cell and $a = 2.0 \pm 0.1$ nm; $b = 2.3 \pm 0.1$ nm; $\gamma = 53 \pm 2^\circ$ (upper part). (c) Close-up of structure 1 with overlaid scaled molecules. The unit cell is marked in blue.

rationalized by the different nature of both solvents: Heptanoic acid is a polar, protic solvent, whereas dodecane is a nonpolar, nonprotic solvent. Since the molecular packing density in the self-assembled monolayer is around 1.4 times higher than in the porous COF, desorption is a necessary preceding step for COF formation. At the liquid–solid interface, the desorption barrier from the surface into the liquid phase depends on the ability of the solvent to accommodate the adsorbate. Since boronic acids can be significantly better dissolved in heptanoic acid where the molecules can be stabilized by hydrogen bonds, a lower desorption barrier promotes COF formation in heptanoic acid. Albeit less obvious, desorption of the monomers into a supernatant liquid phase might also play a key role in the experiments of Guan *et al.*,²⁶ where in a closed system water pressure is built up by the reversible dehydration of $\text{CuSO}_4 \cdot 5\text{H}_2\text{O}$. The authors state that full dehydration would result in a H_2O partial pressure of 8 atm. Although the actual water pressure might be lower, it appears likely that at sizable H_2O partial pressures a thin water film can form even on hydrophobic graphite surfaces. This liquid layer would promote desorption of the water-soluble diboronic acids. Consequently, a comparable reaction mechanism becomes conceivable for both preparation protocols.

Quaterphenyldiboronic Acid (4). Applying the same synthesis protocol with compound **4** yields 2D COFs with domains up to 40×40 nm², and representative STM images are depicted in Figure 3e and f. Again, a good agreement between the experimental lattice parameter of this hexagonal structure of 3.5 ± 0.3 nm with the MM-derived value of 3.8 nm proves formation of the anticipated covalent network. As shown in Figure 3e and f, despite the structural perfection and the long-range order of the networks, only partial surface coverage was accomplished.

Additional changes in the preparation protocol including higher oven temperatures for the thermal treatment (140 °C instead of 120 °C) or iterations of the synthesis protocol on the same sample, where new solution was added to a pre-existing COF and further thermal treatment was applied, did not improve the surface coverage.

Often molecular arrangements at different stages of the polymerization process, *i.e.*, self-assembled structures, larger covalent aggregates, and emerging COF structures, were found to coexist on the surface; an example is shown in Figure 5a.

Noncovalent Self-Assembly of 4. Likewise noncovalent self-assembly of **4** was studied at the liquid–solid interface by the method described above. However, well-ordered self-assembled monolayers were not observed upon room-temperature deposition, but rather disordered adsorption of single molecules. Only if the samples were heated at 50 °C for ~ 1 h (without reactor, residues of solvent still present) were two different well-ordered, noncovalent self-assembled polymorphs observed *ex situ* after the sample had cooled. The first, more often observed structure depicted in Figure 5b exhibits lattice parameters of $a = 1.1 \pm 0.1$ nm, $b = 2.1 \pm 0.1$ nm, and $\gamma = 61 \pm 3^\circ$ with one molecule per unit cell. The second structure is highlighted by the circle in Figure 5b and features two molecules per unit cell with lattice parameters $a = 2.0 \pm 0.1$ nm, $b = 2.3 \pm 0.1$ nm, and $\gamma = 53 \pm 2^\circ$. Here the arrangement in the monolayer is similar to the self-assembled structure found for **3** (cf. Figure 4a). Interestingly, for the quaterphenyldiboronic acid, even a thermal treatment at 70 °C did not initiate the polymerization. Only thermal treatment at temperatures around 100 °C in the reactor eventually yielded COFs.

Pyrene-2,7-diboronic Acid (5). While in the previous examples we have demonstrated the possibility to extend lattice parameters and pore sizes by

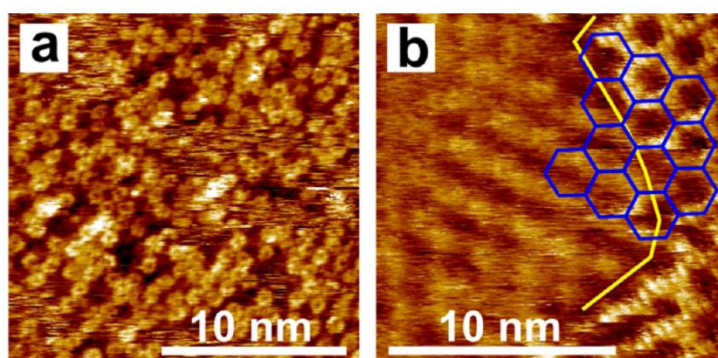


Figure 6. STM images of pyrene-2,7-diboronic acid (**5**) on graphite. (a) Disordered noncovalent arrangement observed at the liquid–solid interface upon room-temperature deposition of heptanoic acid solution. (b) Related 2D COF, obtained after thermal treatment of **5**. At the right-hand side a second layer of the 2D COF can be discerned by the brighter contrast. First and second layer are stacked in an eclipsed manner, as indicated by the blue hexagons.

progressively adding phenyl rings to the organic backbone of diboronic acids, we now demonstrate that the nature of the organic backbone can likewise be modified. To this end we have chosen pyrene-2,7-diboronic acid, because corresponding bulk COFs have shown interesting optoelectronic properties.³⁴ By shining light on electrically contacted COFs in a gap configuration, photocurrents could be measured. The bulk structure obtained from solvothermal self-condensation of **5** exhibits a layered structure with eclipsed stacking of the covalent sheets.

For the synthesis of 2D COFs the same preparation protocol can be applied to **5** and yields 2D COFs with domains up to $100 \times 100 \text{ nm}^2$ in size, as shown in Figure 3g and h. The structural quality of these COFs is high, and the defect density is very low. As for the polyphenyl networks, formation of the desired covalent network is again proven by the good agreement between the experimental ($2.1 \pm 0.1 \text{ nm}$) and theoretical lattice parameter of 2.3 nm . Both values are consistent with the in-plane lattice parameter of 2.22 nm of the corresponding bulk structure.³⁴

Self-assembly of well-ordered noncovalent structures of **5** was never obtained, not even for thermally treated samples. However, short-range-ordered arrangements of **5** were observed at the heptanoic acid–graphite interface; a typical STM image is depicted in Figure 6a. These disordered arrangements persisted, even when the samples were heated at $70 \text{ }^\circ\text{C}$ for $\sim 1 \text{ h}$.

DISCUSSION

All diboronic acids studied were suitable building blocks for the synthesis of long-range-ordered 2D COFs on graphite. The lattice parameters of all COFs agree well with theoretical values from MM calculations and available experimental data, whereby formation of covalent networks through the anticipated cyclization is verified.

An exceptional case is the pyrene-derived COF, where formation of a second layer is often observed;

representative STM images are depicted in Figures 3g and 6b. Formation of bilayer COFs was found in particular for higher concentrations of the monomer **5** in the applied solution. High-resolution images with only partial coverage of the second layer allow to directly deduce the relative arrangement between both covalent layers in real space. This is demonstrated in Figure 6b by superimposing the common hexagonal lattice. The pyrene-derived COF exhibits eclipsed stacking, as similarly proposed for the corresponding bulk COF structure.³⁴

For a better understanding of the underlying reaction mechanism, it is instructive to also study noncovalent self-assembly of the respective diboronic acids. Interestingly, self-assembled structures of the diboronic acids at the liquid–solid interface were observed only for the intermediately sized diboronic acids **3**, **4**, and **5**. Intermolecular hydrogen bonds that are mediated by the free boronic acid groups add to the stabilization of those monolayers. The absence of self-assembled monolayers of the smaller boronic acids **1** and **2** can be explained by their relatively low adsorption energies, which are apparently too small to stabilize the interfacial monolayer (cf. Table 1 for MM-derived values). It is important to note that the MM-derived adsorption energies refer to isolated molecules in the gas phase. Desorption energies with respect to the liquid phase can be vastly different, due to stabilizing contributions from solvation enthalpy. In general, the enthalpic stabilization of monolayers at the liquid–solid interface is comprised of two major contributions, *i.e.*, from molecule–molecule interactions and from molecule–substrate interactions. When the sum of both contributions is too small to compensate the entropic cost of self-assembly, ordered structures are thermodynamically not stable at the liquid–solid interface. On the other hand, when the organic backbone becomes too large, the surface mobility can be inhibited and monolayer self-assembly can become kinetically hindered. This is obviously the

case for compounds **4** and **5** at room temperature, where only disordered adsorption occurred. Only after thermal activation does the enhanced surface mobility facilitate self-assembly of **4** into ordered structures, whereas for **5** even then the disordered structure persisted. Although the adsorption energy of **5** is lower than that of **4** and comparable to that of **3**, its surface mobility appears to be the lowest for the diboronic acids studied here. While large adsorption energies can be taken only as a hint for high surface diffusion barriers, the actual corrugation of the surface potential in relation to thermal energy determines the surface mobility. So apparently the favorable registry between the pyrene core and the graphite substrate results in strongly preferred adsorption sites that are associated with relatively deep energetic minima, hence a high corrugation of the surface potential. Disordered arrangements that are caused by a low surface mobility on graphite were even observed for comparatively small aromatic cores as in naphthalene dicarboxylic acid.⁴⁷

Since the self-assembled monolayers emerge as an intermediate structure en route to the final 2D COF, the observed increase of the required activation temperature for polycondensation from **2** to **4** can be explained along these lines. Experimentally, we find that **2** already polymerizes below 50 °C, while **3** requires temperatures around 70 °C. For **4** even higher temperatures were necessary to observe first covalent structures. Thermal activation is needed not only to initiate the polycondensation but also to break up the preceding noncovalent arrangement, *i.e.*, the self-assembled monolayer. The enthalpic stabilization per molecule within the self-assembled monolayer increases with molecule size, thereby hinting toward a possible explanation for the increasing polymerization temperatures for monomers **2** to **4**. However, also the energetic barriers for many other processes that are vital for the thermally activated polymerization increase with monomer size. An obvious and definitely important example thereof is surface diffusion. Porte *et al.* studied the polymerization of **1** on Cu(111), Ag(100), Ag(111), and Au(111) in great detail and found the lowest degree of reticulation on Cu(111), the surface with the highest diffusion barrier.³⁵ Spontaneous polymerization at room temperature without further thermal activation was observed on Ag(100), yet on a time scale of tens of hours. Here the rate-determining step is most probably surface diffusion. Interestingly, polymerization starting from self-assembled monolayers of **1** on Ag(100) could be greatly accelerated either by electron bombardment or locally by STM imaging with reduced tip–sample distance.³⁶ The authors propose that either enhanced surface diffusion or promoted desorption could account for their observations. The poorly ordered structures observed upon room-temperature deposition of **4** and **5** clearly

indicate that surface diffusion can become a limiting factor, even on weakly interacting graphite surfaces. Desorption as a competing process is another important issue for thermally activated on-surface polymerization of preceding densely packed self-assembled monolayers. For polymerization of **1** on Au(111) preferred desorption upon annealing already results in a greatly diminished surface coverage, and COFs were found only in the vicinity of substrate step-edges, where the monomers were attached more strongly. Yet, the situation at the liquid–graphite surface appears to be beneficial for polymerization as compared to metals in UHV. On one hand the surface-diffusion barriers on graphite are still quite low, and on the other hand desorption is not an irreversible process as in UHV. At the liquid–solid interface desorbing molecules are not irretrievably lost, but are still solvated in the liquid phase and available for the on-surface polymerization. Especially, when the solvent that was initially used for drop-casting evaporates during the thermal treatment, the monomer concentration in solution increases, thereby reinforcing the thermodynamic driving force for readsorption.

In summary, studying the ability of the monomer to form thermodynamically stable self-assembled structures might be useful for understanding trends in activation temperatures and the magnitudes of energetic barriers for surface diffusion and desorption.

CONCLUSION

In the present work, regular and extended 2D COFs were prepared according to a previously developed straightforward synthesis protocol.²⁷ Structural versatility was obtained by polycondensation of four different diboronic acids. By using para-diboronic acids where the size of the organic backbone was incrementally varied from phenyl to quaterphenyl, a series of isoreticular 2D COFs was created. The lattice parameters of these isoreticular networks range from 1.5 nm (**1**) to 3.8 nm (**4**), and the corresponding pore sizes increase from ~1.0 to 3.2 nm. In addition, we could demonstrate that a para-diboronic acid with a pyrene core is similarly suited to yield 2D COFs with *p6mm* symmetry. For this system, indications of bilayer growth are also found with a similar eclipsed stacking to that observed in bulk crystals. In addition to their polymerization the capability of the diboronic acids to self-assemble into stable structures on the surface was studied by STM. Self-assembled, long-range ordered monolayers upon room-temperature deposition were observed only for **3**, while room-temperature deposition of **4** and **5** yielded poorly ordered structures. Since mild heating could improve the structural quality for **4** but not for **5**, a limited surface mobility at room temperature could account for the low degree of order in these kinetically trapped structures. Stable monolayers of **1** and **2** were not observed, because the

molecule–substrate interaction of these smaller molecules is too low to stabilize the interfacial monolayer.

By means of additional studies with varying activation temperature we find that for monomers **2** to **4** the temperature threshold for the onset of polymerization increases with the size of the organic backbone. Several different reaction steps, such as breaking up of hydrogen-bonded aggregates, surface diffusion, re-orientation, and possibly desorption, are required to

convert a noncovalent self-assembled monolayer into a surface-supported 2D COF. Since the energetic barriers of these elementary processes increase with monomer size, it is difficult to reveal the rate-determining reaction step. Hence, for a more detailed understanding of the polymerization mechanism and kinetics it would be highly desirable to study the polymerization *in situ* at the molecular scale by means of temperature-dependent STM experiments.

MATERIALS AND METHODS

The synthesis of biphenyldiboronic acid (**2**) and pyrene-2,7-diboronic acid (**5**) is reported elsewhere.^{48,49} Details of the synthesis of the new diboronic acid building blocks terphenyldiboronic acid (**3**) and quaterphenyldiboronic acid (**4**) can be found in the Supporting Information. Heptanoic acid (Fluka, purity $\geq 98\%$) was used as solvent for all building blocks and additionally dodecane (Sigma-Aldrich, anhydrous, purity $\geq 99\%$) for **3**. For the 2D COF synthesis a small amount (~ 1 mg) of the respective compound was added to 1.5 mL of solvent, sonicated for 90 min, and centrifuged for up to 15 min. This procedure does not fully dissolve the molecules. Subsequently, the solutions were again dispersed by careful shaking, yielding a whitish suspension. Then an amount of ~ 7.5 μL of the respective suspensions was applied to a freshly cleaved (001) surface of highly oriented pyrolytic graphite (HOPG) and immediately transferred to a stainless steel reactor (7.7 mL volume) with the sample surface pointing upward. The reactor was then placed into a preheated oven for 60 min at 120 °C. Reversible reaction conditions were realized by a H_2O atmosphere that was generated by adding 50 μL of water to the bottom of the reactor (not in direct contact with the sample). A slightly opened valve on the reactor allowed gas exchange with the environment; that is, the reactor was operated as an open system. After the thermal treatment, the reactor was taken out of the oven and allowed to cool for at least 20 min before the samples were removed. After this procedure both the solvent and water were completely evaporated. Subsequently, the samples were characterized by scanning tunneling microscopy using a home-built drift-stable instrument driven by an ASC 500 scanning probe microscopy controller from attocube Systems AG. Constant current images were obtained with tunneling voltages between +0.4 and +1.1 V applied to the tip and set point currents between 40 and 110 pA. For all experiments mechanically cut 90/10 PtIr tips were used. In order to study the onset of polymerization, the influence of a thermal treatment at lower temperatures from 50 to 70 °C was studied by placing the samples directly into the oven without the reactor, thereby reducing the influence of thermal inertia.

Noncovalent self-assembly of the diboronic acid building blocks was studied directly at the liquid–solid interface. To this end, 5 μL of solution was deposited on a freshly cleaved HOPG substrate, and self-assembled monolayers were characterized with the STM tip immersed into solution.

Molecular mechanics simulations were conducted for all 2D COFs on a graphite substrate using the Dreiding force field. Similarly adsorption energies of single molecules were estimated for all building blocks. The graphite substrate was approximated by two layers with the atomic positions of the lower layer fixed. Arrangements of six unit cells were optimized for each structure.

Conflict of Interest: The authors declare no competing financial interest.

Acknowledgment. Financial support from the Nano Systems Initiative Munich (NIM) and the Bayerische Forschungsförderung is gratefully acknowledged. D.D.M. would like to thank the Minerva Postdoctoral Fellowship.

Supporting Information Available: Synthesis of terphenyldiboronic acid (**3**) and quaterphenyldiboronic acid (**4**). This material is available free of charge via the Internet at <http://pubs.acs.org>.

REFERENCES AND NOTES

- Perepichka, D. F.; Rosei, F. Extending Polymer Conjugation into the Second Dimension. *Science* **2009**, *323*, 216–217.
- Joo, S. H.; Choi, S. J.; Oh, I.; Kwak, J.; Liu, Z.; Terasaki, O.; Ryoo, R. Ordered Nanoporous Arrays of Carbon Supporting High Dispersions of Platinum Nanoparticles. *Nature* **2001**, *412*, 169–172.
- Spitler, E. L.; Dichtel, W. R. Lewis Acid-Catalysed Formation of Two-Dimensional Phthalocyanine Covalent Organic Frameworks. *Nat. Chem.* **2010**, *2*, 672–677.
- Jiang, D. L.; Wan, S.; Guo, J.; Kim, J.; Ihee, H. A Belt-Shaped Blue Luminescent, and Semiconducting Covalent Organic Framework. *Angew. Chem., Int. Ed.* **2008**, *47*, 8826–8830.
- Lei, S. B.; Tahara, K.; Adisojoso, J.; Balandina, T.; Tobe, Y.; De Feyter, S. Towards Two-Dimensional Nanoporous Networks: Crystal Engineering at the Solid-Liquid Interface. *CrystEngComm* **2010**, *12*, 3369–3381.
- Griessl, S. J. H.; Lackinger, M.; Jamitzky, F.; Markert, T.; Hietschold, M.; Heckl, W. M. Incorporation and Manipulation of Coronene in an Organic Template Structure. *Langmuir* **2004**, *20*, 9403–9407.
- Gutzler, R.; Walch, H.; Eder, G.; Kloft, S.; Heckl, W. M.; Lackinger, M. Surface Mediated Synthesis of 2D Covalent Organic Frameworks: 1,3,5-Tris(4-bromophenyl)benzene on Graphite(001), Cu(111), and Ag(110). *Chem. Commun.* **2009**, 4456–4458.
- Grill, L.; Dyer, M.; Lafferentz, L.; Persson, M.; Peters, M. V.; Hecht, S. Nano-Architectures by Covalent Assembly of Molecular Building Blocks. *Nat. Nanotechnol.* **2007**, *2*, 687–691.
- Lipton-Duffin, J. A.; Ivashenko, O.; Perepichka, D. F.; Rosei, F. Synthesis of Polyphenylene Molecular Wires by Surface-Confining Polymerization. *Small* **2009**, *5*, 592–597.
- Cai, J.; Ruffieux, P.; Jaafar, R.; Bieri, M.; Braun, T.; Blankenburg, S.; Muoth, M.; Seitonen, A. P.; Saleh, M.; Feng, X.; et al. Atomically Precise Bottom-Up Fabrication of Graphene Nanoribbons. *Nature* **2010**, *466*, 470–473.
- Lipton-Duffin, J. A.; Miwa, J. A.; Kondratenko, M.; Ciccoira, F.; Sumpter, B. G.; Meunier, V.; Perepichka, D. F.; Rosei, F. Step-by-Step Growth of Epitaxially Aligned Polythiophene by Surface-Confining Reaction. *Proc. Natl. Acad. Sci. U. S. A.* **2010**, *107*, 11200–11204.
- Blunt, M. O.; Russell, J. C.; Champness, N. R.; Beton, P. H. Templating Molecular Adsorption Using a Covalent Organic Framework. *Chem. Commun.* **2010**, *46*, 7157–7159.
- Bieri, M.; Treier, M.; Cai, J.; Ait-Mansour, K.; Ruffieux, P.; Groning, O.; Groning, P.; Kastler, M.; Rieger, R.; Feng, X.; et al. Porous Graphenes: Two-Dimensional Polymer Synthesis with Atomic Precision. *Chem. Commun.* **2009**, *45*, 6919–6921.
- Walch, H.; Gutzler, R.; Sirtl, T.; Eder, G.; Lackinger, M. Material- and Orientation-Dependent Reactivity for Heterogeneously Catalyzed Carbon–Bromine Bond Homolysis. *J. Phys. Chem. C* **2010**, *114*, 12604–12609.

15. Bieri, M.; Nguyen, M.-T.; Gröning, O.; Cai, J.; Treier, M.; Aït-Mansour, K.; Ruffieux, P.; Pignedoli, C. A.; Passerone, D.; Kastler, *et al.* Two-Dimensional Polymer Formation on Surfaces: Insight into the Roles of Precursor Mobility and Reactivity. *J. Am. Chem. Soc.* **2010**, *132*, 16669–16676.
16. Zwaneveld, N. A. A.; Pawlak, R.; Abel, M.; Catalin, D.; Gigmès, D.; Bertin, D.; Porte, L. Organized Formation of 2D Extended Covalent Organic Frameworks at Surfaces. *J. Am. Chem. Soc.* **2008**, *130*, 6678–6679.
17. Tanoue, R.; Higuchi, R.; Enoki, N.; Miyasato, Y.; Uemura, S.; Kimizuka, N.; Stieg, A. Z.; Gimzewski, J. K.; Kunitake, M. Thermodynamically Controlled Self-Assembly of Covalent Nanoarchitectures in Aqueous Solution. *ACS Nano* **2011**, *5*, 3923–3929.
18. Schmitz, C. H.; Ikonov, J.; Sokolowski, M. Two-Dimensional Ordering of Poly(p-phenylene-terephthalamide) on the Ag(111) Surface Investigated by Scanning Tunneling Microscopy. *J. Phys. Chem. C* **2009**, *113*, 11984–11987.
19. Weigelt, S.; Busse, C.; Bombis, C.; Knudsen, M. M.; Gothelf, K. V.; Lægsgaard, E.; Besenbacher, F.; Linderoth, T. R. Surface Synthesis of 2D Branched Polymer Nanostructures. *Angew. Chem., Int. Ed.* **2008**, *47*, 4406–4410.
20. Weigelt, S.; Bombis, C.; Busse, C.; Knudsen, M. M.; Gothelf, K. V.; Lægsgaard, E.; Besenbacher, F.; Linderoth, T. R. Molecular Self-Assembly from Building Blocks Synthesized on a Surface in Ultrahigh Vacuum: Kinetic Control and Topo-Chemical Reactions. *ACS Nano* **2008**, *2*, 651–660.
21. Treier, M.; Fasel, R.; Champness, N. R.; Argent, S.; Richardson, N. V. Molecular Imaging of Polyimide Formation. *Phys. Chem. Chem. Phys.* **2009**, *11*, 1209–1214.
22. Schmitz, C. H.; Ikonov, J.; Sokolowski, M. Two-Dimensional Polyamide Networks with a Broad Pore Size Distribution on the Ag(111) Surface. *J. Phys. Chem. C* **2011**, *115*, 7270–7278.
23. Jensen, S.; Früchtl, H.; Baddeley, C. J. Coupling of Triamines with Diisocyanates on Au(111) Leads to the Formation of Polyurea Networks. *J. Am. Chem. Soc.* **2009**, *131*, 16706–16713.
24. Faury, T.; Clair, S.; Abel, M.; Dumur, F.; Gigmès, D.; Porte, L. Sequential Linking to Control Growth of a Surface Covalent Organic Framework. *J. Phys. Chem. C* **2012**, *116*, 4819–4823.
25. Schlögl, S.; Sirtl, T.; Eichhorn, J.; Heckl, W. M.; Lackinger, M. Synthesis of Two-Dimensional Phenylene-Boroxine Networks Through in Vacuo Condensation and On-Surface Radical Addition. *Chem. Commun.* **2011**, 47.
26. Guan, C.-Z.; Wang, D.; Wan, L.-J. Construction and Repair of Highly Ordered 2D Covalent Networks by Chemical Equilibrium Regulation. *Chem. Commun.* **2012**, 48, 2943–2945.
27. Dienstmaier, J. F.; Gigler, A. M.; Goetz, A. J.; Knochel, P.; Bein, T.; Lyapin, A.; Reichmaier, S.; Heckl, W. M.; Lackinger, M. Synthesis of Well-Ordered COF Monolayers: Surface Growth of Nanocrystalline Precursors versus Direct On-Surface Polycondensation. *ACS Nano* **2011**, *5*, 9737–9745.
28. Coratger, R.; Calmettes, B.; Abel, M.; Porte, L. STM Observations of the First Polymerization Steps Between Hexahydroxy-tri-phenylene and Benzene-di-boronic Acid Molecules. *Surf. Sci.* **2011**, *605*, 831–837.
29. Sassi, M.; Olson, V.; Debierre, J. M.; Humbel, S. Modelling the Two-Dimensional Polymerization of 1,4-Benzene Diboronic Acid on a Ag Surface. *ChemPhysChem* **2009**, *10*, 2480–2485.
30. Cote, A. P.; Benin, A. I.; Ockwig, N. W.; O’Keeffe, M.; Matzger, A. J.; Yaghi, O. M. Porous, Crystalline, Covalent Organic Frameworks. *Science* **2005**, *310*, 1166–1170.
31. Stepanov, S.; Lingenfelder, M.; Dmitriev, A.; Spillmann, H.; Delvigne, E.; Lin, N.; Deng, X.; Cai, C.; Barth, J. V.; Kern, K. Steering Molecular Organization and Host-Guest Interactions Using Two-Dimensional Nanoporous Coordination Systems. *Nat. Mater.* **2004**, *3*, 229–233.
32. Spitzer, E. L.; Koo, B. T.; Novotney, J. L.; Colson, J. W.; Uribe-Romo, F. J.; Gutierrez, G. D.; Clancy, P.; Dichtel, W. R. A 2D Covalent Organic Framework with 4.7-nm Pores and Insight into Its Interlayer Stacking. *J. Am. Chem. Soc.* **2011**, *133*, 19416–19421.
33. Cote, A. P.; El-Kaderi, H. M.; Furukawa, H.; Hunt, J. R.; Yaghi, O. M. Reticular Synthesis of Microporous and Mesoporous 2D Covalent Organic Frameworks. *J. Am. Chem. Soc.* **2007**, *129*, 12914–12915.
34. Wan, S.; Guo, J.; Kim, J.; Ihee, H.; Jiang, D. A Photoconductive Covalent Organic Framework: Self-Condensed Arene Cubes Composed of Eclipsed 2D Polypyrene Sheets for Photocurrent Generation. *Angew. Chem., Int. Ed.* **2009**, *121*, 5547–5550.
35. Ourdjini, O.; Pawlak, R.; Abel, M.; Clair, S.; Chen, L.; Bergeon, N.; Sassi, M.; Olson, V.; Debierre, J.-M.; Coratger, R.; *et al.* Substrate-Mediated Ordering and Defect Analysis of a Surface Covalent Organic Framework. *Phys. Rev. B* **2011**, *84*, 125421.
36. Clair, S.; Ourdjini, O.; Abel, M.; Porte, L. Tip- or Electron Beam-Induced Surface Polymerization. *Chem. Commun.* **2011**, 47, 8028–8030.
37. Walch, H.; Maier, A.-K.; Heckl, W. M.; Lackinger, M. Isotopological Supramolecular Networks from Melamine and Fatty Acids. *J. Phys. Chem. C* **2008**, *113*, 1014–1019.
38. Tahara, K.; Furukawa, S.; Uji-i, H.; Uchino, T.; Ichikawa, T.; Zhang, J.; Mamdouh, W.; Sonoda, M.; De Schryver, F. C.; De Feyter, S.; *et al.* Two-Dimensional Porous Molecular Networks of Dehydrobenzo[12]annulene Derivatives via Alkyl Chain Interdigitation. *J. Am. Chem. Soc.* **2006**, *128*, 16613–16625.
39. Eddaoudi, M.; Kim, J.; Rosi, N.; Vodak, D.; Wachter, J.; O’Keeffe, M.; Yaghi, O. M. Systematic Design of Pore Size and Functionality in Isoreticular MOFs and their Application in Methane Storage. *Science* **2002**, *295*, 469–472.
40. Schlickum, U.; Decker, R.; Klappenberger, F.; Zoppellaro, G.; Klyatskaya, S.; Ruben, M.; Silanes, I.; Arnau, A.; Kern, K.; Brune; *et al.* Metal–Organic Honeycomb Nanomeshes with Tunable Cavity Size. *Nano Lett.* **2007**, *7*, 3813–3817.
41. Kuhn, P.; Antonietti, M.; Thomas, A. Porous, Covalent Triazine-Based Frameworks Prepared by Ionothermal Synthesis. *Angew. Chem., Int. Ed.* **2008**, *47*, 3450–3453.
42. Tilford, R. W.; Gemmill, W. R.; zur Loye, H. C.; Lavigne, J. J. Facile Synthesis of a Highly Crystalline, Covalently Linked Porous Boronate Network. *Chem. Mater.* **2006**, *18*, 5296–5301.
43. Langner, A.; Tait, S. L.; Lin, N.; Rajadurai, C.; Ruben, M.; Kern, K. Self-Recognition and Self-Selection in Multicomponent Supramolecular Coordination Networks on Surfaces. *Proc. Natl. Acad. Sci. U. S. A.* **2007**, *104*, 17927–17930.
44. Marschall, M.; Reichert, J.; Seufert, K.; Auwärter, W.; Klappenberger, F.; Weber-Bargioni, A.; Klyatskaya, S.; Zoppellaro, G.; Nefedov, A.; Strunskus, T.; *et al.* Supramolecular Organization and Chiral Resolution of p-Terphenylm-Dicarbonitrile on the Ag(111) Surface. *ChemPhysChem* **2010**, *11*, 1446–1451.
45. Rodriguez-Cuamatzi, P.; Vargas-Diaz, G.; Maris, T.; Wuest, J. D.; Hopfl, H. 1,4-Phenylenediboronic Acid. *Acta Crystallogr. E* **2004**, *60*, o1316–o1318.
46. Pawlak, R.; Nony, L.; Bocquet, F.; Olson, V.; Sassi, M.; Debierre, J. M.; Loppacher, C.; Porte, L. Supramolecular Assemblies of 1,4-Benzene Diboronic Acid on KCl(001). *J. Phys. Chem. C* **2010**, *114*, 9290–9295.
47. Heining, C.; Kampschulte, L.; Heckl, W. M.; Lackinger, M. Distinct Differences in Self-Assembly of Aromatic Linear Dicarboxylic Acids. *Langmuir* **2008**, *25*, 968–972.
48. Coutts, I. G. C.; Goldschmid, H. R.; Musgrave, O. C. Organoboron Compounds. Part VIII. Aliphatic and Aromatic Diboronic Acids. *J. Chem. Soc. C* **1970**, 488–493.
49. Coventry, D. N.; Batsanov, A. S.; Goeta, A. E.; Howard, J. A. K.; Marder, T. B.; Perutz, R. N. Selective Ir-Catalysed Borylation of Polycyclic Aromatic Hydrocarbons: Structures of Naphthalene-2,6-bis(boronate), Pyrene-2,7-bis(boronate) and Perylene-2,5,8,11-tetra(boronate) Esters. *Chem. Commun.* **2005**, 2172–2174.

Supporting Information:

Isorecticular Two-Dimensional Covalent Organic Frameworks Synthesized by On-Surface Condensation of Diboronic Acids

*Jürgen F. Dienstmaier^{‡,†}, Dana D. Medina^{#,†}, Mirjam Dogru^{#,†}, Paul Knochel[#], Thomas Bein^{#,†},
Wolfgang M. Heckl^{‡,†}, and Markus Lackinger^{‡,†,*}*

[‡] Deutsches Museum, Museumsinsel 1, 80538 Munich (Germany) and Tech. Univ. Munich,
TUM School of Education, Schellingstrasse 33, 80799 Munich (Germany)

[†] Center for NanoScience (CeNS), Schellingstrasse 4, 80799 Munich (Germany)

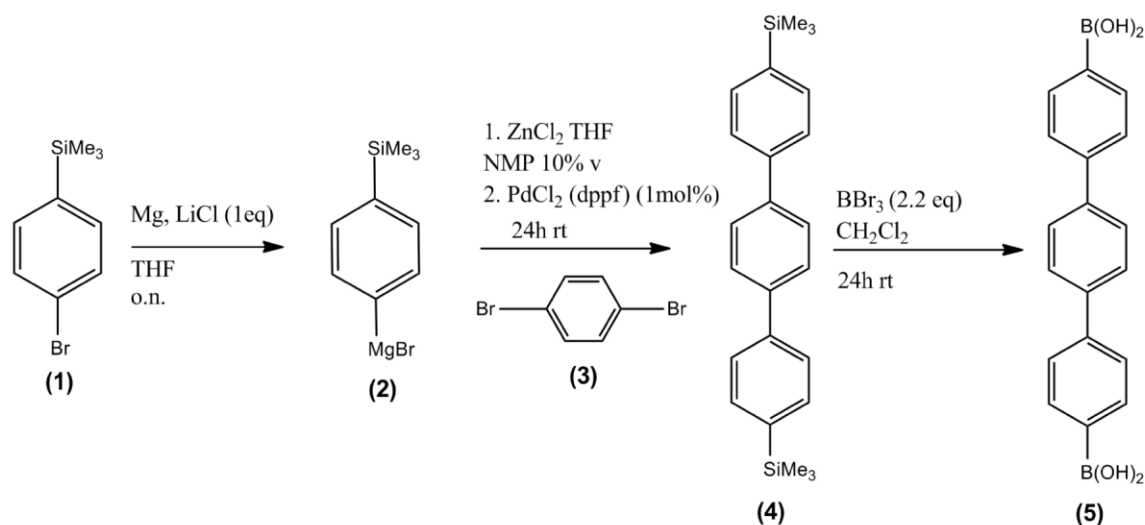
[#] Department of Chemistry, Ludwig-Maximilians-University,
Butenandtstrasse 11 (E), 81377 Munich (Germany)

AUTHOR EMAIL ADDRESS: markus@lackinger.org

- (1) Synthesis of terphenyldiboronic acid ([1,1':4',1''-terphenyl]-4,4''-diyldiboronic acid)
- (2) Synthesis of quaterphenyldiboronic acid ([1,1':4',1'':4'',1'''-quaterphenyl]-4,4'''-diyldiboronic acid)

S1

1. Synthesis of terphenyldiboronic acid ([1,1':4',1''-terphenyl]-4,4''-diyldiboronic acid)



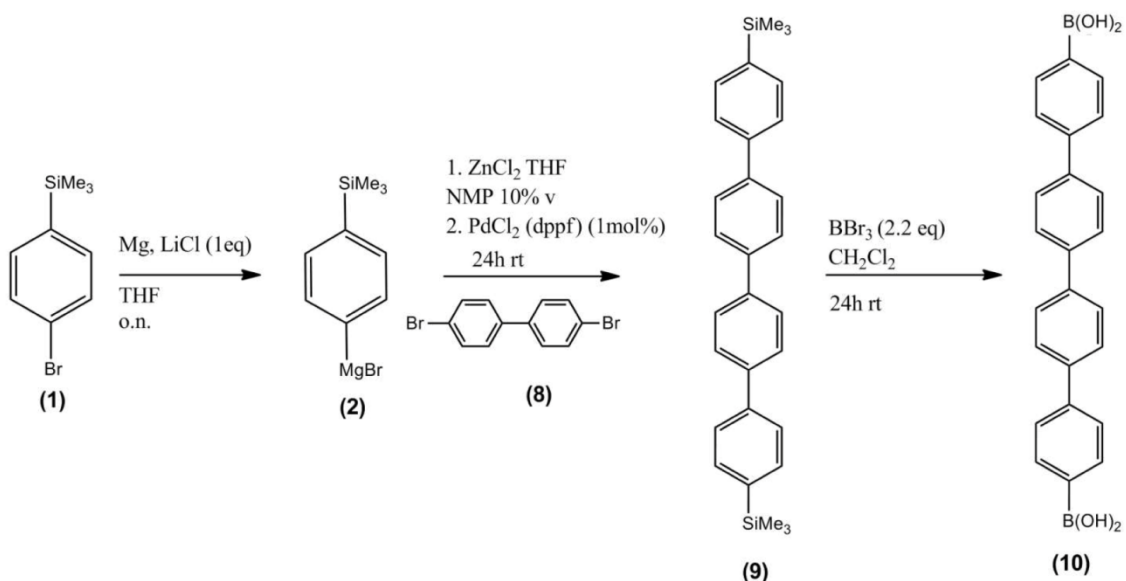
A round-bottom flask equipped with a magnetic stirring bar was charged with magnesium turnings (2.15 g, 88.20 mmol, 1.4 equiv.) and lithium chloride (3.00 g, 63.35 mmol, 90 %, 1.0 equiv). The reactants were dried under vacuum at 250 °C, the mixture was then allow to cool under argon atmosphere. Subsequently 50 ml of anhydrous tetrahydrofuran was added. Activation of the magnesium turnings was achieved by stirring for ca. one hour. Afterwards (4-bromophenyl)trimethylsilane (**1**) (15.21 g, 63.35 mmol, 1.0 equiv) was added dropwise. After 5 minutes, an exothermic reaction set in. The solution was stirred for another hour, and subsequently added dropwise to an ice bath-cooled mixture of zinc (II) chloride (4.36 g, 32.00 mmol, 0.5 equiv.) in 32 ml THF and 3.2 ml (10 %) *N*-Methyl-2-pyrrolidone (NMP).

In a 250 ml round-bottom flask palladium (II) acetate (28.10 mg, 1.13 mmol, 0.50 mol%), 2-dicyclohexylphosphino-2',6'-dimethoxybiphenyl (102.60 mg, 0.25 mmol, 1.0 mol%) and 1, 4-dibromobenzene (**3**) (5.90 g, 25.00 mmol, 0.4 equiv) were dissolved in tetrahydrofuran (20 ml). This mixture was added dropwise to the zinc compound, after a short time the color of the exothermic reaction turned brown and a solid precipitated. The suspension was quenched with a saturated ammonium chloride solution. The mixture was extracted four times with diethylether. Successively the grey solid was filtered and dried at 80 °C in an oven for 16 h. Recrystallization in n-heptane yielded the product as a grey solid (5.68 g, 15.5 mmol, 60 %).

[1,1':4',1''-terphenyl]-4,4''-di-trimethylsilane (**4**) (5.68 g, 15.5 mmol, 1.0 equiv) was dissolved in 140 ml dichloromethane. Subsequently boron tribromide (9.5 g, 37.9 mmol, 2.2 equiv) was added and the reaction mixture was stirred at room temperature for 24 h. The white suspension was poured on ice (250 g) and stirred

until the ice was completely molten. Dichloromethane was removed on the rotary evaporator and the product was filtered. Recrystallization in water yielded a white powder (**5**) (2.83 g, 8.9 mmol, 57 %).

2. Synthesis of quaterphenyldiboronic acid ([1,1':4',1'':4'',1''':4''',1''''-quaterphenyl]-4,4''-diyldiboronic acid)



In a round-bottomed flask bis(di-*tert*-butyl(4-dimethylaminophenyl)phosphine)dichloropalladium(II) (5 mg, 0.007 mmol) and 4,4'-dibromo-1,1'-biphenyl (**8**) (0.624 g, 2.0 mmol, 0.4 equiv.) were dissolved in tetrahydrofuran (20 ml). This mixture was added dropwise to the zinc compound. The suspension was quenched with 50 ml of a saturated ammonium chloride solution. The mixture was extracted four times with 30 ml of diethylether. Subsequently the white solid was filtered and dried *in vacuo* (0.56 g, 1.3 mmol, 65 %).

4,4''-bis(trimethylsilyl)-1,1':4',1'':4'',1''':4''',1''''-quaterphenyl (**9**) (0.56 g, 1.3 mmol, 1.0 equiv) was dissolved in 25 ml dichloromethane. Subsequently boron tribromide (0.715 g, 2.86 mmol, 2.2 equiv) was added and the reaction mixture was stirred at room temperature for 24 h. The white suspension was poured on ice (250 g) and stirred until the ice was completely molten. Dichloromethane was removed on the rotary evaporator and the product was filtered. Recrystallization in water yielded a white powder (**10**) (0.38 g, 0.96 mmol, 74 %).

References

1. Binnig, G.; Rohrer, H.; Gerber, C.; Weibel, E. Tunneling through a controllable vacuum gap. *Appl. Phys. Lett.* **1982**, *40*, 178-180.
2. Meyer, E.; Hug, H. J.; Bennewitz, R. *Scanning Probe Microscopy - The Lab on a Tip*; Springer, **2004**.
3. Hipps, K. W. Scanning Tunneling Spectroscopy; In Book *Handbook of Applied Solid State Spectroscopy*; Vij, D. R.; Springer Science + Business Media, LLC, USA, **2006**, p 305-350.
4. The Future of Futurology. *The Economist* **15.11.2007**.
5. Feynman, R. P. There's Plenty of Room at the Bottom. *Engineering and Science* **1960**, *23*, 22-36.
6. Carruthers, J. A. 'Nano' versus nano: the fight for public understanding of nanotechnology. *Nano* **2009**, *14*, 41-42.
7. The Risk in Nanotechnology - A Little Risky Business. *The Economist* **22.11.2007**.
8. Nanotechnology - Much Ado About Almost Nothing. *The Economist* **18.3.2004**.
9. Shirai, Y.; Osgood, A. J.; Zhao, Y.; Kelly, K. F.; Tour, J. M. Directional Control in Thermally Driven Single-Molecule Nanocars. *Nano Lett.* **2005**, *5*, 2330-2334.
10. Kudernac, T.; Ruangsapapichat, N.; Parschau, M.; Macia, B.; Katsonis, N.; Harutyunyan, S. R.; Ernst, K.-H.; Feringa, B. L. Electrically driven directional motion of a four-wheeled molecule on a metal surface. *Nature* **2011**, *479*, 208-211.
11. Lei, S. B.; Tahara, K.; Adisoejoso, J.; Balandina, T.; Tobe, Y.; De Feyter, S. Towards two-dimensional nanoporous networks: crystal engineering at the solid-liquid interface. *Crystengcomm* **2010**, *12*, 3369-3381.
12. Lackinger, M.; Griessl, S.; Heckl, W. M.; Hietschold, M.; Flynn, G. W. Self-Assembly of Trimesic Acid at the Liquid-Solid Interface: A Study of Solvent-Induced Polymorphism. *Langmuir* **2005**, *21*, 4984-4988.
13. Kampschulte, L.; Lackinger, M.; Maier, A.-K.; Kishore, R. S. K.; Griessl, S.; Schmittel, M.; Heckl, W. M. Solvent Induced Polymorphism in Supramolecular 1,3,5-Benzenetribenzoic Acid Monolayers. *J. Phys. Chem. B* **2006**, *110*, 10829-10836.
14. Gutzler, R.; Lappe, S.; Mahata, K.; Schmittel, M.; Heckl, W. M.; Lackinger, M. Aromatic interaction vs. hydrogen bonding in self-assembly at the liquid-solid interface. *Chem. Commun.* **2009**, 680-682.
15. Cote, A. P.; Benin, A. I.; Ockwig, N. W.; O'Keeffe, M.; Matzger, A. J.; Yaghi, O. M. Porous, crystalline, covalent organic frameworks. *Science* **2005**, *310*, 1166-1170.
16. Colson, J. W.; Woll, A. R.; Mukherjee, A.; Levendorf, M. P.; Spitler, E. L.; Shields, V. B.; Spencer, M. G.; Park, J.; Dichtel, W. R. Oriented 2D Covalent Organic Framework Thin Films on Single-Layer Graphene. *Science* **2011**, *332*, 228-231.

-
17. Giaever, I. Energy Gap in Superconductors Measured by Electron Tunneling. *Phys. Rev. Lett.* **1960**, 5, 147-148.
 18. Young, R.; Ward, J.; Scire, F. The Topografiner: An Instrument for Measuring Surface Microtopography. *Rev. Sci. Instrum.* **1972**, 43, 999-1011.
 19. Adachi, H.; Suzuki, A.; Onodera, T.; Suzuki, K.; Mukasa, K. Stable operation of topografiner in the atmosphere by use of charge injection current in an insulating liquid. *Sensor. Actuat. A. Phys.* **1990**, 23, 954-957.
 20. Villarubia, J. S.; Scire, F.; RTeague, E. C.; Gadzuk, J. W. The Topografiner: An Instrument for Measuring Surface Microtopography. *A Century of Excellence in Measurements, Standards, and Technology: A Chronicle of Selected NBS/NIST Publications, 1901-2000* **2001**, Spec. Publ. 958, 214 - 218.
 21. Bai, C. *Scanning Tunneling Microscopy and its Applications*; 2nd, corrected edition; Springer, **2000**.
 22. Hurst, H. G.; Ruppel, W. Tunnelströme durch Al₂O₃-Schichten bei Kontakten verschiedener Austrittsarbeiten. *Z. Naturforsch. A* **1964**, 19, 573-579.
 23. Whitman, L. J. Tunneling Microscopy and Spectroscopy; In Book *Encyclopedia of Applied Physics*; Trigg, G.; Wiley-VCH: Berlin, **2004**.
 24. Bhushan, B. *Springer Handbook of Nanotechnology*; 2nd edition; Springer, **2007**.
 25. Walch, H. *Thesis*, Molecular Networks Through Surface-Mediated Reactions - From Hydrogen Bonds to Covalent Links, **2011**.
 26. Li, Z.; Han, B.; Meszaros, G.; Pobelov, I.; Wandlowski, T.; Blaszczyk, A.; Mayor, M. Two-dimensional assembly and local redox-activity of molecular hybrid structures in an electrochemical environment. *Faraday Discuss.* **2006**, 131, 121-143.
 27. Gerber, C.; Binnig, G.; Fuchs, H.; Marti, O.; Rohrer, H. Scanning tunneling microscope combined with a scanning electron microscope. *Rev. Sci. Instrum.* **1986**, 57, 221-224.
 28. Schmid, M.; Varga, P. Analysis of vibration-isolating systems for scanning tunneling microscopes. *Ultramicroscopy* **1992**, 42-44, Part 2, 1610-1615.
 29. Okano, M.; Kajimura, K.; Wakiyama, S.; Sakai, F.; Mizutani, W.; Ono, M. Vibration isolation for scanning tunneling microscopy. *J. Vac. Sci. Technol. A* **1987**, 5, 3313-3320.
 30. Márk, G. I.; Biró, L. P.; Lambin, P. Modeling and Interpretation of STM Images of Carbon Nanosystems. *NATO ARW Kiev; Frontiers in Molecular-Scale Science and Technology of Fullerene, Nanotube, Nanosilicon, Biopolymer (DNA, Protein) Multifunctional Nanosystems* **2001**.
 31. Chen, C. J. *Introduction to Scanning Tunneling Microscopy*; Oxford University Press, **1993**.
 32. Bardeen, J. Tunnelling from a Many-Particle Point of View. *Phys. Rev. Lett.* **1961**, 6, 57-59.
 33. Tersoff, J.; Hamann, D. R. Theory and Application for the Scanning Tunneling Microscope. *Phys. Rev. Lett.* **1983**, 50, 1998-2001.

-
34. Tersoff, J.; Hamann, D. R. Theory of the scanning tunneling microscope. *Phys. Rev. B* **1985**, *31*, 805-813.
 35. Wintterlin, J.; Wiechers, J.; Brune, H.; Gritsch, T.; Höfer, H.; Behm, R. J. Atomic-Resolution Imaging of Close-Packed Metal Surfaces by Scanning Tunneling Microscopy. *Phys. Rev. Lett.* **1989**, *62*, 59-62.
 36. Binnig, G.; Rohrer, H.; Gerber, C.; Weibel, E. 7×7 Reconstruction on Si(111) Resolved in Real Space. *Phys. Rev. Lett.* **1983**, *50*, 120-123.
 37. Binnig, G.; Rohrer, H. Scanning tunneling microscopy—from birth to adolescence. *Rev. Mod. Phys.* **1987**, *59*, 615-625.
 38. Gimzewski, J. K.; Jung, T. A.; Cuberes, M. T.; Schlittler, R. R. Scanning tunneling microscopy of individual molecules: beyond imaging. *Surf. Sci.* **1997**, *386*, 101-114.
 39. Ritter, E.; Behm, R. J.; Pötschke, G.; Wintterlin, J. Direct observation of a nucleation and growth process on an atomic scale. *Surf. Sci.* **1987**, *181*, 403-411.
 40. Komeda, T.; Kim, Y.; Kawai, M. Imaging an Isolated molecule on metal: STM Images of CO on Pd(110) and Electronic Configuration Near the Fermi Level. *RIKEN Review* **2001**, *37*, 26 - 33.
 41. Sautet, P.; Dunphy, J. C.; Salmeron, M. The origin of STM contrast differences for inequivalent S atoms on a Mo(100) surface. *Surf. Sci.* **1996**, *364*, 335-344.
 42. Kopatzki, E.; Behm, R. J. STM imaging and local order of oxygen adlayers on Ni(100). *Surf. Sci.* **1991**, *245*, 255-262.
 43. Gimzewski, J. K.; Stoll, E.; Schlittler, R. R. Scanning tunneling microscopy of individual molecules of copper phthalocyanine adsorbed on polycrystalline silver surfaces. *Surf. Sci.* **1987**, *181*, 267-277.
 44. Ramos, M. M. D. Can STM be used to image molecules on surfaces? *J. Phys. Condens. Mat.* **1993**, *5*, 2843.
 45. Lang, N. D. Theory of Single-Atom Imaging in the Scanning Tunneling Microscope. *Phys. Rev. Lett.* **1986**, *56*, 1164-1167.
 46. Lang, N. D. Apparent Size of an Atom in the Scanning Tunneling Microscope as a Function of Bias. *Phys. Rev. Lett.* **1987**, *58*, 45-48.
 47. Eigler, D. M.; Weiss, P. S.; Schweizer, E. K.; Lang, N. D. Imaging Xe with a low-temperature scanning tunneling microscope. *Phys. Rev. Lett.* **1991**, *66*, 1189-1192.
 48. Lippel, P. H.; Wilson, R. J.; Miller, M. D.; Wöll, C.; Chiang, S. High-Resolution Imaging of Copper-Phthalocyanine by Scanning-Tunneling Microscopy. *Phys. Rev. Lett.* **1989**, *62*, 171-174.
 49. Smith, D. P. E.; Horber, J. K. H.; Binnig, G.; Nejh, H. Structure, registry and imaging mechanism of alkylcyanobiphenyl molecules by tunnelling microscopy. *Nature* **1990**, *344*, 641-644.

-
50. Hallmark, V. M.; Chiang, S. Predicting STM images of molecular adsorbates. *Surf. Sci.* **1995**, *329*, 255-268.
 51. Ilan, B.; Florio, G. M.; Hybertsen, M. S.; Berne, B. J.; Flynn, G. W. Scanning Tunneling Microscopy Images of Alkane Derivatives on Graphite: Role of Electronic Effects. *Nano Lett.* **2008**, *8*, 3160-3165.
 52. Sautet, P.; Joachim, C. Electronic transmission coefficient for the single-impurity problem in the scattering-matrix approach. *Phys. Rev. B* **1988**, *38*, 12238-12247.
 53. Sautet, P. Images of Adsorbates with the Scanning Tunneling Microscope: Theoretical Approaches to the Contrast Mechanism. *Chem. Rev.* **1997**, *97*, 1097-1116.
 54. Weiss, P. S.; Eigler, D. M. Site dependence of the apparent shape of a molecule in scanning tunneling microscope images: Benzene on Pt{111}. *Phys. Rev. Lett.* **1993**, *71*, 3139-3142.
 55. Sautet, P.; Dunphy, J.; Ogletree, D. F.; Salmeron, M. The role of electronic interferences in determining the appearance of STM images: application to the S(2 × 2)/Re(0001) system. *Surf. Sci.* **1993**, *295*, 347-352.
 56. Berner, S. *Ph. D. Thesis*, Molecular Diffusion and Self-Organization on Metal Surfaces: Sub-Phthalocyanine on Ag(111), **2002**.
 57. Van der Heide, P. *X-ray Photoelectron Spectroscopy: An Introduction to Principles and Practices*; John Wiley and Sons, Inc., **2012**.
 58. Hertz, H. Ueber einen Einfluss des ultravioletten Lichtes auf die electrische Entladung. *Ann. Phys.* **1887**, *267*, 983-1000.
 59. Einstein, A. Über einen die Erzeugung und Verwandlung des Lichtes betreffenden heuristischen Gesichtspunkt. *Ann. Phys.* **1905**, *322*, 132-148.
 60. Comisso, A. *Thesis*, Modelling the Self-Assembly of Supramolecular Nanostructures Adsorbed on Metallic Substrates, **2006**.
 61. Smekal, A. Zur Quantentheorie der Dispersion. *Naturwissenschaften* **1923**, *11*, 873-875.
 62. Mantica, P., and authors therein. In "Raman and Infrared Spectrophotometry." *Analytical Physical Laboratory II: Raman and Infrared Spectrophotometry*; Michigan State University, Chemistry Department, Michigan, **2000**.
 63. Hahn, D. W. In "Raman Scattering Theory." University of Florida, **2007**, p 1-13.
 64. Yamauchi, S.; Doi, S. Raman spectroscopic study on the behavior of boric acid in wood. *J. Wood Sci.* **2003**, *49*, 227-234.
 65. Connolly, J. R. In "Introduction to X-ray Powder Diffraction." *Earth & Planetary Sciences X-Ray Diffraction Laboratory*; University of New Mexico, Department of Earth and Planetary Science, **2007**.
 66. In "Thermogravimetric Analysis (TGA), A Beginner's Guide." Perkin Elmer: Waltham, MA, USA, **2010**, p 1-19.

-
67. Clemmer, C.; Beebe, T. Graphite: a mimic for DNA and other biomolecules in scanning tunneling microscope studies. *Science* **1991**, *251*, 640-642.
 68. Nawaz, Z.; Knall, J. H.; Richardson, T.; Roberts, G. G.; Pethica, J. B. STM imaging of molecules on well defined substrates. *J. Phy. Condens. Mat.* **1991**, *3*, S11.
 69. Jian-fei, Z.; Geng-yu, C. STM Study of Moiré Patterns on HOPG. *Chin. J. Chem. Phys.* **2006**, *19*, 197.
 70. Simonis, P.; Goffaux, C.; Thiry, P. A.; Biro, L. P.; Lambin, P.; Meunier, V. STM study of a grain boundary in graphite. *Surf. Sci.* **2002**, *511*, 319-322.
 71. Červenka, J.; Flipse, C. F. J. Structural and electronic properties of grain boundaries in graphite: Planes of periodically distributed point defects. *Phys. Rev. B* **2009**, *79*, 195429.
 72. Flores, M.; Vargas, P.; Cisternas, E. Moiré Patterns on STM Images of Graphite from Surface and Subsurface Rotated Layer. *arXiv:1202.1344v1 (Condensed Matter > Mesoscale and Nanoscale Physics (cond-mat.mes-hall))* **2012**, 1-4.
 73. Abelev, E.; Sezin, N.; Ein-Eli, Y. An alternative isolation of tungsten tips for a scanning tunneling microscope. *Rev. Sci. Instrum.* **2005**, *76*, 106105.
 74. Wypych, G. *Handbook of Solvents*; ChemTec Publishing, **2001**.
 75. Whitesides, G. M.; Grzybowski, B. Self-Assembly at All Scales. *Science* **2002**, *295*, 2418-2421.
 76. Koepf, M.; Conradt, J.; Szmytkowski, J. d.; Wytko, J. A.; Allouche, L.; Kalt, H.; Balaban, T. S.; Weiss, J. Highly Linear Self-Assembled Porphyrin Wires. *Inorg. Chem.* **2011**, *50*, 6073-6082.
 77. Fukuda, T.; Kawauchi, Y. Cellular robotic system (CEBOT) as one of the realization of self-organizing intelligent universal manipulator. In *Conferece: 1990 Proceedings. IEEE International Conference on Robotics and Automation* **1990**, p 662-667 vol.661.
 78. Ishiguro, A.; Maegawa, T. Self-Assembly Through the Interplay between Control and Mechanical Systems. In *Conference: 2006 IEEE/RSJ International Conference on Intelligent Robots and Systems* **2006**, p 631-638.
 79. Bigelow, W. C.; Pickett, D. L.; Zisman, W. A. Oleophobic monolayers: I. Films adsorbed from solution in non-polar liquids. *J. Coll. Sci. Imp. U. Tok.* **1946**, *1*, 513-538.
 80. Nuzzo, R. G.; Allara, D. L. Adsorption of bifunctional organic disulfides on gold surfaces. *J. Am. Chem. Soc.* **1983**, *105*, 4481-4483.
 81. Heckl, W. M.; Smith, D. P.; Binnig, G.; Klagges, H.; Hänsch, T. W.; Maddocks, J. Two-dimensional ordering of the DNA base guanine observed by scanning tunneling microscopy. *P. Natl. Acad. Sci. USA* **1991**, *88*, 8003-8005.
 82. Griessl, S.; Lackinger, M.; Edelwirth, M.; Hietschold, M.; Heckl, W. M. Self-Assembled Two-Dimensional Molecular Host-Guest Architectures From Trimesic Acid. *Single Mol.* **2002**, *3*, 25-31.

-
83. Yarema, M.; Pichler, S.; Kriegner, D.; Stangl, J.; Yarema, O.; Kirchschrager, R.; Tollabimazraehno, S.; Humer, M.; Häring, D.; Kohl, M.; Chen, G.; Heiss, W. From Highly Monodisperse Indium and Indium Tin Colloidal Nanocrystals to Self-Assembled Indium Tin Oxide Nanoelectrodes. *ACS Nano* **2012**.
 84. Kühnle, A. Self-assembly of organic molecules at metal surfaces. *Curr. Opin. Colloid. In.* **2009**, *14*, 157-168.
 85. Clair, S.; Pons, S.; Seitsonen, A. P.; Brune, H.; Kern, K.; Barth, J. V. STM Study of Terephthalic Acid Self-Assembly on Au(111): Hydrogen-Bonded Sheets on an Inhomogeneous Substrate. *J. Phys. Chem. B* **2004**, *108*, 14585-14590.
 86. Lin, N.; Langner, A.; Tait, S. L.; Rajadurai, C.; Ruben, M.; Kern, K. Template-directed supramolecular self-assembly of coordination dumbbells at surfaces. *Chem. Commun.* **2007**, 4860-4862.
 87. Ye, Y.; Sun, W.; Wang, Y.; Shao, X.; Xu, X.; Cheng, F.; Li, J.; Wu, K. A Unified Model: Self-Assembly of Trimesic Acid on Gold. *J. Phys. Chem. C* **2007**, *111*, 10138-10141.
 88. Popoff, A.; Fichou, D. Immobilization of paracetamol and benzocaine pro-drug derivatives as long-range self-organized monolayers on graphite. *Colloid. Surface. B.* **2008**, *63*, 153-158.
 89. Caterbow, D.; Künzel, D.; Mavros, M. G.; Groß, A.; Landfester, K.; Ziener, U. Septipyridines as conformationally controlled substitutes for inaccessible bis(terpyridine)-derived oligopyridines in two-dimensional self-assembly. *Beilstein Journal of Nanotechnology* **2011**, *2*, 405-415.
 90. Edelwirth, M.; Freund, J.; Sowerby, S. J.; Heckl, W. M. Molecular mechanics study of hydrogen bonded self-assembled adenine monolayers on graphite. *Surf. Sci.* **1998**, *417*, 201-209.
 91. Bald, I.; Weigelt, S.; Ma, X.; Xie, P.; Subramani, R.; Dong, M.; Wang, C.; Mamdouh, W.; Wang, J.; Besenbacher, F. Two-dimensional network stability of nucleobases and amino acids on graphite under ambient conditions: adenine, l-serine and l-tyrosine. *Phys. Chem. Chem. Phys.* **2010**, *12*, 3616-3621.
 92. Uchihashi, T.; Okada, T.; Sugawara, Y.; Yokoyama, K.; Morita, S. Self-assembled monolayer of adenine base on graphite studied by noncontact atomic force microscopy. *Phys. Rev. B* **1999**, *60*, 8309-8313.
 93. Guix, M.; Orozco, J.; García, M.; Gao, W.; Sattayasamitsathit, S.; Merkoçi, A.; Escarpa, A.; Wang, J. Superhydrophobic Alkanethiol-Coated Microsubmarines for Effective Removal of Oil. *ACS Nano* **2012**.
 94. O'Mahony, C. T.; Farrell, R. A.; Goshal, T.; Holmes, J. D.; Morris, M. A. The Thermodynamics of Defect Formation in Self-Assembled Systems, Thermodynamics - Systems in Equilibrium and Non-Equilibrium. Dr. Juan Carlos Moreno (Ed.). **2011**, 279-306.
 95. Stoddart, J. F. Self-assembly: What does it mean? ; In Book *Self-Assembly in Supramolecular Systems*; Lindoy, L. F., Atkinson, I. M., Eds.; The Royal Society of Chemistry: **2000**, p 1-6.
 96. Dienstmaier, J. F.; Mahata, K.; Walch, H.; Heckl, W. M.; Schmittel, M.; Lackinger, M. On the Scalability of Supramolecular Networks – High Packing Density vs Optimized Hydrogen Bonds in Tricarboxylic Acid Monolayers. *Langmuir* **2010**, *26*, 10708-10716.

-
97. Gutzler, R.; Sirtl, T.; Dienstmaier, J. F.; Mahata, K.; Heckl, W. M.; Schmittl, M.; Lackinger, M. Reversible Phase Transitions in Self-Assembled Monolayers at the Liquid–Solid Interface: Temperature-Controlled Opening and Closing of Nanopores. *J. Am. Chem. Soc.* **2010**, *132*, 5084-5090.
 98. Stephenson, W. K.; Fuchs, R. Enthalpies of interaction of aromatic solutes with organic solvents. *Can. J. Chemistry* **1985**, *63*, 2529-2534.
 99. Józwiak, M.; Piekarski, H. Heat of solution of 15-crown-5 ether in the mixtures of water with DMSO, DMF, DMA and HMPA at 298.15K. *J. Mol. Liq.* **1999**, *81*, 63-70.
 100. Lopes Jesus, A. J.; Ermelinda Eusébio, M.; Redinha, J. S.; Leitão, M. L. P. Enthalpy of solvation of butanediols in different solvents. *Thermochim. Acta* **2000**, *344*, 3-8.
 101. Mammen, M.; Shakhnovich, E. I.; Deutch, J. M.; Whitesides, G. M. Estimating the Entropic Cost of Self-Assembly of Multiparticle Hydrogen-Bonded Aggregates Based on the Cyanuric Acid·Melamine Lattice. *J. Org. Chem.* **1998**, *63*, 3821-3830.
 102. Murray, C. W.; Verdonk, M. L. The consequences of translational and rotational entropy lost by small molecules on binding to proteins. *J. Comput. Aid. Mol. Des.* **2002**, *16*, 741-753.
 103. Ohkubo, Y. Z.; Brooks, C. L. Exploring Flory's isolated-pair hypothesis: Statistical mechanics of helix–coil transitions in polyalanine and the C-peptide from RNase A. *Proc. Natl. Acad. of Sci. USA* **2003**, *100*, 13916-13921.
 104. Xu, B.; Shen, H.; Zhu, X.; Li, G. Fast and accurate computation schemes for evaluating vibrational entropy of proteins. *J. Comput. Chem.* **2011**, *32*, 3188-3193.
 105. Kampschulte, L.; Werblowsky, T. L.; Kishore, R. S. K.; Schmittl, M.; Heckl, W. M.; Lackinger, M. Thermodynamical Equilibrium of Binary Supramolecular Networks at the Liquid–Solid Interface. *J. Am. Chem. Soc.* **2008**, *130*, 8502-8507.
 106. Mali, K. S.; Lava, K.; Binnemans, K.; De Feyter, S. Hydrogen Bonding Versus van der Waals Interactions: Competitive Influence of Noncovalent Interactions on 2D Self-Assembly at the Liquid–Solid Interface. *Chem. Eur. J.* **2010**, *16*, 14447-14458.
 107. Grimme, S. Do Special Noncovalent π – π Stacking Interactions Really Exist? *Angew. Chem. Int. Ed.* **2008**, *47*, 3430-3434.
 108. Rochefort, A.; Wuest, J. D. Interaction of Substituted Aromatic Compounds with Graphene. *Langmuir* **2008**, *25*, 210-215.
 109. Steiner, T.; R. Desiraju, G. Distinction between the weak hydrogen bond and the van der Waals interaction. *Chem. Commun.* **1998**, 891-892.
 110. Desiraju, G. R. The C–H···O Hydrogen Bond: Structural Implications and Supramolecular Design. *Accounts Chem. Res.* **1996**, *29*, 441-449.
 111. Zhao, J.; Khalizov, A.; Zhang, R.; McGraw, R. Hydrogen-Bonding Interaction in Molecular Complexes and Clusters of Aerosol Nucleation Precursors. *J. Phys. Chem. A* **2009**, *113*, 680-689.

-
112. Neuheuser, T.; Hess, B. A.; Reutel, C.; Weber, E. Ab Initio Calculations of Supramolecular Recognition Modes. Cyclic versus Noncyclic Hydrogen Bonding in the Formic Acid/Formamide System. *J. Phys. Chem.* **1994**, *98*, 6459-6467.
113. Winkler, A.; Mehl, J. B.; Hess, P. Chemical relaxation of H bonds in formic acid vapor studied by resonant photoacoustic spectroscopy. *J. Chem. Phys.* **1994**, *100*, 2717-2727.
114. Lackinger, M.; Griessl, S.; Markert, T.; Jamitzky, F.; Heckl, W. M. Self-Assembly of Benzene–Dicarboxylic Acid Isomers at the Liquid Solid Interface: Steric Aspects of Hydrogen Bonding. *J. Phys. Chem. B* **2004**, *108*, 13652-13655.
115. MacLeod, J. M.; Ivasenko, O.; Perepichka, D. F.; Rosei, F. Stabilization of exotic minority phases in a multicomponent self-assembled molecular network. *Nanotechnology* **2007**, *18*, 424031.
116. Desiraju, G. R. The C-H...O hydrogen bond in crystals: what is it? *Accounts Chem. Res.* **1991**, *24*, 290-296.
117. Vishweshwar, P.; Nangia, A.; Lynch, V. M. Recurrence of Carboxylic Acid–Pyridine Supramolecular Synthons in the Crystal Structures of Some Pyrazinecarboxylic Acids. *J. Org. Chem.* **2001**, *67*, 556-565.
118. Gutzler, R. *Thesis* Surface-Confined Molecular Self-Assembly. Dissertation, LMU München: Faculty of Geosciences. **2011**.
119. Beck, J. F.; Mo, Y. How resonance assists hydrogen bonding interactions: An energy decomposition analysis. *J. Comput. Chem.* **2007**, *28*, 455-466.
120. Gilli, G.; Gilli, P. Towards an unified hydrogen-bond theory. *J. Mol. Struct.* **2000**, *552*, 1-15.
121. Steiner, T. Unrolling the hydrogen bond properties of C-H...O interactions. *Chem. Commun.* **1997**, 727-734.
122. Bombis, C.; Weigelt, S.; Knudsen, M. M.; Nørgaard, M.; Busse, C.; Lægsgaard, E.; Besenbacher, F.; Gothelf, K. V.; Linderoth, T. R. Steering Organizational and Conformational Surface Chirality by Controlling Molecular Chemical Functionality. *ACS Nano* **2009**, *4*, 297-311.
123. Walch, H.; Gutzler, R.; Sirtl, T.; Eder, G.; Lackinger, M. Material- and Orientation-Dependent Reactivity for Heterogeneously Catalyzed Carbon–Bromine Bond Homolysis. *J. Phys. Chem. C* **2010**, *114*, 12604-12609.
124. Gutzler, R.; Ivasenko, O.; Fu, C.; Brusso, J. L.; Rosei, F.; Perepichka, D. F. Halogen bonds as stabilizing interactions in a chiral self-assembled molecular monolayer. *Chem. Commun.* **2011**, 47, 9453-9455.
125. Desiraju, G. R. Supramolecular Synthons in Crystal Engineering—A New Organic Synthesis. *Angew. Chem. Int. Ed.* **1995**, *34*, 2311-2327.
126. Schwartz, D. K. Mechanisms and Kinetics of Self-Assembled Monolayer Formation. *Annu. Rev. Phys. Chem.* **2001**, *52*, 107-137.

-
127. Yang, Y.; Wang, C. Solvent effects on two-dimensional molecular self-assemblies investigated by using scanning tunneling microscopy. *Curr. Opin. Colloid In.* **2009**, *14*, 135-147.
128. Shao, X.; Luo, X.; Hu, X.; Wu, K. Solvent Effect on Self-Assembled Structures of 3,8-Bis-hexadecyloxy-benzo[c]cinnoline on Highly Oriented Pyrolytic Graphite. *J. Phys. Chem. B* **2005**, *110*, 1288-1293.
129. Tao, F.; Goswami, J.; Bernasek, S. L. Competition and Coadsorption of Di-acids and Carboxylic Acid Solvents on HOPG. *J. Phys. Chem. B* **2006**, *110*, 19562-19569.
130. Lei, S.; Tahara, K.; De Schryver, F. C.; Van der Auweraer, M.; Tobe, Y.; De Feyter, S. One Building Block, Two Different Supramolecular Surface-Confined Patterns: Concentration in Control at the Solid-Liquid Interface. *Angew. Chem. Int. Ed.* **2008**, *47*, 2964-2968.
131. Tahara, K.; Okuhata, S.; Adisojoso, J.; Lei, S.; Fujita, T.; Feyter, S. D.; Tobe, Y. 2D Networks of Rhombic-Shaped Fused Dehydrobenzo[12]annulenes: Structural Variations under Concentration Control. *J. Am. Chem. Soc.* **2009**, *131*, 17583-17590.
132. Griessl, S. J. H.; Lackinger, M.; Jamitzky, F.; Markert, T.; Hietschold, M.; Heckl, W. M. Incorporation and Manipulation of Coronene in an Organic Template Structure. *Langmuir* **2004**, *20*, 9403-9407.
133. Furukawa, S.; Tahara, K.; De Schryver, F. C.; Van der Auweraer, M.; Tobe, Y.; De Feyter, S. Structural Transformation of a Two-Dimensional Molecular Network in Response to Selective Guest Inclusion. *Angew. Chem. Int. Ed.* **2007**, *46*, 2831-2834.
134. Cardenas, L.; Lipton-Duffin, J.; Rosei, F. Transformations of Molecular Frameworks by Host-Guest Response: Novel Routes toward Two-Dimensional Self-Assembly at the Solid-Liquid Interface. *Jpn. J. Appl. Phys.* **2011**, *50*, 08LA02.
135. Eder, G.; Kloft, S.; Martsinovich, N.; Mahata, K.; Schmittel, M.; Heckl, W. M.; Lackinger, M. Incorporation Dynamics of Molecular Guests into Two-Dimensional Supramolecular Host Networks at the Liquid-Solid Interface. *Langmuir* **2011**, *27*, 13563-13571.
136. Griessl, S. J. H.; Lackinger, M.; Jamitzky, F.; Markert, T.; Hietschold, M.; Heckl, W. M. Room-Temperature Scanning Tunneling Microscopy Manipulation of Single C60 Molecules at the Liquid-Solid Interface: Playing Nanosoccer. *J. Phys. Chem. B* **2004**, *108*, 11556-11560.
137. Cote, A. P.; El-Kaderi, H. M.; Furukawa, H.; Hunt, J. R.; Yaghi, O. M. Reticular synthesis of microporous and mesoporous 2D covalent organic frameworks. *J. Am. Chem. Soc.* **2007**, *129*, 12914-12915.
138. Uribe-Romo, F. J.; Hunt, J. R.; Furukawa, H.; Klock, C.; O'Keeffe, M.; Yaghi, O. M. A crystalline imine-linked 3-D porous covalent organic framework. *J. Am. Chem. Soc.* **2009**, *131*, 4570-4571.
139. Grill, L.; Dyer, M.; Lafferentz, L.; Persson, M.; Peters, M. V.; Hecht, S. Nano-architectures by covalent assembly of molecular building blocks. *Nat. Nanotechnol.* **2007**, *2*, 687-691.
140. Gutzler, R.; Walch, H.; Eder, G.; Kloft, S.; Heckl, W. M.; Lackinger, M. Surface mediated synthesis of 2D covalent organic frameworks: 1,3,5-tris(4-bromophenyl)benzene on graphite(001), Cu(111), and Ag(110). *Chem. Commun.* **2009**, 4456-4458.

-
141. Zwaneveld, N. A. A.; Pawlak, R.; Abel, M.; Catalin, D.; Gimes, D.; Bertin, D.; Porte, L. Organized formation of 2D extended covalent organic frameworks at surfaces. *J. Am. Chem. Soc.* **2008**, *130*, 6678-6679.
 142. Yaghi, O. M.; O'Keeffe, M.; Ockwig, N. W.; Chae, H. K.; Eddaoudi, M.; Kim, J. Reticular synthesis and the design of new materials. *Nature* **2003**, *423*, 705-714.
 143. Tilford, R. W.; Mugavero, S. J.; Pellechia, P. J.; Lavigne, J. J. Tailoring Microporosity in Covalent Organic Frameworks. *Adv. Mater.* **2008**, *20*, 2741-2746.
 144. Miura, A.; De Feyter, S.; Abdel-Mottaleb, M. M. S.; Gesquière, A.; Grim, P. C. M.; Moessner, G.; Sieffert, M.; Klapper, M.; Müllen, K.; De Schryver, F. C. Light- and STM-Tip-Induced Formation of One-Dimensional and Two-Dimensional Organic Nanostructures†. *Langmuir* **2003**, *19*, 6474-6482.
 145. Sullivan, S. P.; Schnieders, A.; Mbugua, S. K.; Beebe, T. P. Controlled Polymerization of Substituted Diacetylene Self-Organized Monolayers Confined in Molecule Corrals. *Langmuir* **2004**, *21*, 1322-1327.
 146. Clair, S.; Ourdjini, O.; Abel, M.; Porte, L. Tip- or electron beam-induced surface polymerization. *Chem. Commun.* **2011**, *47*, 8028-8030.
 147. Hla, S.-W.; Bartels, L.; Meyer, G.; Rieder, K.-H. Inducing All Steps of a Chemical Reaction with the Scanning Tunneling Microscope Tip: Towards Single Molecule Engineering. *Phys. Rev. Lett.* **2000**, *85*, 2777-2780.
 148. Ourdjini, O.; Pawlak, R.; Abel, M.; Clair, S.; Chen, L.; Bergeon, N.; Sassi, M.; Oison, V.; Debierre, J.-M.; Coratger, R.; Porte, L. Substrate-mediated ordering and defect analysis of a surface covalent organic framework. *Phys. Rev. B* **2011**, *84*, 125421.
 149. Bieri, M.; Treier, M.; Cai, J.; Ait-Mansour, K.; Ruffieux, P.; Groning, O.; Groning, P.; Kastler, M.; Rieger, R.; Feng, X.; Müllen, K.; Fasel, R. Porous graphenes: two-dimensional polymer synthesis with atomic precision. *Chem. Commun.* **2009**.
 150. Treier, M.; Richardson, N. V.; Fasel, R. Fabrication of Surface-Supported Low-Dimensional Polyimide Networks. *J. Am. Chem. Soc.* **2008**, *130*, 14054-14055.
 151. Perepichka, D. F.; Rosei, F. Extending Polymer Conjugation into the Second Dimension. *Science* **2009**, *323*, 216-217.
 152. Campbell, N. L.; Clowes, R.; Ritchie, L. K.; Cooper, A. I. Rapid Microwave Synthesis and Purification of Porous Covalent Organic Frameworks. *Chem. Mater.* **2009**, *21*, 204-206.
 153. Wan, S.; Guo, J.; Kim, J.; Ihee, H.; Jiang, D. A photoconductive covalent organic framework: self-condensed arene cubes composed of eclipsed 2D polypyrene sheets for photocurrent generation. *Angew. Chem. Int. Ed.* **2009**, *48*, 5439-5442.
 154. Jiang, D. L.; Wan, S.; Guo, J.; Kim, J.; Ihee, H. A Belt-Shaped, Blue Luminescent, and Semiconducting Covalent Organic Framework. *Angew. Chem. Int. Edit.* **2008**, *47*, 8826-8830.
 155. Nagai, A.; Guo, Z.; Feng, X.; Jin, S.; Chen, X.; Ding, X.; Jiang, D. Pore surface engineering in covalent organic frameworks. *Nat. Commun.* **2011**, *2*, 536.

-
156. Spitler, E. L.; Koo, B. T.; Novotney, J. L.; Colson, J. W.; Uribe-Romo, F. J.; Gutierrez, G. D.; Clancy, P.; Dichtel, W. R. A 2D Covalent Organic Framework with 4.7-nm Pores and Insight into Its Interlayer Stacking. *J. Am. Chem. Soc.* **2011**, *133*, 19416-19421.
157. Feng, X.; Liu, L.; Honsho, Y.; Saeki, A.; Seki, S.; Irle, S.; Dong, Y.; Nagai, A.; Jiang, D. High-Rate Charge-Carrier Transport in Porphyrin Covalent Organic Frameworks: Switching from Hole to Electron to Ambipolar Conduction. *Angew. Chem. Int. Ed.* **2012**, *51*, 2618-2622.
158. Kuhn, P.; Antonietti, M.; Thomas, A. Porous, covalent triazine-based frameworks prepared by ionothermal synthesis. *Angew. Chem. Int. Ed.* **2008**, *47*, 3450-3453.
159. Uribe-Romo, F. J.; Doonan, C. J.; Furukawa, H.; Oisaki, K.; Yaghi, O. M. Crystalline covalent organic frameworks with hydrazone linkages. *J. Am. Chem. Soc.* **2011**, *133*, 11478-11481.
160. Penney, W. G. The Theory of the Stability of the Benzene Ring and Related Compounds. *Proc. R. Soc. Lon. Ser. A* **1934**, *146*, 223-238.
161. Dienstmaier, J. F.; Gigler, A. M.; Goetz, A. J.; Knochel, P.; Bein, T.; Lyapin, A.; Reichmaier, S.; Heckl, W. M.; Lackinger, M. Synthesis of Well-Ordered COF Monolayers: Surface Growth of Nanocrystalline Precursors versus Direct On-Surface Polycondensation. *ACS Nano* **2011**, *5*, 9737-9745.
162. Larson, A. C.; von Dreele, R. B. General Structure Analysis System (GSAS), Los Alamos National Laboratory Report LAUR 86-748. **2000**.
163. Toby, B. H. EXPGUI, a graphical user interface for GSAS. *J. Appl. Crystallogr.* **2001**, *34*, 210-213.
164. Krishnan, K. The Raman spectrum of boric acid. *Proc. Indian. Acad. Sci. (Math. Sci.)* **1963**, *57*, 103-108.
165. Dienstmaier, J. F.; Medina, D. D.; Dogru, M.; Knochel, P.; Bein, T.; Heckl, W. M.; Lackinger, M. Isoreticular Two-Dimensional Covalent Organic Frameworks Synthesized by On-Surface Condensation of Diboronic Acids. *ACS Nano* **2012**, *6* (8), 7234-7242.
166. Birgenau, R. J.; Horn, P. M. Two-Dimensional Rare Gas Solids. *Science* **1986**, *232*, 329-336.
167. Hansen, F. Y.; Frank, V. L. P.; Taub, H.; Bruch, L. W.; Lauter, H. J.; Dennison, J. R. Corrugation in the nitrogen-graphite potential probed by inelastic neutron scattering. *Phys. Rev. Lett.* **1990**, *64*, 764-767.
168. Clinton, W. L.; Esrick, M.; Ruf, H.; Sacks, W. Image potential for stepped and corrugated surfaces. *Phys. Rev. B* **1985**, *31*, 722-726.
169. Todd, M. H.; Balasubramanian, S.; Abell, C. Studies on the Synthesis, Characterisation and Reactivity of Aromatic Diboronic Acids. *Tetrahedron Lett.* **1997**, *38*, 6781-6784.
170. Nishiyabu, R.; Kubo, Y.; James, T. D.; Fossey, J. S. Boronic acid building blocks: tools for self assembly. *Chem. Commun.* **2011**, *47*, 1124-1150.
171. Pawlak, R.; Nony, L.; Bocquet, F.; Olson, V.; Sassi, M.; Debierre, J. M.; Loppacher, C.; Porte, L. Supramolecular Assemblies of 1,4-Benzene Diboronic Acid on KCl(001). *J. Phys. Chem. C* **2010**, *114*, 9290-9295.

-
172. Rodriguez-Cuamatzi, P.; Vargas-Diaz, G.; Maris, T.; Wuest, J. D.; Hopfl, H. 1,4-Phenylenediboronic acid. *Acta Crystallogr. E* **2004**, *60*, o1316-o1318.
173. Coratger, R.; Calmettes, B.; Abel, M.; Porte, L. STM observations of the first polymerization steps between hexahydroxy-tri-phenylene and benzene-di-boronic acid molecules. *Surf. Sci.* **2011**, *605*, 831-837.
174. Blunt, M. O.; Russell, J. C.; Champness, N. R.; Beton, P. H. Templating molecular adsorption using a covalent organic framework. *Chem. Commun.* **2010**, *46*, 7157-7159.
175. Lipton-Duffin, J. A.; Ivashenko, O.; Perepichka, D. F.; Rosei, F. Synthesis of Polyphenylene Molecular Wires by Surface-Confined Polymerization. *Small* **2009**, *5*, 592-597.
176. Tilford, R. W.; Gemmill, W. R.; zur Loye, H. C.; Lavigne, J. J. Facile synthesis of a highly crystalline, covalently linked porous boronate network. *Chem. Mater.* **2006**, *18*, 5296-5301.
177. Lanni, L. M.; Tilford, R. W.; Bharathy, M.; Lavigne, J. J. Enhanced Hydrolytic Stability of Self-Assembling Alkylated Two-Dimensional Covalent Organic Frameworks. *J. Am. Chem. Soc.* **2011**, *133*, 13975-13983.
178. Spitler, E. L.; Giovino, M. R.; White, S. L.; Dichtel, W. R. A mechanistic study of Lewis acid-catalyzed covalent organic framework formation. *Chemical Science* **2011**, *2*, 1588-1593.
179. Du, Y.; Mao, K.; Kamakoti, P.; Ravikovitch, P.; Paur, C.; Cundy, S.; Li, Q.; Calabro, D. Experimental and computational studies of pyridine-assisted post-synthesis modified air stable covalent-organic frameworks. *Chem. Commun.* **2012**, *48*, 4606-4608.
180. Heininger, C.; Kampschulte, L.; Heckl, W. M.; Lackinger, M. Distinct Differences in Self-Assembly of Aromatic Linear Dicarboxylic Acids. *Langmuir* **2008**, *25*, 968-972.
181. Bhat, K. L.; Markham, G. D.; Larkin, J. D.; Bock, C. W. Thermodynamics of Boroxine Formation from the Aliphatic Boronic Acid Monomers R-B(OH)₂ (R = H, H₃C, H₂N, HO, and F): A Computational Investigation. *J. Phys. Chem. A* **2011**, *115*, 7785-7793.
182. Oliveira, M. B.; Pratas, M. J.; Marrucho, I. M.; Queimada, A. J.; Coutinho, J. A. P. Description of the mutual solubilities of fatty acids and water with the CPA EoS. *AIChE J.* **2009**, *55*, 1604-1613.
183. Guan, C.-Z.; Wang, D.; Wan, L.-J. Construction and repair of highly ordered 2D covalent networks by chemical equilibrium regulation. *Chem. Commun.* **2012**, *48*, 2943-2945.
184. Semaltianos, N. G.; Wilson, E. G. Investigation of the surface morphology of thermally evaporated thin gold films on mica, glass, silicon and calcium fluoride substrates by scanning tunneling microscopy. *Thin Solid Films* **2000**, *366*, 111-116.
185. Higginbotham, I. G.; Williams, R. H.; McEvoy, A. J. Metal/non-metal interfaces: adhesion of gold on mica. *J. Phy. D. Appl. Phys.* **1975**, *8*, 1033.
186. Levlin, M.; Laakso, A.; Niemi, H. E. M.; Hautojärvi, P. Evaporation of gold thin films on mica: effect of evaporation parameters. *Appl. Surf. Sci.* **1997**, *115*, 31-38.
187. Smith, D. L. *Thin-Film Deposition. Principles and Practice*; McGraw-Hill, **1995**.

-
188. Höpfner, U.; Hehl, H.; Brehmer, L. Preparation of ordered thin gold films. *Appl. Surf. Sci.* **1999**, *152*, 259-265.
189. Horcas, I.; Fernandez, R.; Gomez-Rodriguez, J. M.; Colchero, J.; Gomez-Herrero, J.; Baro, A. M. WSXM: A software for scanning probe microscopy and a tool for nanotechnology. *Rev. Sci. Instrum.* **2007**, *78*, 013705.
190. Dishner, M. H.; Ivey, M. M.; Gorer, S.; Hemminger, J. C.; Feher, F. J. Preparation of gold thin films by epitaxial growth on mica and the effect of flame annealing. *J. Vac. Sci. Technol. A.* **1998**, *16*, 3295-3300.
191. Zhang, H.-M.; Yan, J.-W.; Xie, Z.-X.; Mao, B.-W.; Xu, X. Self-Assembly of Alkanols on Au(111) Surfaces. *Chem. Eur. J.* **2006**, *12*, 4006-4013.

Acknowledgements

I would like here to thank all the people that helped me during the course of these years to make this work possible. First of all I would like to thank Prof. Wolfgang Heckl. He gave me the opportunity to work in his STM research group. Also no less important, Markus Lackinger, leader of the STM group, contacted me from afar and invited me to join the group. Above all, he gave me enough freedom and many resources to pursue original and creative work, which was probably the most motivating part of this thesis. He also gave me constant support and advice in scientific and technical issues, as well as in some that were plain and simple common daily life problems.

I would also thank Prof. Stefan Sotier, with whom I worked almost from the beginning of my time in the group. He specially helped me with the technicalities of gold deposition via PVD in the small vacuum chamber. He was always eager to try new ideas, modifications and refinements of the methods.

I would also like to thank my other fellow members in the group. Starting with Rico Gutzler, who, aided by our common knowledge of Spanish, taught me the practicalities of the STM, and many details of the molecular modeling software. Christoph Heininger, with whom lots of ideas were discussed, theoretical and practical. Some of them are still lacking solution. He also taught me the fine and subtle details of STM image acquisition, and proof read this thesis. Hermann Walch, with whom I learned almost everything from the “big” vacuum chamber. He always had a good mood in every situation, and made us laugh a lot. Georg Eder, always paying attention to the smallest bureaucratic detail. Stephan Kloft, for building a reliable ambient STM, to which I was first skeptic. Thomas Sirtl, our popular Thommy, revolutionizing the world for good. Marek Janko, organizer of extracurricular activities on Friday evenings, attended by everybody. Alex Gigler, for the Raman measurements, among other things. And the other people in the group and around us that helped in this or the other way: Michael Bauer, Stefan Schlögl, Mark Hennemeyer, Johanna Eichhorn, Andreas Götz, Wentao Song, and Atena Rastgoo. They always produced a very friendly atmosphere to encourage work.

Other people I would like to thank are Dana Medina. Together we made a very hard working team, achieving results in a relative short time. Mirjam Dogru from LMU Großhadern, and Prof. Michael Schmittel and his research group at the University of Siegen, They provided many of the molecular building blocks used in this work. Günter Hesberg, from the fine mechanical workshop at the LMU. With him I learned to use computer-aided design software to later build mechanical parts. He also contributed to this work by improving many of my original designs. Max Häberle and Detlef Körner, from the electric workshop, installed heavy duty cable wires for the small vacuum chamber, fixed shorted resistors, and repaired controllers.

Finally I want to acknowledge the unconditional support from my beloved wife Maricarmen. She waited patiently for me when I stayed working late at night acquiring STM images. My daughter Silke, which has not seen me for long hours during the high hours of this work. Also my parents, who visited me several times during these years. I am grateful for their everlasting support during this time.

Curriculum Vitae

Name: Jürgen Franz Dienstmaier Patten

Birth: 15. December, 1975; in Lima, Peru.

University Studies

Since 2007: PhD candidate, LMU Munich

2006: Master in Material Sciences, TU Ilmenau

2004 – 2006: Further studies in Material Science, TU Ilmenau (TU Ilmenau – PUCP exchange program)

2002 – 2003: Studies of the Master in Material Sciences and Engineering, PUCP; Lima, Peru

1994 – 2001: Studies of Chemistry, Pontificia Universidad Católica del Perú (PUCP); Lima, Peru

Education

1987 – 1992: Secondary School, Colegio Nuestra Señora del Carmen (Carmelitas); Lima, Peru

1982 – 1987: Primary School, Colegio Nuestra Señora del Carmen (Carmelitas); Lima, Peru

Practical Experience

2006 – 2007: Quality Control Department at Kerzenperu; Lima, Peru

2005: Working student, TU Ilmenau

2000 – 2004: Academic assistant of chemistry courses, Estudios Generales Ciencias, PUCP

2003 – 2004: Research assistant, Polymers and Composites Group (POLyCOM), PUCP

2002 – 2003: Instructor, Ciclo Inicial Department, PUCP

2001: Internship, Quality Control Department, Unión de Cervecerías Peruanas Backus y Johnston S. A. A.; Lima, Peru

2000: Internship, Quality Control, Maltería Lima S. A.; Lima, Peru